

Inelastic Tunneling in Superconducting Junctions

Zur Erlangung des akademischen Grades eines
DOKTORS DER NATURWISSENSCHAFTEN
der Fakultät für Physik
des Karlsruher Instituts für Technologie

genehmigte

DISSERTATION

von
Dipl.-Phys. Patrik Christian Hlobil
aus Karlsruhe

Tag der mündlichen Prüfung: 10. Juni 2016

Referent: Prof. Dr. Jörg Schmalian
Korreferent: Prof. Dr. Wulf Wulfhekel



This document is licensed under the Creative Commons Attribution 3.0 DE License
(CC BY 3.0 DE): <http://creativecommons.org/licenses/by/3.0/de/>

*To my family.
For their constant support and advice.*

*To my wife.
For her love and patience.*

*To my son Sam.
For just being there and brightening our lives.*

Introduction

The superconducting condensate might be the most fascinating state of matter and the investigation of superconducting materials has given important insights into the quantum nature of condensed matter systems. When cooling a superconductor below its transition temperature T_c it shows two unique properties. Firstly, superconductors are capable of carrying a dissipationless current, which was first discovered by Kamerlingh Onnes in 1911 [1, 2]. Secondly, a superconductor expels any magnetic field from its interior. This perfect diamagnetism¹ is known as the Meissner-Ochsenfeld effect [3]. The possible applications of superconductors are diverse: lossless electrical networks for energy transportation [4], high magnetic field coils for particle accelerators, materials research and medical uses, etc. Although experimental verification for superconductivity has been found for various different materials, a coherent theoretical description has been lacking for almost half a century. Early phenomenological approaches by the London brothers [5], W. Ginsburg and L Landau [6] could successfully describe the macroscopic properties of superconductors. However, a rigorous microscopic description known as the famous BCS theory [7, 8] has finally been developed by J. Bardeen, R. Schrieffer and L. Cooper in 1957. They realized that the interaction of the electrons with phonons, that describe the collective oscillations of the positively charged atomic lattice, can lead to an effective attraction between the otherwise repulsive electrons. This leads to a bound state of two electrons with opposite momenta and spin called a Cooper pair. The Cooper pairs then condense to the BCS ground state, where the bounded electrons open a gap at the Fermi surface and give rise to long-range phase coherence, that naturally explains the observed phenomena.

Soon, extensions of the BCS theory like the Eliashberg-Migdal theory [9, 10] have been formulated, which added realistic electron-phonon interaction and phonon dispersions to the BCS theory. This particular theory is also capable of describing systems with strong-coupling between the electrons and the lattice vibrations such as Pb. For conventional superconductors, which are defined in the following as materials where the superconductivity is mediated by electron-phonon interaction (e.g. Al, Pb and MgB_2), such an extended BCS theory was extremely successful in describing a large variety of experimental observations. These include specific heat experiments, transition temperatures, critical magnetic fields, optical conductivity measurements, etc [11, 12]. A huge contribution to the quantitative understanding of conventional superconductivity have been the intensive studies of superconducting tunneling junctions starting in the early 1960s. The underlying concept is called Elastic Electron Tunneling Spectroscopy (EETS). Applying a finite bias between the

¹Actually, a superconductor is not just a perfect diamagnet, because the superconducting state is thermodynamic. Therefore, a static magnetic field is also expelled when starting in the normal state and cooling below T_c .

two electrodes of a tunneling junction allows to extract important information about the electronic spectrum of the materials. Effectively, one probes the number of electrons at the Fermi surface that can tunnel *elastically* to the opposite electrode. For a Superconductor-Insulator-Normalconductor (SIN) junction the conductance $\sigma(V) = dI(V)/dV$ of such a device is, under some assumptions, proportional to the electronic density of states (DOS) of the superconductor [13, 14]. In the pioneering work of Rowell and McMillan detailed information about the electron-phonon interaction and phonon spectrum in Pb could be gained from the fine structure of the tunneling conductance [15]. The quantitative agreement between the experimental tunneling data and the predictions of the Eliashberg theory in this particular case as well as for various other conventional superconductors [16] counts as a hallmark of condensed matter physics.

However, the elastic tunneling picture is incomplete as additional *inelastic* tunneling processes alter the interpretation of the tunneling conductance as the DOS of the investigated metal. Inelastic transitions in tunneling junctions, where an electron emits a bosonic excitation during the tunneling process, has been observed first by Lambe and Jaklevic [17, 18]. The so-called Inelastic Electron Tunneling Spectroscopy (IETS) can be used as an alternative way to determine phonon [19, 20] and magnon spectra [21–23]. Usually, the IETS experiments are performed in the normal state and the second derivative $d^2I(V)/dV^2$ of the tunneling current with respect to the bias voltage is, within some rather general assumptions, proportional to the bosonic spectrum of the material. This is a more direct way to extract the dynamics of the relevant bosonic excitations of a system than the comparison of the tunneling conductance with the predictions of the Eliashberg theory. In Ref. [19] it has been shown that using a Scanning Tunneling Microscope (STM) instead of a planar junction, inelastic processes may be enhanced by one order of magnitude. In the case of Pb tunneling, the inelastic features in the conductance are then of the same order as the strong-coupling features predicted by the Eliashberg theory. This implies, that the inclusion of inelastic events for the interpretation of tunneling data in conventional(phonon-mediated) superconductors is essential and one has to use a generalized analysis combining elastic and inelastic tunneling processes. The feasibility of such an analysis has been explicitly shown in Ref. [24] for STM on Pb.

This poses the question if one also has to use such a combined tunneling theory including elastic and inelastic processes for the accurate interpretation of tunneling data in unconventional superconductors. In unconventional superconductors, such as the cuprates and iron-pnictides, the Cooper pairing is believed to be mediated by an electronic pairing glue made of collective particle-hole spin fluctuations. Importantly, due to the electronic origin of the collective spin fluctuations, the bosonic spectrum undergoes a significant change when entering the superconducting state. In contrast to conventional superconductors, where the inelastic conductance is only slightly changed below T_c , the inelastic spectrum for unconventional superconductors is expected to differ strongly between the normal and superconducting state. On the one hand, this complicates the analysis, because one first has to separate elastic from inelastic contributions as the measured conductance is the sum of both channels. On the other hand, this opens up the possibility for a direct determination of the spectrum of the superconducting pairing glue in the high- T_c materials using IETS. Thus, such a combined analysis can be used to verify the nature of the superconducting pairing in the unconventional superconductors, a question that remains open at least for many of the more recently discovered iron-based superconductors.

This main part of this thesis captures the theoretical description of tunneling and its

application to both conventional and unconventional superconductors. Besides the formal derivation of the elastic and inelastic tunneling currents, it is shown that the inelastic transitions come from processes that are not captured in the low-energy description of the BCS theory of superconductivity. Another focus of this work is the actual interpretation of real tunneling data, which is performed explicitly for the example of the phonon-mediated superconductor Pb. For unconventional superconductors the attention is concentrated on materials that show a pronounced V-shaped background conductance up to high energies, which is demonstrated to originate from inelastic tunneling events involving spin fluctuations and not from the electronic DOS.

Furthermore, a closely related topic is covered. Inelastic optical transitions in a semi-conducting p - n junction that is coupled to superconducting leads are studied. Such a Superconducting Light Emitting Diode (SLED) can be described by a theoretical model very similar to that of inelastic tunneling. The main motivation for the investigation of superconductor-semiconductor heterostructures is to combine the unique properties of the two kinds of materials: (i) The capabilities of semiconductors to serve as elements for electrical circuits, e.g. as diodes and transistors, (ii) The phase coherence of the superconducting condensate and the quantum-entanglement of the Cooper pairs. The light of such an SLED may show promising properties such as an squeezing and an enhanced luminescence.

The dissertation is structured in the following way:

The first two chapters introduce the fundamentals for the remainder of the thesis. In **Chapter 1** the basic concept of tunneling is introduced as well as the distinction between elastic and inelastic tunneling processes. The main focus of this chapter lies on superconductor tunneling. Important tunneling experiments in both conventional and unconventional superconductors on planar junctions and STM are presented. In **Chapter 2** the BCS theory is summarized. Furthermore, an overview over important extensions of the BCS theory is presented. The Eliashberg-Migdal theory of strong-coupling superconductivity is derived in detail from a microscopic model involving general electron-phonon interactions. It is then applied to a simple model of a single phonon mode to understand the features in the electronic DOS expected for more realistic phonon spectra. Hereafter, the Eliashberg theory is generalized to systems with electronic pairing glues, e.g. spin fluctuations, and the spin-fermion model is introduced as a phenomenological theory for unconventional superconductors. Finally, motivated by the cuprates the special case of strong-coupling d -wave superconductivity is discussed. In **Chapter 3** a tunneling Hamiltonian that involves both elastic and inelastic tunneling processes is explicitly derived. It is shown that inelastic processes naturally occur for the low-energy theory when integrating out high-energy electronic states far away from the Fermi surface of the superconductor. Thus, when also considering inelastic tunneling processes the low-energy Eliashberg theory can still be used to calculate the electronic DOS for superconducting tunneling. The effective low-energy Hamiltonian is then used to determine explicit expressions for the elastic and inelastic tunneling current, followed by a normal state analysis of the theory of IETS. Subsequently, Chapter 4 and 5 are dedicated to the experimental interpretation of tunneling data in conventional and unconventional superconductors. In **Chapter 4** it is shown that the inelastic tunneling theory is capable of explaining the phonon spectra seen in the $d^2I(V)/dV^2$ spectra of planar junction and STM experiments of conventional superconductors in the normal state. Based on the example of a single phonon mode, typical features that arise from elastic and inelastic tunneling in the spectra of conventional superconductors are discussed. Finally, a

combined analysis of elastic and inelastic tunneling is applied to recent data from STM experiments on Pb [24]. The agreement between theory and experiment demonstrates the potential of the tunneling formalism developed in Chapter 3 for the investigation of experimental tunneling data. The application of the extended tunneling theory to unconventional superconductors is then presented in **Chapter 5**. The striking similarities between the theoretical predictions of the spin-fermion model [25] and spectra of various different cuprate and iron-pnictide superconductors motivate for a common physical pairing mechanism via spin fluctuations. In particular, the occurring peak-dip-hump features in the tunneling spectra for $\text{YBa}_2\text{Cu}_3\text{O}_{7-\delta}$ (YBCO) and LiFeAs are traced back to the change of the spin excitation spectrum when entering the superconducting state. The position of this mode is consistent with the spin fluctuation model of superconductivity, indicating a non-conventional pairing state in this material. The final **Chapter 6** covers the theoretical analysis of the SLED. In particular, the feedback on the emitted light from the superconducting quasiparticles is calculated for the SLED in the steady state. The differences in the electro luminescence in the normal and superconducting state are considered, as well as the squeezing and entanglement character of the emitted photons.

Basic information about the used notation and acronyms are given on page 113 and 115.

Contents

Introduction	v
1. Fundamentals I: History of electronic tunneling into superconductors	1
1.1. Elastic Electron Tunneling Spectroscopy	1
1.1.1. Transfer Hamiltonian	2
1.1.2. Rowell-McMillan Inversion and phonon spectrum	4
1.1.3. Scanning Tunneling Microscopy	5
1.2. Inelastic Electron Tunneling Spectroscopy	6
1.3. Experiments in unconventional superconductors	8
1.3.1. Properties of unconventional superconductors	8
1.3.2. Tunneling spectra of unconventional superconductors	10
2. Fundamentals II: Theory of strong-coupling superconductivity	15
2.1. The Theory of Bardeen, Cooper and Schrieffer	15
2.2. Migdal-Eliashberg theory of superconductivity	18
2.2.1. Electron-phonon interaction and Migdal theorem	19
2.2.2. Eliashberg equations	21
2.2.3. Strong-coupling superconductivity for single phonon mode	24
2.3. Superconductivity from electronic pairing	27
2.3.1. Spin-fermion model	27
2.3.2. Eliashberg formalism for d-wave superconductivity	31
3. Theoretical description of elastic & inelastic electron tunneling	35
3.1. Derivation of the effective tunneling Hamiltonian	35
3.2. Elastic and inelastic tunneling currents	42
3.2.1. Elastic tunneling	44
3.2.2. Inelastic tunneling	45
3.3. IETS in the normal state	45
4. Inelastic tunneling in conventional superconductors	49
4.1. Normal-state IETS with phonons	49
4.1.1. Estimate of the inelastic contribution for phonons	50
4.1.2. Comparison of $\alpha^2 F_{\text{tun}}$ and $\alpha^2 F$	52
4.2. Elastic and inelastic STM for single phonon mode	55
4.2.1. IETS of barrier molecules for superconducting junctions	57
4.2.2. Normalization procedure of Rowell and McMillan	58
4.3. STM on normal- and superconducting Pb films	59
4.3.1. Normal state	60
4.3.2. Superconducting state	64

5. Tunneling in unconventional superconductors	69
5.1. Nature of the background conductance in the normal state	69
5.2. Tunneling spectra in the spin-fermion model	72
5.2.1. Inelastic tunneling as the origin of the peak-dip-hump feature in unconventional superconductors	72
5.2.2. Normalized conductance	76
5.3. Revisiting tunnel experiments in unconventional superconductors	78
5.3.1. LiFeAs: A particle-hole asymmetric superconductor	78
5.3.2. YBCO	79
5.3.3. Asymmetric matrix element for inelastic tunneling	81
5.4. Conclusion of Chapter 5	83
6. Superconducting Light Emitting Diode	85
6.1. Modeling the SLED	85
6.1.1. SLED Hamiltonian	85
6.1.2. Energy scales of the system	87
6.2. Effective photon action	88
6.2.1. Derivation of effective photon action	88
6.2.2. Electronic feedback	91
6.2.2.1. Normal conducting leads	91
6.2.2.2. Superconducting leads	93
6.2.3. Role of the photon bath	95
6.2.4. Photon propagators	96
6.3. Luminescence and Squeezing of the SLED	96
6.3.1. Luminescence	96
6.3.2. Photon squeezing	98
6.4. Steady state and LASER condition	100
6.4.1. Lasing condition from effective action	100
6.4.2. Rate equation approach	102
6.5. Conclusion of Chapter 6	105
Conclusion	107
Acknowledgements	111
Notation	113
Acronyms	115
Appendix	117
A. Hot-spot theory	117
A.1. Derivation of Eliashberg equations for spin-mediated superconductivity	117
A.2. Linearization at the hot-spots	119
B. Derivation of elastic and inelastic tunneling currents	121
C. Keldysh perturbation theory	126
C.1. Closed time contour	126
C.2. Keldysh path integral formalism	128
D. SLED calculations	131
D.1. Integrating out the electrons and bath	131
D.2. Calculation of the $\hat{\Pi}^{\text{el}}$ self-energies	132
D.2.1. Normal conductor	133

D.2.2. Superconductor 134

Bibliography **137**

1. Fundamentals I: History of electronic tunneling into superconductors

In this chapter we introduce the concept of electron tunneling into superconductors, which serves as a starting point for the theoretical analysis in the subsequent chapters. We begin with the early experiments in the 1960's into conventional superconductors and end with the modern Scanning Tunneling Microscopy (STM) experiments on correlated materials, such as the high-temperature superconductors. We discuss the theoretical interpretation based on elastic tunneling processes from one electrode to the other, which can be captured by the concept of the transfer or tunneling Hamiltonian. Consequently, we present a short discussion about the groundbreaking work by Rowell and McMillan, which used the fine structure in superconductor tunneling data to extract detailed information about the spectrum of the bosonic pairing glue of the investigated superconductors. After giving a short description of STM, we will consider the possibility of inelastic tunneling including the emission of a collective boson and discuss the current experimental situation. Finally, a short summary of the unconventional cuprate and iron pnictide superconductors is given followed by an experimental survey of tunneling data in these systems.

1.1. Elastic Electron Tunneling Spectroscopy

The success of the BCS theory¹, which explains most of the thermodynamic and macroscopic properties of weakly coupled superconductors (e.g. specific heat, Meissner effect, zero resistance), was followed in 1960 by a striking experiment by Giaever [26]. He showed that the derivative of the current-voltage characteristic of an SIN junction reflects the BCS DOS, see Figure 1.1. In this way, planar junction experiments were discovered as a tool to directly probe the electronic excitation spectra of materials. Soon theoretical models were found that could explain this behavior by Bardeen [13] and Cohen et al. [14], who introduced the so-called transfer Hamiltonian approach for electron tunneling, see the following discussion below. Let us start by giving a short phenomenological approach to Elastic Electron Tun-

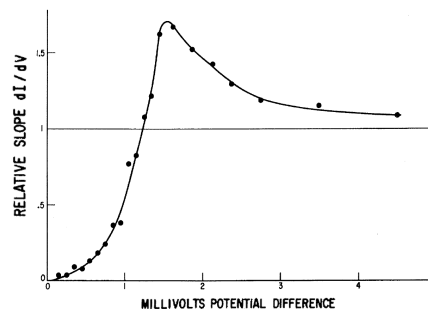


Figure 1.1.: Conductance dI/dV for the Pb-Al₂O₃-Al junction (SIN) for $T = 1.6K > T_{c,Al}$ normalized to the conductance measured for normal conducting Pb. Taken from [26].

¹For a brief introduction see Section 2.1.

neling Spectroscopy (EETS) into solids. Consider the **elastic** tunneling from electronic states $|l\rangle$ of a left electrode to states $|r\rangle$ in a right electrode with applied bias voltage V . One can use Fermi's Golden Rule to write down the expected tunneling current from the left to the right electrode as [27]

$$\begin{aligned} I^e(V) &= 2e \cdot 2\pi \sum_{l,r} |\langle l | \hat{T} | r \rangle|^2 \delta(\epsilon_l - eV - \epsilon_r) \left\{ n_F(\epsilon_l) [1 - n_F(\epsilon_r)] - [1 - n_F(\epsilon_l)] n_F(\epsilon_r) \right\} \\ &= 4\pi |t^e|^2 e \int d\epsilon \nu_l(\epsilon) \nu_r(\epsilon - V) \left\{ n_F(\epsilon) - n_F(\epsilon - eV) \right\}. \end{aligned} \quad (1.1)$$

Here, \hat{T} is the Hamiltonian describing the isolator/tunneling region, $\epsilon_{l/r}$ are the quasiparticle energies of the states $|l/r\rangle$ and $\nu_{l/r}$ the DOS in the left and right electrodes. One has to multiply the result with $2e$ because of the charge and spin of the electrons and also that all matrix elements are equal. We note that the time interval between two tunneling events has to be much smaller than the typical relaxation times in the materials, such that the electronic distributions of the electrodes stay unaffected by the tunneling current. Let us now consider the case where the left electrode is superconducting and the right electrode a normal conductor with a flat DOS $\nu_r(\epsilon) = \nu_r^0$ around the Fermi surface. The (differential) conductance $\sigma(V) = dI/dV$ is for the low temperature limit then proportional to the superconducting DOS:

$$\sigma^e(V) = -4\pi \nu_r^0 |t^e|^2 e^2 \int d\epsilon \nu_l(\epsilon) n'_F(\epsilon - eV) \stackrel{T \rightarrow 0}{=} 4\pi \nu_r^0 |t^e|^2 e^2 \nu_l(eV). \quad (1.2)$$

In Figure 1.2 a sketch of the elastic tunneling is shown including the expected I-V and conductance curves. The net current comes from occupied right states that can tunnel through the barrier to the left electrode and find an empty state with equal energy there. If the electronic spectra of the electrodes are flat for the applied bias, the current is expected to behave ohmic $I \sim V$. Deviations from this behavior are expected if e.g. the electronic DOS of the left electrode has some structure, as is indicated in Figure 1.2. If we increase the voltage from $V \rightarrow V + dV$ the change dI of the current is proportional to the additional empty states dN_l in the left electrode, thus the conductance is given by $dI/dV \sim dN_l/d(eV) = \nu_l(eV)$. The SIN planar junction experiment in Figure 1.1 is exactly such a system since the Al-electrode has a constant DOS for the small applied bias range $eV \sim \Delta$.

1.1.1. Transfer Hamiltonian

After Bardeen [13] introduced the transfer Hamiltonian to describe tunneling phenomena in (interacting) many-body systems, Cohen et al. [14] used a second-quantized version to derive the formula (1.1). The starting point for the derivation of the transfer Hamiltonian is the independent electron assumption where one separates the initial system into three regions: The left electrode (\mathcal{H}_l for $x < -a$), the barrier (\mathcal{H}_B for $-a < x < a$) and the right electrode (\mathcal{H}_r for $x > a$). Thus, the total system is described by $\mathcal{H} = \mathcal{H}_l + \mathcal{H}_B + \mathcal{H}_r$. The corresponding wavefunctions are defined as $\psi_n^{l/r}$ for the left and right subsystem ² as the eigenstates

$$\underbrace{(\mathcal{H}_{l/r} + \mathcal{H}_B)}_{\tilde{\mathcal{H}}_{l/r}} | \psi_n^{l/r} \rangle = \epsilon_n^{l/r} | \psi_n^{l/r} \rangle. \quad (1.3)$$

²Note that the two electrodes do form two sets of non-orthogonal states and are therefore **not** independent. However, it was shown by Prange [28] that the assumptions made in the derivation of the transfer Hamiltonian are controlled when performing a perturbation theory in the tunneling amplitude.

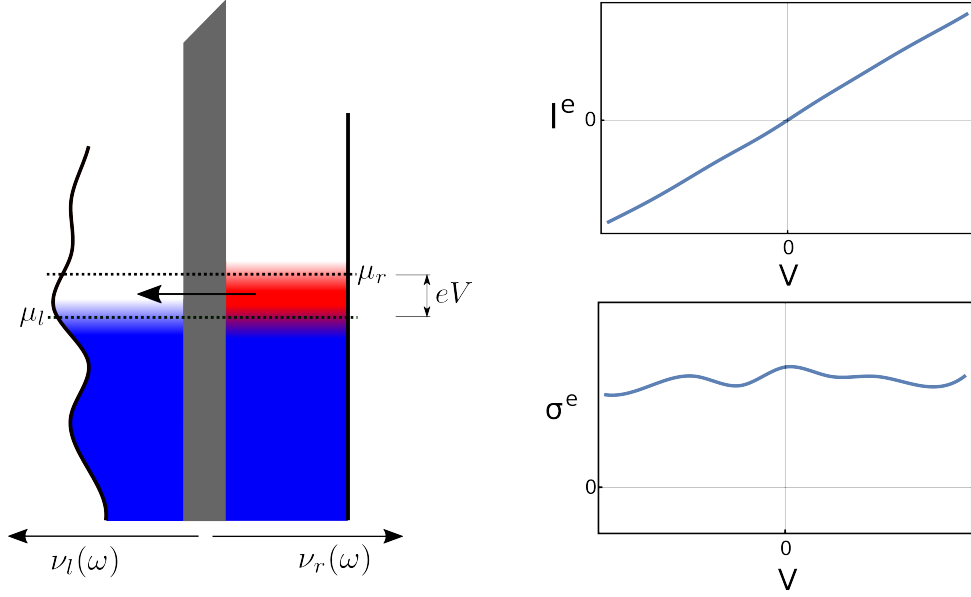


Figure 1.2.: Sketch of elastic tunneling and the expected current and conductance if the spectrum of the right electrode is flat. The conductance is a measure of the additional empty states dN_l in which the electrons of the right electrode can tunnel to if we increase the voltage by $d(eV)$, thus $\sigma \sim dN_l/d(eV) = \nu_l(eV)$.

Here, n are the quantum numbers of the left and right systems. Let us now look at the influence of the right Hamiltonian \mathcal{H}_r for the left states $|\psi_n^l\rangle$. The corresponding matrix element for the transition $|\psi_n^l\rangle \rightarrow |\psi_m^r\rangle$ is given by

$$t_{m,n}^e = \langle \psi_m^r | \mathcal{H}_r | \psi_n^l \rangle = \int_a^\infty dx [\psi_m^r(x)]^* \underbrace{\mathcal{H}_r}_{\mathcal{H} - \tilde{\mathcal{H}}_l} \psi_n^l(x) = \int_a^\infty dx [\psi_m^r(x)]^* [\mathcal{H} - \epsilon_n^l] \psi_n^l(x).$$

In order to bring this to a more convenient form, we add a zero via

$$\begin{aligned} 0 &= - \int_a^\infty dx \psi_n^l(x) \mathcal{H}_l [\psi_m^r(x)]^* = - \int_a^\infty dx \psi_n^l(x) (\mathcal{H} - \tilde{\mathcal{H}}_r) [\psi_m^r(x)]^* \\ &= \int_a^\infty dx [\psi_m^r(x)]^* \epsilon_m^r \psi_n^l(x) - \int_a^\infty dx \psi_n^l(x) \mathcal{H} [\psi_m^r(x)]^*, \end{aligned}$$

where we used the fact that H_l is restricted to the region $x < -a$. If we consider only elastic transitions with $\epsilon_n^l = \epsilon_m^r$, the matrix element reads

$$\begin{aligned} t_{m,n}^e &= \int_a^\infty dx [\psi_m^r(x)]^* [\mathcal{H} - \epsilon_n^l + \epsilon_m^r] \psi_n^l(x) - \int_a^\infty dx \psi_n^l(x) \mathcal{H} [\psi_m^r(x)]^* \\ &= \int_a^\infty dx \left([\psi_m^r(x)]^* \mathcal{H} \psi_n^l(x) - \psi_n^l(x) \mathcal{H} [\psi_m^r(x)]^* \right). \end{aligned} \quad (1.4)$$

Using the usual form $\mathcal{H} = \hat{p}^2/2m + U(\hat{x})$ for the Hamiltonian and Green's theorem one can link this expression to the current density operator. The inverse process where an electron tunnels from the right to the left electrode corresponds to the complex conjugate of this expression. There are several different approaches to calculate the tunneling matrix element for realistic systems, for example using the Wentzel-Kramers-Brillouin (WKB) approximation or boundary conditions, which can be found in the rich literature [27, 29].

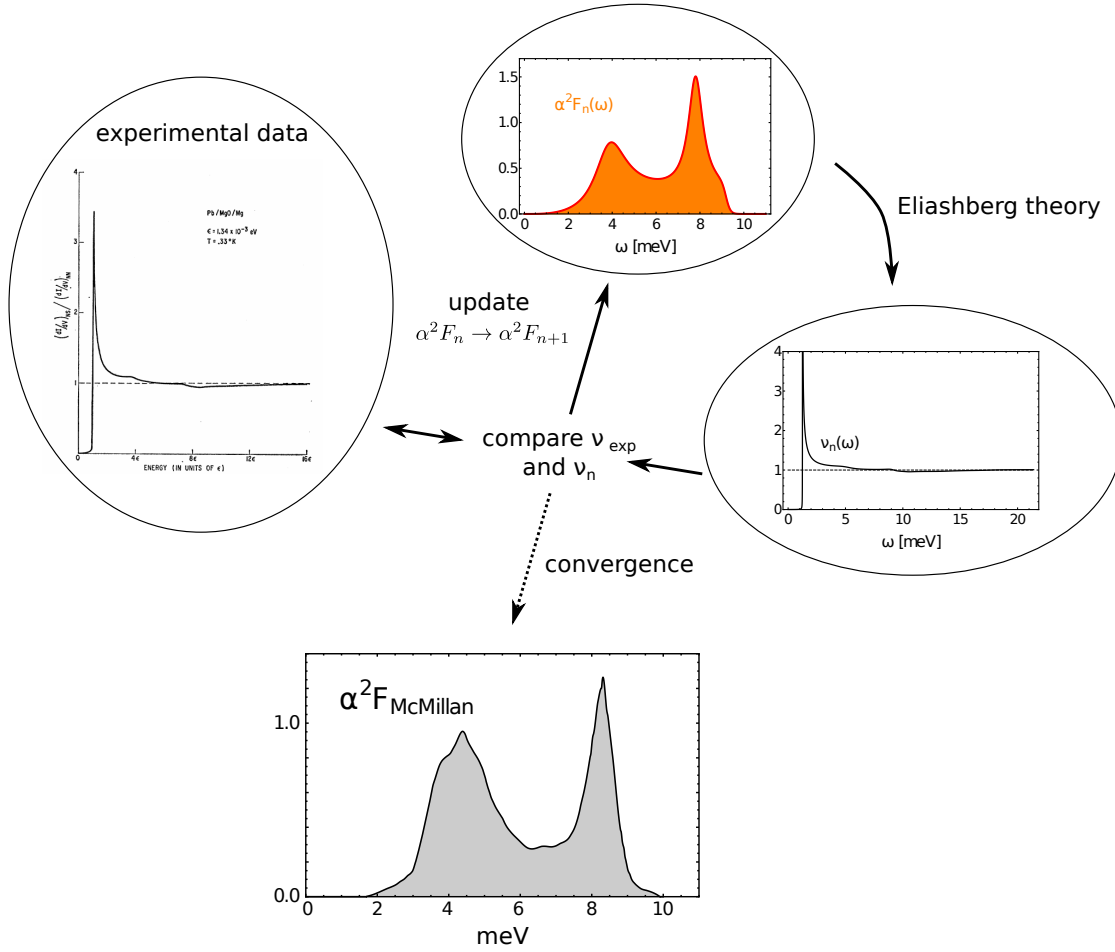


Figure 1.3.: Scheme of the iterative steps of the McMillan gap inversion algorithm for the determination of the Eliashberg function $\alpha^2 F(\omega)$: Shown are the experimental data for the tunneling DOS (left) from Giaever et al. [30] and the Eliashberg function (bottom) obtained from Rowell and McMillan for Pb [11, 15].

To leading order in the tunneling element $t_{m,n}^e$ the Hamiltonian can be written in second quantized form as the **transfer Hamiltonian**

$$\begin{aligned} \mathcal{H} &\approx \sum_n \epsilon_n^l \hat{l}_n^\dagger \hat{l}_n + \sum_m \epsilon_m^r \hat{r}_m^\dagger \hat{r}_m + \sum_{n,m} [t_{m,n}^e \hat{r}_m^\dagger \hat{l}_n + \text{h.c.}] \\ &= \tilde{\mathcal{H}}_l + \tilde{\mathcal{H}}_r + \mathcal{H}_t^e. \end{aligned} \quad (1.5)$$

Here, \hat{l}, \hat{r} are the annihilation operators of the left and right states defined above. In Chapter 3 we show that a perturbative calculation of this transfer Hamiltonian yields the expression (1.1) originally derived from the phenomenological approach.

1.1.2. Rowell-McMillan Inversion and phonon spectrum

Many important conventional superconductors, e.g. lead and niobium, have strong electron-phonon couplings and show strong deviations from the predictions of the weak-coupling BCS theory. The first sign of this strong-coupling nature in superconductor tunneling experiments was seen by Giaever et al. [30] in 1962 as peak-dip features in the tunneling DOS of Pb. Later, Rowell and Anderson [31] showed that these features occur at the typical

transversal and longitudinal phonon frequencies $\omega_{t/l}$ shifted by the superconducting gap Δ_0 . The experimental data were taken at low temperatures $T = 1\text{K}$ and are shown in the left frame of Figure 1.3. The theory that describes strong-coupling superconductors is the Eliashberg theory [9, 10] that was developed in 1960 as an extension of the BCS theory to realistic phonon spectra. In Chapter 2 we present both the BCS theory and the Eliashberg theory in detail. The Eliashberg theory requires only two dimensionless quantities for the calculation the superconducting spectra and properties: The Eliashberg function $\alpha^2F(\omega)$ describing an effective, weighted phonon DOS to which the electrons at the Fermi surface couple to and the Coulomb pseudopotential μ^* taking care of the repulsive interaction between the electrons. Typically, $\alpha^2F(\omega)$ turns out to be very similar to the phonon DOS and μ^* has a rather universal value for most of the simple metals and alloys [16].

In the beautiful work of Rowell and McMillan [15] it was shown how to extract both α^2F and μ^* from tunneling experiments for a Pb-I-Pb junction (Superconductor-Insulator-Superconductor/SIS). The principle idea of the so-called McMillan gap inversion algorithm is shown in Figure 1.3. One starts from a guessed $\alpha^2F_0(\omega)$ function, which is normally based on the phonon DOS from calculations or neutron-scattering experiments. The value of the Coulomb pseudopotential is then chosen in such a way that the Eliashberg theory gives the correct gap value Δ_0 [11]. Using the obtained DOS and the formula (1.1) one can now compute the expected tunneling spectrum and compare it to the experimental data. With a functional derivative method $\delta\nu = \frac{\delta\nu}{\delta(\alpha^2F)}\delta(\alpha^2F)$ the necessary change $\delta(\alpha^2F)$ for the Eliashberg function to improve the agreement between theory and experiment can be calculated in linear response. Next, one uses the updated $\alpha^2F_1 = \alpha^2F_0 + \delta(\alpha^2F)$ and solves the Eliashberg theory again and repeats this steps iteratively until the algorithm converges. For the Pb junction the calculated DOS agrees within ± 0.001 with the measured DOS. The obtained α^2F for Pb is shown in the bottom picture and agrees qualitatively well with the measured and calculated phonon spectrum in Pb [32–34]. Similarly, many other conventional superconductors show such a remarkable agreement [16], indicating that the BCS ground state indeed gives the correct predictions for strong-coupling superconductors.

1.1.3. Scanning Tunneling Microscopy

After the success of tunneling experiments for the determination of the electronic and bosonic spectra of materials, a huge step forward was achieved by Binnig and Rohrer [35] with the invention of the Scanning Tunneling Microscope (STM). In STM one uses a thin metallic tip that is attached to a piezoelectric element which allows to move the tip with sub-Å precision in all three dimensions over a surface. Following the Tersoff-Hamann theory [36], the tunneling current I is given by

$$I \sim e^{-2\kappa d}, \quad \text{with } \kappa = \sqrt{2m\phi}/\hbar. \quad (1.6)$$

Here, d is the tip-sample distance, m the free electron mass and ϕ the average of the work functions (typically several eV) of the tip and sample. In Section 5.3.3 we discuss this model in more detail. From expression (1.6) it follows that the current decreases by one order of magnitude if the tip-sample distance is increased by only 1Å . This allows for sub-Å height resolution of the surface topography when using the topographic mode, where the tip-sample distance

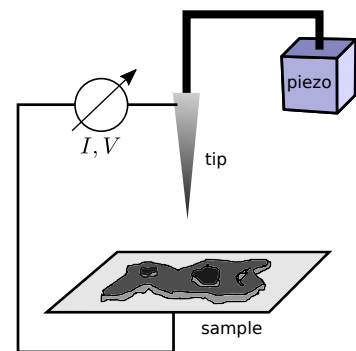


Figure 1.4.: Schematics of an STM.

is varied and I, V are fixed while scanning the probe in x, y -direction. Alternatively, one can probe the electronic structure³ of the sample by fixing d and recording the $I - V$ characteristics similar to the planar junction experiments.

A major advantages of the STM is the high spatial resolution that allows the characterization of nanomaterials. Another improvement is the lack of the insulating barrier of planar junctions, as the vacuum barrier does not influence the behavior of the investigated sample on the surface. Furthermore, the technique of quasiparticle interference (QPI), where a real-space STM picture is recorded in an area around impurities, allows one to obtain detailed momentum-space information of the electronic spectrum, especially in correlated materials [37–39].

1.2. Inelastic Electron Tunneling Spectroscopy

Inelastic Electron Tunneling Spectroscopy (IETS) is for example well known from molecular junction experiment, where a molecule (or a molecular adsorbate in the insulating metal oxides) connects the left and right electrodes of the tunneling junction. When an electron tunnels through the junction it can also excite or absorb a phonon or other collective bosonic mode with energy Ω . This opens up a new inelastic tunneling channel, see Figure 1.5, and increases the current.

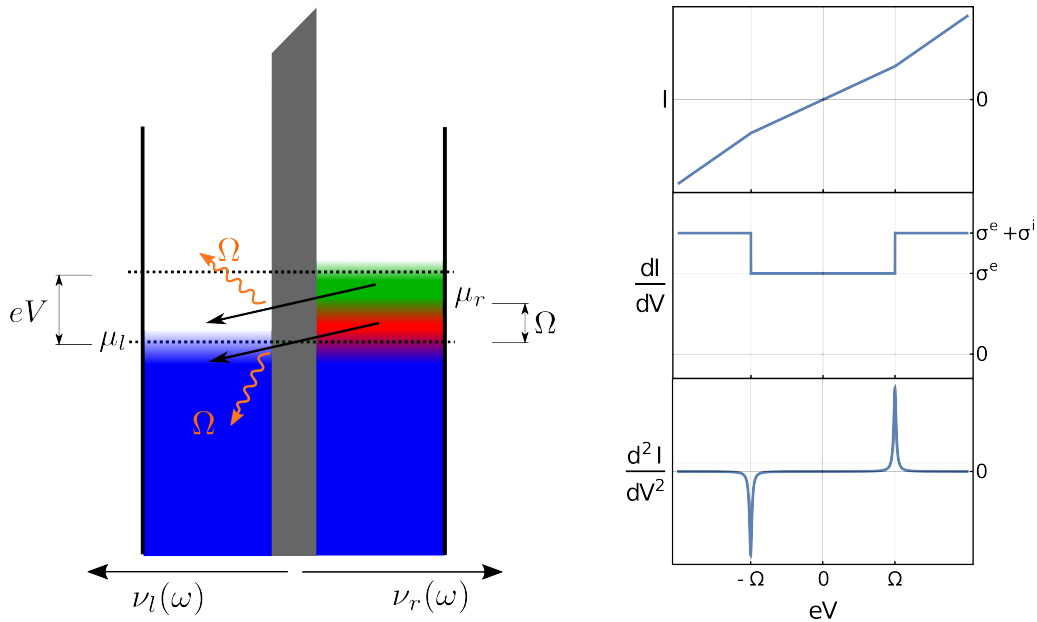


Figure 1.5.: Sketch of inelastic tunneling processes: (left) An electron tunnels between two normal metals through an insulating barrier via the emission of an Einstein phonon with frequency Ω . (right) Also shown are the expected current I , conductance dI/dV and d^2I/dV^2 . The latter is for small temperature proportional to the phonon spectrum.

Let us now discuss the expected tunneling spectrum if we include such inelastic events. We consider a simple model consisting of two electrodes with constant DOS and a single bosonic mode with frequency Ω at zero temperature, as shown in Figure 1.5. Following Section 1.1 the **elastic** current is $I^e = \sigma^e \cdot V$ at voltages $eV < \Omega$. At voltages $eV > \Omega$,

³Also the bosonic spectrum can be probed by inelastic tunneling as we will see in the following section.

also the tunneling of an electron with the emission of a boson can occur, which opens the **inelastic** channel with $I^e = \sigma^i \cdot (V - \Omega/e)\Theta(eV - \Omega)$. The expected total current and its derivatives are shown in Figure 1.5. The opening of the inelastic tunneling channel appears as a step-like increase of the conductance at $eV = \pm\Omega$, resulting in a valley-like shape of the conductance. Furthermore, a sharp δ -like peak in the second derivative at the boson energy Ω arises. Thus, the second derivative gives some indication about the bosonic spectrum and using IETS the vibrational spectra of various molecules have been intensively studied in planar junctions [40] and using STM [41–44].

The concept of inelastic tunneling also was not new in the 1960’s. In indirect semiconducting p - n junctions it was known that the transition of electrons from the conduction to the valence band was accompanied by the emission of a phonon to account for momentum conservation. It was shown that in such indirect diodes the phonon spectrum is clearly visible [45–48] in the I - V characteristics. Later, Lambe and Jaklevic [17, 18] showed that such inelastic tunneling can also occur between the interfaces of two metallic contacts. They could resolve the vibrational spectra of molecules contained in the barrier region, see Figure 1.6. In 1969, Leger and Klein [49] saw first signs of inelastic tunneling of Al-bulk phonons in the current characteristics of Al-Al-junctions. They showed that above T_c the second derivative d^2I/dV^2 shows a good agreement with the phonon DOS obtained in neutron scattering experiment [33]. In another experiment [50], the normal-state I-V characteristics of several Pb, Al, In and Sn junctions were investigated, see right picture in Figure 1.6. The authors concluded that the second derivative is “a crude measurement of the phonon density on the normal metal”. This is not very surprising as for these tunneling events there exists not only a coupling of electrons to the phonons in the barrier (which consists of the isolating oxide) but also to vibrational modes in the surface regions of the normal metals. Therefore, it is possible to excite/absorb bulk phonons during the tunneling process which adds a second, inelastic contribution to the elastic tunneling current given in Eq. (1.1). The actual physical process will be discussed in detail in Chapter 3, where we show how to derive an inelastic transfer Hamiltonian that yields the result $d^2I/dV^2 \sim \alpha^2 F(\omega)$ in the normal state.

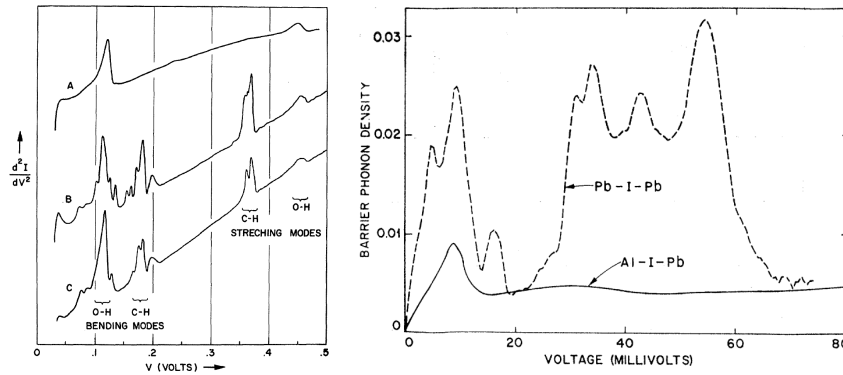


Figure 1.6.: Normal state data of d^2I/dV^2 for: (left) three Al-Al oxide-Pb junctions taken at 4.2K. The two lower curves show junctions exposed to $\text{CH}_3(\text{CH}_2)\text{COOH}$ and CH_3COOH with characteristic vibration frequencies of the acid molecules [17]. (right) a Pb-PbO-Pb junction that shows the phonon spectrum of Pb ($< 10\text{meV}$) and of the Pb-oxide interface ($> 10\text{meV}$) [50].

For planar junctions experiments on conventional superconductors these inelastic contributions are weak. The increase of the conductance, hence the depth of the “valley” in the

conductance of Figure 1.5, from 0 to $eV = \omega_D$ is only about 1% for the Pb junction [50]. Thus, the superconducting strong-coupling features are at least one order of magnitude larger in Pb. In Ref. [51], Rowell discusses this issue and shows that inelastic effects can be significantly absorbed by normalizing the superconducting spectrum by the one in the normal state $\sigma_{\text{norm}}(V) = \sigma_{\text{sc}}(V)/\sigma_{\text{nc}}(V)$, see also Section 4.2.2. Using such a normalization procedure the elastic electron tunneling theory is able to explain the SIN and SIS spectra for these junctions. However, as we will see in Chapter 4 and 5, this normalization method will not work for strong inelastic tunneling contributions and for systems in which the superconducting pairing glue is of electronic nature.

In a more recent work, Schackert et al. [19] demonstrated that they could gain direct access to the Eliashberg function/phonon spectrum of Pb thin films using IETS with a Scanning Tunneling Microscope (STM). Interestingly, for a tungsten tip on Pb the inelastic contributions were about one order of magnitude larger compared to the spectra seen in the planar junction experiments of Ref. [50]. This is of particular interest since now the strong-coupling features calculated from the Eliashberg theory are of the same amplitude as the inelastic features in the normal state. Since one expects the inelastic contributions to be of the same order also in the superconducting state, the question arises if it is required to incorporate inelastic tunneling processes for the interpretation of the observed tunneling spectra [24]. In Chapter 4 this issue will be discussed in detail for Pb and we show that one can explain the observed STM data in the superconducting state consistently by using the phonon spectrum observed in IETS in the normal state.

For completeness, we also remark that inelastic tunneling is of course not only restricted to phonons and photons, but can also occur for other collective excitations as magnons [21–23] or spin fluctuations (see Chapter 5). Another method to measure the phonon spectrum in metals is point-contact spectroscopy [52, 53], which uses metallic contacts and is therefore not in the tunneling limit discussed in the following.

1.3. Experiments in unconventional superconductors

In this section we give a short overview of experiments in unconventional superconductors. We start with the phenomenology of unconventional superconductors motivated by a common phase diagram upon charge doping and mention several additional phases realized in the cuprate and iron pnictide systems. The focus will lie on the dynamics of the collective spin fluctuations in this system, which are likely responsible for the Cooper pairing in these compounds. Finally, we present an overview of experimental tunneling spectra seen on unconventional superconductors.

1.3.1. Properties of unconventional superconductors

The discovery of superconductivity in the cuprates [54] was not only surprising because of their exceptionally high transition temperatures (up to $T_c = 133\text{K}$ in a HBCCO system [55]), but also because the parent compound has an antiferromagnetic ground state. As can be seen in Figure 1.7(a), the superconducting dome emerges from this antiferromagnetic phase with antiferromagnetic ordering vector (AFV) \mathbf{Q} when doping the system inducing holes or electrons. For a long time superconductivity and magnetic order have been thought to be antagonistic since scattering off magnetic moments breaks up the singlet Cooper pairs [56].

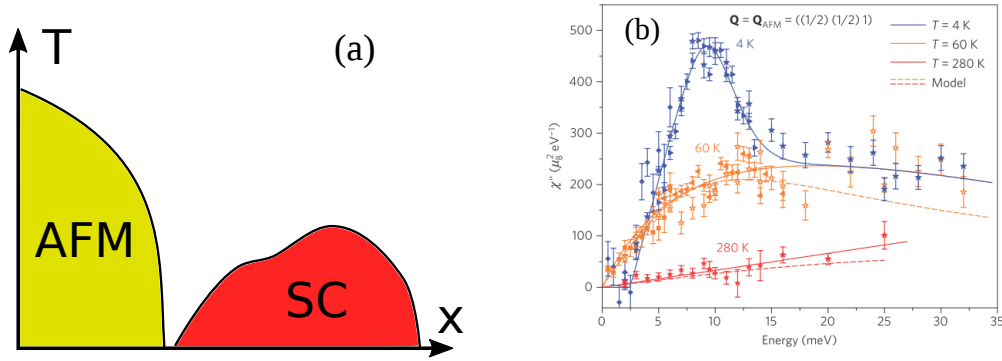


Figure 1.7.: (a) Generic phase diagram for high-temperature superconductors with the antiferromagnetic parent compound and the superconducting dome that appear upon doping x . (b) Spin spectrum from neutron scattering experiments in the normal and superconducting state for optimally doped $\text{BaFe}_{1.85}\text{Co}_{0.15}\text{As}_2$ clearly showing the neutron resonance below T_c (adapted from [59]).

However, in 2008 a second group of high-temperature superconductors was discovered: The iron pnictides. In these compounds the magnetic iron atoms are combined with elements from the pnictogen group. The first iron pnictide superconductor was $\text{LaO}_{1-x}\text{F}_x\text{FeAs}$ [57], which has transition temperatures up to $T_c = 55\text{K}$ when substituting La with rare earth elements [58]. In both groups of high-temperature superconductors the superconducting dome is, apart from some rare exceptions, accompanied by an antiferromagnetic dome⁴. This indicates that spin-fluctuations could serve as the “pairing glue” for the Cooper pairs in these materials.

The spin excitation spectrum can be experimentally accessed by inelastic neutron scattering experiments. Early measurements for $\text{YBa}_2\text{Cu}_3\text{O}_{7-\delta}$ (YBCO) [60] showed that when entering the superconducting state, the spin spectrum undergoes a drastic change. First, a spin gap develops as the spin fluctuations are collective modes made of fermionic quasiparticles that are gapped by the superconducting gap Δ (which is momentum-dependent such that the spin gap also depends on the position in the reciprocal space). The more surprising finding was a sharp peak in the spectrum around the antiferromagnetic vector \mathbf{Q} , but at an energy ω_{res} clearly below 2Δ . Such a feature was seen in many cuprate [60–62] and iron pnictide systems [59, 63–65] as well as heavy fermion superconductors as CeCoI_5 [66, 67] and is usually referred to as the neutron resonance mode. Such a spin resonance mode is expected if the superconducting gap obeys an unconventional gap symmetry (as d - or s_{\pm} -wave) where the the order parameter changes sign for the electronic states that are connected by the AFV \mathbf{Q} [68]. This issue is related to the coherence factors occurring in the calculation of the particle-hole polarization operator and will be discussed in more detail in Section 2.3.

The temperature evolution of the neutron resonance mode is not the only hint of unconventional pairing (symmetries) in the high- T_c compounds. Angle-Resolved Photoemission Spectroscopy (ARPES) [69, 70] and interference experiments [71, 72] demonstrated the d -wave nature of the ordering parameter in the cuprates. However, there is still an ongoing debate about the pairing symmetry in the iron pnictide superconductors for the different

⁴In these strongly correlated materials a diverse phase diagram appears for many systems including charge- and spin-order, structural transitions (e.g. nematic/orthorhombic), pseudogap states, strange-metal behavior and more. For a detailed discussion of these issue we refer to the rich literature.

compounds. The most prominent candidates vary from conventional s - to gapped or nodal s_{\pm} -wave. Tunneling experiments into these materials can give a detailed insight into the nature of the superconducting state as will be shown in Chapter 5.

1.3.2. Tunneling spectra of unconventional superconductors

Due to the success of tunneling experiments in the determination of the phononic pairing glue in conventional superconductors, EETS experiments were performed soon after the discovery of superconductivity in the cuprate superconductors in the hope to unravel the underlying physics. However, obtaining reproducible tunneling spectra in these doped systems has been challenging for a long time. A novel feature in many spectra was the V-shaped background conductance present in both the normal and the superconducting spectra, first seen in YBCO and in bismuth oxide superconductors [73–75]. Here and in the following, the V-shape refers to the linear background conductance in the normal state (and in the superconducting state for higher biases) and **not** to the typical V-shaped form between the superconducting coherence peaks as seen in the cuprates, which originates from the d -wave symmetry of the superconducting gap, see also Sec. 2.3.2. In Ref. [73] it was pointed out that the linear background in the bismuth superconductors scales with T_c , thus the origin of the superconducting pairing seems to be related to the background conductance seen in these strongly-correlated systems. In Figure 1.8 experimental spectra displaying such a clear V-shape for YBCO and bismuth oxide superconductors are shown, as well as similar curves that were observed for various other CuO_2 compounds, e.g. $\text{NdBa}_2\text{Cu}_3\text{O}_{7-\delta}$ (NBCO) [76], electron-doped $\text{Pr}_{1-x}\text{LaCe}_x\text{CuO}_4$ (PLCCO) [77], optimally doped $\text{La}_{2-x}\text{Sr}_x\text{CuO}_4$ (LSCO) [78], $\text{Ca}_{2-x}\text{Na}_x\text{CuO}_2\text{Cl}_2$ [79] and $\text{Sr}_{0.9}\text{La}_{0.1}\text{CuO}_2$ [80]. Further, in a recent work superconducting features on top of a V-shaped background have been found in K-doped Sr_2IrO_4 [81], a compound isostructural to La_2CuO_4 .

However, there are different high- T_c materials that show no clear V-shapes spectrum for high-energies, e.g. $\text{Bi}_2\text{Sr}_2\text{CaCu}_2\text{O}_{8+\delta}$ (BSCCO) [82, 83] shown in Figure 1.9(a),(d). The conductance here only shows a d -wave DOS and a dip feature above the coherence peaks. On the other side, other tunneling experiments as shown in Figure 1.9(b) still show a clear sign of a V-shaped linear background. Further, STM spectra for BSCCO can differ for different conductances (which means tip-sample distance) [83], probably due to the different distance dependences of the tunneling matrix elements to the orbitals of the BiO and CuO_2 planes. An explanation for the observed diversity of the spectra could be given by Misra et al. [84], who showed in a STM experiment that the differential conductance measured on the BiO layer differs significantly from the spectra obtained on the CuO_2 planes, see Figure 1.9(c). The conductance in the superconducting CuO_2 sheet again shows a clear background conductance that is absent for the BiO layer spectrum.

Also for the iron pnictide superconductors a variety of different spectra have been reported. The electronic spectrum for the different iron compounds can be quite diverse as the mixing of the five 3d orbitals in general leads to several (hole and electron) bands crossing the Fermi energy. In contrast, the cuprate superconductors usually only have one band at the Fermi edge. In many iron pnictides one observes Γ -centered hole pockets and M-centered electron pockets and also here spin flip quasiparticle excitations between these pockets are believed to cause superconductivity with the possibility of multiple gaps on the different Fermi sheets. Also for the iron pnictide superconductors there exists a variety of different observed spectra, sometimes even for the same compound. In the case of $\text{BaFe}_{1.8}\text{Co}_{0.2}\text{As}_2$

there is data showing a flat background and clear strong-coupling or double-gap features (Figure 1.10(b)) as well as spectra with a clear background conductance (see Figure 1.10(d)). As can be seen in Figure 1.10 many of the observed spectra have strong similarities with the ones seen in the cuprate superconductors, indicating a common underlying pairing mechanism.

In Chapter 5 we will discuss the state-of-the-art theoretical interpretation of tunneling spectra in unconventional superconductors in detail. We will focus on the question how the inclusion of inelastic tunneling changes the picture drawn in many publications so far.

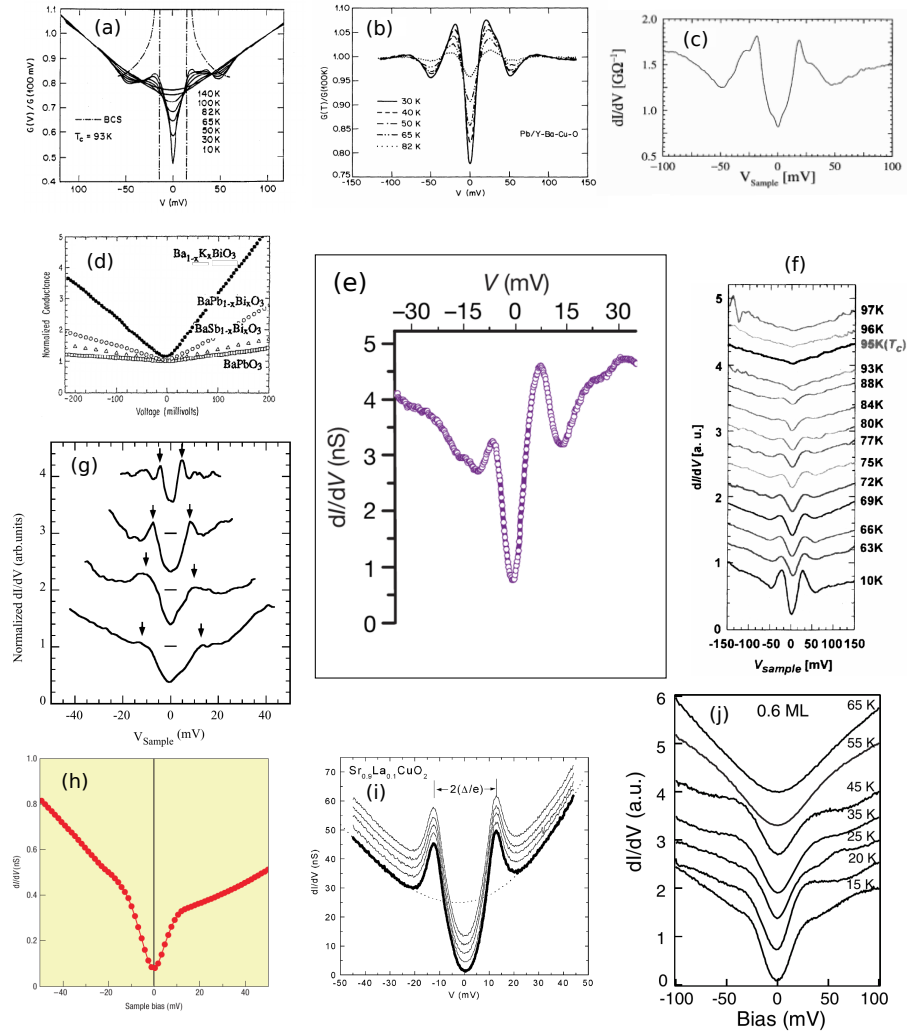


Figure 1.8.: Cuprate tunneling spectroscopy experiments showing V-shape background: (a) Measured differential conductance dI/dV for YBCO planar junction experiment [73], (b) Normalized conductance (σ_{sc}/σ_{nc}) for YBCO planar junction [74], (c) YBCO conductance for STM experiment [85], (d) normal state conductance for various bismuth oxide superconductors [73], (e) STM on electron-doped PLCCO [77], (f) Conductance spectra for NCBO [76], (g) STM on optimally doped LSCO for different positions on the surface [78], (h) Conductance for $\text{Ca}_{2-x}\text{Na}_x\text{CuO}_2\text{Cl}_2$ [79], (i) STM conductance on $\text{Sr}_{0.9}\text{La}_{0.1}\text{CuO}_2$ [80], (j) spatially averaged dI/dV for K-doped Sr_2IrO_4 (isostructural to the cuprate superconductor La_2CuO_4) [81].

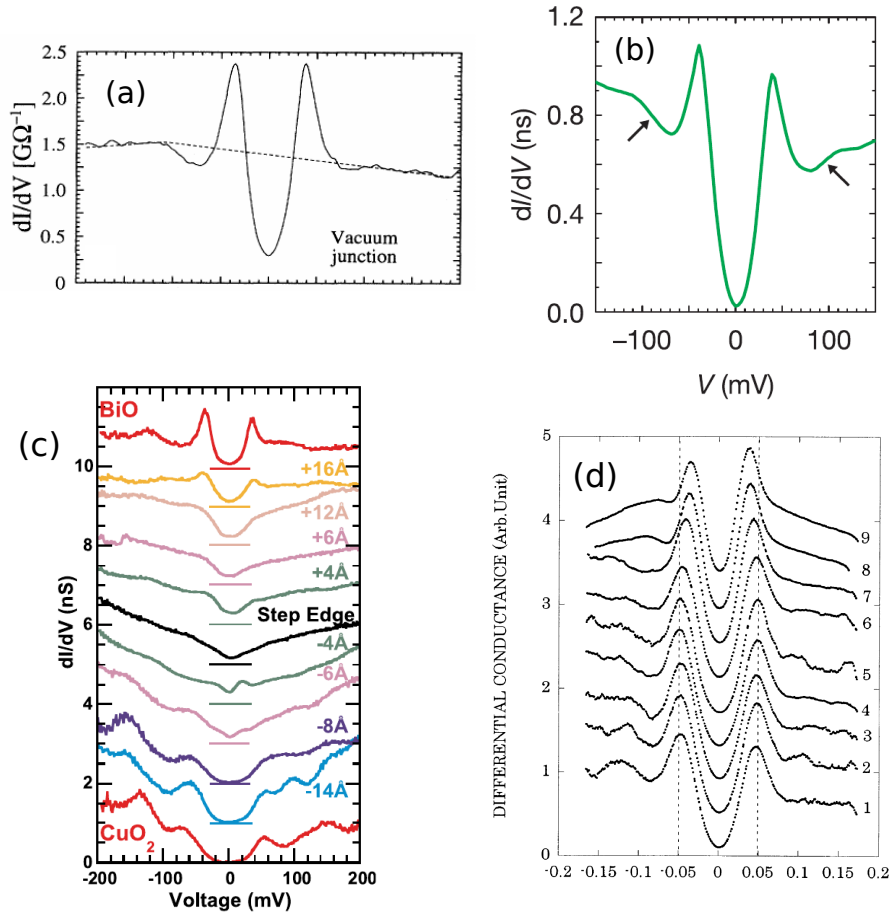


Figure 1.9.: Differential conductance for experiments on BSCCO: (a) Spectra taken on BiO surface without background conductance showing a clear dip above the coherence peak [82], (b) Averages STM spectra taken from Ref. [86], (c) STM across a step edge of CuO_2 and BiO surface layers showing different characteristic spectra [84], (d) STM spectra for different tip-sample distances [83].

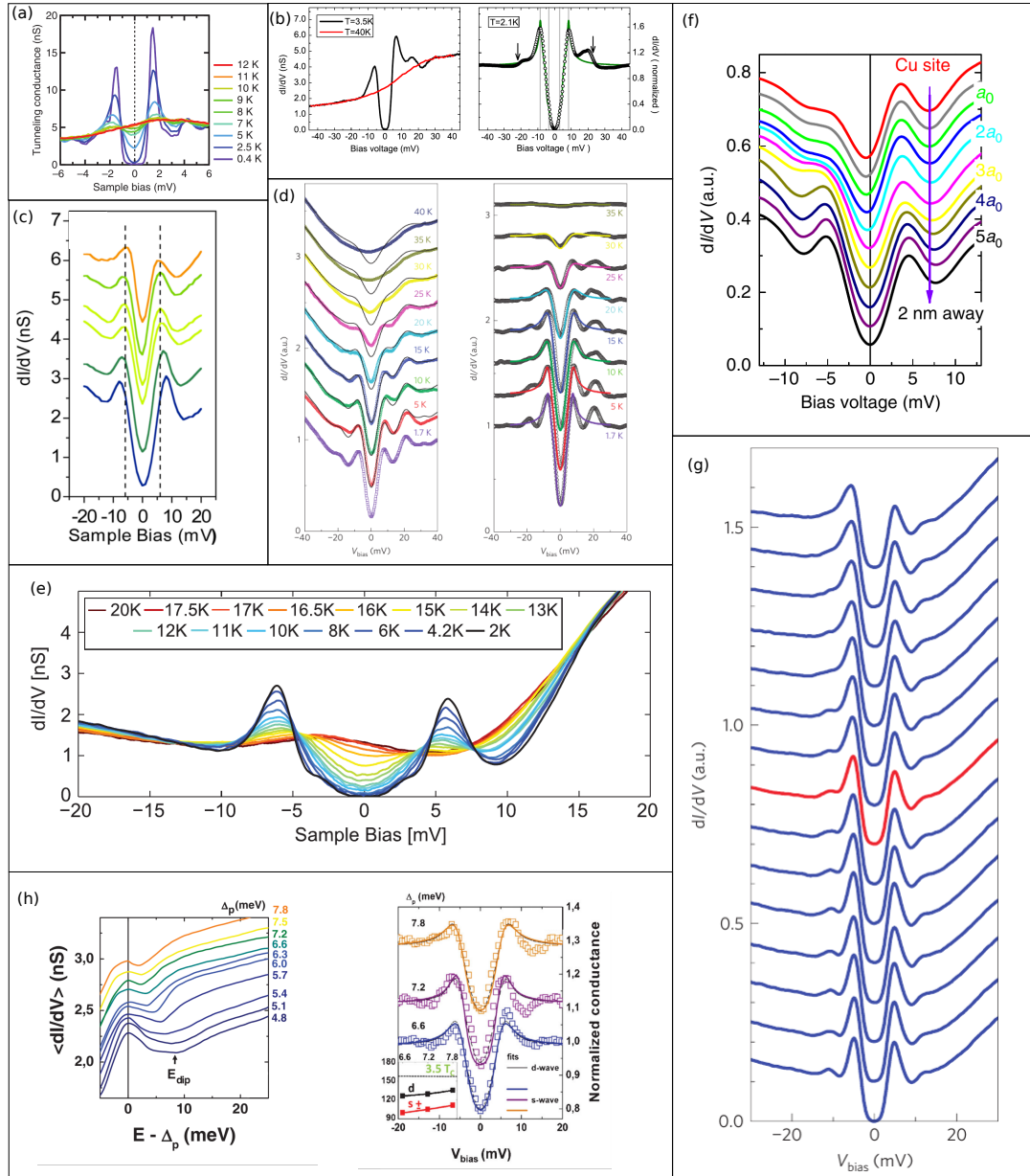


Figure 1.10.: Differential conductance for experiments on iron-based superconductors: (a) STM on single crystalline Fe(Se,Te) [87], (b) Conductance and normalized Conductance (σ_{sc}/σ_{nc}) for $\text{Ba}_{0.6}\text{K}_{0.4}\text{Fe}_2\text{As}_2$ from Ref. [88], (c) Conductance for $\text{BaFe}_{1.8}\text{Co}_{0.2}\text{As}_2$ [89] (d) Different spectra for $\text{Ba}_{0.6}\text{K}_{0.4}\text{Fe}_2\text{As}_2$ showing a V-shape background for higher energies [90], (e) STM on LiFeAs [91], (f) Differential conductance for varying with distance to a Cu-impurity in $\text{Na}(\text{Fe}_{0.96}\text{Co}_{0.03}\text{Cu}_{0.01})\text{As}$ [92], (g) dI/dV for $\text{Na}(\text{Fe}_{0.975}\text{Co}_{0.025})\text{As}$ [90], (h) Conductance and normalized conductance from STM for $\text{SmFeAsO}_{1-x}\text{F}_x$ [93].

2. Fundamentals II: Theory of strong-coupling superconductivity

In this chapter a summary of different models for the theoretical description of superconducting systems is presented. We start with some basics about the theoretical understanding of superconductivity introducing the well-known Bardeen-Cooper-Schrieffer (BCS) theory. Then, we discuss the Eliashberg-Migdal theory of strong-coupling, phonon-mediated superconductivity in conventional superconductors as well as extended models for studying superconductivity where the pairing glue is of electronic nature.

2.1. The Theory of Bardeen, Cooper and Schrieffer

Superconductivity is without debate one of the most fascinating manifestations of quantum mechanics in our macroscopic world. In 1911, Heike Kammerlingh Onnes [1, 2] studied the low-temperature resistance of mercury and surprisingly found a sudden drop of the electrical resistance at a critical temperature $T_c = 4.2$ K. It soon became clear that the resistance in this new state was absolute zero, thus the system is able to carry a dissipationless current. Another extraordinary property is the Meissner-Ochsenfeld effect [3], which describes the expulsion of the magnetic field smaller than the critical field H_c from a superconductor and which can be used to levitate a superconductor in a magnetic field¹.

Even though the experimental detection of superconductivity is fairly simple it took nearly 50 years for a microscopic theoretical explanation², which was given by Bardeen, Cooper and Schrieffer in their famous papers “(Microscopic) Theory of Superconductivity” [7, 8]. Their theory had been preceded by three major insights:

1. The discovery of the isotope effect which showed a suppression of T_c for mercury isotopes with increasing masses in 1950 in two independent experimental groups [94, 95].
2. In 1950 Fröhlich showed that the scattering between two electrons with (quasi)momenta \mathbf{k} and $\mathbf{k} + \mathbf{q}$ via the exchange of a virtual phonon with momentum \mathbf{q} , whose energy difference $|\epsilon_{\mathbf{k}+\mathbf{q}} - \epsilon_{\mathbf{k}}| < \omega_{\mathbf{q}}$ is smaller than the corresponding phonon energy $\omega_{\mathbf{q}}$, is attractive [96]. The physical origin behind this effect is as follows: Consider a Bloch

¹For a detailed discussion about the difference between type-I and type-II superconductors we refer to the literature.

²Here, we do not want to discuss other phenomenological approaches to the topic, e.g. the London equations [5] or the Ginzburg-Landau theory [6].

electron propagating through a static lattice potential of a crystal. When it comes by a positively charged ion, this ion will be displaced towards the path of the electron and will locally create a positively charged potential at the former position of the electron. Since the electron is much faster than the ion (since $M \gg m$ and therefore $v_F/c \gg 1$), it will rapidly move away from the atomic position, whereas the ion only slowly relaxes to its equilibrium position. During the relaxation time another electron can be attracted by the positive charge of the displaced ion and is thereby effectively attracted to the initial electron. Thus, we are dealing with a retarded interaction mechanism in phonon-mediated superconductors. Later, Bardeen and Pines could demonstrate that this attractive interaction can also survive near the Fermi surface of a metal if one includes the Coulomb repulsion³ between the electrons [97].

3. Cooper demonstrated that an attractive interaction between the quasiparticles near the Fermi surface of an electron gas could cause electrons with opposite momentum and spin $|\mathbf{k}, \uparrow\rangle \otimes |-\mathbf{k}, \downarrow\rangle$ to form stable pairs [98]. The new ground state of the system has a lower energy than the Fermi surface below a critical temperature T_c , which is known as the Cooper instability.

The so-called BCS Hamiltonian is obtained by only keeping the interactions between Cooper pairs with opposite momentum and spin, and by replacing the in general momentum (and energy) dependent phonon-induced interaction by a constant

$$V_{\mathbf{k}, \mathbf{k}'} = -\lambda/\nu_F \Theta(\omega_D - |\epsilon_{\mathbf{k}}|) \Theta(\omega_D - |\epsilon_{\mathbf{k}'}|).$$

Here, we introduced the dimensionless electron-phonon coupling constant λ and ν_F is the normal state electron DOS at the Fermi surface. The positive interaction is only present for electrons that have energies within the range of the Debye frequency ω_D of the phonons and the BCS Hamiltonian reads

$$\hat{\mathcal{H}}_{\text{BCS}} = \sum_{\mathbf{k}, \sigma} \epsilon_{\mathbf{k}} c_{\mathbf{k}, \sigma}^\dagger c_{\mathbf{k}, \sigma} + \sum_{\mathbf{k}, \mathbf{k}'} V_{\mathbf{k}, \mathbf{k}'} c_{\mathbf{k}, \uparrow}^\dagger c_{-\mathbf{k}, \downarrow}^\dagger c_{-\mathbf{k}', \downarrow} c_{\mathbf{k}', \uparrow}. \quad (2.1)$$

Within the BCS theory the interaction is decoupled using a mean-field theory. Therefore, we introduce the superconducting mean-field parameter $\Delta_{\mathbf{k}} = -\sum_{\mathbf{k}'} V_{\mathbf{k}, \mathbf{k}'} \langle c_{-\mathbf{k}', \downarrow} c_{\mathbf{k}', \uparrow} \rangle$ describing the condensation of two electrons into a Cooper pair and write down the BCS mean-field Hamiltonian as⁴

$$\hat{\mathcal{H}}_{\text{BCS}}^{\text{MF}} = \sum_{\mathbf{k}, \sigma} \epsilon_{\mathbf{k}} c_{\mathbf{k}, \sigma}^\dagger c_{\mathbf{k}, \sigma} - \sum_{\mathbf{k}} \Delta_{\mathbf{k}} c_{\mathbf{k}, \uparrow}^\dagger c_{-\mathbf{k}, \downarrow}^\dagger - \sum_{\mathbf{k}} \Delta_{\mathbf{k}}^* c_{-\mathbf{k}, \downarrow} c_{\mathbf{k}, \uparrow}. \quad (2.2)$$

This quadratic mean-field theory can easily be diagonalized via a unitary Bogoliubov transformation mixing particle and hole states with opposite momenta and spin orientation

$$\begin{pmatrix} a_{\mathbf{k}, \uparrow} \\ a_{-\mathbf{k}, \downarrow}^\dagger \end{pmatrix} = \begin{pmatrix} u_{\mathbf{k}} & v_{\mathbf{k}} \\ -v_{\mathbf{k}} & u_{\mathbf{k}} \end{pmatrix} \begin{pmatrix} c_{\mathbf{k}, \uparrow} \\ c_{-\mathbf{k}, \downarrow} \end{pmatrix}, \quad (2.3)$$

³When we discuss the strong coupling theory, we will discuss this issue in more detail.

⁴Here, we absorbed the constant term arising in the mean-field approach in the chemical potential.

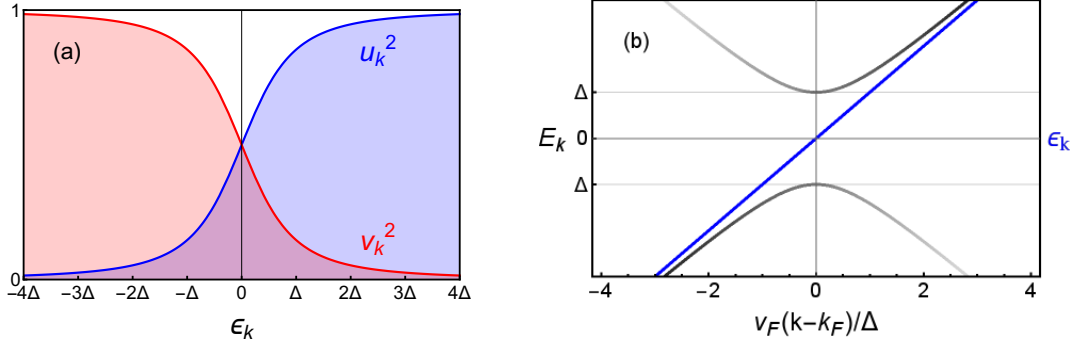


Figure 2.1.: (a) Superconducting coherence factors $u_{\mathbf{k}}^2, v_{\mathbf{k}}^2$ of the BCS theory, (b) Superconducting dispersion $E_{\mathbf{k}}$ (black curve) of the Bogoliubov quasiparticles in comparison to the normal conducting dispersion $\epsilon_{\mathbf{k}}$ (blue curve) near the Fermi surface for an s -wave superconductor $\Delta_{\mathbf{k}} = \Delta = \text{const.}$. The intensity of the black curve indicates the spectral weight of the quasiparticle dispersion given by the coherence factors $u_{\mathbf{k}}^2$ ($v_{\mathbf{k}}^2$) for the particle (hole) band.

with the superconducting dispersion and coherence factors

$$\begin{aligned} E_{\mathbf{k}} &= \sqrt{\epsilon_{\mathbf{k}}^2 + |\Delta_{\mathbf{k}}|^2}, \\ u_{\mathbf{k}}^2 &= \frac{1}{2} \left(1 + \frac{\epsilon_{\mathbf{k}}}{E_{\mathbf{k}}} \right), \\ v_{\mathbf{k}}^2 &= \frac{1}{2} \left(1 - \frac{\epsilon_{\mathbf{k}}}{E_{\mathbf{k}}} \right). \end{aligned} \quad (2.4)$$

These coherence factors describe the particle and hole contribution of an excitation in the superconductor, see also Figure 2.1, which becomes clear when one calculates the particle Green's function in a superconductor on the imaginary axis

$$G_{\mathbf{k}}^{(p)}(i\Omega_n) = -\frac{1}{\sqrt{\beta V}} \int_0^\beta d\tau \langle T_\tau \hat{c}_\uparrow(\mathbf{r}, \tau) \hat{c}_\uparrow^\dagger(0, 0) \rangle e^{i\omega_n \tau - i\mathbf{k} \cdot \mathbf{r}} = \frac{u_{\mathbf{k}}^2}{i\Omega_n - E_{\mathbf{k}}} + \frac{v_{\mathbf{k}}^2}{i\Omega_n + E_{\mathbf{k}}}. \quad (2.5)$$

Here, we defined V as the volume of the solid, $(\hat{c}, \hat{c}^\dagger)$ are the electronic field operators of the system in the Heisenberg picture and \mathcal{T}_τ is the time-ordering operator in Matsubara imaginary time. The diagonalized mean-field Hamiltonian can be written as

$$\hat{\mathcal{H}}_{\text{BCS}}^{\text{MF}} = \sum_{\mathbf{k}, \sigma} E_{\mathbf{k}} a_{\mathbf{k}, \sigma}^\dagger a_{\mathbf{k}, \sigma}. \quad (2.6)$$

Obviously, the superconducting system acquires an excitation gap of $|\Delta_{\mathbf{k}}|$ that covers the whole Fermi surface, which can be calculated using the relation (2.4) between the electronic and Bogoliubov quasiparticles. This leads to the BCS-self-consistency equation

$$\Delta_{\mathbf{k}} = - \sum_{\mathbf{k}'} V_{\mathbf{k}, \mathbf{k}'} \frac{\Delta_{\mathbf{k}'}}{2E_{\mathbf{k}'}} \tanh\left(\frac{E_{\mathbf{k}'}}{2T}\right), \quad (2.7)$$

which will be derived later as the BCS limit of the Eliashberg equations. For the BCS model the leading instability is the s -wave state with isotopic superconducting gap $\Delta_{\mathbf{k}} = \Delta = \text{const.}$ and we only want to list the most important conclusions that can be made from the weak-coupling result (2.7):

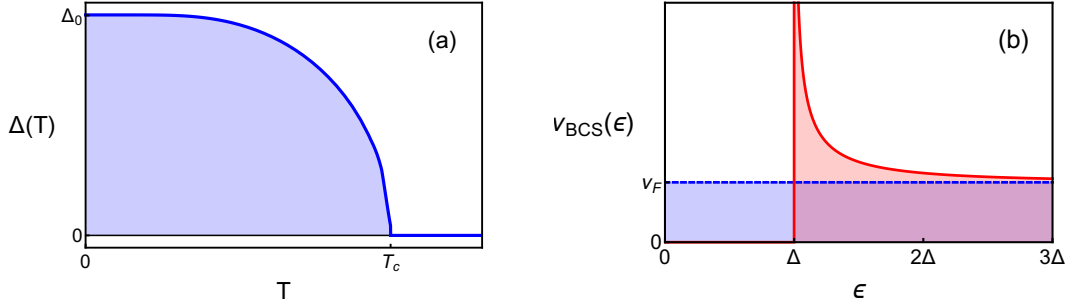


Figure 2.2.: Left: Temperature dependence of the superconducting gap $\Delta(T)$ in the BCS theory as calculated from relation (2.7). Right: Superconducting (red) and normal conducting (blue) density of states close to the Fermi surface.

- (a) At $T = 0$ the superconducting gap is given by $|\Delta(T = 0)| = 2\omega_D e^{-\frac{1}{\lambda}}$ and is thus exponentially small in the electron-phonon coupling λ . Note: The non-analytic structure $\sim 1/\lambda$ of the result in the interaction strength does not allow for the usual perturbative approach via a Taylor expansion starting from a non-interacting Fermi gas.
- (b) The ratio between the transition temperature T_c and the zero temperature gap is given by $\frac{2|\Delta(T=0)|}{T_c} = 3.53$.
- (c) Close to the transition temperature the superconducting gap vanishes as $|\Delta(T \rightarrow T_c)| = 3.2T_c \sqrt{1 - \frac{T}{T_c}}$ as can be seen in Figure 2.2(a) indicating a second order phase transition also seen as a jump in the specific heat.
- (d) The DOS of the fermionic quasiparticles in the BCS state can be calculated to be

$$\nu_{\text{BCS}}(\epsilon) = \frac{1}{V} \sum_{\mathbf{k}} \delta(|\epsilon| - E_{\mathbf{k}}) = \nu_F \int_{-\infty}^{\infty} d\omega \delta(|\epsilon| - \sqrt{\omega^2 - \Delta^2}) = \mathbf{Re} \left[\frac{\nu_F |\epsilon|}{\sqrt{\epsilon^2 - \Delta^2}} \right]. \quad (2.8)$$

It shows the characteristic van-Hove square-root singularity at the superconducting band edges $\epsilon = \pm\Delta$ and the gapped region without fermionic states for $\epsilon \in [-\Delta, \Delta]$, see Figure 2.2(b). For energies above the gap $\epsilon \gg \Delta$ the DOS approaches quickly the normal state value indicating its low-energy character.

2.2. Migdal-Eliashberg theory of superconductivity

The BCS theory presented in the previous section is a weak-coupling theory only valid for *small* electron-phonon interactions⁵ λ . Its simplifications, e.g. the constant phonon-induced interaction between the electron within the Debye energy range, works well for weak-coupling materials like aluminum or tin, but fails for other materials as lead or niobium with strong electron-phonon interaction. Based on the work of Migdal [99] about the electron-phonon interaction in normal metals, Eliashberg [9, 10] successfully extended the BCS theory to the strong-coupling regime using the Green's function technique. In this section, we will first discuss the role of the Migdal theorem in the normal state and

⁵We will later see about how exactly the electron-phonon coupling constant λ can be related to the microscopic details of the electronic and phononic systems.

then give a derivation of the strong-coupling Eliashberg equations including a discussion about the superconducting properties of system with a single phonon mode.

2.2.1. Electron-phonon interaction and Migdal theorem

The Migdal theorem [99] is an alternative way of expressing the Born-Oppenheimer theorem in the Green's function framework. Thus, to first order the electrons can be approximated to see only the static ion potential and one can separate the electronic and ionic system. Corrections come from the interaction of collective lattice vibrations (phonons) with the electrons that can be described via the Fröhlich Hamiltonian [100]

$$\hat{\mathcal{H}}_{\text{el-ph}} = \frac{1}{\sqrt{V}} \sum_{\substack{\mathbf{k}, \mathbf{q} \\ \sigma, \lambda}} \alpha_q^\lambda \hat{c}_{\mathbf{k}+\mathbf{q}}^\dagger \hat{c}_{\mathbf{k},\sigma} (\hat{b}_{\mathbf{q},\lambda} + \hat{b}_{-\mathbf{q},\lambda}^\dagger), \quad (2.9)$$

where the $\hat{b}_{\mathbf{q},\lambda}, \hat{b}_{\mathbf{q},\lambda}^\dagger$ are the creation/annihilation operators of a phonon with momentum \mathbf{q} and of the branch λ with the electron-phonon coupling element α_q^λ . Applying perturbation theory the original vertex $\alpha_{\mathbf{k},\mathbf{k}',\mathbf{q}}^\lambda$ is renormalized and can be described by the infinite series

Let us quickly recast Migdal's argument: As the electron in the first vertex correction is scattered from \mathbf{k} to $\mathbf{k} + \mathbf{q}$, the corresponding time scale on which the phonon can interact with the electron to scatter it is $t \sim \frac{1}{v_F q}$. Since the phonons respond on the typical frequency ω_D , the corresponding displacement of the lattice due to the interaction with the electrons is proportional to $\frac{\omega_D}{v_F q} \sim \frac{\omega_D}{E_F}$ if we take the typical values $|\mathbf{q}| \approx k_F$ for the electron scattering near the Fermi surface. Only for very small momentum transfers \mathbf{q} vertex corrections can be of order unity, but these contributions usually have a highly restricted phase space. Let us also sketch the diagrammatic argumentation: Consider the leading order vertex correction seen in Eq. (2.10) in the normal state for zero temperature on the imaginary axis

$$\delta\Gamma_{\mathbf{k},\mathbf{q}} = \alpha_q \times \int_{q'} |\alpha_{q'}|^2 D_{q'} G_{k_0+q'_0} G_{k_0+q_0+q'_0}, \quad (2.11)$$

where $D_q = \frac{2\omega_q}{(iq_0)^2 - \omega_q^2}$ is the phonon propagator, $G_k = \frac{1}{i\Omega_m - \epsilon_k}$ the electron propagator and we neglected spin and phonon degrees of freedom to simplify the expressions. Since $\omega_q < \omega_D$ we have the Debye frequency as a natural frequency cutoff for the integration. Furthermore both the bosonic spectrum ω_q and the coupling α_q are only slowly momentum dependent, such that we can replace $|\alpha_{q'}|^2 D_{q'} \approx \frac{|\alpha^2|}{\omega_D} \Theta(\omega_D - |q_0|)$ by an effective average⁶, yielding

$$\delta\Gamma_{\mathbf{k},\mathbf{q}} \sim \alpha_q \times \frac{|\alpha^2|}{\omega_D} \times \int_{-\omega_D}^{\omega_D} \frac{dq_0}{2\pi} \int \frac{d^3 q'}{(2\pi)^3} \frac{1}{ik_0 + iq'_0 - \epsilon_{\mathbf{k}+\mathbf{q}'}} \frac{1}{ik_0 + iq_0 + iq'_0 - \epsilon_{\mathbf{k}+\mathbf{q}+\mathbf{q}'}}. \quad (2.12)$$

⁶This average will later be introduced as the dimensionless coupling constant $\lambda \approx \frac{|\alpha|^2 v_F}{\omega_D}$.

Since $\mathbf{q} \sim \mathbf{k}_F$ is typically of order of the Fermi momentum, one can separate the two integrations $\int \frac{d^3\mathbf{q}'}{(2\pi)^3} \sim \frac{\nu_F}{v_F^2} \int d\epsilon_{\mathbf{k}+\mathbf{q}'} \int d\epsilon_{\mathbf{k}+\mathbf{q}'}$. The remaining integrations then yield

$$\delta\Gamma_{k,q} \sim \alpha_q \times \frac{|\alpha_q^2|}{\omega_D} \times \nu_F \frac{\omega_D}{E_F} \sim \sqrt{\frac{m}{M}}. \quad (2.13)$$

Thus, vertex corrections always come with a factor $\omega_D/E_F \sim \sqrt{\frac{m}{M}}$, where m is the electron effective mass and M is the ion mass of the system. Note, that there is no Migdal theorem for the interaction induced by spin-fluctuations, nevertheless using a hot spot theory one can still neglect vertex corrections for the important contributions around the AFV \mathbf{Q} [101].

In what follows, we will proceed in the language of path integral methods on the imaginary axis or on the Keldysh contour, such that we switch to an action-based description of the many-body system [102, 103]. When integrating out the phonons, see also picture below, an effective phonon-induced electron-electron interaction appears for the fermionic Grassmann fields $\psi, \bar{\psi}$

$$S_{\text{el-el}}^{\text{ph-ind.}} = \int_{k,k',q} \sum_{\sigma,\sigma'} |\alpha_q^\lambda|^2 D_{q,\lambda} \bar{\psi}_{\mathbf{k}+\mathbf{q},\sigma} \bar{\psi}_{\mathbf{k}'-\mathbf{q},\sigma'} \psi_{\mathbf{k}',\sigma'} \psi_{\mathbf{k},\sigma}. \quad (2.14)$$

For frequencies $\omega < \omega_q \sim \omega_D$ this interaction becomes attractive, as was already pointed out in Section 2.1.

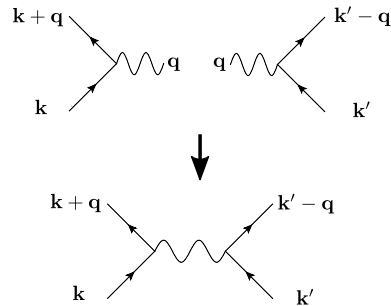
On the other hand one could ask why one should bother with a rather small phonon-induced attraction if there also exists a strong Coulomb repulsion in metals. The answer to this questions shows in a beautiful way how renormalization group (RG) arguments enter in the properties of real materials. As was initially derived by Morel and Anderson [104] using an RG approach, the dimensionless Coulomb interaction $\mu = U \cdot \nu_F$ becomes renormalized in the low-energy theory of the electrons near the Fermi surface in such a way that the effective, dressed interaction μ^* on energy scales below the Debye frequency ω_D behaves as

$$\mu^* = U_{\text{eff}} \cdot \nu_F = \frac{\mu}{1 + \mu \log(E_F/\omega_D)}. \quad (2.15)$$

In the limit $\omega_D/E_F \ll 1$ and for μ of order unity it then follows that the effective Coulomb interaction is given by

$$\mu^* \simeq \frac{1}{\log(E_F/\omega_D)} \ll \mu. \quad (2.16)$$

Hence, the Coulomb interaction is reduced for processes as slow as $1/\omega_D$ typical for ionic relaxations. Physically, this reduction is associated with the fact that scatterings far from the Fermi surface lead to a smaller probability for two electrons being within the range of the screened Coulomb potential. Therefore, for electrons close to the Fermi surface, the matrix elements μ^* are much smaller than the usual screened Coulomb interaction of the plane-wave quasiparticles. Since the ratio of the Debye frequency and the Fermi energy in most metals is pretty much universal, one expects that the effective Coulomb interaction is small and comparable in most of the conventional superconducting systems. Indeed it was found that for most materials the so-called Coulomb pseudopotential has values of order $\mu^* \approx 0.1-0.2$ [16].



gauge freedom to choose $F_k = \bar{F}_k$ (and thus $\Phi_k = \bar{\Phi}_k$). The self-energy in Eq. (2.20) can be written conveniently as a matrix

$$\hat{\Sigma}_k = - \int_q V_q \hat{\tau}_z \hat{G}_{k-q} \hat{\tau}_z = \begin{pmatrix} \Sigma_k & \Phi_k \\ \bar{\Phi}_k & -\Sigma_{-k} \end{pmatrix}, \quad (2.22)$$

with the entries

$$\begin{aligned} \Sigma_k &= - \int_q V_q G_{k-q} = \text{diagram with a loop and a wavy line}, \\ \Phi_k &= \int_q V_q F_{k-q} = \text{diagram with a loop and a wavy line}, \end{aligned} \quad (2.23)$$

that renormalize the Green's function to $\hat{G}_k^{-1} = \hat{G}_{k,0}^{-1} - \hat{\Sigma}_k = Z_k i\omega_n \hat{\tau}_0 - \tilde{\epsilon}_k \hat{\tau}_z - \Phi_k \hat{\tau}_x$. Here, we defined $Z_k = 1 - \Sigma_k - \Sigma_{-k}/2i\omega_n$ as the renormalization factor and $\tilde{\epsilon}_k = \epsilon_k + \Sigma_k + \Sigma_{-k}/2$ as the dispersion change of the electronic quasiparticles due to the coupling to the phonons. In particle-hole symmetric systems also the self-energy $\Sigma_k = -\Sigma_{-k}$ obeys this symmetry, thus the change of the dispersion can be neglected and $Z_k = 1 - \Sigma_k/i\omega_n$. For the electronic propagator follows

$$\hat{G}_k = \frac{Z_k i\omega_n \hat{\tau}_0 + \epsilon_k \hat{\tau}_z + \phi_k \hat{\tau}_x}{[Z_k i\omega_n]^2 - [\epsilon_k^2 + \phi_k^2]} = \frac{1}{Z_k} \frac{i\omega_n \hat{\tau}_0 + \epsilon_k/Z_k \hat{\tau}_z + \phi_k/Z_k \hat{\tau}_x}{(i\omega_n)^2 - [(\epsilon_k/Z_k)^2 + (\phi_k/Z_k)^2]}. \quad (2.24)$$

From this representation we can directly read off the spectrum from the poles of the Green's function at $i\omega_n = \sqrt{(\epsilon_k/Z_k)^2 + (\phi_k/Z_k)^2}$ and we find a frequency (and in general also momentum dependent) superconducting gap $\Delta_k = \Phi_k/Z_k$ as well as a renormalized dispersion ϵ_k/Z_k . Inserting equation (2.24) into the expression for the self-energy in (2.22) results in

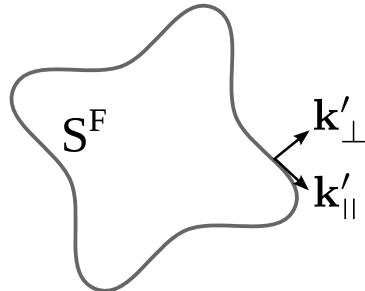
$$\hat{\Sigma}_k(i\omega_n) = -\frac{T}{V} \sum_{\mathbf{k}', \omega_m} V_{\mathbf{k}-\mathbf{k}'}(i\omega_n - i\omega_m) \cdot \frac{Z_{k'} i\omega_m \hat{\tau}_0 + \epsilon_{k'} \hat{\tau}_z - \Phi_{k'} \hat{\tau}_x}{[Z_{k'} i\omega_m]^2 - [\epsilon_{k'}^2 + \Phi_{k'}^2]}. \quad (2.25)$$

For isotropic *s*-wave superconductors the wave vector dependence is unimportant for the self-energy, because superconductivity is a low-energy phenomenon and everything occurs at the Fermi surface $|\mathbf{k}| \approx k_F$. Thus, one averages the slowly varying functions on the Fermi surface via

$$\begin{aligned} \hat{\Sigma}(i\omega_n) &:= \frac{1}{\nu_F} \frac{1}{V} \sum_{\mathbf{k}} \delta(\epsilon_{\mathbf{k}}) \hat{\Sigma}_{\mathbf{k}}(i\omega_n) \\ &\approx -\frac{T}{V^2 \nu_F} \sum_{\mathbf{k}, \mathbf{k}', \omega_m} \delta(\epsilon_{\mathbf{k}}) V_{\mathbf{k}-\mathbf{k}'}(i\omega_n - i\omega_m) \cdot \frac{Z(i\omega_m) i\omega_m \hat{\tau}_0 + \epsilon_{k'} \hat{\tau}_z - \Phi(i\omega_m) \hat{\tau}_x}{[Z(i\omega_m) i\omega_m]^2 - [\epsilon_{k'}^2 + \Phi(i\omega_m)^2]}. \end{aligned} \quad (2.26)$$

The next step is to split up the momentum integration in \mathbf{k}' near the Fermi surface into components k'_{\perp} and k'_{\parallel} that are perpendicular and parallel to the Fermi surface:

$$\frac{1}{V} \sum_{\mathbf{k}'} \approx \int_{\epsilon_{\mathbf{k}'} \approx 0} \frac{d^3 k'}{(2\pi)^3} \approx \frac{1}{(2\pi)^3} \int dS_{k'}^F \int dk'_{\perp}$$



$$\begin{aligned}
&= \frac{1}{(2\pi)^3} \int dS_{\mathbf{k}'}^F \int \frac{d\epsilon_{\mathbf{k}'}}{|d\epsilon_{\mathbf{k}'}/dk'_{\perp}|} = \frac{1}{(2\pi)^3} \underbrace{\int \frac{dS_{\mathbf{k}'}^F}{v_{\mathbf{k}'}}}_{\frac{1}{V} \sum_{\mathbf{k}'} \delta(\epsilon_{\mathbf{k}'})} \int d\epsilon_{\mathbf{k}'} \\
&= \frac{1}{V} \sum_{\mathbf{k}'} \delta(\epsilon_{\mathbf{k}'}) \int d\epsilon_{\mathbf{k}'}.
\end{aligned}$$

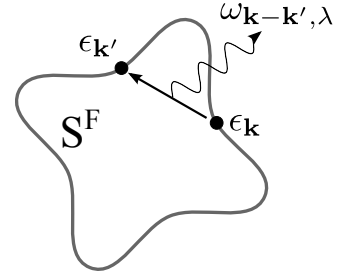
The dominant contributions for the perpendicular integration comes from the electronic dispersion $\epsilon_{\mathbf{k}'} \approx v_F \cdot \mathbf{k}'_{\perp}$ in the fermionic propagator since the bosonic part from $V_{\mathbf{k}-\mathbf{k}'}$ has the typical slow momentum dependence of the phonon spectrum $\omega_{\mathbf{q}} \sim c \cdot k'_{\perp}$. The errors that we make are therefore again of the order of $c/v_F \sim \sqrt{m/M} \ll 1$ and can be neglected like the vertex corrections. In the end, we can write down the self-consistent equations

$$\begin{aligned}
\hat{\Sigma}(i\omega_n) &= -\frac{T}{V^2 \nu_F} \sum_{\mathbf{k}, \mathbf{k}', \omega_m} \delta(\epsilon_{\mathbf{k}}) \delta(\epsilon_{\mathbf{k}'}) V_{\mathbf{k}-\mathbf{k}'}(i\omega_n - i\omega_m) \cdot \int d\epsilon_{\mathbf{k}'} \frac{Z(i\omega_m) i\omega_m \hat{\tau}_0 - \Phi(i\omega_m) \hat{\tau}_x}{[Z(i\omega_m) i\omega_m]^2 - [\epsilon_{\mathbf{k}'}^2 + \Phi(i\omega_m)^2]} \\
&= -T \sum_{\omega_m} \left[-\int_0^{\infty} d\omega \frac{2\omega \cdot \alpha^2 F(\omega)}{(\omega_n - \omega_m)^2 + \omega^2} + \mu^* \right] \int d\epsilon_{\mathbf{k}'} \frac{Z(i\omega_m) i\omega_m \hat{\tau}_0 - \Phi(i\omega_m) \hat{\tau}_x}{[Z(i\omega_m) i\omega_m]^2 - [\epsilon_{\mathbf{k}'}^2 + \Phi(i\omega_m)^2]},
\end{aligned} \tag{2.27}$$

with the following definitions of the Coulomb pseudopotential and Eliashberg function

$$\begin{aligned}
\mu^* &= \frac{1}{V^2 \nu_F} \sum_{\mathbf{k}, \mathbf{k}'} \delta(\epsilon_{\mathbf{k}}) \delta(\epsilon_{\mathbf{k}'}) V_{\mathbf{q}, \text{eff}}^{\text{C}}, \\
\alpha^2 F(\omega) &= \frac{1}{V^2 \nu_F} \sum_{\mathbf{k}, \mathbf{k}', \lambda} \delta(\epsilon_{\mathbf{k}}) \delta(\epsilon_{\mathbf{k}'}) |\alpha_{\mathbf{q}}^{\lambda}|^2 \frac{-\text{Im} D_{\mathbf{k}-\mathbf{k}', \lambda}^R(\omega) \Theta(\omega)}{\pi}.
\end{aligned} \tag{2.28}$$

Note that for unperturbed phonons in a single-particle picture we have $-\text{Im} D_{\mathbf{k}-\mathbf{k}', \lambda}^R(\omega)/\pi = \delta(\omega - \omega_{\mathbf{k}-\mathbf{k}', \lambda})$. The Eliashberg function $\alpha^2 F(\omega)$ can be seen as an effective, weighted phonon DOS for the electrons that scatter inelastically between different states on the Fermi surface via the emission/absorption of a phonon, see figure on the right. Since both Φ and Z are even functions on the imaginary axis and the self-energy can be written as $\hat{\Sigma}(i\omega_n) = i\omega_n [1 - Z(i\omega_n)] \hat{\tau}_0 + \Phi(i\omega_n) \hat{\tau}_z$, we can separate Eq. (2.27) to



$$Z(i\omega_n) = 1 + \frac{T}{\omega_n} \int_0^{\infty} d\omega \frac{2\omega \cdot \alpha^2 F(\omega)}{(\omega_n - \omega_m)^2 + \omega^2} \int d\epsilon_{\mathbf{k}'} \frac{Z(i\omega_m) \omega_m}{[Z(i\omega_m) \cdot \omega_m]^2 + \epsilon_{\mathbf{k}'}^2 + \Phi(i\omega_m)^2}, \tag{2.29}$$

$$\Phi(i\omega_n) = T \sum_{\omega_m} \left[\int_0^{\infty} d\omega \frac{2\omega \cdot \alpha^2 F(\omega)}{(\omega_n - \omega_m)^2 + \omega^2} - \mu^* \right] \int d\epsilon_{\mathbf{k}'} \frac{\Phi(i\omega_m)}{[Z(i\omega_m) \cdot \omega_m]^2 + \epsilon_{\mathbf{k}'}^2 + \Phi(i\omega_m)^2}.$$

Eliashberg equations on imaginary axis

These are the famous Eliashberg equations that have been used to study conventional superconductivity with strong electron-phonon interaction, see also Chapter 1. The

enormous success of the Rowell-McMillan inversion algorithm⁸ for Pb [15] and other strong-coupling materials [16] is a hallmark of how the theoretical interpretation of experimental data can lead to a quantitative understanding of solid state systems. To end our discussion of the Eliashberg equations on the imaginary axis, let us consider the BCS approximation of (2.29). This is the weak-coupling and static limit without Coulomb repulsion:

- $Z(i\omega_n) \approx 1$
- $\Phi(i\omega_n) \approx \Phi$
- $\int_0^\infty d\omega \frac{2\omega \cdot \alpha^2 F(\omega)}{(\omega_n - \omega_m)^2 + \omega^2} \approx 2 \int_0^\infty d\omega \frac{\alpha^2 F(\omega)}{\omega} := \lambda$
- $\mu^* = 0$

Here, λ is the dimensionless electron-phonon coupling constant (also called the mass enhancement parameter), which gives the correction of the electrons effective mass $m^*/m = 1 + \lambda$ in the normal state. For strong coupling superconductors λ is typically of order unity, which is the reason that BCS theory does not work for these materials and strong deviations from the conclusions made in Section 2.1 occur. In the BCS limit $\lambda \ll 1$, we find the usual self-consistency equation for the superconducting gap

$$\Delta = \Phi = T \sum_{\omega_m} \lambda \cdot \int d\epsilon_{\mathbf{k}'} \frac{\Delta}{\omega_m^2 + \epsilon_{\mathbf{k}'}^2 + \Delta^2} = \lambda \int d\epsilon_{\mathbf{k}} \frac{\Delta}{2E_{\mathbf{k}}} \tanh\left(\frac{E_{\mathbf{k}}}{2T}\right). \quad (2.30)$$

Thus, one can directly link the electron-phonon coupling constant λ to the phenomenological parameter introduced in the BCS theory.

2.2.3. Strong-coupling superconductivity for single phonon mode

In order to investigate further the implications of the Eliashberg theory, let us give the corresponding equations for $Z^R(\omega) = Z(\omega + i0)$ and $\Delta^R(\omega) = \Delta(\omega + i0) = \Phi(\omega + i0)/Z(\omega + i0)$ on the real axis after the usual analytical continuation $i\omega_n \rightarrow \omega + i0$ [12]

$$Z^R(\omega) = 1 - \frac{1}{\omega} \int_0^\Lambda d\omega_1 \mathbf{Re} \left[\frac{\omega_1}{\sqrt{\omega_1^2 - [\Delta^R(\omega_1)]^2}} \right] \left[K_+(\omega, \omega_1) + K_+(\omega, -\omega_1) \right], \quad (2.31)$$

$$Z^R(\omega) \Delta^R(\omega) = \int_0^\Lambda d\omega_1 \mathbf{Re} \left[\frac{\Delta^R(\omega_1)}{\sqrt{\omega_1^2 - [\Delta^R(\omega_1)]^2}} \right] \left[K_-(\omega, \omega_1) - K_-(\omega, -\omega_1) - \mu^* [1 - 2n_F(\omega_1)] \right].$$

Eliashberg equations on real axis

⁸see Section 1.1.2

Here, the integral kernel is defined as

$$K_{\pm}(\omega, \omega_1) = \int_0^{\Lambda} d\omega_2 \alpha^2 F(\omega_2) [n_B(\omega_2) + n_F(-\omega_1)] \left(\frac{1}{\omega + \omega_1 + \omega_2 + i0} \pm \frac{1}{\omega - \omega_1 - \omega_2 + i0} \right). \quad (2.32)$$

It contains the information about the spectrum $\alpha^2 F(\omega)$ and the thermal occupation of the phonons. Importantly, the (formally divergent) integrals are cutoff not by the Fermi energy E_F or some fermionic band edge, but by a low-energy cutoff $\Lambda \sim \omega_D$ that is typically chosen as a multiple of the Debye frequency. This is why we use the effective low-energy parameters $\alpha^2 F$ and μ^* , see the discussion in the previous Section 2.2.1. We have to consider the Eliashberg equations on the real axis, because most of the experimentally accessible observables are related to the real-frequency functions. For example, the superconducting DOS (per spin degree of freedom) can be computed via

$$\begin{aligned} \nu(\epsilon) &= \frac{1}{V} \sum_{\mathbf{k}} \frac{\mathbf{Im} G_{\mathbf{k}}^R(\epsilon)}{-\pi} = \frac{\nu_F}{-\pi} \mathbf{Im} \int d\epsilon_{\mathbf{k}} \frac{Z^R(\epsilon)\epsilon + \epsilon_{\mathbf{k}}}{[Z^R(\epsilon)\epsilon]^2 - \epsilon_{\mathbf{k}}^2 - [\Phi^R(\epsilon)]^2} \\ &= \mathbf{Re} \left[\frac{\nu_F |\epsilon|}{\sqrt{\epsilon^2 - [\Delta^R(\epsilon)]^2}} \right]. \end{aligned} \quad (2.33)$$

Note that the expression is similar to Eq. (2.8) of the BCS theory, apart from the energy-dependent gap function $\Delta^R(\omega)$ which mirrors the dynamical and retarded nature of the electron-phonon interaction and of the phonon spectrum. We also want to emphasize that even for the case of strong electron-phonon coupling, where a significant renormalization of the bare electronic mass and dispersion takes place, the electronic DOS in the normal state stays unaffected. This can be seen directly by considering Eq. (2.33) in the limit $\Delta^R(\omega) \sim \Phi^R(\omega) = 0$.

To get a feeling for the impact of the phonon spectrum on the fermionic spectra, we follow Scalapino et al. [11] and discuss the strong-coupling features of a single phonon mode. The phonon spectral function is shown on the right and characterized by

$$\alpha^2 F(\omega) = A_0 \cdot \frac{\omega^2}{\omega^2 + \omega_0^2} \cdot \frac{\gamma}{(\omega - \omega_{\text{ph}})^2 + \gamma^2}. \quad (2.34)$$

Here, A_0 is a normalization factor which will be fixed by our choice of λ , ω_{ph} is the characteristic phonon energy, $\omega_0 \ll \omega_{\text{ph}}$ is some low-energy cutoff for small phonon energies and γ is the half-width at half-maximum (HWHM) of the phonon mode. The dimensionless electron-phonon coupling constant is chosen to be $\lambda = 1.5$ and the Coulomb pseudopotential as $\mu^* = 0.1$. These parameters are close to the values in Pb [11] and are in the strong-coupling regime. Note that for our calculations of the spin-fermion model we do not solve the Eliashberg equations (2.31) directly, but we follow Ref. [108] and perform the analytical continuation in a different manner using the properties of Laplace transformations.

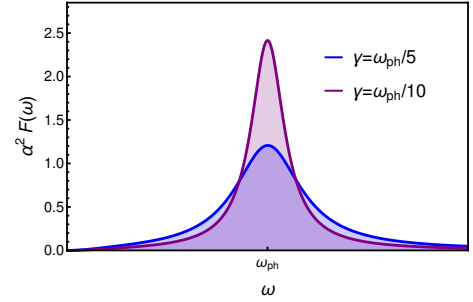


Figure 2.3.: Eliashberg function for single phonon mode at frequency ω_{ph} and with different half-width γ .

In Figure 2.4 we show the computed gap function $\Delta^R(\omega)$ and the electron DOS $\nu(\omega)$ calculated from Eq. (2.33) in the zero temperature limit. The gap value Δ_0 is defined

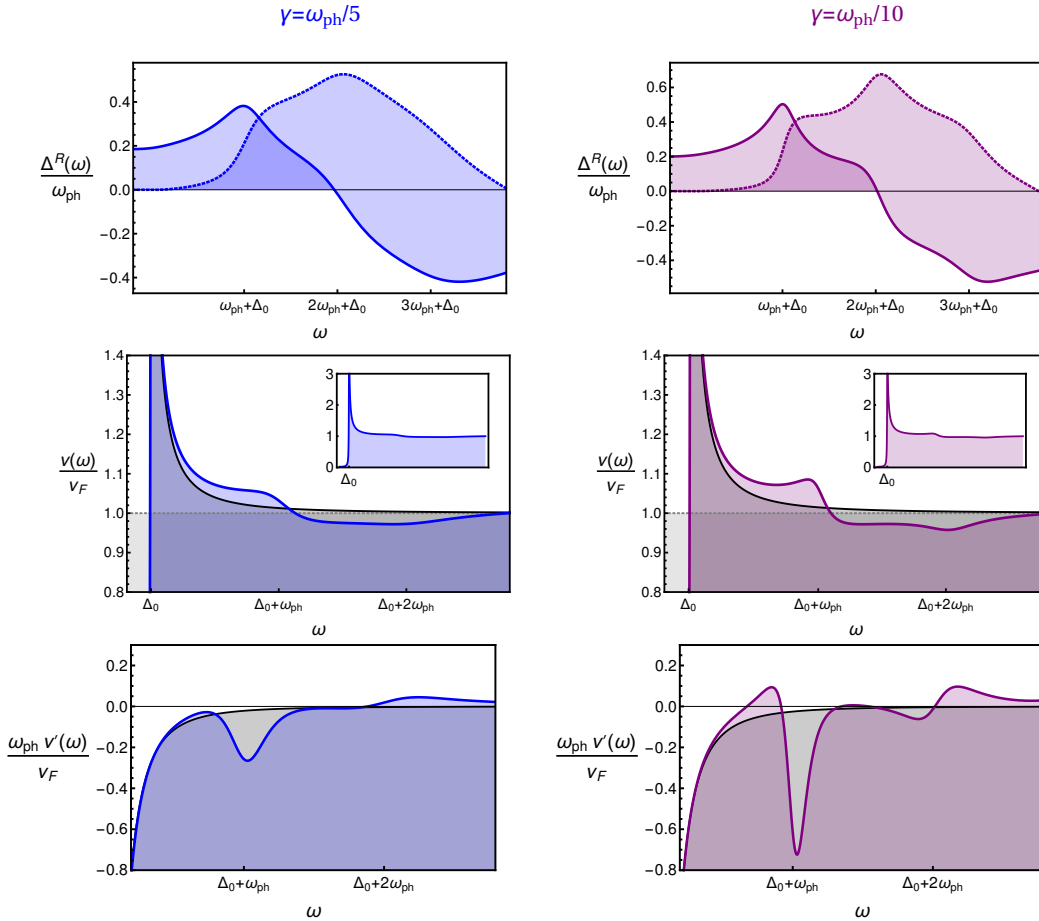


Figure 2.4.: Real (solid lines) and imaginary parts (dashed lines) of the superconducting gap function $\Delta^R(\omega)$, corresponding electronic DOS (and derivative) compared to the BCS DOS (black) for $T = 0$.

as the point where the van-Hove singularity of (2.33) occurs, which yields the condition $\Delta_0 = \text{Re}[\Delta^R(\Delta_0)]$. From Figure 2.4 we see that the real part of the gap function is positive and has its maximum at $\omega_{\text{ph}} + \Delta_0$, followed by a strong decrease and a sign change. Thus, $\text{Re} \Delta^R(\omega)$ follows the effective phonon-induced electron-electron interaction as for energies⁹ $\omega < \omega_{\text{ph}} + \Delta_0$ the electron interacts with the cores at energies smaller than their characteristic oscillation frequency ω_{ph} and creates an in-phase response of the positive background. This creates the attractive interaction discussed earlier in Section 2.2.1, followed by a net repulsive interaction for $\omega > \omega_{\text{ph}} + \Delta_0$ as the ions now oscillate out-of-phase. The imaginary part of the gap gives the information about the possible decay mechanisms in the system. It is therefore zero for energies smaller than $\omega_{\text{ph}} + \Delta_0$, which is the minimal energy where a Bogoliubov quasiparticle can emit a phonon and still ends up in an allowed electronic state with energy larger than Δ_0 . Due to the van-Hove singularity in the electronic spectrum there are peaks present at $\omega = \omega_{\text{ph}} + \Delta_0$ and $\omega = 2\omega_{\text{ph}} + \Delta_0$, the latter coming from higher order processes where two phonons are involved. For very small phonon line-widths γ the peaks and features become more prominent and even third order features at $\omega = 3\omega_{\text{ph}} + \Delta_0$ are present. The structures visible in the gap function transfer to the electronic DOS (also often called tunneling DOS due to the elastic tunneling

⁹Note that the energy that can be emitted by a fermionic quasiparticle with energy ω in the superconductor is $\omega - \Delta_0$ since there are no states inside the gap.

picture described in Chapter 1). The Van-Hove singularity at $\omega = \Delta_0$ follows the typical square-root behavior and dominates the BCS DOS, but for frequencies comparable to $\omega_{\text{ph}} + \Delta_0$ deviations are clearly visible. Below $\omega < \omega_{\text{ph}} + \Delta_0$ the strong-coupling DOS becomes larger than the BCS DOS as the attractive interaction between the electrons for energies smaller than the phonon frequency increases the pairing amplitude, whereas the repulsive interaction and the possible decay of quasiparticles via phonon-scattering reduced the DOS for energies higher than ω_{ph} . The result is a characteristic peak-dip feature around $\omega_{\text{ph}} + \Delta_0$ in the tunneling DOS. Further, in the derivative of the DOS a pronounced dip occurs at $\omega = \Delta_0 + \omega_{\text{ph}}$. The effect of changing the Coulomb pseudopotential is not shown in Figure 2.4, but is obvious if one looks at the the real part of the gap which becomes negative for higher energies $\omega \gg \omega_{\text{ph}}$ due to the repulsive nature of the Coulomb interaction between the electrons. Further, increasing μ^* leads to a reduction of Δ_0 and T_c as one would naturally expect.

2.3. Superconductivity from electronic pairing

In this section, we present analytical models that extend the BCS theory to non-phononic pairing mechanisms. A prominent example is the spin-fermion model, where spin fluctuations are responsible for the Cooper pairing. Such an electronic pairing can also lead to non-isotropic gap symmetries and we explicitly discuss an extension of the Eliashberg theory to interactions with d -wave form factors.

2.3.1. Spin-fermion model

Let us introduce the spin-fermion model as a minimal low-energy theory describing the antiferromagnetic and superconducting phase in unconventional superconductors. It is motivated by the closeness of superconducting phase to the antiferromagnetic quantum critical point in the phase diagrams of many cuprate and iron pnictide superconductors, see Figure 1.7. The microscopic justification of the spin-fermion model starts with the Hubbard-model including on-site interactions [109]. When integrating out the high-energies degrees of freedom it is assumed that the spin-spin channel of the fermion-fermion interaction dominates and a collective spin mode is introduced via a Hubbard–Stratonovich transformation. The *bare* spin susceptibility is assumed to be of the regular Ornstein-Zernike form centered around the antiferromagnetic ordering vector \mathbf{Q}

$$\chi_0(\mathbf{q}, \omega) = \frac{\chi_0}{\xi^{-2} + (\mathbf{q} - \mathbf{Q})^2 - \omega^2/v_s^2}. \quad (2.35)$$

Here, ξ is the spin correlation length (note that we are in the non-magnetically ordered state), $v_s \sim v_F$ the spin velocity and the term quadratic in energy comes from the dynamics of the high-energy fermions. It is purely real as damping in the low-energy theory can only come from fermions near the Fermi edge. This dynamic part is then neglected as the frequency-dependent part that originates from the interaction with the low-energy fermions will dominate this expression (due to the separation of energy scales). This results in the approximation $\chi_{\mathbf{q},0}^{-1} = r + c_s(\mathbf{q} - \mathbf{Q})^2$ and the effective action

$$S = \int_k \sum_{\sigma} \bar{\psi}_{k,\sigma}(i\omega_n - \epsilon_{\mathbf{k}})\psi_{k,\sigma} + \frac{1}{2} \int_q \mathbf{S}_q \mathbf{S}_{-q} \chi_{\mathbf{q},0}^{-1} + g \int_{k,q} \sum_{\sigma,\sigma'} \bar{\psi}_{k+q,\sigma} (\boldsymbol{\tau}_{\sigma,\sigma'} \cdot \mathbf{S}_q) \psi_{k,\sigma'}. \quad (2.36)$$

Here, \mathbf{S}_q is the collective spin mode, g the spin-fermion coupling constant of the theory and the momentum sums are restricted to the two-dimensional Brillouin zone that model the superconducting planes. Starting from this model one can derive the self-consistent coupled integral equations (see Appendix A) as

$$\begin{aligned}\Sigma_p &= 3g^2 \int_q \chi_q G_{p-q}^{(p)}, \\ \Phi_p &= 3g^2 \int_q \chi_q F_{p-q}, \\ \Pi_q &= 2g^2 \int_k [G_k^{(p)} G_{k+q}^{(p)} + F_k F_{k+q}].\end{aligned}\tag{2.37}$$

The dressed propagators read ($Z_k = 1 - \Sigma_k/i\omega_n$):

$$\begin{aligned}G_p^{(p)} &= \frac{Z_p i\omega_n + \epsilon_p}{[Z_p i\omega_n]^2 - \epsilon_p^2 - \Phi_p^2}, \\ F_p &= \frac{\Phi_p}{[Z_p i\omega_n]^2 - \epsilon_p^2 - \Phi_p^2}, \\ \chi_q &= \frac{1}{\chi_{q,0}^{-1} - \Pi_q}.\end{aligned}\tag{2.38}$$

In the derivation of these equations vertex-corrections have been neglected following Ref. [110], where it was shown that the spin fluctuations for $\mathbf{q} \approx \mathbf{Q}$ are slow modes compared to the fermionic quasiparticles such that we can apply the Migdal theorem. There are two main differences compared to the conventional Eliashberg theory for phonon-mediated superconductivity:

1. In the definition of Φ_p there is a relative + sign compared to Σ_p in contrast to the conventional Eliashberg theory. Thus, the points connected by the interaction χ_q need to have a relative sign-change for the order parameter, giving rise to unconventional pairing symmetries.
2. The renormalization of the bosonic spin spectrum via the self-energy Π_q is important for the spin-fermion theory. In contrast to phonons, whose dynamics can to first order be treated as independent degrees of freedom (Born-Oppenheimer approximation), the dynamics of the collective spin degrees of freedom is determined by the coupling to the low-energy fermions. The reason is that this collective mode is made out of fermions and therefore must be considered in a self-consistent way together with the fermionic quasiparticles, as described by Eqs. (2.37,2.38).

Solving the set of coupled equations in (2.37) for a general fermionic dispersion is an expensive computational task, see e.g. Ref.[108]. Instead, we follow Ref. [110] and employ a hot spot approximation to get a principle idea of the underlying physics of the problem. The main motivation behind the hot-spot theory is the fact that the spin-fermion model is only valid for quasiparticles close to the Fermi edge and the interaction is peaked around \mathbf{Q} , such that the most interesting parts of the fermionic Brillouin zone are the so called ‘‘hot-spots’’. These are defined as regions on the Fermi surface that are connected by the AFV \mathbf{Q} , see Figure 2.5. Thus, to make the problem analytically treatable it makes sense to restrict oneself to these regions and to expand the above equations around the hot-spots \mathbf{k}_h . The general procedure of this expansion is described in detail in Appendix A. In the following we define $\Pi_m = \Pi_{\mathbf{Q}}(i\Omega_m)$, $\Sigma_n = \Sigma_{\mathbf{k}_h}(i\omega_n) = \Sigma_{\mathbf{k}_h+\mathbf{Q}}(i\omega_n)$, $Z_n = Z_{\mathbf{k}_h}(i\omega_n) = Z_{\mathbf{k}_h+\mathbf{Q}}(i\omega_n)$

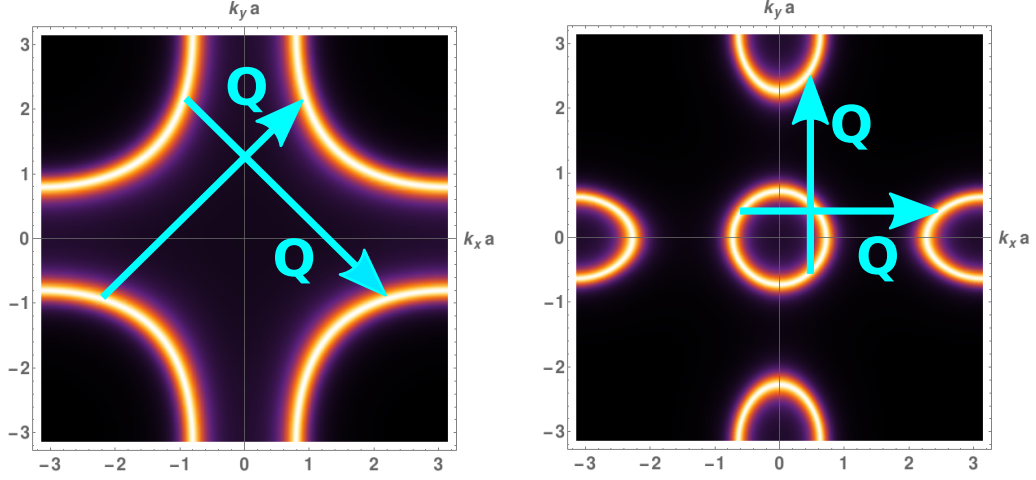


Figure 2.5.: Generic (unfolded) Fermi surface of the cuprate and iron pnictide superconductors including their antiferromagnetic ordering vectors \mathbf{Q} . The hot spots are the points/regions on the Fermi surface that are connected by \mathbf{Q} .

and $\Phi_n = \Phi_{\mathbf{k}_h}(i\omega_n) = -\Phi_{\mathbf{k}_h+\mathbf{Q}}(i\omega_n)$. The sign-change in the latter is necessary to find an attractive pairing channel for the spin-mediated superconductivity as was already mentioned earlier. The resulting equations are summarized as

$$\begin{aligned}\Sigma_n &= \frac{3g^2}{(2\pi)^2} T \sum_{\Omega_m} \int dq_{\parallel} \frac{1}{r + c_s q_{\parallel}^2 - \Pi_m} \int dq_{\perp} \frac{Z_{n-m}(i\omega_n - i\Omega_m)}{[Z_{n-m}(i\omega_n - i\Omega_m)]^2 - (v_F q_{\perp})^2 - \Phi_{n-m}^2}, \\ \Phi_n &= -\frac{3g^2}{(2\pi)^2} T \sum_{\Omega_m} \int dq_{\parallel} \frac{1}{r + c_s q_{\parallel}^2 - \Pi_m} \int dq_{\perp} \frac{\Phi_{n-m}}{[Z_{n-m}(i\omega_n - i\Omega_m)]^2 - (v_F q_{\perp})^2 - \Phi_{n-m}^2}, \\ \Pi_m &= \frac{g^2 N}{2\pi^2 v_F^2} T \sum_{\omega_n} \int d\epsilon d\epsilon' \frac{Z_n Z_{n+m} i\omega_n (i\omega_n + i\Omega_m) - \Phi_n \Phi_{n+m}}{\left([Z_n i\omega_n]^2 - \epsilon^2 - \Phi_n^2\right) \left([Z_{n+m}(i\omega_n + i\Omega_m)]^2 - \epsilon'^2 - \Phi_{n+m}^2\right)},\end{aligned}$$

where v_F is the Fermi velocity of the N hot-spots of the Fermi surface. The parameters contained in this equations can be reduced to a dimensionless coupling constant $\lambda = \frac{3g^2}{4\pi v_F \sqrt{c_s r}}$ and a characteristic bosonic energy scale $\omega_{\text{sf}} = r/\gamma$, where we defined $\gamma = \frac{g^2 N}{2\pi v_F^2}$. The self-consistency equations can then be written in the compact form

$$\begin{aligned}\Sigma_n &= \frac{\lambda T}{\pi} \sum_{\Omega_m} \int dx \frac{1}{1 + x^2 - \tilde{\Pi}_m/\omega_{\text{sf}}} \int d\epsilon \frac{Z_{n-m}(i\omega_n - i\Omega_m)}{[Z_{n-m}(i\omega_n - i\Omega_m)]^2 - \epsilon^2 - \Phi_{n-m}^2} \\ \Phi_n &= -\frac{\lambda T}{\pi} \sum_{\Omega_m} \int dx \frac{1}{1 + x^2 - \tilde{\Pi}_m/\omega_{\text{sf}}} \int d\epsilon \frac{\Phi_{n-m}}{[Z_{n-m}(i\omega_n - i\Omega_m)]^2 - \epsilon^2 - \Phi_{n-m}^2} \quad (2.39) \\ \tilde{\Pi}_m &= \Pi_m/\gamma = \frac{T}{\pi} \sum_{\omega_n} \int d\epsilon d\epsilon' \frac{Z_n Z_{n+m} i\omega_n (i\omega_n + i\Omega_m) - \Phi_n \Phi_{n+m}}{\left([Z_n i\omega_n]^2 - \epsilon^2 - \Phi_n^2\right) \left([Z_{n+m}(i\omega_n + i\Omega_m)]^2 - \epsilon'^2 - \Phi_{n+m}^2\right)}\end{aligned}$$

Before solving these equations in the superconducting state, let us quickly recast the properties of the spin-fermion model in the normal state following the conventions of Ref. [111]. The bosonic self-energy can be calculated as $\Pi_m = \gamma |\Omega_m|$, which translates to a pure Landau damping term $\Pi^R(\Omega) = i\gamma\Omega$ on the real axis. Thus, the spin mode is overdamped in the normal state, which originates from the gapless fermionic quasiparticles at the hot-spots. This overdamped boson gives rise to a self-energy $\Sigma_n = -i\lambda \sqrt{\omega_{\text{sf}}} \text{sign}(\omega) [\sqrt{\omega_{\text{sf}} + |\omega_n|} - \sqrt{\omega_{\text{sf}}}]$,

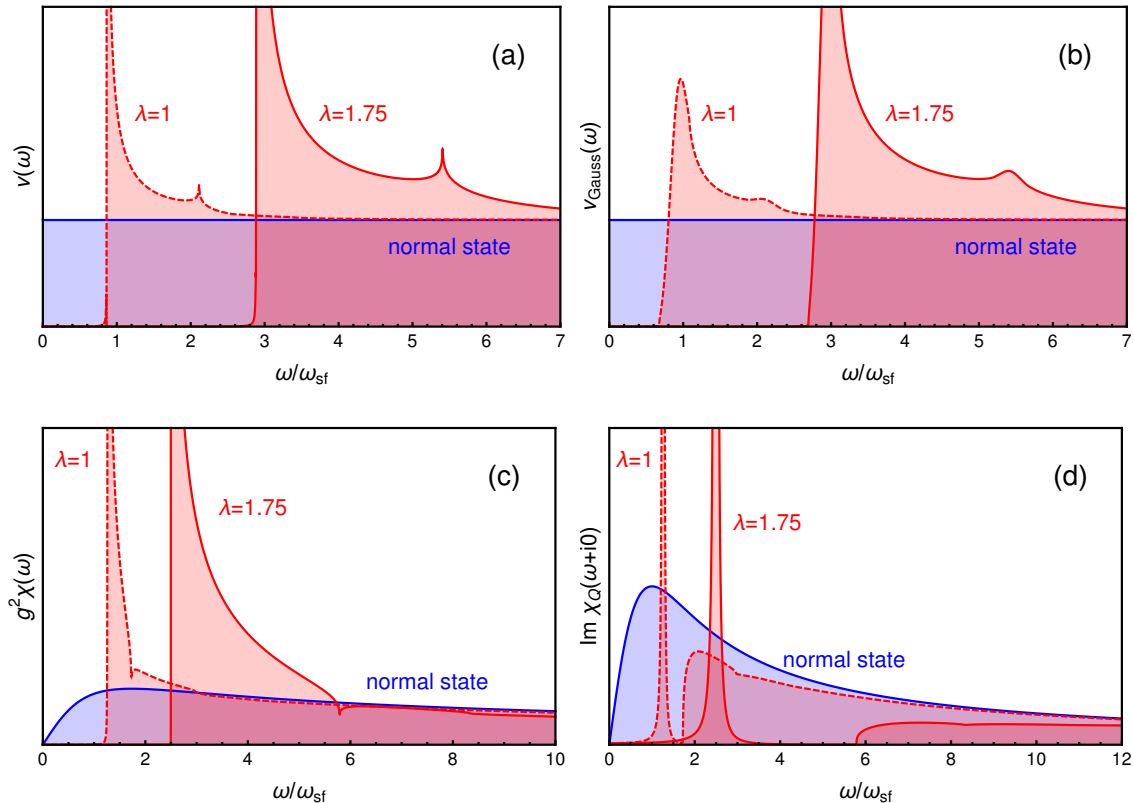


Figure 2.6.: Electron and spin spectrum for the hot-spot theory of the spin-fermion model for different values of the dimensionless coupling parameter λ in the superconducting (red curves) and in the normal state (blue curve): (a) Fermionic DOS including the coherence peak and the strong-coupling features at $\Delta + \omega_{\text{res}}$, (b) Fermionic DOS convoluted with Gaussian distribution with standard deviation $\sigma = 0.2\omega_{\text{sf}}$ to simulate broadening effects, (c) Effective Eliashberg function for the spin-fermion model that changes significantly when entering the superconducting state, (d) Spin spectrum at the antiferromagnetic ordering vector \mathbf{Q} showing a clear resonance peak.

which displays a Fermi-liquid behavior for $|\omega_n| \ll \omega_{\text{sf}}$, whereas for $\omega \gg \omega_{\text{sf}}$ it possesses an unusual self-energy $\Sigma_n = i\lambda \text{sign}(\omega) \sqrt{|\omega_n|}$ that exhibits a non-Fermi liquid behavior with $\text{Im} \Sigma^R(\omega) \sim \sqrt{|\omega|}$ on the real axis. Nevertheless, the normal state electron DOS remains constant also with the inclusion of the self-energy term due to the same arguments as in Eq. (2.33). Only if one allows for a momentum-dependence of the fermion self-energy, the normal state electronic spectrum shows a weak renormalization.

Next, we solve equations (2.39) numerically in the superconducting state for low temperatures $T = 0.1\omega_{\text{sf}}$ using the method of Laplace transformations described in Ref. [108]. The calculated electronic and bosonic spectra are shown in Figure 2.6. Below the transition temperature T_c a spin gap evolves in the bosonic spectrum as the energy of 2Δ is needed to break up a Cooper pair and to create a particle-hole excitation, where $\Delta := |\Delta_{\mathbf{k}_h}|$ is the absolute value of the superconducting gap at the hot spot. Thus, spin spectral weight is shifted to higher energies due to the opening of the superconducting gap Δ for the fermionic quasiparticles. For a sign-changing gap symmetry $\Delta_{\mathbf{k}_h} = -\Delta_{\mathbf{k}_h + \mathbf{Q}}$ a sharp resonance peak occurs near the AFV \mathbf{Q} and the energy $\omega_{\text{res}} < 2\Delta$ [112], as can be seen in Figure 2.6(d). This peak can explain the resonance mode seen in the

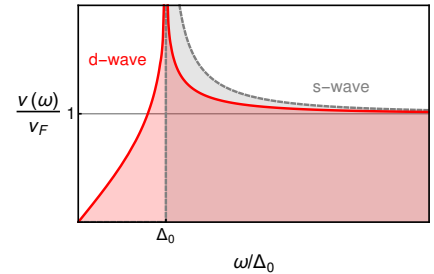
neutron scattering experiments discussed in Section 1.3.1. Note that for an s-wave gap symmetry the spin spectrum would be fully gapped by 2Δ , which comes from the different coherence factors $\Phi_n \Phi_{n+m} \rightarrow -\Phi_n \Phi_{n+m}$ in the expression for the bosonic self-energy Π_m . The effective Eliashberg function for the spin-fermion model is obviously given by $g^2\chi(\omega) = \mathbf{Im} \int dx \frac{1}{1+x^2-\tilde{\Pi}^R(\omega)/\omega_{sf}} = \mathbf{Im} \frac{1}{\sqrt{1-\tilde{\Pi}^R(\omega)/\omega_{sf}}}$ and is shown in Figure 2.6(d). Also $g^2\chi(\omega)$ displays a sharp feature at ω_{res} , which in turn affects the superconducting spectrum of the fermions. For the fermionic degrees of freedom a superconducting gap Δ appears and a sharp strong-coupling feature in the fermionic DOS $\nu(\omega)$ evolves at $\Delta + \omega_{\text{res}}$ due to the coupling to the spin resonance mode, see red curves of Figure 2.6(a). When convoluted with a Gaussian distribution to simulate the effect of disorder or experimental broadening, typical peak-dip strong-coupling features as known from conventional Eliashberg theory arise as can be seen in Figure 2.6(b). We note that this theory is only valid for the regions around the hot-spots and can therefore not capture the correct physics of the whole Brillouin zone and features arising from angular dependencies of the gap function. It is therefore mainly suitable for explaining the resonance mode occurring in the unconventional superconductors (for which only the hot-spot regions are important) and for the iron pnictide compounds with nodeless s_{\pm} pairing symmetry.

2.3.2. Eliashberg formalism for d-wave superconductivity

When dealing with true d-wave superconductivity, the hot-spot theory obviously fails to describe the nodal parts of the Fermi surface. Before proceeding with a strong-coupling analysis of a d-wave superconductor, let us quickly consider the mean-field DOS of a superconductor with pairing gap $\Delta_{\mathbf{k}} = \Delta_0 \cos(2\phi)$ and isotropic dispersion $\epsilon_{\mathbf{k}}$. Here, $\phi = \arctan(k_y/k_x)$ is the angle relative to the positive k_x direction. The corresponding electronic mean-field spectrum per spin can be calculated as

$$\begin{aligned} \nu_d(\omega) &= \frac{1}{V} \sum_{\mathbf{k}, \sigma} \delta(|\omega| - \sqrt{\epsilon_{\mathbf{k}}^2 + \Delta_{\mathbf{k}}^2}) = \nu_F \int d\epsilon \int_0^{2\pi} \frac{d\phi}{2\pi} \delta(|\omega| - \sqrt{\epsilon^2 + \Delta_0^2 \cos(2\phi)^2}) \\ &= \nu_F \mathbf{Re} \int_0^{2\pi} \frac{d\phi}{2\pi} \frac{|\omega|}{\sqrt{\omega^2 - \Delta_0^2 \cos(2\phi)^2}}. \end{aligned} \quad (2.40)$$

The plot of the mean-field d-wave DOS is shown on the right side. For energies $\omega \ll \Delta_0$ much smaller than the maximum gap on the Fermi surface, the DOS scales linear and displays a logarithmic divergence at $\omega = \Delta_0$. Therefore, there is still a clear superconducting coherence peak for a d-wave superconductor besides the fact that it has nodal contributions. However, the nature of the singularity at the coherence peak is strongly suppressed compared to the s-wave case.



The extension of the Eliashberg framework described in Section 2.2 to more general pairing symmetries can be done in the following way. Let us again consider a two dimensional Fermi-liquid and a pairing interaction $\alpha^2 F$ that cannot be treated as isotropic. Instead, we assume that the interaction possesses both s- and d-wave contributions. Thus, when performing the momentum-average over the Fermi surface as in

Eq. (2.28) this results in the angle-dependent Eliashberg function

$$\alpha^2 F(\omega, \phi - \phi') = \alpha^2 F(\omega) \left[c_s + c_d \cdot \cos[2(\phi - \phi')] \right]. \quad (2.41)$$

Here, ϕ and ϕ' are the angles of the two interacting electrons as defined above. Further, $c_{s/d}$ are the amplitudes of the s- and d-wave pairing channels, respectively. Due to this non-isotropic form of the interaction both the renormalization function $Z^R(\omega, \phi) = Z_s^R(\omega) + Z_d^R(\omega) \cos(2\phi)$ and the gap function $\Delta^R(\omega, \phi) = \Delta_s^R(\omega) + \Delta_d^R(\omega) \cos(2\phi)$ obtain an s- and d-wave part. However, the authors of Ref. [113] showed that the d-wave part of the renormalization function $Z^R(\Omega)$ is rather exotic and small. When assuming a purely isotropic $Z^R(\omega, \phi) = Z^R(\omega)$ and a pure d-wave gap $\Delta^R(\omega, \phi) = \Delta^R(\omega) \cos(2\phi)$ the coupled Eliashberg equations have the form [114]:

$$\begin{aligned} Z^R(\omega) &= 1 - \frac{1}{\omega} \int_0^{2\pi} \frac{d\phi}{2\pi} \int_0^\Lambda d\omega_1 \mathbf{Re} \left[\frac{c_s \omega_1}{\sqrt{\omega_1^2 - \Delta^2(\omega_1) \cos^2(\phi)}} \right] \left[K_+(\omega, \omega_1) + K_+(\omega, -\omega_1) \right], \\ Z^R(\omega) \Delta^R(\omega) &= \int_0^{2\pi} \frac{d\phi}{2\pi} \int_0^\Lambda d\omega_1 \mathbf{Re} \left[\frac{c_d \Delta(\omega_1) \cos^2(\phi)}{\sqrt{\omega_1^2 - \Delta^2(\omega_1) \cos^2(\phi)}} \right] \left[K_-(\omega, \omega_1) - K_-(\omega, -\omega_1) \right], \end{aligned} \quad (2.42)$$

with the same kernels defined in Eq.(2.32). The Coulomb pseudopotential is not included here as we assume that the pairing interaction originates from the electronic interactions between the particles as described in the previous section. The above equations were used by Refs. [114, 115] to explain the strong dip feature seen on the BiO layers of BSCCO. Let us quickly point out the important differences between the s-wave and d-wave equations by comparing the results for a single boson mode. We use a Lorentzian with characteristic energy $\omega_0 \simeq 36.5\text{meV}$ and full width at half maximum (FWHM) $\Gamma = 8\text{meV}$, which was found in Ref. [115] as best fit¹⁰ of the bosonic spectral function for the tunneling spectra in BSCCO, see inset in Figure 2.7. As can be seen in the blue curve of Figure 2.7, the superconducting (maximum) d-wave gap Δ_0 resulting from the fit is given by $\Delta = 32\text{meV}$. The coherence peak follows the mean-field log-behavior as was described above and additional strong-coupling features arise for higher energies. Also for the d-wave case, typical peak-dip strong-coupling features arise, but the dip is much stronger pronounced due to the logarithmic nature of the coherence peak. Additionally, at the energy $\Delta_0 + \omega_0$ a strong dip occurs, which is followed by a weak hump feature. Such characteristic have also been seen in momentum-resolved Eliashberg calculations [108, 116].

In Figure 2.7 we also show the curve of the corresponding s-wave DOS with the same gap amplitude Δ_0 ¹¹ in red. In contrast to the d-wave case, for the s-wave superconductor $\Delta_0 + \omega_0$ is the position of the maximal slope of the strong-coupling features. In comparison with the s-wave plots in Section 2.2.3, we here considered a bosonic mode with characteristic energy $\omega_0 \approx \Delta$ comparable to the superconducting gap. Therefore, the peak position of the strong-coupling peak-dip feature is very close to the coherence peak such that the additional electronic spectral weight from to the peak at $\omega \approx \Delta_0 + \omega_0$ has to be equated by a strong dip that occurs for energies $\omega \gg \Delta_0 + \omega_0$.

¹⁰The authors of Ref. [115] only considered the fit to a Lorentzian function.

¹¹Note, that we needed to increase the amplitude of the Eliashberg function for the s-wave case to obtain the same gap value $\Delta_0 = 32\text{meV}$ as for the d-wave solutions. The reason for this is, that the average gap value $\langle \Delta \rangle = \int_0^{\pi/4} \frac{d\phi}{\pi/4} \Delta_0 \cos(2\phi) = 2/\pi \cdot \Delta_0$ for the d-wave case is of course smaller than the maximum gap Δ_0 .

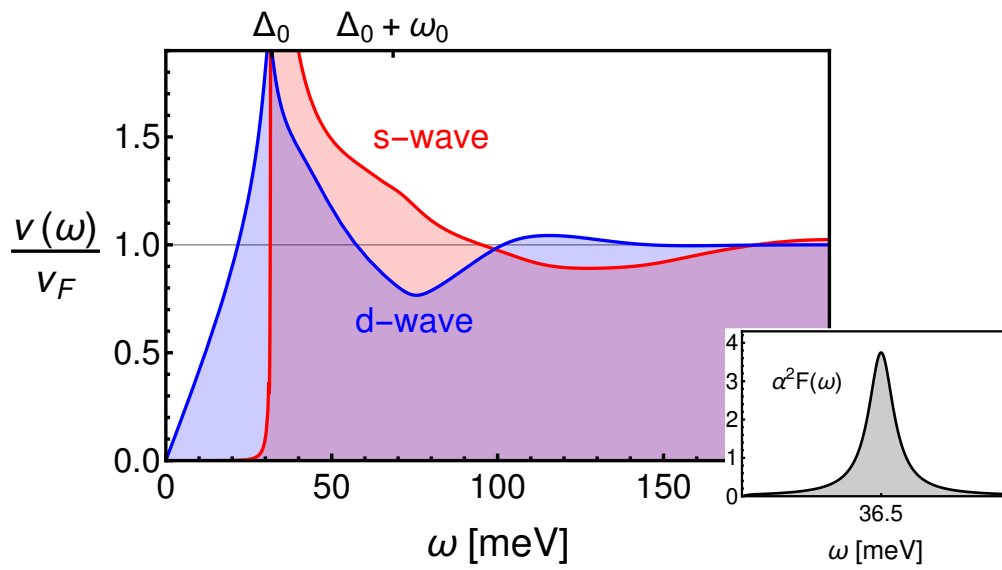


Figure 2.7.: Comparison of strong-coupling DOS for an s-wave and d-wave superconductor with gap $\Delta_0 = 32$ meV for single boson mode with $\omega_0 = 36.5$ meV and FWHM $\Gamma = 8$ meV (see inset).

3. Theoretical description of elastic & inelastic electron tunneling

In this chapter the theoretical framework for inelastic tunneling is presented. It is shown that the effective low-energy theory of a tunneling junction naturally possesses two contributions: (i) An elastic transition where the initial and final energy of the electron on the left and on the right electrode is conserved, and (ii) the inelastic tunneling process involving the emission/absorption of a collective bosonic mode. We derive this effective theory by integrating out high-energy fermions and show that this inelastic tunneling events correspond to transitions involving a virtual off-shell state far away from the Fermi surface of the investigated material. Employing the Keldysh perturbation theory, we derive the explicit forms for the elastic and inelastic tunneling currents, which will then be interpreted in terms of distinct physical tunneling processes. Finally, we discuss the implications of inelastic tunneling processes for normal-state measurements and how temperature and experimental recording techniques set limits for the resolution of IETS.

3.1. Derivation of the effective tunneling Hamiltonian

In Chapter 1 we already discussed the transfer Hamiltonian approach that describes the elastic transition of an electron from one electrode to the other assuming two initially separated electrodes. We now want to start with a *purely elastic* high-energy tunnel model and derive the corresponding low-energy theory by integrating out high-energy degrees of freedom [25]. The high-energy Hamiltonian has the form

$$\begin{aligned} \hat{\mathcal{H}} = & \sum_{\mathbf{k}, \sigma} [\epsilon_{\mathbf{k}}^s \hat{s}_{\mathbf{k}, \sigma}^\dagger \hat{s}_{\mathbf{k}} + \epsilon_{\mathbf{k}}^t \hat{t}_{\mathbf{k}, \sigma}^\dagger \hat{t}_{\mathbf{k}}] + \hat{\mathcal{H}}_{\Phi} + \sum_{\substack{\mathbf{k}, \mathbf{k}' \\ \sigma, \sigma'}} \sum_n \alpha_{\mathbf{k}, \sigma, \mathbf{k}', \sigma'}^n \hat{s}_{\mathbf{k}, \sigma}^\dagger \hat{s}_{\mathbf{k}', \sigma'} \hat{\Phi}_{\mathbf{k}-\mathbf{k}'}^n \\ & + \sum_{\substack{\mathbf{k}, \mathbf{k}' \\ \sigma}} [t_{\mathbf{k}, \mathbf{k}'}^e \hat{s}_{\mathbf{k}, \sigma}^\dagger \hat{t}_{\mathbf{k}', \sigma'} + \underbrace{(t_{\mathbf{k}', \mathbf{k}}^e)^*}_{\bar{t}_{\mathbf{k}, \mathbf{k}'}} \hat{t}_{\mathbf{k}, \sigma}^\dagger \hat{s}_{\mathbf{k}', \sigma'}]. \end{aligned} \quad (3.1)$$

Here, $\hat{s}_{\mathbf{k}, \sigma}^\dagger$ and $\hat{t}_{\mathbf{k}, \sigma}^\dagger$ are the creation operator¹ of an electron in the sample s and tip t , respectively, and the momentum sums cover the whole Brillouin zone. The electrons in the sample s interact with the collective bosonic degree of freedom $\Phi_{\mathbf{q}}^n$, where n numerates the

¹We restrict ourselves to the case of one band in both electrodes here to simplify the derivation, however the implementation of multiple bands is straightforward and can be done later in the effective action. If one wishes, we can see σ not only as spin index, but as a multitude of other possible quantum numbers as band indices. Also, we omit the normalization of the momentum sums with the volume $V_{s/t}$ of the tip and superconductor in the following, which is implicitly incorporated.

different branches of the boson and $\alpha_{\mathbf{k},\sigma,\mathbf{k}',\sigma'}^n$ stands for the corresponding electron-boson coupling. The unperturbed dynamics of the boson is described by the part $\hat{\mathcal{H}}_{\Phi}^0$. The *elastic* tunneling amplitude is defined as $t_{\mathbf{k},\mathbf{k}'}^e$. We note that we do not consider the Coulomb interaction between the electrons as they will not give rise to inelastic tunneling events. We will however include the electronic repulsion later in the effective action via the Coulomb pseudopotential. Deriving the low-energy action is most transparent in the path integral formalism, thus we write down the action of the Hamiltonian (3.1)

$$S = - \int_{k,k'} \hat{\Psi}_k^\dagger \left[\hat{G}_{k,0}^{-1} \delta_{k,k'} + \hat{\Lambda}_{k,k'} \right] \hat{\Psi}_{k'} + S_{\Phi}, \quad (3.2)$$

where we defined the spinor $\hat{\Psi}_k^T = (s_k, t_k)$ and combined energy, momentum and spin in the index k . In this basis, the bare electronic propagator and the vertex can be written down as

$$\begin{aligned} \hat{G}_{k,0}^{-1} &= \begin{pmatrix} G_{k,s,0}^{-1} & 0 \\ 0 & G_{k,t,0}^{-1} \end{pmatrix} & \text{with } G_{k,s/t,0}^{-1} &= i\omega_n - \epsilon_k^{s/t}, \\ \hat{\Lambda}_{k,k'} &= \begin{pmatrix} \sum_n \alpha_{k,k'}^n \Phi_{k,k'}^n & t_{k,k'}^e \\ t_{k,k'}^e & 0 \end{pmatrix} & \text{with } t_{k,k'}^e &= t_{\mathbf{k},\mathbf{k}'}^e \delta_{k_0,k'_0}. \end{aligned} \quad (3.3)$$

We now divide the fermionic fields into low-energy modes and high-energy modes with respect to the momentum cutoff k_{EM} of the low-energy Eliashberg theory,

$$\hat{\Psi}_k = \begin{cases} \hat{\Psi}_k^< & \text{for } |\mathbf{k} - \mathbf{k}_F| < k_{\text{EM}}, \\ \hat{\Psi}_k^> & \text{for } |\mathbf{k} - \mathbf{k}_F| > k_{\text{EM}}. \end{cases} \quad (3.4)$$

Note, that here we assume the momentum cutoff for the tip and sample to be the same. We could easily assume different momentum cutoffs, but as we will see later the high-energy states of the tip will have no influence on the low-energy theory. The action (3.2) can be rewritten as

$$S = - \int_{k,k'} \begin{pmatrix} \hat{\Psi}_k^< \\ \hat{\Psi}_k^> \end{pmatrix}^\dagger \begin{pmatrix} [\hat{G}_{k,k'}^{\ll}]^{-1} & \hat{\Lambda}_{k,k'} \\ \hat{\Lambda}_{k,k'} & [\hat{G}_{k,k'}^{\gg}]^{-1} \end{pmatrix} \begin{pmatrix} \hat{\Psi}_{k'}^< \\ \hat{\Psi}_{k'}^> \end{pmatrix} + S_{\Phi}, \quad (3.5)$$

where the bare dynamics of the low-energy and high-energy sectors are governed by the propagators

$$[\hat{G}_{k,k'}^{\ll/\gg}]^{-1} = [\hat{G}_{k,0}^{</>}]^{-1} \delta_{k,k'} + \hat{\Lambda}_{k,k'} \quad (3.6)$$

with the free low- and high-energy propagators

$$\begin{aligned} [\hat{G}_{k,0}^<]^{-1} &= \hat{G}_{k,0}^{-1} \cdot \Theta(k_{\text{EM}} - |\mathbf{k} - \mathbf{k}_F|), \\ [\hat{G}_{k,0}^>]^{-1} &= \hat{G}_{k,0}^{-1} \cdot \Theta(|\mathbf{k} - \mathbf{k}_F| - k_{\text{EM}}). \end{aligned} \quad (3.7)$$

The formal solution of the propagators of Eq. (3.6) is for the high-energy field

$$\hat{G}_{k,k'}^{\gg} = \hat{G}_{k,0}^> \delta_{k,k'} - \int_p \hat{G}_{k,0}^> \hat{\Lambda}_{k,p} \hat{G}_{p,k'}^{\gg} \quad (3.8)$$

and similarly for the low-energy sector. The non-diagonal elements $\hat{\Lambda}_{k,k'}$ couple the high- and low-energy sector and will give rise to additional inelastic vertices for the tunneling.

We are now in the position to integrate out the high-energy fields $\hat{\psi}^>$ and using the identity [102] for Grassmann fields ψ, η

$$\int D(\bar{\psi}, \psi) e^{-\begin{pmatrix} \bar{\psi} \\ \bar{\eta} \end{pmatrix}^T \begin{pmatrix} \hat{a} & \hat{b} \\ \hat{b} & \hat{d} \end{pmatrix} \begin{pmatrix} \psi \\ \eta \end{pmatrix}} = \det(\hat{a}) e^{-\bar{\eta}(\hat{d} - \hat{b}\hat{a}^{-1}\hat{b})\eta}. \quad (3.9)$$

we end up with the effective low-energy action

$$e^{-S_{\text{eff}}} = \int D(\hat{\Psi}^>, [\hat{\Psi}^>]^\dagger) e^{-S} \\ S_{\text{eff}} = \underbrace{S_\Phi - \text{tr} \ln [\hat{G}^{\gg}]}_{S_\Phi^{\text{eff}}} - \int_{k,k'} [\hat{\Psi}_k^<]^\dagger \left([\hat{G}_{k,k'}^{\ll}]^{-1} - \int_{p,p'} \hat{\Lambda}_{k,p} \hat{G}_{p,p'}^{\gg} \hat{\Lambda}_{p',k'} \right) \hat{\Psi}_{k'}^<. \quad (3.10)$$

Let us now interpret the resulting action. The first two terms summarized in S_Φ^{eff} describe the renormalization of the boson mode and of the electron-boson coupling due to the coupling to the high-energetic particle-hole excitations of the system, see Figure 3.1(e). Thus, the bosonic spectra that have to be considered in the following represent the effective low-energy collective modes. Importantly, the polarization operator does not depend on the elastic tunneling elements t^e , which only occur in higher-order terms. Therefore, the screening to leading order is not affected by the presence of the tunneling term in the Hamiltonian. The second part involving the $\hat{G}_{k,k'}^{\ll}$ propagator describes the low-energy theory of the uncoupled t and s fermions as well as the coupling of the s electrons to the boson as becomes apparent when inserting expressions (3.3) and (3.6). The last term of (3.10) gives rise to additional interaction vertices in the effective low-energy theory. This becomes apparent when we write down all terms via

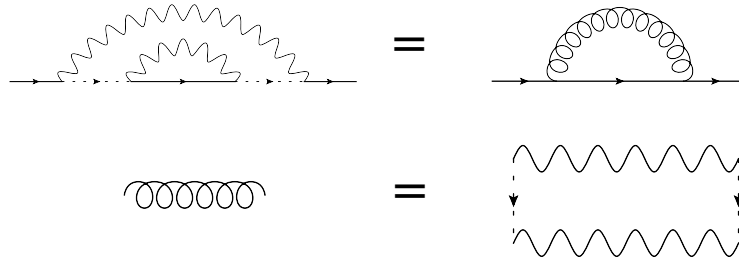
$$\int_{p,p'} \hat{\Lambda}_{k,p} \hat{G}_{p,p'}^{\gg} \hat{\Lambda}_{p',k'} = \begin{pmatrix} \sum_n \alpha_{k,p}^n \Phi_{k,p}^n & t_{k,p}^e \\ \bar{t}_{k,p}^e & 0 \end{pmatrix} \begin{pmatrix} [G_{p,p'}^{ss}]^{\gg} & [G_{p,p'}^{st}]^{\gg} \\ [G_{p,p'}^{ts}]^{\gg} & [G_{p,p'}^{tt}]^{\gg} \end{pmatrix} \begin{pmatrix} \sum_m \alpha_{p',k'}^m \Phi_{p',k'}^m & t_{p',k'}^e \\ \bar{t}_{p',k'}^e & 0 \end{pmatrix} \\ = \begin{pmatrix} \sum_{n,m} \alpha_{k,p}^n \Phi_{k,p}^n [G_{p,p'}^{ss}]^{\gg} \alpha_{p',k'}^m \Phi_{p',k'}^m & \sum_n \alpha_{k,p}^n \Phi_{k,p}^n [G_{p,p'}^{ss}]^{\gg} t_{p',k'}^e \\ \bar{t}_{k,p}^e [G_{p,p'}^{ss}]^{\gg} \sum_m \alpha_{p',k'}^m \Phi_{p',k'}^m & 0 \end{pmatrix} + \mathcal{O}([t^e]^2). \quad (3.11)$$

Here, we used the fact that $G^{st}, G^{ts} \sim t^e$ which can be directly read off from Eq. (3.8). Terms of higher order than t^e in the tunneling action can be neglected as they will appear in the tunneling action only in higher order. The additional vertices are presented in Figure 3.1(a)-(c). The (1,1) component of (3.11) described the scattering of a low-energy electron to an off-shell state via the scattering off a boson followed by another boson-scattering back to a state near the Fermi surface. These vertices will give rise to new contributions to the self-energy such as



$$\text{Diagram (3.12)} \quad (3.12)$$

and



$$\text{Diagram (3.13)} \quad (3.13)$$

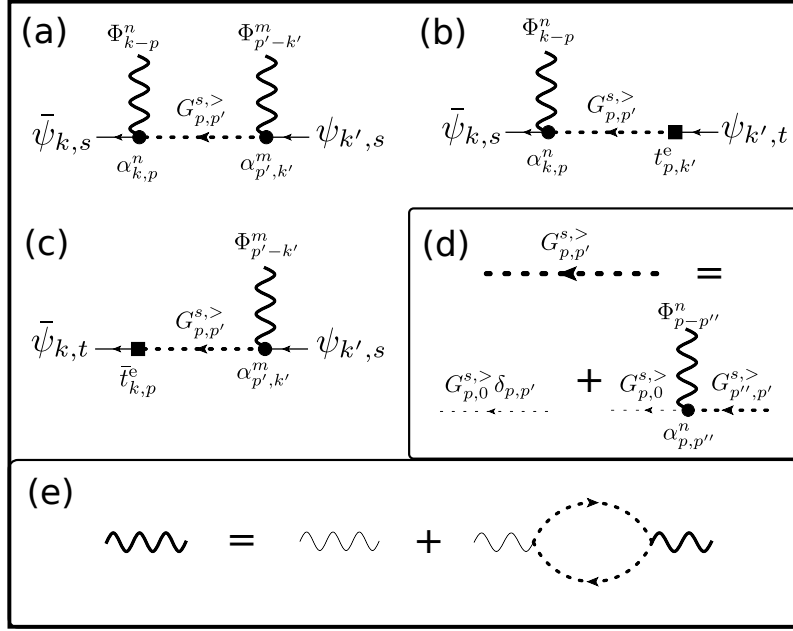


Figure 3.1.: Interaction vertices generated by integrating out the high-energy fermions for the effective low-energy theory: Solid lines represent the low-energy fermions and dashed lines the high-energy fermions that were integrated out. The Feynman diagram shown in (a) show the two-boson scattering vertex involving an off-shell state. The diagrams (b) and (c) describe the additional inelastic tunneling matrix element that emerge in the low-energy theory. The graph (d) represents the dressed high-energy electron propagators and (e) the renormalization of the bosons in the superconductor due to the high-energy fermionic quasiparticles. Taken from Ref. [25].

where the solid lines represent the low-energy electrons, the dashed lines the high-energy electrons, the wavy lines the bosonic propagator χ , and the curly lines a composite bosonic propagator $\tilde{\chi}$ consisting of two bosonic interactions with an intermediate high-energy off-shell electronic state $G \gg$ [117]. Since the off-shell state is far away from the Fermi surface, we can neglect the dynamics of the propagator and approximate $G \gg \sim 1/E_{\text{off}}$, where E_{off} is the characteristic energy scale of the electronic off-shell states. Therefore, the self-energy in (3.12) has no dynamics and can be absorbed into the chemical potential to give rise to the effective low-energy dispersion of the electronic quasiparticles. In contrast, the composite propagator in (3.13) gives rise to a dynamical self-energy. The corresponding imaginary part (and thus the effective spectral weight) of the retarded composite propagator at $T = 0$ is given by [117]

$$\begin{aligned} \text{Im } \tilde{\chi}_q^R(\omega) &= \frac{1}{E_{\text{off}}^2} \frac{1}{V} \sum_{q'} \int \frac{d\Omega}{2\pi} |\alpha_{q'}|^2 \text{Im } \chi_{q'}^R(\Omega) |\alpha_{q-q'}|^2 \text{Im } \chi_{q-q'}^R(\omega - \Omega) \\ &\sim \frac{1}{V E_{\text{off}}^2} \frac{\alpha^4}{\omega_0} \sim V \left(\frac{\nu_F \alpha^2}{\omega_0} \right)^2 \omega_0 \sim V \cdot \lambda^2 \cdot \omega_0. \end{aligned} \quad (3.14)$$

Here, we considered for simplicity only one bosonic mode, approximated the bosonic propagator to be inversely proportional to the characteristic bosonic energy scale ω_0 (in the case of phonons this would correspond to the Debye frequency) as well as $E_{\text{off}} \sim E_F \sim (V\nu_F)^{-1}$. We also introduced the dimensionless coupling constant $\lambda \sim \alpha^2 \nu_F / \omega_0$ similar to Section 2.2. In comparison to the bare bosonic interaction between the fermions that is

governed by

$$\alpha_q^2 \mathbf{Im} \chi_q(\omega) \sim \frac{\alpha^2}{\omega_0} = V \left(\frac{\alpha^2}{E_F V \omega_0} \right) E_F \sim V \cdot \lambda \cdot E_F. \quad (3.15)$$

We see that the composite propagator is suppressed by a small fraction $\omega_0/E_F \ll 1$. Thus, we can neglect the (1,1) part of the matrix in Eq. (3.11) as it will only give rise to interactions that are small compared to the bare electron-boson interaction of the low-energy theory. Furthermore, if the above estimate were not valid (e.g. for $\omega_0 \sim E_F$) one would formally combine the phonon and composite propagator to a new *effective* phonon propagator that describes the coupling of the low-energy electrons to the phonons.

Let us now have a closer look at the off-diagonal parts of the matrix in Eq. (3.11). These give rise to new inelastic tunneling channels that are sketched in Figure 3.1(b) and (c). Since we are only interested in tunnel vertices of order t^e it is sufficient to expand the off-shell propagator (3.8) to zeroth order in t^e :

$$\begin{aligned} [G_{k,k'}^{ss}]^{\gg} &= G_{k,s,0}^> \delta_{k,k'} - \int_p G_{k,s,0}^> \sum_n \alpha_{k,p}^n \Phi_{k,p}^n [G_{p,k'}^{ss}]^{\gg} + \mathcal{O}(t^e) \\ &= G_{k,s,0}^> \delta_{k,k'} - G_{k,s,0}^> \sum_n \alpha_{k,k'}^n \Phi_{k,k'}^n G_{k',s,0}^> \\ &\quad + \int_p G_{k,s,0}^> \sum_n \alpha_{k,p}^n \Phi_{k,p}^n G_{p,s,0}^> \sum_m \alpha_{p,k'}^m \Phi_{p,k'}^m G_{k',s,0}^> + \dots \end{aligned} \quad (3.16)$$

Inserting this into Eq. (3.11) we find a new kind of vertex that appears in the low-energy action of the form

$$\begin{aligned} \delta S_{\text{eff}} &= \int_{k,k'}^< \bar{s}_k^< \int_{p,p'}^> \alpha_{k,p}^n \Phi_{k,p}^n [G_{p,p'}^{ss}]^{\gg} t_{p',k'}^e t_k^< \quad (3.17) \\ &= \int_{k,k'}^< \bar{s}_k^< \left(\int_p^> \sum_n \alpha_{k,p}^n \Phi_{k,p}^n G_{p,s,0}^> t_{p,k'}^e \right) t_k^< \quad (i) \\ &\quad - \int_{k,k'}^< \bar{s}_k^< \left(\int_{p,p'}^> \sum_n \alpha_{k,p}^n \Phi_{k,p}^n G_{p,s,0}^> \sum_m \alpha_{p,p'}^m \Phi_{p,p'}^m G_{p',s,0}^> t_{p',k'}^e \right) t_k^< \quad (ii) \\ &\quad + \dots \end{aligned}$$

The physical processes behind these terms are the following: (i) We start with a state \mathbf{k}' in the tip and tunnel elastically to an off-shell state \mathbf{p} far away from the Fermi surface (with the probability $t_{p,k}^e$), which is then scattered inelastically via the excitation/absorption of a boson Φ to a state \mathbf{k} which again lies close to the Fermi surface², see Figure 3.2. (ii) The same process as (i), but after the tunneling process the off-shell electron is first scattered inelastically via a boson to another high-energy state and then again scattered to the low-energy state \mathbf{k} . There are also inelastic tunneling processes that involve three or more inelastic scatterings, but let us first focus on the leading-order term (i). Similar to the estimate above, we approximate the off-shell propagator as non-dynamical object $G_{p,s,0}^> = (i\omega - \epsilon_p^s)^{-1} \approx -1/E_{\text{off}}$, where E_{off} is the typical energy scale of the high-energy electrons. In this case, the vertex reads

$$\delta S_{\text{eff}}^{(i)} \approx \int_{k,k'}^< \bar{s}_k^< \left(\int_p^> \frac{\sum_n \alpha_{k,p}^n \Phi_{k,p}^n t_{p,k'}^e}{-E_{\text{off}}} \right) t_k^<, \quad (3.18)$$

²A similar inelastic tunneling process involving an intermediate high-energy state has been described in Ref. [118], where IETS was used to detect phonon-modes in graphene sheets on Si-oxide.

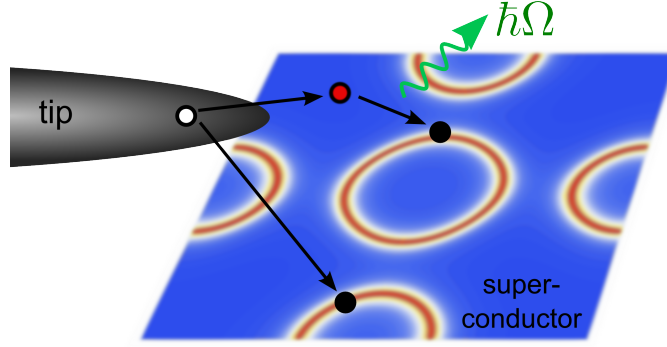


Figure 3.2.: Sketch of elastic and inelastic tunneling: The elastic tunneling process describes a tip electron that tunnels directly to a state near the Fermi surface of the superconductor. In contrast, inelastic tunneling involves the tunneling to an intermediate off-shell state followed by the emission/absorption of a boson that scatters the electron to a state near the Fermi surface. Taken from Ref. [25].

where the \mathbf{k}, \mathbf{k}' momenta are restricted to low-energy states and the \mathbf{p} momentum to high energies. In general, the momenta $\mathbf{q} = \mathbf{p} - \mathbf{k}$ that connect the low- and high-energy states cover most of the Brillouin zone, so we approximate the corresponding integrals as

$$\delta S_{\text{eff}}^{(i)} \approx \int_{\mathbf{k}, \mathbf{k}'}^< \bar{s}_{\mathbf{k}} \left(\int_{\mathbf{q}} \frac{\alpha_{\mathbf{q}}^n \Phi_{\mathbf{q}}^{n_e} t_{\mathbf{k}+\mathbf{q}, \mathbf{k}'}}{-E_{\text{off}}} \right) t_{\mathbf{k}'}^<. \quad (3.19)$$

We are now in the position to rewrite the resulting low-energy action to an effective transfer Hamiltonian

$$\hat{\mathcal{H}}_{\text{eff}} = \hat{\mathcal{H}}_0^{\text{EM}} + \hat{\mathcal{H}}_{\text{tun}} \quad (3.20)$$

where H_0^{EM} described the dynamics of uncoupled low-energy systems of the tip and the superconductor (via the Eliashberg-Migdal theory) and the tunneling part of the Hamiltonian³

$$\hat{\mathcal{H}}_{\text{tun}} = \sum_{\substack{\mathbf{k}, \mathbf{k}' \\ \sigma}} [t_{\mathbf{k}, \mathbf{k}'}^e \hat{s}_{\mathbf{k}, \sigma}^\dagger \hat{t}_{\mathbf{k}', \sigma} + \sum_{\mathbf{q}, n, \sigma'} t_{(\mathbf{k}, \sigma), (\mathbf{k}', \sigma'), \mathbf{q}, n}^i \hat{s}_{\mathbf{k}, \sigma}^\dagger \hat{t}_{\mathbf{k}', \sigma'} \hat{\Phi}_{\mathbf{q}}^n] + \text{h.c.} \quad (3.23)$$

now consists of an elastic and an inelastic part. The inelastic tunneling amplitude reads

$$t_{(\mathbf{k}, \sigma), (\mathbf{k}', \sigma'), \mathbf{q}, n}^i = \frac{t_{\mathbf{k}+\mathbf{q}, \mathbf{k}'}^e \alpha_{\mathbf{q}, \sigma, \sigma'}^n}{-E_{\text{off}}}. \quad (3.24)$$

Such an inelastic tunneling term has been phenomenologically proposed in the literature [119] to explain phonon signatures seen in tunneling spectra through barriers, see also Section 1.2. Our theory would also work for such a case, see discussion below, however

³Higher-order inelastic contributions involving the interaction with j bosons have the structure:

$$\hat{\mathcal{H}}_{\text{tun}}^{i, (j)} = \sum_{\substack{\mathbf{k}, \mathbf{k}' \\ \sigma}} \sum_{\substack{\mathbf{q}_1, \dots, \mathbf{q}_j \\ n_1, \dots, n_j}} t_{(\mathbf{k}, \sigma), (\mathbf{k}', \sigma'), \mathbf{q}_1, n_1, \dots, \mathbf{q}_j, n_j}^i \hat{s}_{\mathbf{k}, \sigma}^\dagger \hat{t}_{\mathbf{k}', \sigma'} \hat{\Phi}_{\mathbf{q}_1}^{n_1} \dots \hat{\Phi}_{\mathbf{q}_j}^{n_j} + \text{h.c.} \quad (3.21)$$

with inelastic tunneling matrix element

$$t_{(\mathbf{k}, \sigma), (\mathbf{k}', \sigma'), \mathbf{q}_1, n_1, \dots, \mathbf{q}_j, n_j}^i = \frac{t_{\mathbf{k}+\mathbf{q}_1+\dots+\mathbf{q}_j, \mathbf{k}'}^e \alpha_{\mathbf{q}_1, \sigma_{j-1}, \sigma'}^{n_1} \dots \alpha_{\mathbf{q}_j, \sigma, \sigma_1}^{n_j}}{(-E_{\text{off}})^j}. \quad (3.22)$$

our results imply an even more interesting aspect: STM into metals in general consists of elastic contributions that describe the electronic DOS, but also of inelastic contributions which can give direct informations about the bosonic spectrum in the metal!

In the next section, we will calculate the corresponding tunneling currents that can be derived from the effective tunneling Hamiltonian (3.20), but before let us briefly summarize the main conclusion of this section:

1. When using an effective low-energy theory for describing the properties of a solid state system (e.g. the BCS or Eliashberg-Migdal theory for describing superconductivity), there will be both elastic and inelastic contributions to the electron tunneling process. The elastic tunneling process describes the transition of an electron from the tip to a state near the Fermi surface, whereas for the inelastic process the electron first tunnels to an off-shell high-energy state followed by the inelastic scattering to a state near the Fermi surface via the excitation or absorption of a boson, see Figure 3.2.
2. The tunneling amplitude of the inelastic process is linked to the one of the elastic process. For the elastic tunneling amplitude t^e , the inelastic process has the amplitude $t^e \alpha / E_{\text{off}}$, where α is the electron-boson coupling and E_{off} is the typical energy scale of the off-shell electrons.
3. The presence of tunneling does not affect the dynamics of neither the electronic nor the bosonic particles for the current in leading order to the tunneling amplitude t^e .

Let us conclude this section by remarking that the presented inelastic transfer Hamiltonian is not only valid for STM junctions. Our derivation was based on the assumption that the elastic electron tunneling occurs directly from the tip t to the sample s . However, we could also consider the case that there is an intermediate oxide junction or surface impurity atoms [120], which naturally contain high-energy electronic states and low-energy bosonic excitations like phonons. When integrating out the high-energy degrees of freedom there can now also be transitions where the oxide off-shell states serve as the intermediate virtual states for the inelastic tunneling process as is depicted in Figure 3.3. This opens an additional inelastic channel, which can easily be captured in our theory by adding another barrier boson spectrum in the inelastic tunneling expression that is derived in the next section.

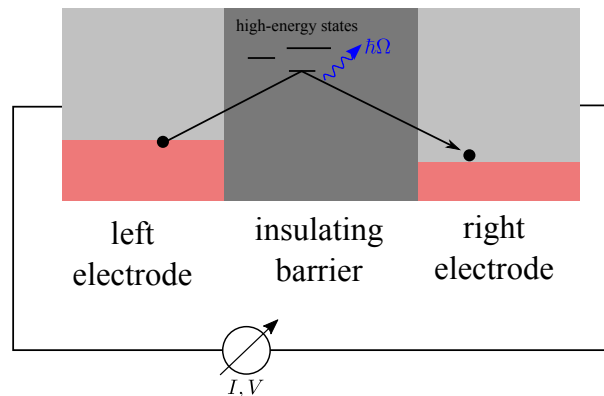


Figure 3.3.: Sketch of inelastic tunneling in the barrier: The inelastic transition is mediated by an intermediate high-energy state of the insulator, from where it can inelastically scatter to the right electrode.

3.2. Elastic and inelastic tunneling currents

In this section we will summarize the important steps in the derivation of the elastic and inelastic currents from the effective low-energy tunneling Hamiltonian (3.21) of the previous section and discuss the physical elastic and inelastic tunneling processes that can occur for an STM setup. We will perform a perturbation theory in the tunneling amplitude t^e , based on Ref. [24], using the Keldysh technique, which is briefly summarized in Appendix C. For a STM setup, the tunneling current⁴ is given by the elementary charge times the change of the number of electrons $\hat{n}_s = \sum_{\mathbf{k},\sigma} \hat{s}_{\mathbf{k},\sigma}^\dagger \hat{s}_{\mathbf{k},\sigma}$ in the superconductor

$$I(t) = e \frac{d}{dt} \langle \hat{n}_s(t) \rangle = e \frac{d}{dt} \frac{\text{tr}(\hat{\rho}(t)\hat{n}_s)}{\text{tr}(\hat{\rho}(t))} = e \frac{d}{dt} \frac{\text{tr}(\hat{\rho}(t)\hat{n}_s)}{\text{tr}(\hat{\rho}_0)} = e \frac{d}{dt} \text{tr}(\hat{\rho}(t)\hat{n}_s), \quad (3.25)$$

where $\hat{\rho}(t) = \hat{U}(t, -\infty)\hat{\rho}_0\hat{U}^\dagger(t, -\infty)$ is the time-dependent density matrix in the Heisenberg picture with the time-evolution operator \hat{U} and the (normalized) density matrix $\hat{\rho}_0 = e^{-\beta\hat{H}}/\text{tr}(e^{-\beta\hat{H}})$ of the system in thermal equilibrium. Here, we assume that the tunneling current is sufficiently small such that the steady state of the connected system does not affect the thermal equilibrium of the tip and sample subsystems and therefore the tunneling current is not time-dependent $I(t) = I(0)$. Using the Heisenberg equation of motion it is possible to express the current $I = \langle \hat{I}(0) \rangle$ as the expectation value of the current operator

$$\hat{I}(t) = \frac{e}{i} \sum_{\substack{\mathbf{k}, \mathbf{k}' \\ \sigma, \sigma'}} \left[T_{(\mathbf{k},\sigma),(\mathbf{k}',\sigma')}(t) \hat{s}_{\mathbf{k},\sigma}^\dagger(t) \hat{t}_{\mathbf{k}',\sigma'}(t) - [T_{(\mathbf{k},\sigma),(\mathbf{k}',\sigma')}(t)]^* \hat{t}_{\mathbf{k}',\sigma'}^\dagger(t) \hat{s}_{\mathbf{k},\sigma}(t) \right], \quad (3.26)$$

with $T_{(\mathbf{k},\sigma),(\mathbf{k}',\sigma')}(t) = t_{\mathbf{k},\mathbf{k}'}^e \delta_{\sigma,\sigma'} + \sum_{\mathbf{q},n} t_{(\mathbf{k},\sigma),(\mathbf{k}',\sigma'),\mathbf{q},n}^i \hat{\Phi}_{\mathbf{q}}^n(t)$. In Appendix B, the detailed calculation of this expectation value using the Keldysh formalism is shown. When applying a voltage V between the tip and the sample, we can separate the elastic and inelastic contribution to the tunneling current as

$$I^e(V) = 2\pi e \int_{-\infty}^{\infty} d\epsilon \sum_{\mathbf{k}, \mathbf{k}', \sigma} |t_{\mathbf{k},\mathbf{k}'}^e|^2 A_{s,\mathbf{k},\sigma}(\epsilon) A_{t,\mathbf{k}',\sigma}(\epsilon - eV) [n_F(\epsilon - eV) - n_F(\epsilon)] \quad (3.27)$$

$$I^i(V) = 2\pi e \int_{-\infty}^{\infty} d\epsilon d\omega \sum_{\substack{\mathbf{k}, \mathbf{k}', \mathbf{q} \\ \sigma, \sigma', n}} |t_{(\mathbf{k},\sigma),(\mathbf{k}',\sigma'),\mathbf{q},n}^i|^2 \times \quad (3.28)$$

$$\begin{aligned} & \left(A_{\mathbf{q},n}(\omega) A_{s,\mathbf{k},\sigma}(\epsilon) A_{t,\mathbf{k}',\sigma'}(\epsilon - \omega - eV) n_F(\epsilon - \omega - eV) n_B(\omega) [1 - n_F(\epsilon)] \right. \\ & - A_{\mathbf{q},n}(\omega) A_{s,\mathbf{k},\sigma}(\epsilon) A_{t,\mathbf{k}',\sigma'}(\epsilon - \omega - eV) n_F(\epsilon) [1 + n_B(\omega)] [1 - n_F(\epsilon - \omega - eV)] \\ & + A_{\mathbf{q},n}(\omega) A_{s,\mathbf{k},\sigma}(\epsilon) A_{t,\mathbf{k}',\sigma'}(\epsilon + \omega - eV) n_F(\epsilon + \omega - eV) [1 + n_B(\omega)] [1 - n_F(\epsilon)] \\ & \left. - A_{\mathbf{q},n}(\omega) A_{s,\mathbf{k},\sigma}(\epsilon) A_{t,\mathbf{k}',\sigma'}(\epsilon + \omega - eV) n_F(\epsilon) n_B(\omega) [1 - n_F(\epsilon + \omega - eV)] \right). \end{aligned}$$

Here, the spectral weight functions are defined in the usual way via

$$\begin{aligned} A_{s/t,\mathbf{k},\sigma}(\omega) &= -\frac{1}{\pi} \text{Im} G_{s/t,\mathbf{k},\sigma}^R(\omega), \\ A_{\mathbf{q},n}(\omega) &= -\frac{1}{\pi} \text{Im} D_{\mathbf{q},n}^R(\omega) \cdot \Theta(\omega), \end{aligned} \quad (3.29)$$

⁴as measured from the tip to the superconductor

with the electronic and bosonic retarded Green's functions

$$\begin{aligned} G_{s,\mathbf{k},\sigma}^R(\tau) &= -i\langle [\hat{s}_{\mathbf{k},\sigma}(\tau), \hat{s}_{\mathbf{k},\sigma}^\dagger(0)] \rangle \Theta(\tau) \\ D_{\mathbf{q},n}^R(\tau) &= -i\langle [\hat{\Phi}_{\mathbf{q},n}(\tau), \hat{\Phi}_{-\mathbf{q},n}(0)] \rangle \Theta(\tau). \end{aligned} \quad (3.30)$$

Note that the bosonic spectral function is confined to positive energies as the information of the negative energies is redundant for the boson spectrum. Such negative energies correspond to the absorption of a boson that is automatically captured by the Bose functions in the expression (3.28) of the inelastic tunneling current. Before we discuss the different physical processes described by (3.27,3.28), we apply the usual approximation that the elastic tunneling amplitude is basically constant $t_{\mathbf{k},\mathbf{k}'}^e \approx t^e$. In general the tunneling amplitude depends on both the energy and the wavevector of the tunneling quasiparticle [121, 122]. However, as the applied biases (of the order of the Debye frequency for conventional superconductors) are usually small compared to the band width and work function of the system, the approximation that there is no energy dependence for the tunneling matrix element holds well. Furthermore, for the case of an STM there is no quasimomentum conservation (see also Section 4.1.1) and since the wave-vectors are mostly of the order of the Fermi momentum, also the dependency on the in- and outgoing momenta may be insignificant. We can also reformulate this approximation: We assume that the energy and momentum dependencies of the corresponding spectral functions $A(\omega)$ defined in (3.29) are much stronger than the variations of the tunneling matrix elements in the energy range of interest. Within this picture, the inelastic tunneling element becomes $t_{(\mathbf{k},\sigma),(\mathbf{k}',\sigma'),\mathbf{q},n}^i = -t^e \alpha_{\mathbf{q},\sigma,\sigma'}^n / E_{\text{off}}$ and we define the spin-resolved density of states of the sample/tip and weighted bosonic spectrum

$$\begin{aligned} \nu_{s/t,\sigma}(\omega) &= \sum_{\mathbf{k}} A_{s/t,\mathbf{k},\sigma}(\omega), \\ B_{\sigma,\sigma'}(\omega) &= \sum_{\mathbf{q},n} |\alpha_{\mathbf{q},\sigma,\sigma'}^n|^2 A_{\mathbf{q},n}(\omega). \end{aligned} \quad (3.31)$$

The corresponding elastic and inelastic currents can then be conveniently expressed as

$$\begin{aligned} I^e(V) &= 2\pi e |t^e|^2 \int_{-\infty}^{\infty} d\epsilon \sum_{\sigma} \nu_{s,\sigma}(\epsilon) \nu_{t,\sigma}(\epsilon - eV) \left(n_F(\epsilon - eV)[1 - n_F(\epsilon)] - [1 - n_F(\epsilon - eV)]n_F(\epsilon) \right) \\ I^i(V) &= 2\pi e |t^e|^2 \int_{-\infty}^{\infty} d\epsilon d\omega \sum_{\sigma,\sigma'} \times \\ &\quad \left(B_{\sigma,\sigma'}(\omega) \nu_{s,\sigma}(\epsilon) \nu_{t,\sigma'}(\epsilon - \omega - eV) n_F(\epsilon - \omega - eV) n_B(\omega) [1 - n_F(\epsilon)] \right. \\ &\quad - B_{\sigma,\sigma'}(\omega) \nu_{s,\sigma}(\epsilon) \nu_{t,\sigma'}(\epsilon - \omega - eV) n_F(\epsilon) [1 + n_B(\omega)] [1 - n_F(\epsilon - \omega - eV)] \\ &\quad + B_{\sigma,\sigma'}(\omega) \nu_{s,\sigma}(\epsilon) \nu_{t,\sigma'}(\epsilon + \omega - eV) n_F(\epsilon + \omega - eV) [1 + n_B(\omega)] [1 - n_F(\epsilon)] \\ &\quad \left. - B_{\sigma,\sigma'}(\omega) \nu_{s,\sigma}(\epsilon) \nu_{t,\sigma'}(\epsilon + \omega - eV) n_F(\epsilon) n_B(\omega) [1 - n_F(\epsilon + \omega - eV)] \right). \end{aligned} \quad (3.32)$$

This is the most general formula for the expression of the elastic and inelastic tunneling current and is also valid for systems with broken time-reversal symmetry where the spin-degeneracy is broken. However, in what follows, we will only consider the case where the fermionic spectra $\nu_{s/t,\sigma}(\omega) = \nu_{s/t}(\omega)$ have no spin dependency and define the normalized

electronic DOS $\tilde{\nu}_{s/t}$ and the dimensionless bosonic tunnel spectrum⁵ $\alpha^2 F_{\text{tun}}$

$$\begin{aligned}\tilde{\nu}_{s/t}(\omega) &= \frac{\nu_{s/t}(\omega)}{\nu_F^{s/t}}, \\ \alpha^2 F_{\text{tun}}(\omega) &= \frac{\nu_F^s}{2} \sum_{\substack{\mathbf{q}, n \\ \sigma, \sigma'}} |\alpha_{\mathbf{q}, \sigma, \sigma'}^n|^2 A_{\mathbf{q}, n}(\omega),\end{aligned}\tag{3.33}$$

where $\nu_F^{s/t}$ is the normal state sample/tip DOS at the Fermi surface. The corresponding currents are given by

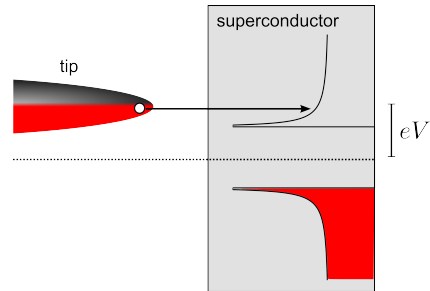
$$\begin{aligned}I^e(V) &= \frac{\sigma_0}{e} \int_{-\infty}^{\infty} d\epsilon \tilde{\nu}_s(\epsilon) \tilde{\nu}_t(\epsilon - eV) \left(n_F(\epsilon - eV) [1 - n_F(\epsilon)] - [1 - n_F(\epsilon - eV)] n_F(\epsilon) \right) \\ I^i(V) &= \frac{\sigma_0}{e} \frac{1}{E_{\text{off}}^2 \nu_F^s} \int_{-\infty}^{\infty} d\epsilon d\omega \times\end{aligned}\tag{3.34}$$

$$\begin{aligned}& \left(\alpha^2 F_{\text{tun}}(\omega) \tilde{\nu}_s(\epsilon) \tilde{\nu}_t(\epsilon - \omega - eV) n_F(\epsilon - \omega - eV) n_B(\omega) [1 - n_F(\epsilon)] \right. & \text{(i)} \\ & - \alpha^2 F_{\text{tun}}(\omega) \tilde{\nu}_s(\epsilon) \tilde{\nu}_t(\epsilon - \omega - eV) n_F(\epsilon) [1 + n_B(\omega)] [1 - n_F(\epsilon - \omega - eV)] & \text{(ii)} \\ & + \alpha^2 F_{\text{tun}}(\omega) \tilde{\nu}_s(\epsilon) \tilde{\nu}_t(\epsilon + \omega - eV) n_F(\epsilon + \omega - eV) [1 + n_B(\omega)] [1 - n_F(\epsilon)] & \text{(iii)} \\ & \left. - \alpha^2 F_{\text{tun}}(\omega) \tilde{\nu}_s(\epsilon) \tilde{\nu}_t(\epsilon + \omega - eV) n_F(\epsilon) n_B(\omega) [1 - n_F(\epsilon + \omega - eV)] \right). & \text{(iv)}\end{aligned}$$

Here, we defined the conductance constant $\sigma_0 = 4\pi e^2 \nu_t^0 \nu_s^0 |t^e|^2$, which is the purely elastic conductance for a flat sample and tip DOS. Expressions very similar to (3.34) have been derived for (barrier-)phonon IETS [119, 123, 124] and for normal-state cuprate tunneling [125] of planar junction. The result also agrees well with studies on inelastic tunneling in Josephson-contacts consisting of an SIS junctions [126], but we will only focus on SIN junctions in the following. Since the expressions in Eq. (3.34) for the elastic and inelastic current are one of the main results of this thesis, let us take a deep breath and investigate the contributions for the elastic and inelastic currents in more detail.

3.2.1. Elastic tunneling

The term for the elastic tunneling in Eq. (3.34) is of the usual form (1.1) that could be derived using Fermi's Golden Rule. It simply counts the number of occupied states in the tip electrode whose energies lie above the chemical potential μ^S of the sample and multiplies this with the quantized conductance e^2/\hbar , see also Figure 1.2. When we assume the tip DOS $\tilde{\nu}_t(\omega) = 1$ to be constant in the energy range of interest, we can



⁵In Section 4.1.2 we discuss the relation between the Eliashberg function $\alpha^2 F(\omega)$ and the tunneling spectrum $\alpha^2 F_{\text{tun}}(\omega)$ and show for a specific example that they coincide qualitatively.

easily calculate the corresponding differential conductance

$$\sigma^e(V) = \frac{dI^e(V)}{dV} = -\sigma_0 \int_{-\infty}^{\infty} d\epsilon \tilde{\nu}_s(\epsilon) n'_F(\epsilon - eV) \stackrel{T=0}{=} \sigma_0 \cdot \tilde{\nu}_s(eV), \quad (3.35)$$

The elastic conductance is therefore proportional to the thermally smeared DOS⁶ of the sample, see also the introductory Chapter 1. In the case of conventional elastic SIN tunneling the BSC DOS is measured by the conductance, see picture above.

3.2.2. Inelastic tunneling

The inelastic contribution to the tunneling current in (3.34) have been written down in such a way that the different physical processes are separated. In Figure 3.4 the four different inelastic transitions are depicted⁷:

- (i) An electron tunnels from the tip to the sample via the absorption of a boson in the sample.
- (ii) An electron tunnels from the sample to the tip via the (spontaneous and stimulated) emission of a boson in the sample.
- (iii) An electron tunnels from the tip to the sample via the (spontaneous and stimulated) emission of a boson in the sample .
- (iv) An electron tunnels from the sample to the tip via the absorption of a boson in the sample.

We emphasize that one could of course also imagine the same inelastic process with the absorption/emission of a boson in the tip. In order to prevent this from happening, in IETS one usually uses a very simple metal such as tin or gold that has no significant coupling to any collective bosonic mode as phonons, magnons, spin excitations, etc.. In the zero temperature limit only the spontaneous emission of a boson via the process (2) or (3) is allowed because there are no excited bosons.

3.3. IETS in the normal state

Before proceeding with the general consequences of inelastic processes for tunneling experiments into superconducting samples, let us first consider STM tunneling in the normal-state of an investigated metal with the assumption that the normal-state DOS $\tilde{\nu}_{s/t}(\omega) = 1$ of the sample and the tip are flat. In the $T = 0$ case the inelastic tunneling current in Eq. (3.34) can then be simplified to

$$I^i(V) = \frac{\sigma_0}{e} \frac{1}{E_{\text{off}}^2 \nu_F^s} \int_{-\infty}^{\infty} d\epsilon d\omega \alpha^2 F_{\text{tun}}(\omega) \left(n_F(\epsilon + \omega - eV) [1 - n_F(\epsilon)] - n_F(\epsilon) [1 - n_F(\epsilon - \omega - eV)] \right) \quad (3.36)$$

and the corresponding second derivative is

⁶The FWHM of the thermal smearing function $n'_F(x)$ is given by $3.5T$.

⁷We remind the reader that the bosonic spectrum $\alpha^2 F_{\text{tun}}(\omega) \sim \Theta(\omega)$ is defined only on the positive branch.

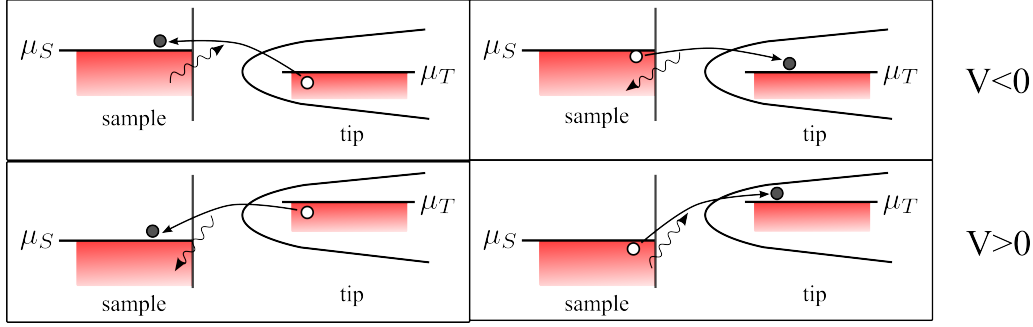


Figure 3.4.: Basic inelastic tunneling processes involving the excitation and the absorption of a collective bosonic excitation, e.g. a phonon in the investigated substrate. Taken from Ref. [24].

$$\frac{d^2 I^i(V)}{dV^2} = \frac{e}{E_{\text{off}}^2 \nu_F^s} \sigma_0 \text{sign}(V) \alpha^2 F_{\text{tun}}(e|V|). \quad (3.37)$$

Since the second derivative of the elastic tunneling current $d^2 I^e(V)/dV^2 \sim \nu_s'(eV) = 0$ vanishes above T_c as is apparent from Eq. (3.35), the total $d^2 I(V)/dV^2 = d^2 I^i(V)/dV^2$ spectrum that is seen in the normal state consists only of the inelastic contribution. It is directly proportional to the bosonic tunnel spectrum $\alpha^2 F_{\text{tun}}$, thus normal-state STM tunneling can be used to directly access the DOS of the dominant bosonic degrees of freedom of a system. We emphasize, that for the case of phonons the tunnel spectrum $\alpha^2 F_{\text{tun}} \neq \alpha^2 F$ does not coincide with the Eliashberg function, as defined in (2.28), due to a different kind of momentum average. However, in general, it should capture the main features of the Eliashberg functions and we will discuss this issue later for the case of a realistic phonon spectrum in Section 4.1.2, which has also been confirmed by the experimental STM spectra seen on Pb [19, 20, 24]. Furthermore, the bosonic spectra of molecules and barrier phonons seen in planar junctions of metals [17, 18, 49, 50] can be understood from Eq. (3.37) because, as explained earlier, our inelastic theory is also applicable to tunnel junctions with an insulating barrier, where the intermediate off-shell state sits in the barrier.

Let us proceed our investigation of the normal-state properties of IETS by having a closer look at the temperature dependence of the inelastic tunneling current. When allowing for finite temperatures $T \sim \omega_0$ of the order of the characteristic bosonic energy, not only the spontaneous emission of bosons, but also the absorption and stimulated emission is an allowed process during the tunneling transition. Also for finite temperatures, the elastic conductance $\sigma^e(V) = \sigma_0$ is constant in the normal state (for flat electronic DOSs), thus any variations of the differential conductance originates from inelastic tunneling processes. Using the inherent symmetry properties $n_F(\epsilon) + n_F(-\epsilon) = 1$ of the Fermi function, we can derive the following expression for inelastic tunneling conductance

$$\sigma^i(V) = \frac{\sigma_0}{E_{\text{off}}^2 \nu_F^s} \int_0^\infty d\omega \alpha^2 F_{\text{tun}}(\omega) K^i(\omega, V) \quad (3.38)$$

with the integral kernel

$$\begin{aligned} K^i(\omega, V) &= \int_{-\infty}^\infty d\epsilon [n_F'(\epsilon - \omega - eV) + n_F'(\epsilon - \omega + eV)] \cdot [n_B(\omega) + n_F(\epsilon)] \\ &= n_B(\omega) - n_B(\omega + eV) + \frac{\omega + eV}{4T \sinh^2(\frac{\omega + eV}{2T})} + \{V \rightarrow -V\} \end{aligned} \quad (3.39)$$

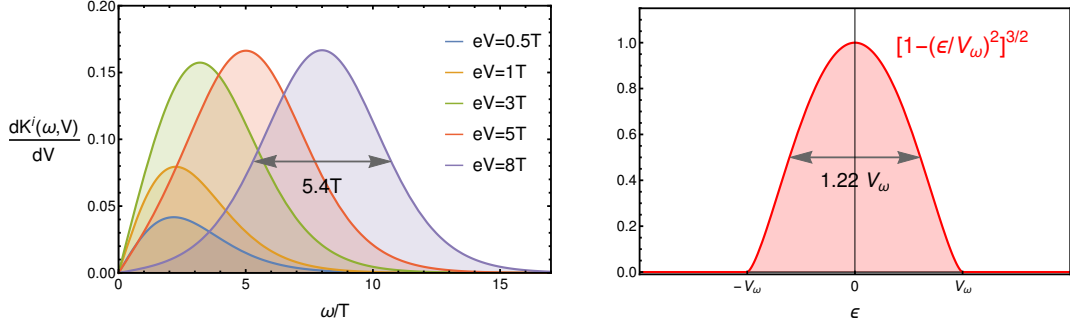


Figure 3.5.: Convolution kernels for inelastic tunneling spectrum $d^2I^i(V)/dV^2$ due to temperature (left) and the lock-in technique (right).

As we have seen in Eq. (3.37), the most convenient quantity to look at for IETS is the second derivative of the tunneling current, which is then given by

$$\frac{d^2I^i(V)}{dV^2} = \frac{e\sigma_0}{E_{\text{off}}^2\nu_F^s} \int_0^\infty d\omega \alpha^2 F_{\text{tun}}(\omega) \frac{dK^i(\omega, V)}{dV} \quad (3.40)$$

In comparison with Eq. (3.37) we see that for finite temperatures the bosonic tunneling spectrum has to be convoluted with the kernel $dK(\omega, V)/dV$, which is shown in Figure 3.5. This kernel is the generalization of the kernel defined in Ref. [123] for the case where the temperature T is not small compared to the bosonic frequencies ω_0 and the occupation of bosonic quasiparticles is allowed. The function is linear for energies $\omega \ll T$ and for applied voltages $eV \gg T$ it corresponds to a thermal function with FWHM = $5.4T$. In the limit $T \rightarrow 0$, the kernel becomes a δ -function and we recover the expression (3.37). Therefore, the temperature gives an upper limit for the energy resolution of IETS.

However, this is not the only reason for a finite experimental resolution. Another contribution to the broadening of the inelastic tunneling spectra is the lock-in technique often used in tunneling experiments. For obtaining the $d^2I(V)/dV^2$ curve one can in principle record the I - V curve and from this calculate the second derivative numerically. In reality the experimental data is noisy, which can lead to large errors when performing the numerical derivative. Alternatively, one usually uses a lock-in technique to gain direct access to the $d^2I(V)/dV^2$ spectrum, which works as following: Mixing a small AC modulation voltage $V_\omega \cos(\omega t)$ to the constant tunneling voltage V_0 , the experimental current $I(V) = I(V_0 + V_\omega \cos(\omega t))$ is recorded. Using a lock-in amplifier, the second harmonic of the signal is recorded

$$\begin{aligned} I_{2h}(V_0) &= \frac{2}{T_0} \int_0^{T_0/2} dt I(V_0 + V_\omega \cos(\omega t)) \cos(2\omega t) \quad , T_0 = \frac{2\pi}{\omega} \\ &= V_\omega \cdot \int_{-V_\omega}^{V_\omega} d\epsilon \left. \frac{d^2I(V)}{dV^2} \right|_{V=V_0+\epsilon} \cdot \frac{2[1 - (\epsilon/V_\omega)^2]^{3/2}}{3\pi} \end{aligned} \quad (3.41)$$

which is obviously a convolution of the second derivative $d^2I(V)/dV^2$ of the tunneling current and an instrumental function, which is shown normalized in Figure 3.5 on the right. The instrumental function has a typical FWHM = $1.22eV_\omega$ and one could come to the conclusion that in order to maximize the experimental resolution, one should choose the modulation voltage to be very small, but then one has the complication that due to the V_ω factor in front of the integral the recorded signal will also be reduced. Therefore, in experiments one has to carefully fine-tune the modulation voltage to get a signal that is

sufficiently pronounced, but also small enough that the desired experimental resolution of the measurement is maintained. ⁸ Hereafter, we will model the broadening due to the lock-in technique by a Gaussian distribution with FWHM= $1.22eV_\omega$. This will be of importance for the IETS of phonons in conventional superconductors in the next chapter, where we exploit our formalism for elastic and inelastic tunneling and find an excellent agreement between theory and experiment for STM on Pb thin films.

⁸Since this work is focused on the theoretical understanding of experimental tunneling spectra of conventional and especially unconventional superconductors, we do not wish to go into greater detail about the difficulties of recording techniques of tunneling experiments such as phase shifts between the current and the modulation voltage due to capacitive and inductive elements in the circuit.

4. Inelastic tunneling in conventional superconductors

In this chapter, we will discuss the consequences of inelastic tunneling processes for STM measurements of conventional, phonon-mediated superconductors. As was discussed in Chapter 1, the elastic picture of tunneling (conductance is proportional to the DOS of the investigated superconductor) was extremely insightful for planar tunnel junctions, where inelastic tunneling is significantly suppressed compared to STM experiments. Here, we will use our extended tunneling formalism developed in the previous chapter, which combines EETS and IETS on the same footing, to get a coherent picture of the STM spectra on conventional superconductors in both the normal- and the superconducting state.

We start with interpretations of normal-state IETS experiments on conventional superconductors as lead and niobium and show that the observed magnitude of the inelastic current is consistent with the predictions of our theory. Hereafter, the toy model of a conventional superconductor coupled to a single phonon mode with energy ω_{ph} is discussed and we show how inelastic tunneling changes the picture drawn by the purely elastic tunneling interpretation. Finally, we apply our tunneling theory to experimental STM data on thin Pb films [24], which shows excellent agreement of theory and experiment and serves as a proof of principle for our formalism.

4.1. Normal-state IETS with phonons

In the introductory Chapter 1 we already presented several early tunneling experiments on metals which saw phonon signatures of barrier oxides [49, 50] or molecules absorbed into the oxide interfaces of tunnel junctions [17, 18] in $d^2I(V)/dV^2$, see also Figure 1.5. Also in STM on graphene clear phonon features have been seen [118]. As shown in Chapter 3, inelastic tunneling processes can be understood in the following way: An electron tunnels from the left electrode to some intermediate high-energy off-shell state (which can lie either in the insulating barrier region, e.g. in oxide junctions, or in the right electrode) and from here it scatters inelastically to a state near the Fermi surface of the right electrode. Our theory predicts that for low-temperature tunneling the $d^2I(V)/dV^2$ curve in the normal state is proportional to the (thermally smeared) bosonic excitation spectrum α^2F_{tun} . As we will see in the following section 4.2, such inelastic processes involving phonons will typically lead to a valley-like structure of the conductance around zero bias. In case of junction tunneling on Pb-PbO-Pb junctions both the Pb-oxide barrier and the Pb phonons were observed in agreement with our inelastic theory [11, 50]. However, for such planar junctions the inelastic signal has been reported to be very weak: The increase of the conductance due to Pb and Pb-oxide phonons in the whole energy range from 0 to $\pm 70\text{meV}$ was only about

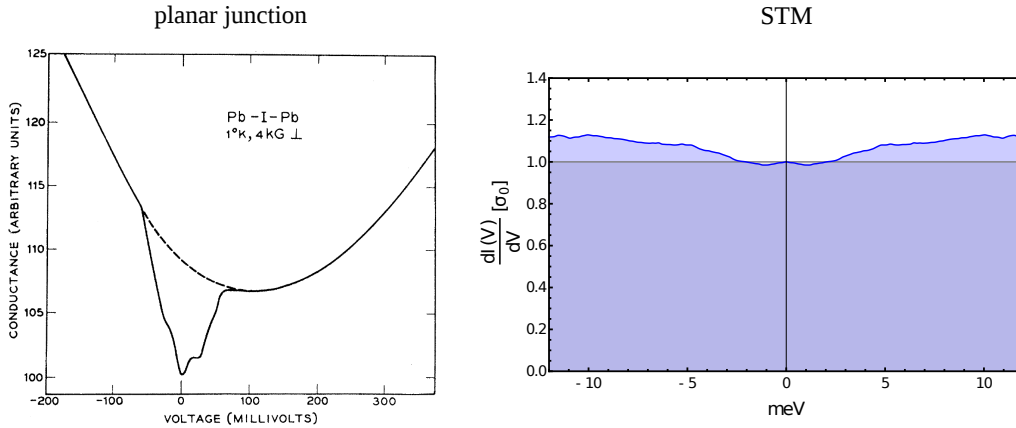


Figure 4.1.: Comparison of normal-state Pb tunneling data of planar junctions and STM showing valley-like structure coming from inelastic transitions: (left) Tunneling conductance measured on Pb-PbO-Pb planar junctions showing only weak inelastic features within $\pm 70\text{meV}$ coming from Pb and Pb-oxide phonons [50], (right) Symmetrized conductance for STM experiment with tungsten tip on Pb thin films showing a much stronger inelastic signal from the Pb-phonons (data from Ref. [24]).

10%. In contrast, more recent STM experiments on Pb thin films [19, 24, 127] showed an increase of 10% solely due to the Pb phonons in the energy window $[0, \pm 10\text{meV}]$ as can be seen in Figure 4.1. In Section 4.2 we will show for the simple example of a single phonon mode, that for such strong inelastic features as seen in the STM experiments, the inelastic tunneling features are of the same order as the strong-coupling Eliashberg features that arise in the elastic conductance below T_c . Hence, we conclude that a combined analysis has to be performed, which is presented in Section 4.3.

Since the thermal smearing $\sigma = 5.4T$ increases with temperature leading to a decrease in energy resolution, the usual method of choice for forcing the metals to the normal state is applying a strong magnetic field. However, in Type-II superconductors and especially the unconventional superconductors the critical magnetic fields often exceed the experimental capabilities and one can only use STM of vortices¹ to gain information about the normal state inelastic spectrum [85, 89, 128].

4.1.1. Estimate of the inelastic contribution for phonons

Let us start our quantitative investigations of the elastic and inelastic tunnel equations (3.34) by estimating the typical inelastic contribution that we expect for the inelastic STM in a usual metal with electron-phonon coupling. For a regular metal we expect the DOS at the Fermi edge to be of order $\nu_F \sim 1/E_F$, where E_F is the Fermi energy of the material². The Debye frequency of a metal is typically $\omega_D \approx E_F/100$ and the low-energy cutoff of the Eliashberg theory is usually chosen to be $\Lambda_{\text{eff}} \approx 5\omega_D$. The typical inverse energy scale $1/E_{\text{off}}$ introduced in the previous section can be estimated via the average over the off-shell

¹We note that vortex tunneling has the additional difficulty that the pair potential $\Delta(r)$ inside the vortex can lead to bound states similar to a 2d potential well [85].

²In the following we will use ν_F instead of ν_F^s as the normal-state Fermi edge DOS of the superconductor since the information about the trivial tip spectrum is not important for our analysis. Also, we will denote $\epsilon_{\mathbf{k}}$ as the normal-state spectrum of the superconductor.

energies from Λ_{eff} up to the band width $D \approx E_F$

$$\frac{1}{E_{\text{off}}} \approx \frac{1}{E_F - \Lambda_{\text{eff}}} \int_{\Lambda_{\text{eff}}}^{E_F} \frac{d\epsilon}{\epsilon} \approx \frac{\log(E_F/\Lambda_{\text{eff}})}{E_F}. \quad (4.1)$$

Following Eq. (3.37) the change of the conductance due to inelastic tunneling from zero bias to $eV = \omega_D$ at zero temperature in a normal conductor with constant DOS can be calculated as

$$\begin{aligned} \frac{\delta\sigma^i}{\sigma_0} &= \frac{1}{E_{\text{off}}^2 \nu_F} \int_0^{\omega_D} d\omega \alpha^2 F_{\text{tun}}(\omega) \approx \frac{\omega_D \log^2(E_F/\Lambda_{\text{eff}})}{2E_F} \int_0^{\omega_D} d\omega \frac{2\alpha^2 F_{\text{tun}}(\omega)}{\omega_D} \\ &\approx \frac{\omega_D \log^2(E_F/\Lambda_{\text{eff}}) \lambda}{2E_F} \approx 0.045\lambda. \end{aligned} \quad (4.2)$$

We used $\int_0^\infty d\omega 2\alpha^2 F_{\text{tun}}(\omega)/\omega_D \approx \int_0^\infty d\omega 2\alpha^2 F(\omega)/\omega_D \approx \lambda$ since the Eliashberg function and the tunnel spectrum are expected to be very similar, see the discussion in Section 4.1.2. For weak-coupling materials like aluminum inelastic contributions are therefore expected to be very small, whereas for the case of Pb with $\lambda = 1.5$ we would expect an increase of the conductance of $\delta\sigma^i/\sigma_0 \approx 7\%$ from 0 to 10meV, which comes close to the value of 10-12% determined in recent STM experiments [19, 24]. Similar results have been reported for Niobium, where the increase is about 4% [129], which is exactly the value we would expect from our estimation.

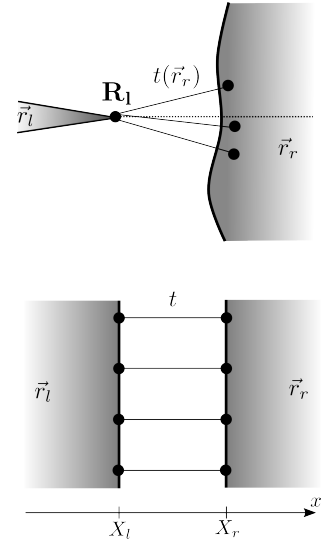
We note, that this estimate is only valid for STM geometries. For planar junctions the momentum conservation for the wave-vectors parallel to the junction surface restricts the phase space for the inelastic events drastically. In order to see that, let us follow Ref. [130] and consider the form of the tunneling amplitude in real space. For an STM tip at the position

\mathbf{R}_l the amplitude for a quasiparticle at \mathbf{r}_l tunneling to the left position \mathbf{r}_r has a form $t_{\mathbf{r}_l, \mathbf{r}_r} = t(\mathbf{r}_r) \cdot \delta_{\mathbf{R}_l, \mathbf{r}_l}$, where $t(\mathbf{r}_r)$ is a rapidly decaying function around the position $\mathbf{r}_r = 0$ of the right electrode directly opposite the STM tip. In what follows we assume this ‘‘tunneling cone’’ [36] to be so thin, that $t(\mathbf{r}_r) \approx \delta(\mathbf{r}_r)$. In contrast, for a *perfect* planar junction the transition can only occur when the electron tunnels from one surface to the nearest point on the opposite surface. Therefore, the tunnel matrix elements reads $t_{\mathbf{r}_l, \mathbf{r}_r} = t\delta(x_l - X_l)\delta(x_r - X_r)\delta(\mathbf{r}_{r,\parallel} - \mathbf{r}_{l,\parallel})$, where $\mathbf{r}_{r/l,\parallel}$ give the position of the particle in the yz -direction. Fourier transforming these expressions one arrives at

$$t_{\mathbf{k}, \mathbf{k}'} = \begin{cases} t & \text{for STM junction} \\ t\delta_{\mathbf{k}_{\parallel}, \mathbf{k}'_{\parallel}} & \text{for planar junction} \end{cases} \quad (4.3)$$

This is of course just a mathematical formulation for the fact that while the planar junction conserves the translational symmetry and therefore also the momentum parallel to the surface, the STM breaks translational symmetry in all direction and has therefore no momentum restrictions for the transition.

This momentum restrictions for the planar junction will reduce the allowed inelastic tunneling processes considerably. To see this, let us first consider the case of an inelastic



tunneling event for the **STM junction** with applied bias V : We start with an arbitrary state at the Fermi surface (low-energy momentum $(\mathbf{k}_l)^<$) in the STM tip and tunnel to an high-energy off-shell state with energy-momentum $[eV, (\mathbf{k}_r)^>$ in the metal under consideration. The electron is now scattered via the emission of a boson with $[eV, \mathbf{q}]$ to a low-energy state $[0, (\mathbf{k}^r - \mathbf{q})^<$. As there is no momentum restriction for the boson and the high-energy momentum $(\mathbf{k}_r)^>$ there are plenty of possible inelastic processes allowed. Now, let us have a look at the same situation in the **planar junction**: Again we start with a state at the Fermi surface in the left electrode $[0, (\mathbf{k}_l)^<$ and tunnel to the right in a state $[eV, (\mathbf{k}_r^\perp + \mathbf{k}_l^\parallel)^>$ with the same momentum parallel to the junction surface. From there we scatter with a boson with energy-momentum $[eV, \mathbf{q}]$ and have to end up in a state $[0, (\mathbf{k}_r^\perp + \mathbf{k}_l^\parallel - \mathbf{q})^<$ at the Fermi surface of the right electrode. In contrast to the STM there is a strong restriction in the phase space of the off-shell state $(\mathbf{k}_r^\perp + \mathbf{k}_l^\parallel)^>$ with only one free momentum direction \mathbf{k}_r^\perp and therefore also for the boson momentum \mathbf{q} (with corresponding energy eV) as we have to end up in a state near the right electrodes Fermi surface. From this phase-space arguments we can understand the observed reduction of inelastic contributions in the Pb-junctions for planar junctions compared to STM experiments. However, the exact ratio of elastic and inelastic events depends strongly on the topology of the two Fermi surfaces of the electrodes and the bosonic dispersion as well as on the junctions geometry. Further, there can also be deviations for systems containing several bands crossing the Fermi surface, as the overlap of the different wavefunctions of the tip and superconductor bands may be different. Note that due to the orbital character of bands, states from different parts of the Brillouin zone will in general have a different tip-sample distance dependence [83] which can lead to varying elastic and inelastic contributions when changing the average conductance/distance is experiments. As before, we will restrict ourselves to the case of a constant tunneling amplitude $t_{\mathbf{k}, \mathbf{k}'} = t$ in the following, which is most suitable for the STM geometry.

4.1.2. Comparison of $\alpha^2 F_{\text{tun}}$ and $\alpha^2 F$

For systems where the electron-phonon interaction is the dominant interaction of the electrons with collective bosonic modes, e.g. in many regular metals, the IETS signal $d^2 I(V)/dV^2$ is not directly proportional to the Eliashberg function $\alpha^2 F$ given in Eq. (2.28), as was discussed in Chapter 3. Instead, the normal state IETS spectrum gives direct access to the bosonic tunneling spectrum $\alpha^2 F_{\text{tun}}$, which is defined in Eq. (3.33). For a better comparison, let us present both of the two definitions side by side

$$\begin{aligned}\alpha^2 F(\omega) &= \frac{1}{\nu_F} \sum_{\mathbf{k}, \mathbf{k}', \lambda} \delta(\epsilon_{\mathbf{k}}) \delta(\epsilon_{\mathbf{k}'}) |\alpha_{\mathbf{k} - \mathbf{k}'}^\lambda|^2 A_{\mathbf{k} - \mathbf{k}', \lambda}(\omega), \\ \alpha^2 F_{\text{tun}}(\omega) &= \nu_F \sum_{\mathbf{q}, \lambda} |\alpha_{\mathbf{q}}^\lambda|^2 A_{\mathbf{q}, \lambda}(\omega).\end{aligned}\tag{4.4}$$

Here, $A_{\mathbf{q}, \lambda}(\omega) = -\mathbf{Im} D_{\mathbf{q}, \lambda}^R(\omega) \Theta(\omega) / \pi$ is the spectral weight function of a phonon with momentum \mathbf{q} of the phonon branch λ . The obvious difference lies in the way the momentum average is performed. Let us now consider the example of perfect phonon quasiparticles $A_{\mathbf{q}, \lambda} = \delta(\omega - \omega_{\mathbf{q}, \lambda})$ with realistic phonon dispersions in a cubic material that has a spherical Fermi surface, which should serve as a simple model for Pb phonons. As usual, we start from the ansatz $M_n \ddot{u}_{in}^\alpha = -\sum_{j, m, \beta} \Phi_{in, jm}^{\alpha\beta} u_{jm}^\beta$ of coupled harmonic oscillators in order to describe the collective dynamics of the phonons. Here, α and β enumerate Cartesian axes, i and j enumerate the positions \mathbf{r}_i of the Bravais lattice of the system, n and m indicate

the atoms of the basis of the crystal, Φ is the second derivative of the potential energy $\Phi_{i,j}^{\alpha,\beta} = \frac{\delta^2 U}{\delta u_i^\alpha \delta u_j^\beta}$, M_n is the mass and u_{in}^α the displacement of the n -th atom of the basis at the position i in the Bravais lattice. If we assume a harmonic movement of the atoms we can use the ansatz $u_{in}^\alpha(t) = \frac{v_n^\alpha}{\sqrt{M_n}} \exp[i(\mathbf{q} \cdot \mathbf{r}_i - \omega t)]$ for solving the equation of motion

$$\begin{aligned} \sqrt{M_n} \omega^2 v_n^\alpha &= \sum_{j,m,\beta} \frac{\Phi_{in,jm}^{\alpha\beta}}{\sqrt{M_m}} v_m^\beta e^{i\mathbf{q}(\mathbf{r}_j - \mathbf{r}_i)}, \\ 0 &= \sum_{m,\beta} \left[\omega^2 \delta_{m,n} \delta_{\alpha,\beta} - \sum_j \frac{\Phi_{in,jm}^{\alpha\beta}}{\sqrt{M_n M_m}} e^{i\mathbf{q}(\mathbf{r}_j - \mathbf{r}_i)} \right] v_m^\beta. \end{aligned} \quad (4.5)$$

Because of translational invariance of the crystal, $\Phi_{in,jm}^{\alpha\beta} = \Phi_{n,m}^{\alpha\beta}(\mathbf{r}_i - \mathbf{r}_j)$ can only depend on the relative distance between the Bravais lattice points \mathbf{r}_i . Therefore, we can write

$$\begin{aligned} 0 &= \sum_{m,\beta} \left[\omega^2 \delta_{m,n} \delta_{\alpha,\beta} - \sum_j \frac{\Phi_{n,m}^{\alpha\beta}(\mathbf{r}_i - \mathbf{r}_j)}{\sqrt{M_n M_m}} e^{-i\mathbf{q}(\mathbf{r}_i - \mathbf{r}_j)} \right] v_m^\beta, \\ 0 &= \sum_{m,\beta} \left[\omega^2 \delta_{m,n} \delta_{\alpha,\beta} - \sum_j \frac{\Phi_{n,m}^{\alpha\beta}(\mathbf{r}_j)}{\sqrt{M_n M_m}} e^{-i\mathbf{q} \cdot \mathbf{r}_j} \right] v_m^\beta. \end{aligned} \quad (4.6)$$

If we define the matrix $\hat{M}(\mathbf{q})$ with coefficients

$$M_{n\alpha,m\beta}(\mathbf{q}) = \sum_j \frac{\Phi_{n,m}^{\alpha\beta}(\mathbf{r}_j)}{\sqrt{M_n M_m}} e^{-i\mathbf{q} \cdot \mathbf{r}_j} \quad (4.7)$$

the dispersions $\omega_\lambda(\mathbf{q})$ of the phonons can be derived by solving

$$\det[\omega^2 \mathbb{1} - \hat{M}(\mathbf{q})] = 0. \quad (4.8)$$

In the case of Pb, the crystal has an fcc(face centered cubic)-structure with a single-atomic basis, such that we can write

$$\hat{M}(\mathbf{q}) = \begin{pmatrix} M_{xx}(\mathbf{q}) & M_{xy}(\mathbf{q}) & M_{xz}(\mathbf{q}) \\ M_{xy}(\mathbf{q}) & M_{yy}(\mathbf{q}) & M_{yz}(\mathbf{q}) \\ M_{xz}(\mathbf{q}) & M_{yz}(\mathbf{q}) & M_{zz}(\mathbf{q}) \end{pmatrix}, \quad (4.9)$$

to obtain the two transversal modes and the one longitudinal mode. In the next-nearest neighbor approximation with spring constant k_1 between nearest neighbors and k_2 between next-nearest neighbors one finds with the lattice spacing a (the other matrix elements are symmetry related)

$$M_{xx}(\mathbf{q}) = \frac{1}{M} \left(2k_1 [1 - \cos(q_x a)] + 2k_2 [2 - \cos(q_y a) - \cos(q_z a)] \right), \quad (4.10)$$

$$M_{xy}(\mathbf{q}) = \frac{2k_2}{M} \sin(q_x a) \sin(q_y a). \quad (4.11)$$

This spring model is of course far too simple to capture the detailed DOS of Pb. Nevertheless, there are prominent features arising from the transversal and longitudinal modes similar to the known Pb phonon spectra, as can be seen in Figure 4.2 with parameters $k_2 = k_1/2$. In order to compare the Eliashberg function and the phonon tunneling spectrum we assume that the electron-phonon coupling $\alpha_q^\lambda \approx \alpha$ is constant in the energy range of interest,

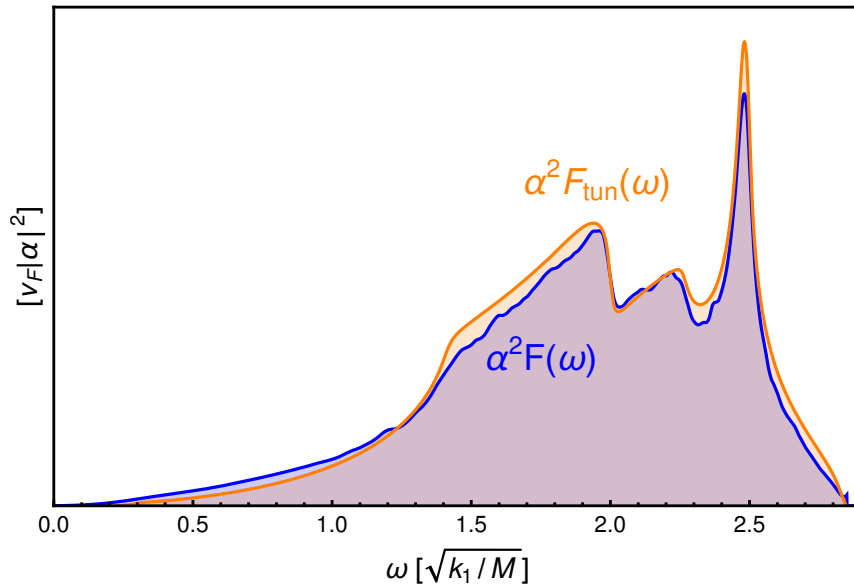


Figure 4.2.: Comparison of $\alpha^2 F(\omega)$ and $\alpha^2 F_{\text{tun}}(\omega)$ for phonons in a simple cubic crystal.

see also the extensive discussion of Scalapino [11]. Thus, the dynamics of the spectrum is determined by the bosonic dispersion and not by the momentum dependence of the electron-phonon matrix element. For the calculation of the Eliashberg-function we assume a simple quadratic dispersion relation $\epsilon_{\mathbf{k}} = \frac{k^2 - k_F^2}{2m}$ with $k_F = \pi$.³ This model yields the normal state DOS

$$\nu_F = \sum_{\mathbf{k}} \delta(\epsilon_{\mathbf{k}}) = \int \frac{dk d\Omega k^2}{(2\pi)^3} \delta\left(\frac{k_F}{m}(k - k_F)\right) = \frac{k_F m}{2\pi^2}, \quad (4.12)$$

and we are able to rewrite the momentum integral in (4.4) as

$$\begin{aligned} \alpha^2 F(\omega) &= \frac{\nu_F |\alpha|^2}{2^4 \pi^2} \sum_{\lambda} \int d\Omega d\Omega' A_{\mathbf{k}_F - \mathbf{k}'_F, \lambda}(\omega), \\ \alpha^2 F_{\text{tun}}(\omega) &= \frac{\nu_F |\alpha|^2}{(2\pi)^3} \sum_{\lambda} \int d^3 q A_{\mathbf{q}, \lambda}(\omega), \end{aligned} \quad (4.13)$$

The numerical results are shown in Figure 4.2: Obviously, both spectra show striking similarities and they only differ slightly in the fine-structure of the spectrum. This confirms our conclusion, that the different momentum averages are rather unimportant and that both $\alpha^2 F(\omega)$ and $\alpha^2 F_{\text{tun}}(\omega)$ are mostly determined by the phonon dispersion, i.e. the Van-Hove singularities at the border of the Brillouin zone. We note that our simple model probably overestimates the contributions from very low energies as the electron-phonon coupling vanishes in the limit of small momenta \mathbf{q} for acoustic phonons. Furthermore, depending on the actual band structure of the metal the momentum sum in $\alpha^2 F_{\text{tun}}(\omega)$ is constrained in such a way that \mathbf{q} are restricted to momenta that connect high-energy and low-energy electronic states and we also approximated the electronic off-shell energy to be constant in the whole Brillouin zone. Nevertheless, we just have shown that the bosonic dispersion gives the dominant contribution to the bosonic tunneling spectrum and that we can safely set $\alpha^2 F_{\text{tun}}(\omega) \approx \alpha^2 F(\omega)$ for phonon-mediated systems in the remainder of this chapter.

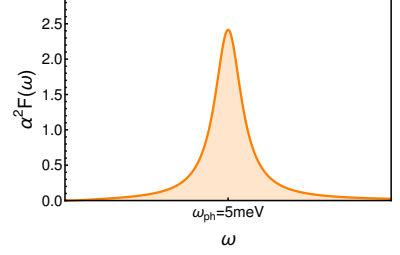
³We set the interatomic distance to $a = 1$ such that the momenta are restricted to $q_{x,y,z} \in [-\pi, \pi)$.

4.2. Elastic and inelastic STM for single phonon mode

In order to understand the implication of the inelastic channel for the interpretation of tunneling data in the superconducting state, we here discuss the expected features that arise in the tunneling current for a conventional, phonon-mediated superconductor with a single phonon mode with energy $\omega_{\text{ph}} = 5\text{meV}$ in the zero temperature limit. The corresponding phonon-spectrum is modeled similar to Section 2.2.3 via

$$\alpha^2 F_{\text{tun}}(\omega) \simeq \alpha^2 F(\omega) = A_0 \cdot \frac{\omega^2}{\omega^2 + \omega_0^2} \cdot \frac{\gamma}{(\omega - \omega_{\text{ph}})^2 + \gamma^2} \Theta(\omega) \quad (4.14)$$

where $\gamma = \omega_{\text{ph}}/10$ is the phonon half-width and the function in front of the Lorentzian ensures the proper low-frequency behavior of the acoustic phonon branch that rapidly approaches unity for $\omega \approx \omega_0 = 1\text{meV} \ll \omega_{\text{ph}}$. The normalization factor A_0 is chosen such that $\lambda = 1.5$ lies in the strong coupling regime of Pb and we use a characteristic pseudopotential $\mu^* = 0.1$ that yields a gap value of $\Delta \simeq 1\text{meV}$. Furthermore, the inelastic tunneling magnitude is chosen to be of the same order as seen in the lead experiments [19, 24], meaning that



$$\delta\sigma = \sigma(\omega_D) - \sigma(0) = \frac{\sigma_0}{E_{\text{off}}^2 \nu_F} \int_0^{\omega_D} d\omega \alpha^2 F_{\text{tun}}(\omega) \approx 10\% \sigma_0, \quad (4.15)$$

where we chose $\omega_D = 2\omega_{\text{ph}}$ as the Debye frequency of the phonon. This will fix the prefactor and the yet unknown off-shell energy E_{off} . When the sample s is in the superconducting state at zero temperature, the inelastic contribution can be written as

$$\begin{aligned} \sigma^i(V) &= \frac{\sigma_0}{E_{\text{off}}^2 \nu_F} \int_{-\infty}^{\infty} d\epsilon \nu_s(\epsilon) \left[\alpha^2 F_{\text{tun}}(\epsilon - eV) \Theta(-\epsilon) + \alpha^2 F(-\epsilon + eV) \Theta(\epsilon) \right] \\ &\stackrel{\text{p.h. sym.}}{=} \frac{\sigma_0}{E_{\text{off}}^2 \nu_F} \int_{-\infty}^0 d\epsilon \nu_s(\epsilon) \alpha^2 F_{\text{tun}}(\epsilon + e|V|) \end{aligned} \quad (4.16)$$

which is just a convolution of the electronic and bosonic spectrum of the superconductor [123]. In Figure 4.3 the elastic, inelastic and total conductance $\sigma(V) = dI(V)/dV$ and its derivative $d\sigma(V)/dV = d^2I(V)/dV^2$ are shown for the normal- and superconducting state. In the following paragraph we will discuss them in detail.

Normal state

Let us start our investigation with the normal state tunneling spectra that are shown as the blue curves in Figure 4.3. The elastic conductance is proportional to the electron DOS, which is constant and therefore $\sigma^e(V) = \sigma_0$ and $d\sigma^e(V)/dV = 0$ as shown in Figure 4.3(a) and (b). The IETS spectrum $d^2I^i(V)/dV^2$ shown in Figure 4.3(d) is proportional to the phonon spectrum $\alpha^2 F_{\text{tun}}$ as becomes apparent from Eq. (3.37). For the inelastic conductance $\sigma^e(V)$ plotted in Figure 4.3(c) this results in a valley-like structure with maximum increase at $eV = \pm\omega_{\text{ph}}$ and a saturation at ω_D with $\sigma^i(\omega_D) = 0.1\sigma_0$. The total conductance (Figure 4.3(e)) therefore also increases when moving away from zero bias due to the possibility of inelastic tunneling processes and saturates at $1.1\sigma_0$ for the voltage $eV = \omega_D$ where all inelastic tunneling channels are open. The total second derivative $d^2I(V)/dV^2$ of the tunneling current, as shown in Figure 4.3(f), is exactly the same as the pure inelastic contribution since in the normal state the elastic conductance is trivial.

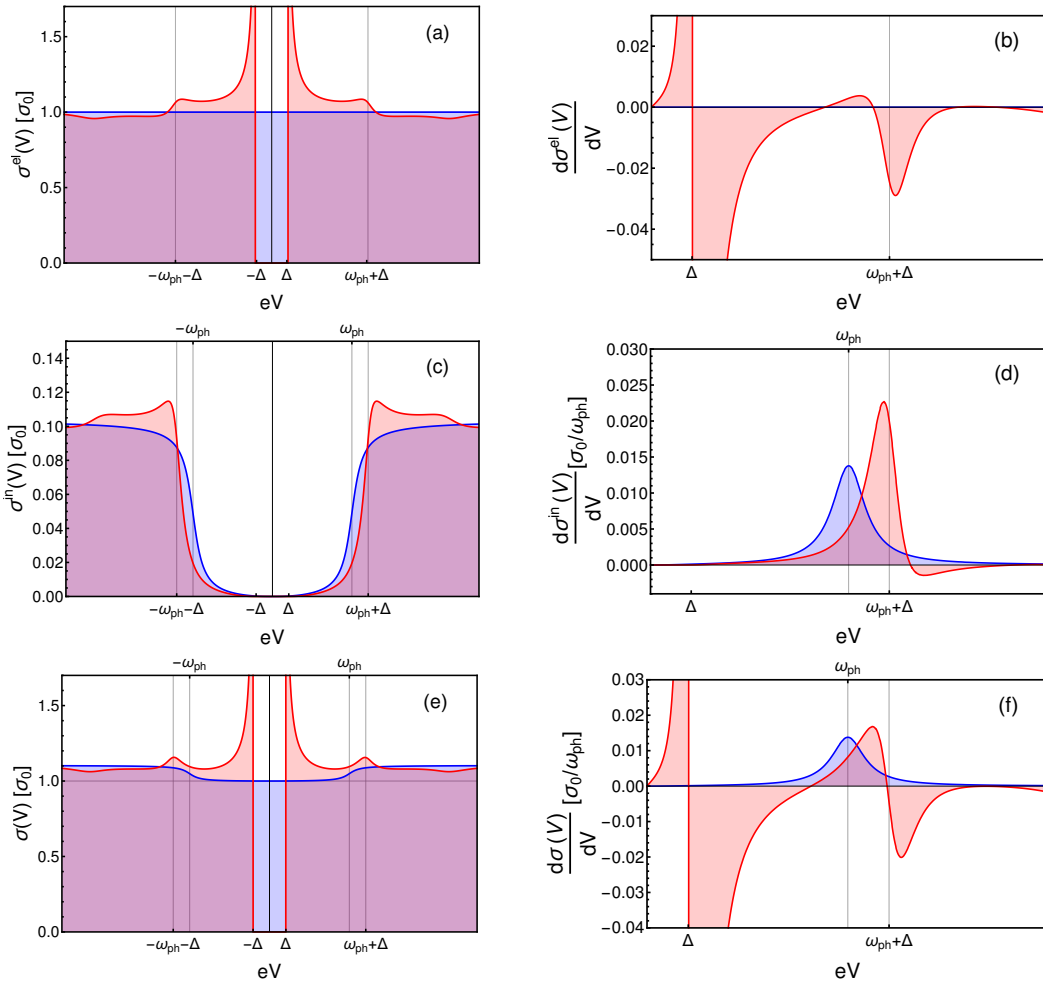


Figure 4.3.: Elastic, inelastic and total tunneling spectra for single-phonon mode. Shown in blue (normal state) and red (superconducting state) are the $\sigma(V) = dI(V)/dV$ and $d\sigma(V)/dV = d^2I(V)/dV^2$ curves that are calculated for a single-phonon mode with characteristic energy ω_{ph} . The inelastic tunneling amplitude was chosen such that in the normal state the increase of the conductance from the inelastic contributions is $\delta\sigma = 0.1\sigma_0$, where σ_0 is the purely elastic conductance above T_c .

Superconducting state

In the superconducting state the picture changes and not only the inelastic processes but also the elastic processes give dynamical contributions for the conductance, see the red curves in Figure 4.3(a) and (b). The elastic conductance in Figure 4.3(a) shows the typical strong-coupling DOS of the Eliashberg theory, see also Section 2.2.3, with the main fine-structure around $eV = \Delta + \omega_{\text{ph}}$, where $d^2I^e(V)/dV^2$ has a clear dip (see Figure 4.4(b)). Interestingly, the inelastic conductance $\sigma^i(V)$ now shows a peak close above $eV = \Delta + \omega_{\text{ph}}$ and then decreases to the normal state value for higher voltages. In the $d^2I^i(V)/dV^2$ spectrum (Figure 4.3(d)) this manifests as a pronounced peak just below $\Delta + \omega_{\text{ph}}$ with a following small dip feature. Such features have been seen in IETS spectroscopy of molecules, which we will discuss in Section 4.2.1. In Figure 4.3(e) the total conductance $\sigma(V)$ in the superconducting state has changed significantly compared to the pure elastic tunneling conductance $\sigma^e(V)$ in Figure 4.3(a). The peak-dip feature of the strong-coupling theory at $eV = \Delta + \omega_{\text{ph}}$ has become a more pronounced peak-feature and $\sigma(V)$ is larger than σ_0 for

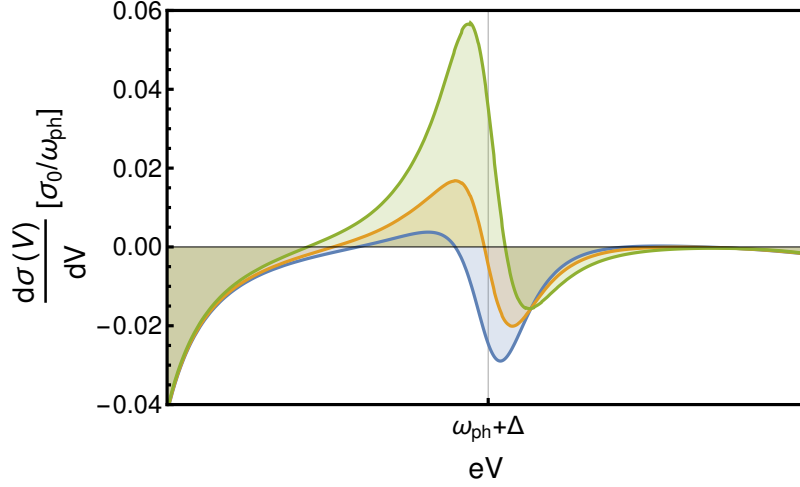


Figure 4.4.: Tunneling $d^2I(V)/dV^2$ spectrum for single-phonon mode and different inelastic tunneling amplitudes: (blue) $\sigma^i(\omega_D) = 0$, (orange) $\sigma^i(\omega_D) = 0.1\sigma_0$, (green) $\sigma^i(\omega_D) = 0.3\sigma_0$.

biases $eV > \Delta + \omega_{\text{ph}}$. In $d\sigma(V)/dV$ the clear dip of the elastic tunneling (Figure 4.3(b)) is replaced by a pronounced antisymmetric peak-dip feature relative to the zero-axis centered around $\Delta + \omega_{\text{ph}}$. In Ref. [24] such antisymmetric peak-dip features in the IETS spectrum for STM tunneling into Pb thin films have been observed and we will discuss this experiment in great detail in Section 4.3.

Note that the exact shape of the IETS spectrum can differ depending on the parameters of the system. For large inelastic contributions or when the phonon energy is much larger than the superconducting gap $\omega_{\text{ph}} \gg \Delta$ the peak will be more pronounced and vice versa. This is illustrated in Figure 4.4, where we vary the inelastic tunneling amplitude. Thus, the nice antisymmetry of the peak-dip feature in Figure 4.3(f) is actually a result of a certain ratio of the input parameters similar to the ones observed in the Pb STM experiment [19, 24].

4.2.1. IETS of barrier molecules for superconducting junctions

The first phonon signatures, seen in IETS experiments on planar junction, originated from molecules that contaminated the barrier oxide during the fabrication process [17, 18]. These molecules typically contained hydrogen such that OH or CH bending and stretching modes could be detected via IETS with typical frequencies of $\omega_{\text{ph}} \sim 100\text{meV}$ far larger than the superconducting gap $\Delta \sim 1\text{meV}$ of conventional superconductors. One could think that the phonon line-shapes in the IETS spectra should not change when entering the superconducting state due to this separation of energy scales. As was first pointed out by Klein [123] there are small but clear changes of the inelastic signal below T_c , see Figure 4.5, similar to the changes seen in Figure 4.3(d). In contrast to the previous section, where we assumed a phonon mode with frequency comparable to the superconducting gap, we can here neglect the elastic contribution to d^2I/dV^2 as we are interested in energies $eV \approx \omega_{\text{ph}} \gg \Delta$ where the electronic DOS is constant again. Therefore, we find for zero temperature

$$\frac{d^2I(V)}{dV^2} = \frac{d^2I^i(V)}{dV^2} \stackrel{(4.16)}{\sim} \int_{-\infty}^0 d\epsilon \text{sign}(V) \nu_s(\epsilon) \alpha^2 F'_{\text{tun}}(\epsilon + e|V|), \quad (4.17)$$

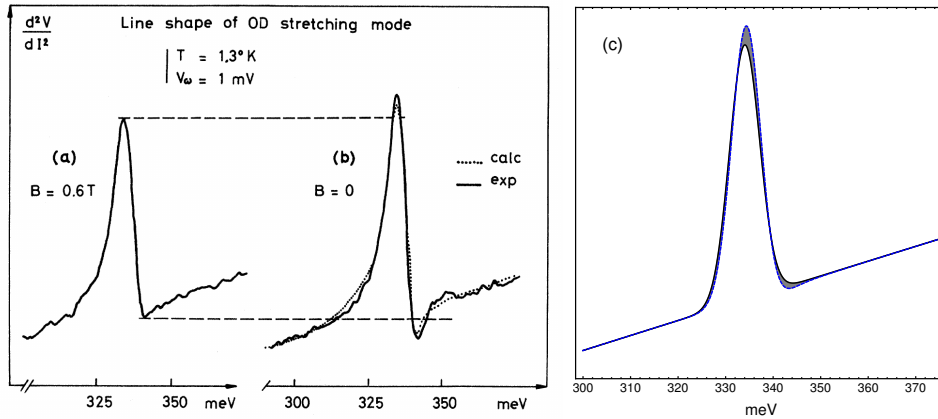


Figure 4.5.: IETS of oxygen-deuterium stretching mode on Mg-MgO-Pb junctions taken from Ref. [123]: (a) Data with Pb forced to normal state via magnetic field, (b) IETS with superconducting Pb electrode, (c) Comparison of normal state (black) and superconducting (blue) IETS spectra calculated using Eq. (4.17).

The peak of the IETS curve occurs for voltages V , where the overlap of the electronic and bosonic DOS in the convolution is maximized. For a very sharp phonon mode, this happens for the conditions⁴ $\epsilon + e|V| = \omega_{\text{ph}}$ and $\epsilon = -\Delta$, yielding that the IETS phonon peak is shifted to higher energies at $e|V| = \Delta + \omega_{\text{ph}}$ in the superconducting state. We emphasize that for the inelastic spectrum in Eq. (4.17) it is sufficient to consider only a simple mean-field BCS DOS since the important contributions of the integral come from the coherence peak and not from the Eliashberg features. In Section 4.3 we will show how this can be used to unravel the elastic and inelastic contributions of the measured STM spectra.

In Figure 4.5 the experimental $d^2I(V)/dV^2$ spectrum in the normal and superconducting state for a Mg-MgO-Pb planar junction is shown [123]. When forcing the Pb to the normal state by applying a magnetic field, the IETS curve displays the oxygen-deuterium (OD) stretching mode, see Figure 4.5(a). For the spectrum with the superconducting Pb in Figure 4.5(b) small changes of the line-shape are clearly visible: The maximum is enhanced and shifted to higher energies and a small dip occurs at the tail of the OD mode. These three features can be captured very well by using Eq. (4.17) with a BCS DOS of gap magnitude $\Delta = 1.3\text{meV}$ as is shown in Figure 4.5(c), which serves as a strong argument that the derived tunneling theory works for both the normal as well as the superconducting state.

4.2.2. Normalization procedure of Rowell and McMillan

Tunneling experiments on conventional superconductors in the normal state often show deviations from a flat tunnel spectrum, two examples are shown in Figure 4.1. As is pointed out in the review of McMillan and Rowell in Ref. [11] one usually normalizes the superconducting conductance by the normal state conductance at each voltage

$$\sigma_{\text{norm}}(V) = \frac{\sigma_{\text{sc}}(V)}{\sigma_{\text{nc}}(V)}. \quad (4.18)$$

⁴Note, that in Eq. (4.17) the derivative of the bosonic tunnel spectrum has to be convoluted. Thus for broader phonon modes, the maximum in $\alpha^2F'_{\text{tun}}$ will occur just below ω_{ph} . The phonon peak in the IETS spectrum will therefore occur below $e|V| = \Delta + \omega_{\text{ph}}$.

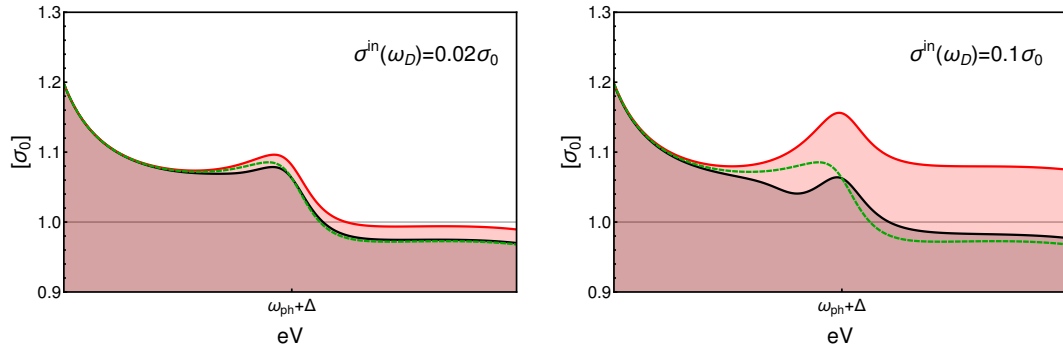


Figure 4.6.: Conventional normalization of superconducting tunneling spectra: Shown are the total tunneling spectrum (red) in the superconducting state, the normalized conductance $\sigma_{\text{norm}}(V)$ (black) and the purely elastic conductance (green) that represents the electronic DOS.

This normalization procedure is expected to work well in the case where the non-constant DOS originates from a varying normal state electron DOS, i.e. for purely elastic tunneling. However, when inelastic tunneling is present the above normalization will not cause the inelastic conductance to vanish, because the inelastic tunneling spectrum changes when entering the superconducting state, see Figure 4.3. Let us apply the normalization (4.18) for our single-phonon model and compare the obtained spectrum with the actual electronic DOS. This is shown in Figure 4.6, where the total superconducting tunneling conductance is plotted in red and the normalized conductance is plotted in black. For small inelastic contributions $\sigma^i(\omega_D) = 0.02\sigma_0$, typical for the planar tunneling junctions [11, 50], the normalization works well and we see that the deviations of the normalized conductance and the actual electronic DOS (green) are very small compared to the magnitude of the strong-coupling features. For strong inelastic amplitudes, e.g. $\sigma^i(\omega_D) = 0.1\sigma_0$ as in the Pb STM experiment [19, 24], the deviations of the normalized conductance and the electronic DOS are strong as seen in the right plot of Figure 4.6. In the normalized curve the peak-feature is significantly more pronounced and the following dip feature is reduced compared to the pure electronic spectrum.

Hence, we conclude that for conventional superconductors the normalization procedure (4.18) only works for small inelastic tunneling contributions, e.g. for the planar junction experiments on Pb [50]. When dealing with stronger inelastic tunneling amplitudes however, e.g. in the case of STM tunneling [19, 24], the conventional normalization will not lead to a spectrum that can be directly compared to the electronic DOS. In the next section, we will explicitly show that using the tunneling formalism presented in Section 3.2 it is still possible to separate the elastic and inelastic contributions of the measured conductance, which will give direct access to both the electronic and the bosonic spectrum of the investigated metal.

4.3. STM on normal- and superconducting Pb films

In the past, fine structure of the tunneling spectra of superconductors have been widely used to identify fingerprints of the mechanism responsible for Cooper pairing. In this section, we show that for STM experiments on Pb thin films the inclusion of inelastic tunneling processes as described in the previous Chapter 3 is essential for the proper interpretation of these fine structures. Hence, we demonstrate that the McMillan inversion algorithm can be an incomplete description and has, in general, to be modified to account for additional

inelastic tunneling processes. We have chosen Pb films as a perfect trial candidate for studying the role of elastic and inelastic tunneling for STM of superconductors, since the electron and phonon spectra are known from various experiments [15, 32–34, 131] and we can thus easily compare the STM spectra to the calculated curves of our theory. The following analysis is based on Ref. [24] and the STM experiments were performed by Jasmin Jandke and Wulf Wulfhekkel at the KIT.

4.3.1. Normal state

Let us start by describing the experimental setup of the Pb STM tunneling experiment. The measurements were performed with a home-built Joule-Thomson low-temperature STM [132] at a temperature of about $T = 0.8\text{K}$. The Joule-Thomson cryostat is accompanied by a coil made of superconducting NbTi that is able to produce magnetic fields up to 5T that can be used to force the Pb film to the normal state [133]. A tungsten tip, known to have a very weak electron-phonon coupling [16], is used to avoid inelastic contributions from tip phonons. The Pb film was grown in-situ on top of a highly n-doped Si(111) crystal and immediately transferred to the cryogenic STM. In Figure 4.7 the topography of the surface is shown with large extended 3D islands⁵ of about 30 Pb monolayers (with their $\langle 111 \rangle$ axis perpendicular to the substrate) on top of the wetting layer, as previously reported by Refs. [134–138]. The measurements of the first and second derivative of the tunneling current $I(V)$ have been performed using a lock-in amplifier with modulation voltage $V_\omega = 621\mu\text{V}$ ⁶. The modulation voltage leads to an experimental broadening with $\text{FWHM} = 1.2eV_\omega = 745\mu\text{eV}$, see Section 3.3. As the temperature is much smaller than the typical phonon frequencies, we can use the zero temperature expressions for the tunneling currents and model the combined experimental broadening due to temperature and lock-in by a convolution of the theoretical spectra with a Gaussian distribution of $\text{FWHM} = \sqrt{(5.4T)^2 + (1.2eV_\omega)^2} = 832\mu\text{eV}$ [123], which corresponds to a standard deviation $\sigma = \text{FWHM}/\sqrt{8 \ln 2} = 353\mu\text{eV}$.

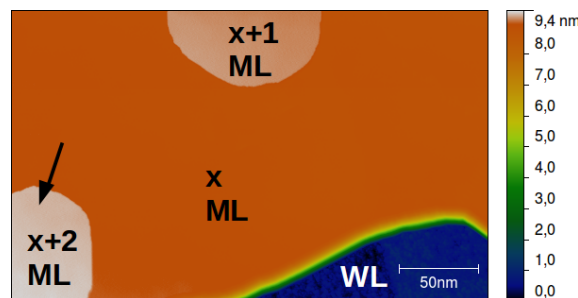


Figure 4.7.: STM topography of Pb/Si(111) recorded with 1V, 1nA: On top of the wetting layer (WL) extended Pb islands of typically $x = 30$ monolayers (ML) appear. Taken from Ref. [24].

Due to the finite number (≈ 30) of monolayers, the bosonic and electronic states have quantized momenta k_z in z -direction perpendicular to the surface. Nevertheless, first principle calculations [139, 140] show that in a 4 monolayer system the phonon spectrum displays a clear resemblance to the bulk spectrum and that for a 10 monolayer system it is already very close to the bulk spectrum. The experiments were performed for 30

⁵The extension of the islands are larger than 400 nm in diameter excluding Coulomb blockage physics.

⁶The modulation voltage $V_\omega = 439\mu\text{V}$ given in Ref. [24] is defined as the root mean square value of the AC voltage, however we wish to work with the maximum voltage similar to Ref. [123].

monolayers and we expect that differences between this system and the bulk are therefore negligible. As a more quantitative analysis let us consider the phonon model for cubic systems of Section 4.1.2 and compare the bulk phonon spectrum and the thin film spectrum (N monolayers) with quantized $q_z = \frac{\pi}{a \cdot N}(-N, N]$, where a is the lattice spacing. In Figure 4.8 we see that the 5 monolayer spectrum has additional peaks that come from the strong quantization of the z -direction, but the 30 monolayer phonon DOS is basically indistinguishable from the bulk phonon spectrum. This behavior originates from the fact, that the phonon peaks in the DOS are caused by van Hove singularities at the Brillouin zone boundary with characteristic wave length $\lambda \sim a \ll 30a$. Therefore, the relevant wavelength of the phonons is small compared to the system size. Further, the high energy phonons of the lead film have a substantially different dispersion than those of the Si substrate, such that phonons in the Pb films are expected to be reflected at the interface, i.e. they are basically localized in the film and do not couple to the Si phonons.

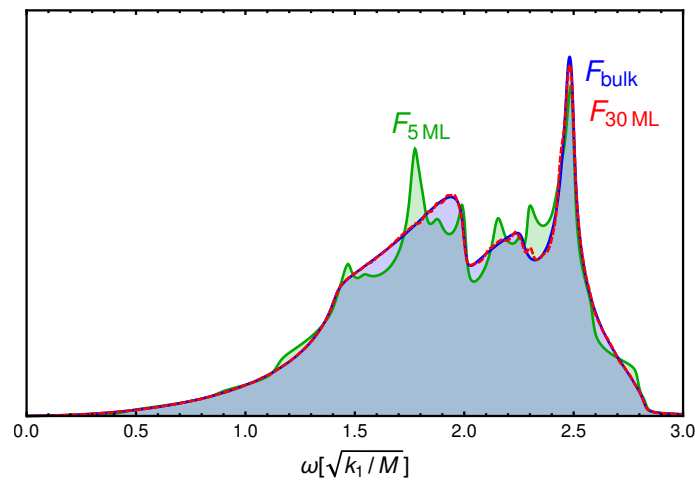


Figure 4.8.: Phonon spectrum for cubic systems as defined in Section 4.1.2: (green) Thin film phonon spectrum with 5 ML, (red) thin film phonon spectrum with 30 ML, (blue) bulk phonon spectrum.

Hence, when performing STM IETS on the 30 monolayer Pb thin films in the normal state we expect to see the bosonic tunneling spectrum $\alpha^2 F_{\text{tun}}(\omega)$ of the bulk phonons. Since the electron spectrum of Pb is known to be flat for energies comparable to the Debye frequency $\omega_D = 10\text{meV}$ of Pb⁷, only inelastic contributions will lead to variations in the normal state conductance $\sigma(V) = \sigma^e(V) + \sigma^i(V) = \sigma_0 + \sigma^e(V)$. In Figure 4.9 the first and second symmetrized derivative of the tunneling current is shown. The first derivative shows a valley-like structure with an increase of about 12% from 0mV to 10mV as expected from the inelastic tunneling theory just like in Figure 4.3(e) for a single phonon mode. This behavior originates from more and more inelastic tunnel channels that open when increasing the bias voltage up to the Debye frequency $\omega_D \approx 10\text{meV}$ of Pb. The maximum slope of the conductance occurs at the positions of the Van-Hove singularities of the phonon spectrum. The phonon features can be seen more clearly when looking at the measured second derivative, shown as the blue curve in Figure 4.9(b). Features well known from complementary experiments like tunneling inversion [11, 15] and neutron scattering [32–34] can be identified in the IETS spectrum, i.e. the typical peaks of the transversal and longitudinal phonon modes at $\omega_t = 4.4\text{meV}$ and $\omega_l = 8.5\text{meV}$. A zero bias anomaly, maybe due to a quantum well state close to the Fermi surface [19], leads to a clear deviation of

⁷Renormalization effects by virtual phonons will not affect the electronic DOS in the normal state as explained in Section 2.2.3.

$d^2I(V)/dV^2$ from the Eliashberg function for very small biases. Earlier STM experiment on 13 monolayer Pb films [19] have shown similar results, see the green curve in Figure 4.9, but they were able to better reproduce $\alpha^2F(\omega)$ in the region between the phonon peaks that is significantly reduced for the bosonic tunneling spectrum of this experiment. The rapid fluctuations on top of the measured spectrum come from small mechanical vibrations of the STM apparatus. Additionally, a clear third peak at $eV \approx \omega_t + \omega_l$ is seen in the d^2I/dV^2 spectrum that coincides with the sum of the transversal and longitudinal phonon frequencies, which suggests to interpret this feature with two-phonon inelastic tunneling.

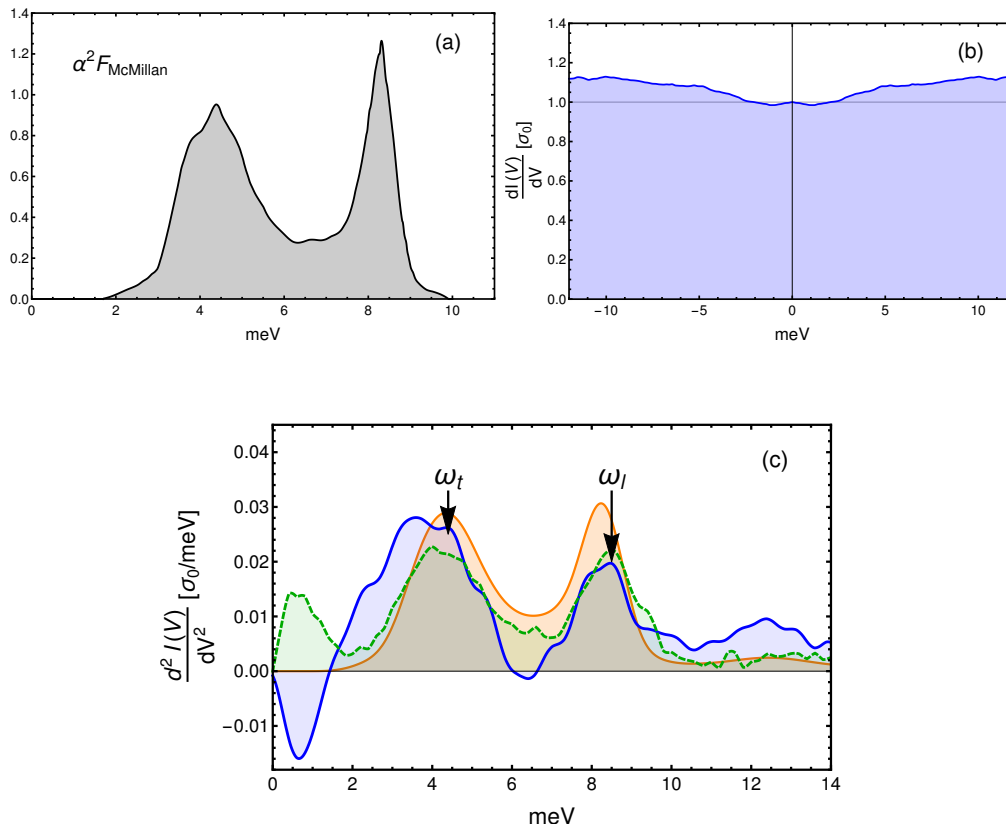


Figure 4.9.: Normal state STM on thin Pb films: (a) Eliashberg function determined via tunneling inversion from Ref. [11], (b) Conductance $\sigma(V)$ for Pb STM in normal state at $T = 0.8\text{K}$ [24], (c) IETS spectrum from: (blue) 30 monolayer Pb thin film from Ref. [24], (green) 13 monolayer Pb thin film from Ref. [19], (orange) theoretical d^2I/dV^2 curve including multiple-phonon excitations.

In the following paragraph, we will interpret the normal state IETS data in more detail. Let us first consider the one-phonon inelastic contributions in the normal state. The actual amplitude seen in the experiment can be used to determine the value of the typical off-shell energy states via the observed increase of the conductance due to inelastic processes⁸

$$\sigma(10\text{meV}) - \sigma(0\text{meV}) \stackrel{(4.16)}{=} \frac{\sigma_0}{E_{\text{off}}^2 \nu_F} \int_0^{10\text{meV}} d\omega \alpha^2 F_{\text{tun}}(\omega) \approx 0.12\sigma_0. \quad (4.19)$$

When approximating the tunnel spectrum by the Eliashberg function $\alpha^2 F_{\text{tun}} \approx \alpha^2 F$, see

⁸We can use the zero temperature limit here as the typical phonon frequencies are much higher than the experimental temperature $T = 0.8\text{K}$. In the end, we will include the experimental broadening by convoluting the spectrum with a Gaussian distribution of $\text{FWHM} = 5.4T$ as described in Section 3.3.

also the discussion in Section 4.1.2, this yields

$$E_{\text{off}} \approx \sqrt{\frac{\int_0^{10\text{meV}} d\omega \alpha^2 F(\omega)}{0.12\nu_F}} = 313\text{meV}, \quad (4.20)$$

where we used the Eliashberg function for Pb from Ref. [11] and the Pb DOS $\nu_F \approx 0.3/\text{eV}$ determined from de Haas-van Alphen [131] and specific heat measurements [141]. This is a reasonable value, as averaging over all inverse energies from the low-energy cutoff $\omega_c \approx 10\omega_D \approx 100\text{meV}$ up to $E_F \approx 1\text{eV}$ agrees well with the above estimate from the experiment

$$\frac{1}{E_{\text{off}}} \approx \frac{1}{E_F - \omega_c} \int_{\omega_c}^{E_F} d\epsilon \frac{1}{\epsilon} \approx \frac{1}{400\text{meV}}. \quad (4.21)$$

We can also use Eq. (4.19) to directly determine the prefactor $E_{\text{off}}^2 \nu_F = 29.5\text{meV}$. Let us now consider the two-phonon inelastic events that are included in the inelastic transfer Hamiltonian derived in Section 3.1. It is straightforward to write down the corresponding tunneling current and conductance in the zero temperature limit for the STM setup similar to Eq. (3.34)

$$\begin{aligned} I^{i,(2)}(V) &= \frac{\sigma_0}{e} \left(\frac{1}{E_{\text{off}}^2 \nu_F^s} \right)^2 \int_{-\infty}^{\infty} d\epsilon d\omega d\omega' \alpha^2 F_{\text{tun}}(\omega) \alpha^2 F_{\text{tun}}(\omega') \tilde{\nu}_s(\epsilon) \\ &\quad \left[n_F(\epsilon + \omega + \omega' - eV) [1 - n_F(\epsilon)] - n_F(\epsilon) [1 - n_F(\epsilon - \omega - \omega' - eV)] \right], \\ \sigma^{i,(2)}(V) &= \sigma_0 \left(\frac{1}{E_{\text{off}}^2 \nu_F^s} \right)^2 \int_{-\infty}^{\infty} d\epsilon \nu_s(\epsilon) \alpha^4 F_{\text{tun}}^2(\epsilon + e|V|), \end{aligned} \quad (4.22)$$

where we assumed particle-hole symmetry and defined the convolution of two tunneling spectra as

$$\alpha^4 F_{\text{tun}}^2(x) = \int_{-\infty}^{\infty} dy \alpha^2 F_{\text{tun}}(x - y) \alpha^2 F_{\text{tun}}(y). \quad (4.23)$$

Note the striking similarity between the relation for one- and two-phonon inelastic tunneling in Eqs. (4.16) and (4.22). Generalizing these expressions we can write down the IETS spectrum including multiple-phonon inelastic processes

$$\frac{d^2 I^i}{dV^2} = \text{sign}(V) \cdot \frac{\sigma_0}{e} \left[\frac{\alpha^2 F_{\text{tun}}(e|V|)}{E_{\text{off}}^2 \nu_F^s} + \frac{\alpha^4 F_{\text{tun}}^2(e|V|)}{(E_{\text{off}}^2 \nu_F^s)^2} + \frac{\alpha^6 F_{\text{tun}}^3(e|V|)}{(E_{\text{off}}^2 \nu_F^s)^3} + \dots \right] \quad (4.24)$$

where $\alpha^{2n} F_{\text{tun}}^n$ is the convolution over n bosonic tunneling spectra similar to (4.23). The total contribution of the n -th order for the IETS spectrum can be calculated by integrating

$$\int d(eV) \frac{\alpha^{2n} F_{\text{tun}}^n(e|V|)}{(E_{\text{off}}^2 \nu_F^s)^n} = \left(\frac{\int_{-\infty}^{\infty} d\omega \alpha^2 F(\omega)}{E_{\text{off}}^2 \nu_F^s} \right)^n \stackrel{(4.19)}{=} (0.12)^n \quad (4.25)$$

Therefore, each $n + 1$ -phonon tunneling process is roughly suppressed by n orders of magnitude compared to the leading one-phonon tunneling process⁹. In Figure 4.9 we compare the measured $d^2 I(V)/dV^2$ with the theoretical spectrum (orange curve) of Eq. (4.24). Shown in

⁹This smallness of higher-order inelastic processes serves retrospectively as a justification for the use of the leading order when normalizing the spectra in (4.19), as two-phonon processes can already take place at voltages $eV = 2\omega_t \approx 8$ smaller than the Debye frequency.

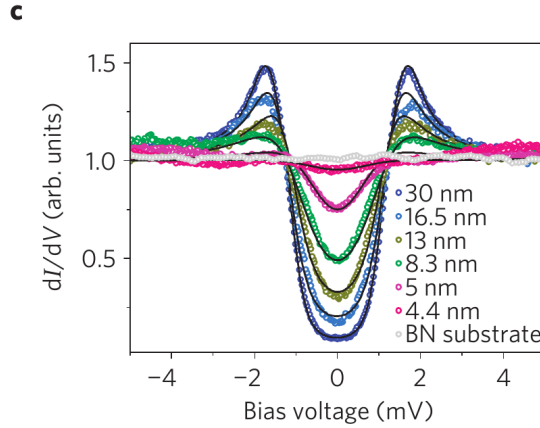


Figure 4.10.: Evolution of coherence peaks for thin Pb films: STM tunneling data for the investigation of the coherence peak on Pb nanoparticles of different heights, taken from Ref. [142].

blue (30 monolayers) are the normal state IETS data from Ref. [24] and in green the older data (13 monolayers) from Ref. [19]. Both spectra show similar features¹⁰ with the typical phonon peaks at ω_t/γ_1 of the theoretical curve. However, the 13 monolayer data shows a better agreement with the model of Eq. (4.24), especially the amplitude of the two-phonon process at $\omega_t + \omega_1$. Nevertheless, the similarities between the Eliashberg function and the IETS spectrum are apparent for both experiments, supporting the inelastic tunneling formalism presented in Chapter 3.

4.3.2. Superconducting state

When turning off the magnetic field, the Pb sample is superconducting. The diameter ($\approx 400\text{nm}$) of the Pb island is far greater than the bulk coherence length ($\xi_0 = 83\text{nm}$) of Pb [143], but the thickness of the Pb films is only about 30 monolayer $\approx 10\text{nm}$, which is significantly smaller than the latter. Therefore, the gap cannot fully develop and the spectral weight of the coherence peaks is reduced, see Figure 4.10. This issue has been intensively investigated in Refs [127, 134, 135, 142, 144, 145].

In Figure 4.12(a) the measured conductance in the superconducting state is plotted together with a Dynes-fit [146]

$$\nu_{\text{Dynes}}(\omega) = \text{Re} \left[\frac{\omega + i\Gamma}{\sqrt{(\omega + i\Gamma)^2 - \Delta^2}} \right], \quad (4.26)$$

that yields the parameters $\Gamma = 0.61\text{meV}$ for the quasiparticle broadening and $\Delta = 1.05$ for the gap value¹¹. This is significantly smaller than the bulk value $\Delta = 1.36\text{meV}$ [143]. In contrast, the maximum of the coherence peaks is at $\approx 1.65\text{meV}$. The confinement of

¹⁰Note that the STM spectra seen on the same Pb films already show some variation when moving the STM tip. This may come due to local impurities or vacancies, that can also be located below the surface and may therefore not be visible directly in the STM topography image. Also, comparing STM data from different experiments can be difficult, because usually the tip geometry and therefore the tunneling matrix element may be totally different enhancing the contributions of certain areas of the Brillouin zone of the superconductor.

¹¹For the Dynes-fit we only used the region around the superconducting coherence peak, because for higher biases inelastic tunneling occurs and the Dynes model is based on the purely elastic picture. We also do

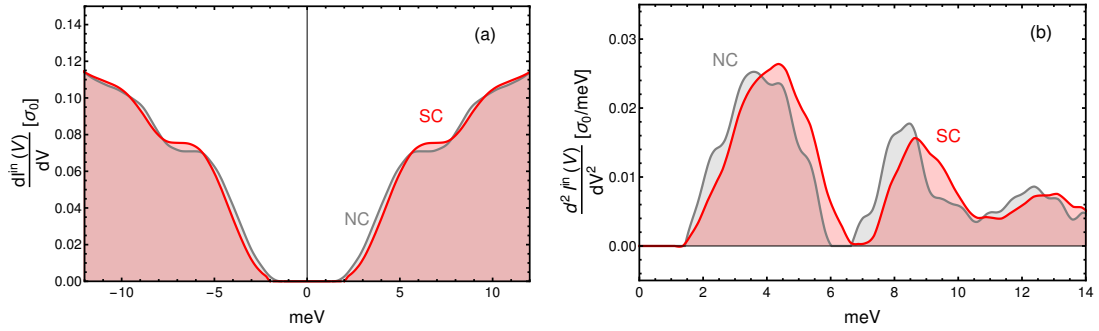


Figure 4.11.: Inelastic Pb spectra calculated for the superconducting state. Inelastic conductance (a) and its derivative (b) for the normal (gray) and superconducting state (red) using the normal state phononic tunneling spectrum and a Dynes-fit for the electron DOS.

the electrons in the z -direction and our energy resolution make it impossible to resolve the two-gap feature reported in Ref. [149]. The observed shape in the gap and coherence peak region of the conductance is in good agreement with other experiments [127, 134, 135, 144] on Pb thin films. However, when looking at energies comparable to $\Delta + \omega_t \approx 5.5\text{meV}$ a clear increase of conductance takes place because now inelastic tunneling via the emission of a transversal phonon is allowed. Exactly such features have also been seen in tunneling experiments on Niobium [129]. Obviously, such a behavior cannot be described by the purely elastic theory and we have to include inelastic tunneling processes to understand the experimental data.

In the following, we will present a quantitative analysis of the superconducting tunneling spectra using our extended tunneling formalism. For calculating the inelastic contributions in the superconducting state, we will use Eq. (4.16) and the following electronic and bosonic spectrum:

- The electronic spectrum $\nu(\omega)$ will be modeled by the Dynes-fit given in Eq. (4.26). Strong-coupling features on top of this broadened BSC DOS can be safely neglected, as they are suppressed due to the finite film size and furthermore give no significant contributions to the calculated d^2I/dV^2 spectrum as was discussed in Section 4.2.1.
- The phonon tunneling spectrum $\alpha^2 F_{\text{tun}}(\omega)$ is chosen as the bosonic tunneling spectrum $d^2I/dV^2 \sim \alpha^2 F_{\text{tun}}(eV)$ from the normal state measurements. However, we will cut-off the negative contributions of the zero-bias anomaly as this feature cannot arise from inelastic tunneling. We emphasize that the use of the measured phonon spectrum naturally includes higher-order inelastic processes described by Eq. (4.24) for the calculated superconducting tunneling spectra. Further, we should not broaden the calculated inelastic curves as such a broadening is already included using the measured bosonic spectrum [24].

In Figure 4.11 the calculated inelastic conductance and its derivative are plotted together with the curves in the normal state. In a fully gapped superconductor with gap Δ , inelastic tunneling processes can only occur for biases $eV > \Delta + \omega_{\text{ph}}$, however for the thin film

not wish to discuss extensively the question about the validity of the Dynes formula in this work [147]. As pointed out by Ref. [148] the strong superconducting fluctuations around the mean-field gap in superconducting thin films can often be conveniently modeled via the proposed Dynes-fit.

there is a significant electronic spectral weight below the coherence peak as can be seen in Figure 4.12(a). Therefore, the sharp IETS spectrum calculated in the previous Section 4.2 will be less pronounced in the experiment here. The inelastic conductance $dI^i(V)/dV$ shows a clear valley-like structure similar to the normal state curve, but slightly shifted to higher biases. The same is also visible in the $d^2I^i(V)/dV^2$ curve¹², which bears a clear resemblance to the bosonic tunneling spectrum of the normal state shifted to some higher energies. This originates from shifted electronic spectral weight from the gap region to higher energies when entering the superconducting state as becomes apparent from the Dynes-fitted electron DOS, see Figure 4.12(a).

The calculated inelastic curves can now be used to divide the experimental spectra in the superconducting state into elastic and inelastic contributions. In Figure 4.12(b) we plot the pure elastic conductance $\sigma^e(V) = \sigma(V) - \sigma^i(V)$ by subtracting the inelastic contribution shown in Figure 4.11(a) from the measured *total* conductance. Suddenly, clear strong-coupling features become visible with inflection points at the positions $\Delta + \omega_{t/1}$, with the gap $\Delta = 1.05\text{meV}$ determined in the Dynes-fit. In Figure 4.12(b) we also plotted a strong-coupling Dynes-fit, which we define in the following way

$$\nu_{\text{Dynes}}^{\text{strong-coupling}}(\omega) = \text{Re} \left[\frac{\omega + i\Gamma}{\sqrt{(\omega + i\Gamma)^2 - [\beta\Delta(\omega)]^2}} \right], \quad (4.27)$$

with the gap function $\Delta(\omega)$ calculated from the self-consistent solution of the Eliashberg equation with the known Eliashberg function and pseudopotential for Pb from Ref. [11]. We choose $\beta = 0.79$ which yields a gap value of $\Delta = 1.05$ and $\Gamma = 0.61$ as used in the conventional Dynes-fit (4.26). This phenomenological strong-coupling DOS displays the same peak-dip features as the measured elastic conductance¹³, in the experiment however there is an additional suppression of electronic spectral weight above the coherence peak which is shifted into the gap region.

Let us now compare the measured second derivative of the current, which is shown as the red curve in Figure 4.12(c), with the calculated total spectrum shown in black. For the elastic contributions we are using the strong-coupling Dynes-fit and for the inelastic contributions the spectra shown in Figure 4.11. Both the experimental and the theoretical IETS curve show two clear symmetric peak-dip features around the zero-axis at $eV \approx \Delta + \omega_{t/1}$, which is exactly what we found for the single phonon mode of Section 4.2. This is not surprising since for the single phonon model we used parameters that were chosen to be similar to Pb. The agreement between the experiment and theory is good, especially the positions of the peak and dip positions are captured well and only the magnitude is reduced, probably due to the decoherence physics of the thin film confinement. Similar to the conductance we can also calculate the pure elastic $d^2I^e(V)/dV^2$ curve by subtracting the inelastic contributions from the experimental data, which is shown as the red curve in Figure 4.12(d). The elastic second derivative shows two clear dip features at $\Delta + \omega_{t/1}$ as expected from Eliashberg-theory, see e.g. Figure 4.3(f). For comparison, we also plotted in black the bulk

¹²Here, we applied a small Gaussian filter to the inelastic curve in the superconducting state to get rid of the mechanical oscillations of the experimental phonon tunneling spectrum in the normal state.

¹³Note that the strong-coupling features are shifted to slightly higher energies since the Eliashberg solution of $\Delta(\omega)$ was solved using the original bulk gap value $\Delta_0 = 1.37\text{meV}$. However, there is no clear theory how to describe the electronic spectrum of a superconductor for films much thinner than the coherence length and we will use our strong-coupling Dynes-fit in the following for the electron DOS. Actually, an STM experiment with bulk Pb would be preferable for more quantitative interpretation of the elastic and inelastic contributions.

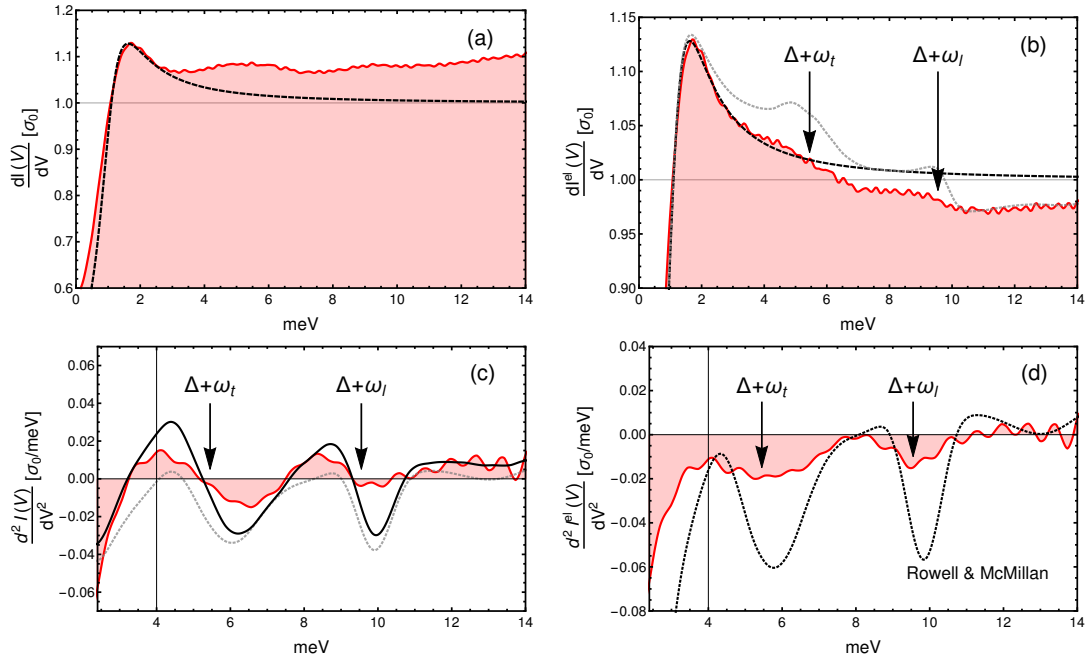


Figure 4.12.: STM on thin Pb films in the superconducting state: (a) Shown are the measured conductance (red) and a Dynes fit (black) with the parameter $\Gamma = 0.61\text{meV}$ and $\Delta = 1.05\text{meV}$, (b) Pure elastic conductance (red), that is proportional to the electron DOS, obtained by subtracting the calculated inelastic conductance from the experimental data $\sigma^e(V) = \sigma^{\text{exp}}(V) - \sigma^i(V)$. Comparison with BCS Dynes fit (black) and strong-coupling Dynes-fit (gray) using the Eliashberg function by Rowell and McMillan [11] shows strong-coupling features at characteristic energies $\Delta + \omega_{t/l}$ with gap value of Dynes-fit $\Delta = 1.05\text{meV}$, (c) $d^2I(V)/dV^2$ from experiment (red) compared to calculated spectrum (black) using the strong-coupling Dynes-fit for the electronic spectrum (gray), (d) Purely elastic IETS spectrum calculated by subtracting the inelastic contribution from the measured $d^2I(V)/dV^2$. Shown in black is the curve for a bulk Pb electron DOS using the parameters of Rowell and McMillan [11].

Pb DOS calculated using the Eliashberg function determined by Rowell and McMillan [11], which shows a larger superconducting gap as was already discussed earlier.

In summary, we demonstrated that one can only understand Pb thin film STM data in both the normal- and superconducting state by considering the possibility of both elastic and inelastic tunneling paths as described by the tunneling theory presented in Chapter 3. The normal state $d^2I(V)/dV^2$ spectrum is indeed proportional to the bosonic tunneling spectrum $\alpha^2F_{\text{tun}}(\omega)$ that is very similar to the Eliashberg function determined in earlier tunneling experiments [11, 15]. Thus, IETS in the normal state can serve as a complementary tool for the determination of the phononic pairing glue in conventional superconductors¹⁴. In the superconducting state there is a clear deviation from the conventional elastic picture that the conductance is proportional to the superconducting DOS $\sigma(V) \sim \nu(eV)$ as inelastic contributions lead to an increase of the conductance when $eV \approx \Delta + \omega_{\text{ph}}$. When including those inelastic contributions we can understand the observed spectra and are even able to separate elastic and inelastic contributions to get access to the pure elastic conductance

¹⁴At this point, we also wish to refer to the great work of Ref. [150], which gives another alternative for detecting the Eliashberg function. The authors could resolve the dispersion in the normal state and thereby got direct access to the real part of the self-energy $\text{Re}\Sigma^R(\omega)$, which was then used to determine $\alpha^2F(\omega)$.

and thereby the electronic spectrum. Therefore, the neglect of inelastic processes in the interpretation of STM data is in general not justified and one has to carefully subtract the inelastic spectrum before analyzing the tunnel conductance via the Rowell-McMillan inversion algorithm¹⁵.

The experience gained from the STM experiment into the conventional superconductor Pb can now be used to reinterpret tunneling data of unconventional superconductors to gain insights into the pairing mechanisms in the cuprate and iron-based systems, which will be discussed in the following Chapter 5.

¹⁵see Section 1.1.2

5. Tunneling in unconventional superconductors

In this chapter the extended tunneling formalism combining elastic and inelastic transitions that was developed in Chapter 3 is applied to the cuprate and iron-based superconductors. In contrast to tunneling into conventional superconductors, where the Cooper-pairs binding is supported by phonons that are only slightly affected by the occurrence of superconductivity, the electronic pairing glue in high- T_c superconductors is changed significantly and obtains a spin gap below T_c . We demonstrate that this leads to a drastic change in the inelastic tunneling spectrum when entering the superconducting state and show that we can explain the experimental tunneling spectra of various unconventional superconductors. Explicitly we show that the extended tunneling formalism developed in the previous chapters can be used to understand the tunneling conductances of YBCO and LiFeAs naturally by the coupling to collective spin fluctuations. The majority of this Chapter is based on Ref. [25].

5.1. Nature of the background conductance in the normal state

In Section 1.3.2 a short review about the variety of tunneling spectra into the cuprate and iron pnictide superconductors has been given. A feature constantly reappearing is a pronounced V-shaped background conductance in the normal state leading to a minimum in the $dI(V)/dV$ curve at zero bias, see Figs. 1.8 and 1.10. Such background conductances have been observed also in the normal state for tunneling spectra of various superconductors, see Figure 5.1, and have been proposed to originate from inelastic tunneling processes [125, 151, 152].

When following the conventional elastic tunneling theory such a symmetric increase around $V = 0$ in the tunneling spectra would correspond to a minimum in the electronic DOS at the Fermi energy, which is not expected in most of these systems, especially not in the “one-band” cuprate systems. In case of the iron pnictide materials [153–155], the superposition of the hole and electron bands (with band-edges close to the Fermi energy) can in principle lead to a local minimum, but even then fine-tuning is needed to fix the position of this minimum to the Fermi edge. The reduction of electron spectral weight at the Fermi surface above T_c could also originate from additional gaps, e.g. from charge or spin order. Indeed, for the cuprate superconductors there is more and more evidence that spin and/or charge order occurs in the pseudogap region above T_c of the phase diagram [156–162]. For BSCCO [128, 163] a clear evolution of the superconducting gap to a pseudogap that persists up to the pseudogap temperature T^* seen in ARPES [69, 164–166] has been

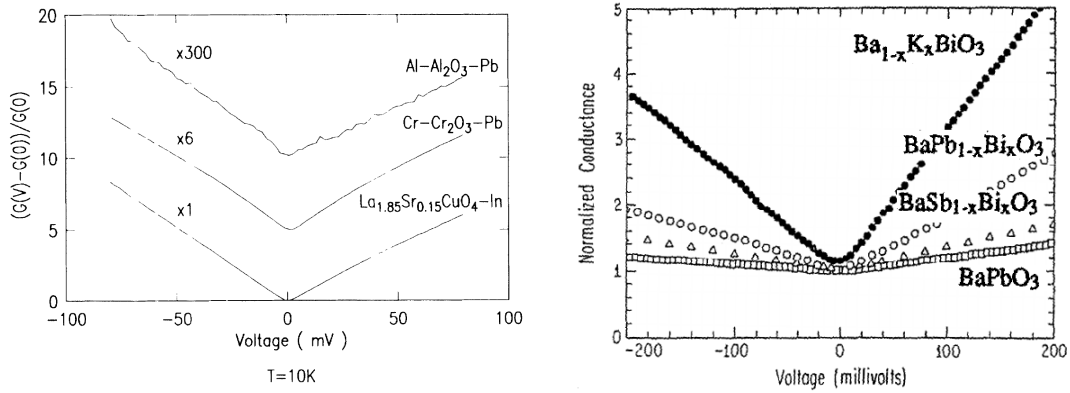


Figure 5.1.: Background conductance in the normal state for a variety of systems taken from Ref. [73, 125].

observed, supporting the picture that the pseudogap comes from preformed Cooper pairs. Also in Ref. [167, 168] clear gap-features have been seen in tunneling data above T_c at similar energies on different sheets of BSCCO. Besides the ARPES experiments also optical conductivity measurements [169–171] indicate that the amplitude of the pseudogap, i.e. the region where the depletion of electronic states occurs, is of the order of the superconducting gap. If however the quasilinear background conductance persists far above the superconducting coherence peaks, as shown for the spectra in Figure 1.8, originated from pseudogap physics, the corresponding pseudogap would have to be much bigger than the superconducting gap. Therefore, we believe that the pseudogap is not responsible for the linear background conductance seen in the unconventional superconductors. Another proposed origin is the marginal Fermi liquid state of cuprate superconductors [172], however to explain the linear conductance one has to assume a special tunnel matrix element that serves as a band-filter for high-energy states.

Here, we instead want to propose that the background conductance in high- T_c superconductors emerges from inelastic tunneling processes involving collective spin fluctuations as pointed out in Refs. [25, 125]. Similar to the tunneling analysis in Pb of the previous Chapter 4, we show that the inclusion of inelastic processes is not only necessary for the theoretical interpretation of tunneling data, but it also allows for a direct investigation of the collective bosonic degrees of freedom beyond the indirect strong-coupling signatures in the electronic spectrum. As pointed out first by Kirtley and Scalapino [125] the coupling to an overdamped particle-hole spectrum, i.e. spin fluctuations, leads to a V-shaped inelastic conductance in the normal state. This can be seen easily by assuming a Ornstein-Zernike form centered around the AFV \mathbf{Q} with Landau-damping due to the coupling to ungapped quasiparticles at the Fermi surface [109, 111] for the spin susceptibility

$$\chi^R(\mathbf{q}, \omega) = \frac{\xi^2 \chi_0}{1 + \xi^2(\mathbf{q} - \mathbf{Q})^2 - i\omega/\omega_{sf}}. \quad (5.1)$$

Here ω_{sf} is the typical energy scale¹ and ξ the correlation length of the overdamped spin fluctuations as introduced in the spin-fermion model, see also Section 2.3.1 and Figure 5.2(a). When integrating over the whole two-dimensional Brillouin zone of the

¹which is in general temperature dependent

layered superconducting plane, the bosonic tunneling spectrum is given by

$$g^2 \chi_{\text{tun}}(\omega) = \nu_F \sum_{\mathbf{q}} |g|^2 \frac{\text{Im} \chi^R(\mathbf{q}, \omega)}{-\pi} = \frac{\nu_F |g|^2 \chi_0}{2\pi} \arctan(\omega/\omega_{\text{sf}}), \quad (5.2)$$

which is a linear spectrum for low energies $\omega \ll \omega_{\text{sf}}$ and saturates for higher energies

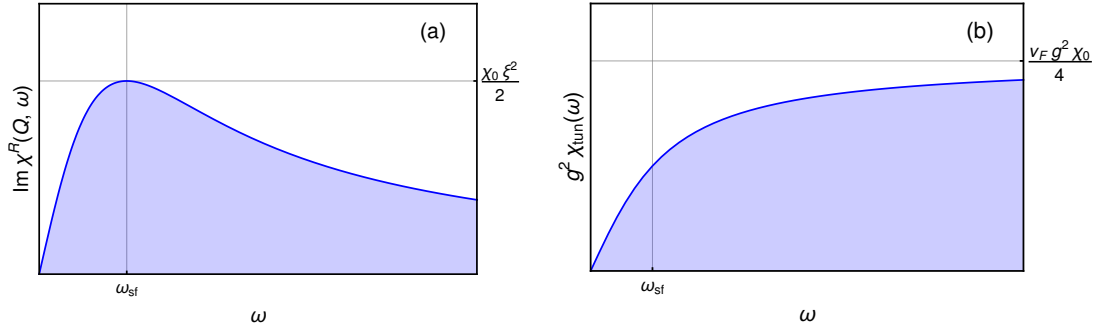


Figure 5.2.: Normal state spin spectrum in unconventional superconductors: (a) Spin spectrum at the antiferromagnetic wave vector \mathbf{Q} , (b) Bosonic tunneling spectrum given by the momentum summation of the spin fluctuation spectrum weighted by the electron-spin coupling g .

to a constant value, see Figure 5.2(b). At $T = 0$ and in the normal state the inelastic conductance is just given by the integral over the bosonic tunneling spectrum $g^2 \chi_{\text{tun}}$, see Eq. (3.37), yielding

$$\begin{aligned} \frac{dI^i(V)}{dV} &\sim \int_0^{eV} d\omega g^2 \chi_{\text{tun}}(\omega) \sim \frac{eV}{\omega_{\text{sf}}} \arctan(eV/\omega_{\text{sf}}) - \frac{\ln[1 + (eV/\omega_{\text{sf}})^2]}{2} \\ &\sim \begin{cases} (eV)^2 & \text{for } eV \ll \omega_{\text{sf}} \\ eV & \text{for } eV \gg \omega_{\text{sf}} \end{cases}. \end{aligned} \quad (5.3)$$

For energies smaller than ω_{sf} we have a parabolic conductance which evolves into a linear background conductance for $\omega \gg \omega_{\text{sf}}$ coming from the emission of spin fluctuations in the tunneling process. Thus, the so-called V-shaped background conductance is actually an U-shape for small energies. When increasing the temperature also the absorption of bosons is allowed² leading to an increase of inelastic tunneling for all energies, especially also for zero bias. This can be seen in the right picture of Figure 5.3. Such a model has successfully been used to fit tunneling data³ of optimally doped LSCO ($\text{La}_{1.85}\text{Sr}_{0.15}\text{CuO}_4$)-In junctions [125] quantitatively, see Figure 5.3. The slight tilting of the experimental spectra can be easily modeled by assuming a non-constant DOS, see the later discussion in Section 5.3.1. Hence, inelastic tunneling gives a natural explanation for the background conductance in these systems, since strong spin-fluctuations are known to be present in most of the unconventional superconductors [173–178]. Furthermore, it has been shown that in the unconventional bismuth-oxide superconductors the slope of the background conductance and therefore the electron-boson coupling g increases with the transition temperature T_c [179], which is a strong argument for an electronic pairing by spin fluctuations in these systems. Depending

²Note that in the normal state the overdamped spectrum has no gap and therefore allows for low-energy excitations.

³Note that the presented data shows no sign of superconductivity, probably because of a non-superconducting surface layer. However, using transport measurements bulk superconductivity up to $T_c = 36\text{K}$ has been observed in the sample.

on the actual system the amplitude of inelastic tunneling can further be very different, e.g. due to tunneling matrix elements selecting certain bands or from isolating barriers/surface impurities with high-energy excitations that can serve as virtual intermediate states for the tunneling process.

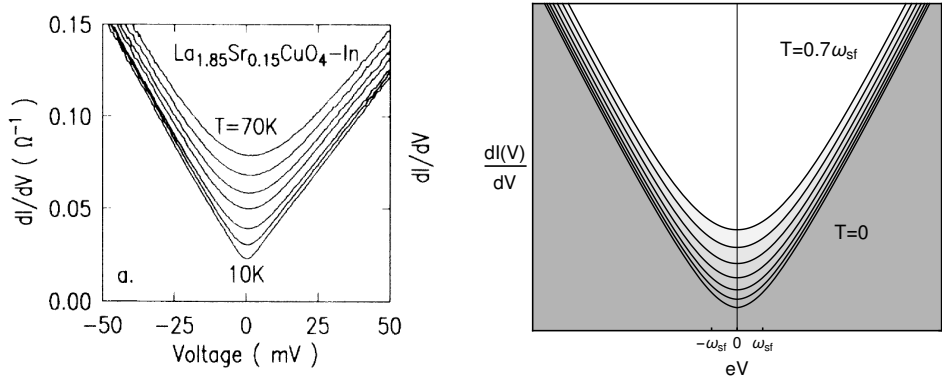


Figure 5.3.: Comparison of experimental and theoretical background conductance: (left) Experimental data for $\text{La}_{1.85}\text{Sr}_{0.15}\text{CuO}_4\text{-In}$ junctions taken from Ref. [125] for various temperatures ($T_c = 36\text{K}$) on a nonsuperconducting surface layer, (right) Theoretical conductance with strong inelastic background calculated from the overdamped spin spectrum in Eq. (5.2).

5.2. Tunneling spectra in the spin-fermion model

So far, we considered the effect of inelastic tunneling via overdamped spin fluctuations in the normal state [125]. In the following section, we will consider the effect of the combination of elastic and inelastic processes for tunneling spectroscopy in the superconducting state of unconventional superconductors based on the description of the spin-fermion model⁴ and compare it to the normal state tunneling spectra based on Ref. [25].

5.2.1. Inelastic tunneling as the origin of the peak-dip-hump feature in unconventional superconductors

As discussed in Section 2.3.1, a spin gap evolves for the originally overdamped spin fluctuations below the superconducting transition temperature $T < T_c$ since the electronic quasiparticles are gapped and we therefore need a finite energy to create a particle-hole excitation. This is in contrast to conventional superconductors, where the phonon modes are only slightly renormalized when entering the superconducting state [180]. Thus, for an electronic pairing glue like spin fluctuations it is essential to solve the Eliashberg equations for the electrons and bosons self-consistently, e.g. using the coupled integral Eqs. (2.39). As was pointed out in Section 2.3.1, a spin resonance develops below T_c at energies $\omega_{\text{res}} < 2\Delta$ at the AFV Q for a sign-changing superconducting gap, see red curve in Figure 5.4(b). The coupling of this resonance mode to the electrons gives rise to moderate strong-coupling features at $\Delta + \omega_{\text{res}}$ in the electronic DOS shown in red in Figure 5.4(a). The total integrated bosonic tunnel spectrum $g^2\chi_{\text{tun}}(\omega)$ in the superconducting state is presented in Figure 5.4(c) and deviates strongly from the spectrum in the normal state. In general, the characteristic energy scale ω_{sf} of the antiferromagnetic fluctuations is temperature

⁴see Section 2.3.1

dependent and thus the integrated spectra will differ from the ones calculated here, where it holds that the integrated susceptibility $\int d\omega d^2q \mathbf{Im} \chi^R(\mathbf{q}, \omega)$ is the same for the considered energy range $\omega = [0, 5\Delta]$ in the normal- and superconducting state. However, the important feature that is captured well by our spin spectrum is that spin spectral weight is shifted from low energies $\omega < \omega_{\text{res}}$ towards higher energies leading to a spin gap $\Delta_s = \omega_{\text{res}}$ as has been seen in neutron scattering experiments [59, 60, 181–184]. Note that the presented hot-spot theory is not capable of describing the linear behavior of the electronic DOS in the gap region for nodal superconductors like the cuprates, however in this section we will focus on tunneling features above the superconducting coherence peak or on fully gapped systems like some iron-pnictide compounds.

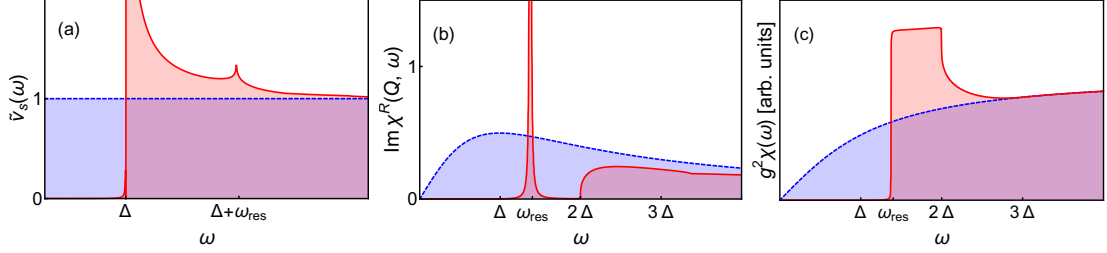


Figure 5.4.: Calculated spectra for the spin-fermion model in the normal (blue) and superconducting state (red): (a) Electronic density of states, (b) Spin spectrum $\mathbf{Im} \chi_{\mathbf{Q}}^R(\omega)$ at the antiferromagnetic ordering vector \mathbf{Q} with the resonance mode occurring at ω_{res} below T_c , (c) spin spectrum $g^2 \chi$ integrated over the 2-dimensional Brillouin zone.

In the following analysis, we have chosen our input parameter λ and ω_{sf} of the theory in such a way that the observed gap amplitude⁵ Δ and spin spectrum including the spin resonance at ω_{res} agrees well with the experimental observations $\omega_{\text{sf}} \simeq \Delta$ [59, 181, 183] and $\omega_{\text{res}}/2\Delta \approx 0.7$ [62]. The calculated spectra presented in Figure 5.4 are now used to calculate the elastic and inelastic conductance using Eqs. (3.34), where we choose $T = 0.1\Delta$ for the superconducting and $T = 0.5\Delta$ for the normal state spectra. The corresponding tunneling spectra are shown in Figure 5.5.

Let us start with the **elastic** conductance in Figure 5.5(a): In the normal state the elastic conductance $\sigma^e(V) = \sigma_0$ is just constant as we assume a constant electron DOS. The elastic conductance in the superconducting state reflects the BCS DOS including the strong-coupling features at $\Delta + \omega_{\text{res}}$, which is thermally smeared due to the small but finite temperature. Note that the strong-coupling features do *not* display a pronounced dip, but a rather moderate peak-dip feature. The reason for the weakness of the strong-coupling features is that the contribution of the resonance mode to the actual pairing glue is in general small [101, 185], i.e. small compared to the overdamped spin fluctuations at higher energies $\omega > 2\Delta$. Also, the resonance mode itself cannot be the origin of the high T_c since it only develops deep inside the superconducting state $T \ll T_c$ and is therefore not present when the superconducting transition occurs.

The **inelastic** conductance $\sigma^i(V)$ is shown in Figure 5.5(b). In the normal state it is the same as the spectra presented in the previous Section 5.1, meaning that a pronounced V-shape with parabolic behavior at low biases $eV < \omega_{\text{sf}}$ appears on top of the constant elastic conductance. We emphasize that the inelastic conductance shows no interesting fine-structure due to the overdamped nature of the normal-state spin fluctuations and is

⁵Here, $\Delta = |\Delta_{\mathbf{k}_h}|$ is the gap magnitude at the hot-spots of the Fermi surface.

finite at zero bias because of to the finite temperature $T = 0.5\Delta$. This has already been seen in the previous Section 5.1 and a proper normalization procedure has to be developed when comparing theory and experiment, which will be discussed in the following paragraph. In the superconducting state the inelastic conductance changes drastically: Due to the gap in both the electronic (superconducting gap Δ) and the bosonic spectrum (spin gap ω_{res}) the inelastic conductance vanishes up to $\Delta + \omega_{\text{res}}$, where it shows a sharp increase. However, it does not approach the normal state value due to the lower temperature assumed in the calculation. Importantly, the spin gap and the shift of spin spectral weight to higher energies that occurs below T_c can be directly seen by the suppression of inelastic tunneling contributions for the red curve of Figure 5.5(b) in the energy range from Δ to $\Delta + \omega_{\text{res}}$.

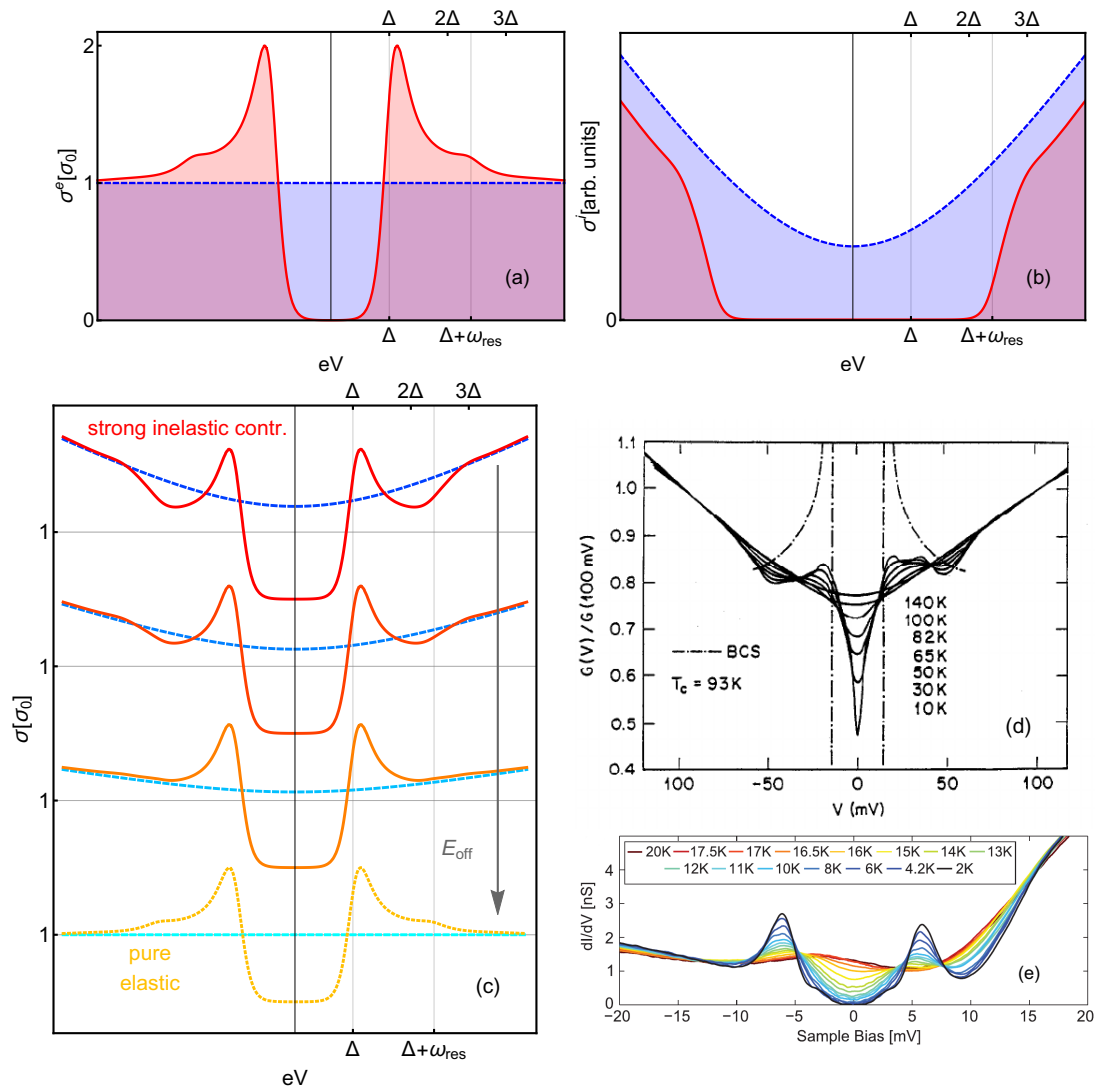


Figure 5.5.: Calculated conductance spectra for the spin-fermion model in the normal (cyan/blue) and superconducting state (yellow/orange/red): (a) Elastic conductance $\sigma^e(V)$ displaying the smeared electronic DOS, (b) Inelastic conductance $\sigma^i(V)$ showing a V-shaped background conductance for large biases eV and a suppression for $eV < \Delta + \omega_{\text{res}}$ below T_c , (c) Total conductance $\sigma(V) = \sigma^e(V) + \sigma^i(V)$ for different inelastic tunneling amplitudes (increasing cutoff energy E_{off} lowers inelastic contributions), (d) Tunneling spectrum for YBCO planar junctions normalized to the conductance at 100meV [73], (e) Conductance for STM on LiFeAs with normalization to $I(50\text{meV})$ [91].

Naturally, only the sum $\sigma(V) = \sigma^e(V) + \sigma^i(V)$ of the elastic and inelastic processes can be directly observed by tunneling experiments, which is shown in Figure 5.5(c) for different inelastic tunneling amplitudes. In contrast to the Pb experiments of Section 4.3, where the normal state could be accessed at the same low-temperature $T \ll \Delta, \omega_D$ via the application of an external magnetic field, the information about the normal state in unconventional superconductor tunneling is usually determined for high temperatures $T > T_c$, as the critical magnetic fields are generally very high. This poses a normalization issue for the STM experiments since the usual way of normalizing STM data for different temperatures is by adjusting the tip-sample distance such that the current-voltage curves $I(V)$ or the conductance curves $\sigma(V)$ coincide at high bias voltages. This way of fixing the tip-sample distance (and therefore the elastic tunneling amplitude t^e) is necessary, because the sample and tip materials thermally expand when increasing the temperature and thereby enhance the tunneling rate significantly (remember that the STM current typically increases by one order of magnitude when lowering the distance by only 1 Å). Interestingly, the same normalization procedure is usually applied to planar-junction experiments, where the thermal expansion of the barrier thickness is not expected to have a reasonable effect on the tunneling spectrum. Here, the most probable reason why the curves for different temperatures do not meet for high biases is the increase of inelastic contributions for higher energies as can clearly be seen in Figure 5.3. In what follows, we normalized the total conductances such that the current I at $eV = 10\Delta$ is the same in the normal and superconducting state similar to Ref. [91].

Let us now discuss the changes in the expected conductance when increasing the inelastic tunneling amplitude gt^e/E_{off} in Eq. (3.34). Without inelastic tunneling we just see a constant conductance $\sigma^e(V) = \sigma_0$ in the normal state and the electronic DOS with Eliashberg features at $\Delta + \omega_{\text{res}}$ in the superconducting state as shown in the yellow curve of Figure 5.5(c). When increasing the inelastic tunneling a pronounced V-shaped background conductance develops in the normal state and the Eliashberg features below T_c are washed out by the sharp increase of the inelastic conductance as seen in the second curve from below. For a strong inelastic contribution, see the upper two curves in Figure 5.5(c), the Eliashberg features from the elastic transitions are completely overshadowed by the strong increase in the inelastic conductance leading to an effective peak-dip-hump feature in the superconducting state. Interestingly, the superconducting curve has a significant dip **below** the normal state curve around $eV \approx 2\Delta$, which originates from the spin gap below T_c . We emphasize that the dip of the peak-dip-hump feature does not originate from Eliashberg-like strong-coupling physics, therefore not from a renormalization of electronic quasiparticles due to the coupling to virtual bosons, but from inelastic events via the emission⁶ of spin fluctuations. Exactly such peak-dip-hump characteristics have been seen in many unconventional superconductors showing a background conductance as was discussed in Section 1.3.2. In Figure 5.5(d) and (e) experimental tunneling conductances for YBCO planar junctions [73] and STM on LiFeAs [91] are shown in comparison to our calculated tunneling spectrum $\sigma(V)$ and striking similarities can be observed. In both experiments one can observe a general background conductance and also a clear dip below the the normal state above the coherence peak of the tunneling conductance in the superconducting state, leading to the peak-dip-hump feature discussed in the literature. We also note that as we normalized our tunneling spectra with the current-voltage $I(V)$ characteristics, the superconducting curve exceeds the normal state conductance for higher biases as was seen in the LiFeAs data, which used the same way of normalization for

⁶In the superconducting state, there are basically no excited spin fluctuations as $T \ll \omega_{\text{res}}$ and therefore absorption processes are suppressed.

their experiments. In contrast to the nodeless superconducting pairing state in LiFeAs, where we expect the hot-spot theory to work well, its validity to give quantitatively correct strong-coupling features for d -wave superconductors like the cuprates is questionable. Obviously, we cannot reproduce the linear gap-region in Figure 5.5(d) typical for nodal superconductors. Also, it was shown by Zasadinski [114, 115] that a peaked mode at ω_{res} can give rise to a single pronounced dip feature in the electron DOS at $\Delta + \omega_{\text{res}}$, see also the discussion in Section 2.3.2. Nevertheless, the d -wave physics is not capable of explaining the background conductance and the additional dip in the electron DOS would only lead to a more pronounced dip feature in Figure 5.5(c).

5.2.2. Normalized conductance

Of course, in many unconventional superconductors the electronic DOS in the normal state is already non-flat. Therefore, already the normal-state elastic spectra shows a clear deviation from a constant conductance $\sigma^e(V) \neq \sigma_0$ and is energy-dependent. We can include this in two ways: (i) We can use a non-flat normal-state DOS for the calculation of the tunneling spectra, which will be done in the following Section 5.3 for a more quantitative interpretation of the STM data in LiFeAs. (ii) We normalize our superconducting conductance by the one in the normal-state. In this paragraph, we will employ the second option and use the normalized conductance proposed in Refs. [91, 186]

$$\sigma_{\text{norm}}(V) = \frac{\sigma_{\text{sc}}(V)}{\sigma_{\text{nc}}(\sqrt{V^2 - \Delta^2/e^2})}, \quad (5.4)$$

which is very similar to the normalized conductance by Rowell and McMillan in Eq. (4.18) and reduces the effect of a non-flat electron DOS significantly.

The normalized conductance $\sigma_{\text{norm}}(V)$ and its derivative for the spin-fermion model are shown and compared to LiFeAs data from Ref. [91] in Figure 5.6. Our model and the experiment show an excellent agreement assuming strong inelastic tunneling. Let us start with the normalized conductance: Inside the gap region there are clear deviations between the two curves since LiFeAs is a multiband superconductor with three hole-like bands centered around the Γ -point and two electron-like bands centered around the M -point of the Brillouin zone [187–189], which show two distinct superconducting gaps. However, the dominant gap is the larger gap $\Delta := \Delta_1$ and we will neglect the second gap $\Delta_2 < \Delta_1$ in our ongoing analysis. Above the coherence peak at Δ the experimental and theoretical curves both show a clear dip visible around $eV \approx 2\Delta$ in σ_{norm} , followed by a strong increase with a small peak that saturates above 1 due to the normalization procedure explained above.

Also for the derivative $\sigma_{\text{norm}}(V)/dV$ of the normalized conductance, shown in the lower pictures of Figure 5.6, the experimental and theoretical spectra share the same features for $eV > \Delta$ when assuming a strong inelastic tunneling contribution. The most important fine-structure is the clear peak that occurs at energies between 2Δ and 3Δ in the experimental curve, which has been seen in many unconventional superconductors [74, 77, 91, 190]. Such a clear peak is only expected when the inelastic contributions dominate and occurs at $\Delta + \omega_{\text{res}}$ (red curve), while the pure elastic curve would have a dip at this position (yellow curve). Therefore, when the conductance shows a clear V-shaped background conductance and inelastic tunneling is important, the peak in $d\sigma_{\text{norm}}(V)/dV$ can be used to deduce a spin gap and therefore a possible resonance mode⁷ in the spin spectrum of

⁷In Ref. [77] even a second smaller peak was found at $eV \approx \Delta + 2\omega_{\text{res}}$ that probably originates from

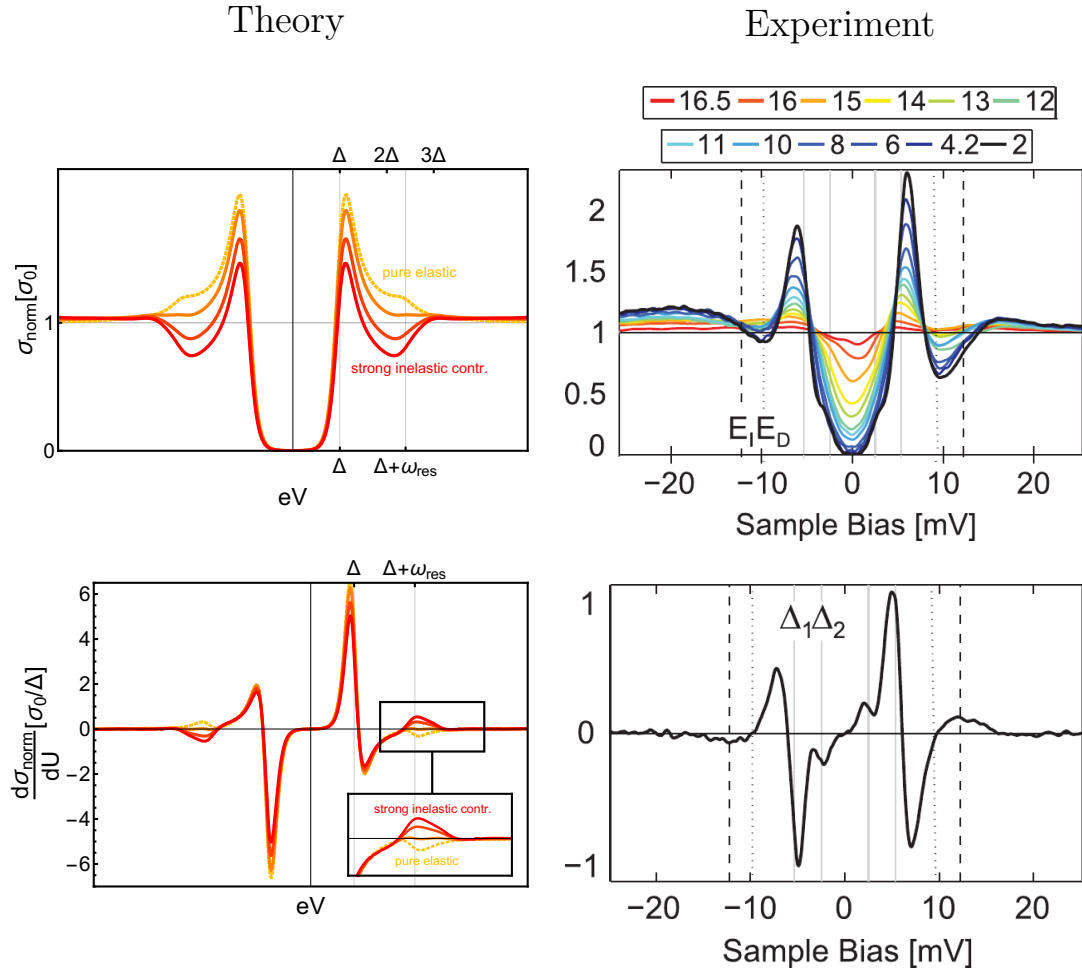


Figure 5.6.: Comparison of theoretical and experimental normalized tunneling conductances: Normalized conductance $\sigma_{\text{norm}}(V)$ and $d\sigma_{\text{norm}}(V)/dV$ calculated from the spin-fermion model (left) and comparison with normalized data from LiFeAs (right) adapted from Ref. [91].

unconventional superconductors. Let us remark at this point that this shift of spin spectral weight, which leads to the features explained above in the tunneling spectra, has been seen also in inelastic neutron scattering of LiFeAs [184, 191]. However, LiFeAs is a rather unique iron-pnictide because the stoichiometric parent compound is already superconducting and not magnetically ordered [192]. This poses the question if spin fluctuations are responsible for the moderate $T_c \sim 18\text{K}$ and what the underlying superconducting pairing state looks like. The excellent agreement of the tunneling data with the presented theory leads us to the conclusion that the spin fluctuations are the dominant interaction channel, which gives evidence for an electronic pairing with an unconventional s_{\pm} gap symmetry in LiFeAs. Further support for this picture comes from recent QPI studies [193] that could determine the real part of the self-energy that is consistent with the coupling to a collective spin mode at energy $\approx 6 - 7\text{meV}$.

Further, we conclude that the interpretation of earlier publications [77, 86, 91, 190], who used the peak in the second derivative to deduce the resonance energy in cuprate and iron-

two-boson inelastic tunneling that has been neglected here as it will not be of importance for the bias ranges discussed here.

based superconductors, is indeed correct. Also the d^2I/dV^2 curves of $\text{Na}(\text{Fe}_{0.975}\text{Co}_{0.025})\text{As}$ from Ref. [90] look very similar to the calculated curve in Figure 5.6 and a clear peak feature is seen around 2.3Δ , however the authors followed the conventional elastic picture and searched for a dip in the $d^2I(V)/dV^2$ spectrum. Since there is no dip present, they misinterpret the right tail of the peak feature as the dip and thereby overestimate the energy of the resonance mode. Obviously, the similarity of the presented tunneling spectra in the normal and superconducting state with many curves in the cuprate and iron-based superconductors showing background conductances is remarkable, which becomes apparent in the comparison of the theoretical predictions in Figure 5.5 with the experimental curves presented in Figs. 1.8 and 1.10. In the following, we will use the lessons learned from the calculation of the tunneling spectra in the spin-fermion model to improve the theoretical interpretation of tunneling data for selected high- T_c superconductors.

5.3. Revisiting tunnel experiments in unconventional superconductors

In this section, we will show for how to quantitatively interpret tunneling experiments in unconventional superconductors which show a pronounced background conductance using our extended tunneling formalism. We will explicitly revisit experiments performed on LiFeAs as well as YBCO and show that we can naturally reproduce the observed experimental conductances combining EETS and IETS.

5.3.1. LiFeAs : A particle-hole asymmetric superconductor

In Figure 5.5(e) the experimental tunneling data of Ref. [91] for STM on LiFeAs single crystals is shown. The spectrum is obviously not symmetric, calling for a non-constant normal-state electron DOS. Indeed, ARPES measurements [187–189] and Density Functional Theory (DFT) calculations [154, 194] indicate that the upper edge of a hole-band lies very close to the Fermi energy, giving rise to a clear energy-dependency for the electronic spectrum that breaks particle-hole symmetry on the energy scale of the superconducting order parameter. However, the normalized conductance and its derivative showed striking similarities to the tunneling spectra calculated using the rather simplistic spectra from the spin-fermion model. This gives us confidence that the main ingredients for understanding the tunneling spectra are the opening of a gap in the electronic **and** bosonic spectrum, which is well captured by the spin-fermion model. Details about actual electronic band structure and more realistic spin spectra can then be used to make a more quantitative fit to the experiments. In the case of LiFeAs , the spectrum shows a clear tilting and in the following we will show that this is consistent with a linear electronic DOS around the Fermi energy.

The typical tunneling spectrum for a linear electron spectrum (see Figure 5.7(a)) interacting with collective spin fluctuations is presented in Figure 5.7(c). The electronic spectrum in the superconducting state is modeled by a Dynes-fit with gap $\Delta = 5.5\text{meV}$ and quasiparticle broadening of $\Gamma = 0.25\text{meV}$ [91]. For the spin spectrum we use a form similar to the one of the spin-fermion model in Section 5.2, with overdamped fluctuations in the normal state and a gapped spectrum with spin gap $\omega_{\text{res}} = 1.3\Delta$ [62] in the superconducting state as shown in Figure 5.7(b). The total conductance below T_c shows the typical features seen in the previous Section 5.2 with a V-shaped background conductance and a clear dip below

the normal state curve around $eV = 2\Delta$, followed by a sharp increase around $\Delta + \omega_{\text{res}}$. This curve agrees well with the conductance spectra in the normal and superconducting state of LiFeAs shown in Figure 5.5(e), but the dip for negative biases is less pronounced in experiments. This has been seen also in other experiments on iron-based superconductors, see e.g. Figure 1.10, and cannot be captured by our model. The origin of this effect may lie in a bias dependence of the inelastic tunneling matrix element, which will be discussed later in Section 5.3.3. We also neglected possible strong-coupling features here, because for a fully gapped system like LiFeAs they are not expected to give rise to such a pronounced dip and there is no sign of the typical peak-dip features of Eliashberg theory.

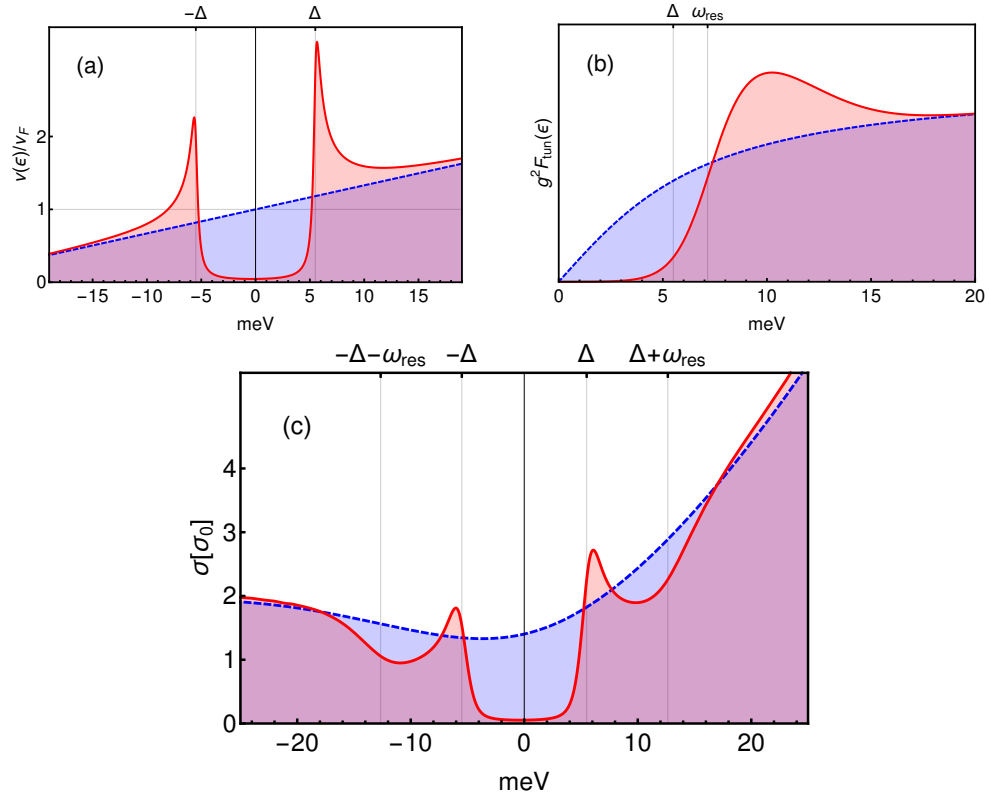


Figure 5.7.: Tunneling for broken particle-hole symmetry in the normal- (blue) and superconducting state (red):(a) Electronic spectrum with significant linear increase around the Fermi-surface, (b) Overdamped bosonic tunneling spectrum in the normal state and corresponding gapped spectrum below T_c , (c) Typical total tunneling spectrum including elastic and inelastic processes for unconventional superconductors with broken particle-hole symmetry.

5.3.2. YBCO

The tunneling data in YBCO already show an astonishing agreement with the calculated spectra from the spin-fermion model for the region outside the gap. This is particularly interesting because YBCO is established to be a d -wave superconductor and the features above the gap, especially the clear dip (see Figure 5.8(d) have been frequently interpreted as strong-coupling feature that arise from the coupling to virtual spin fluctuations similar to the strong-coupling features in conventional superconductors [9, 10, 15]. In Figure 5.8 we improved our model for YBCO by assuming a d -wave electronic DOS shown in Figure 5.8(a), which is substantially broadened similar to the experiments. Assuming a reasonable spin spectrum for the normal- and superconducting state [182], see Figure 5.8(b), we again find a

striking similarity of the tunneling conductance and the normalized tunneling conductance when comparing the calculated spectra with the experiment.

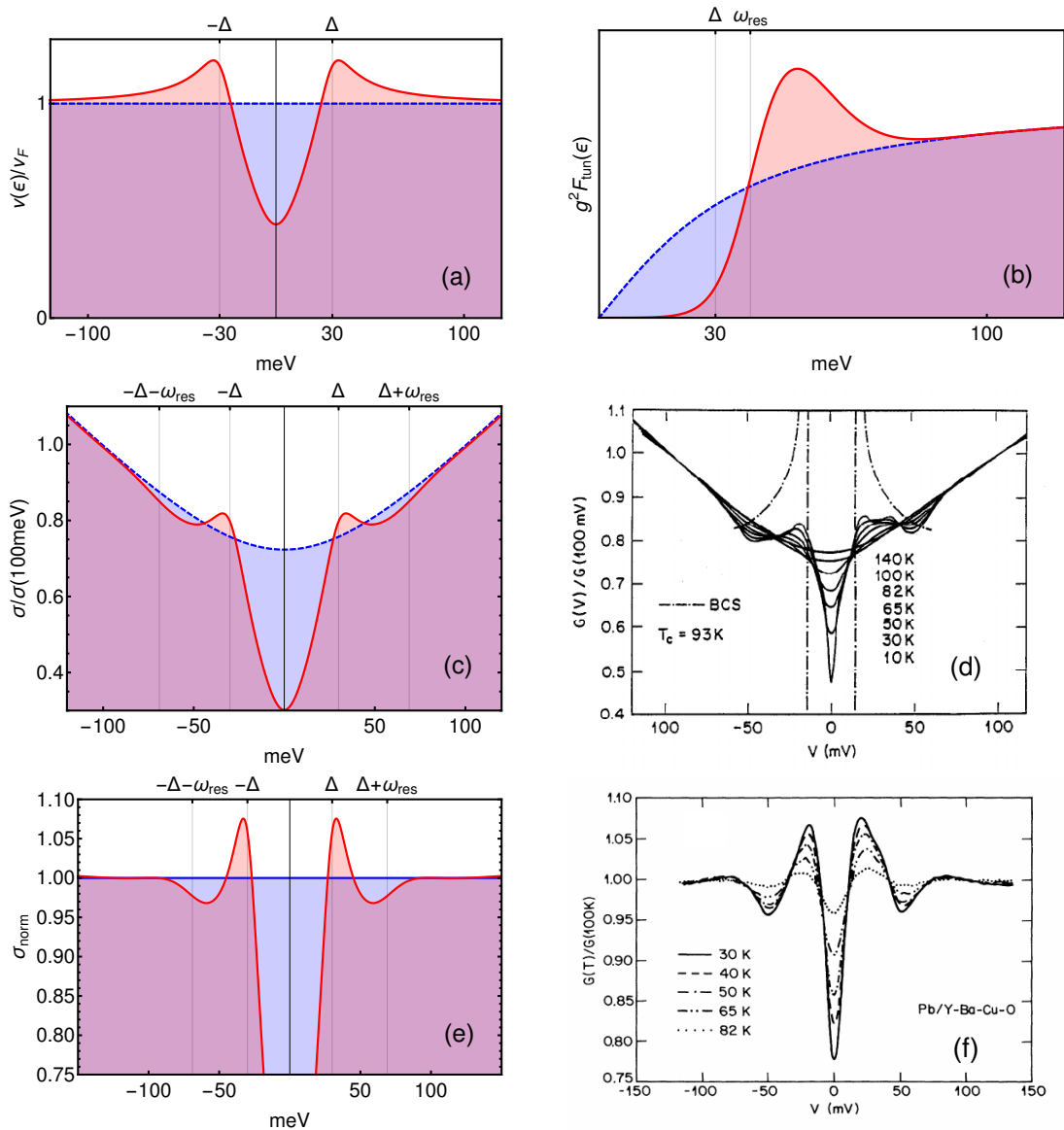


Figure 5.8.: Spectra for YBCO tunneling in the normal- (blue, $T = 100\text{K}$) and superconducting state (red, $T = 10\text{K}$):(a) d -wave superconducting DOS with maximum gap $\Delta = 30\text{meV}$ including quasiparticle broadening of $\Gamma = 7.5\text{meV}$, (b) Overdamped bosonic tunneling spectrum in the normal state and gapped spectrum below T_c motivated by neutron scattering experiments [182], (c) Calculated tunneling conductance normalized to $\sigma(100\text{meV})$ using an inelastic tunneling amplitude to fit the experimental data in the normal state, (d) Experimental conductance for an $\text{YBa}_2\text{Cu}_4\text{O}_7/\text{Pb}$ junction normalized to $\sigma(100\text{meV})$ [73], (e) Calculated normalized conductance using Formula (4.18), (f) Experimental normalized conductance for $\text{YBa}_2\text{Cu}_4\text{O}_7/\text{Pb}$ junction [74].

Let us quickly discuss the possibility of other mechanisms which could generate such features that have been observed in the YBCO tunneling conductance and why we think that they can be excluded here. In Section 2.3.2 we have presented an extended Eliashberg formalism for d -wave superconductors [113], which is capable of explaining a clear dip in the electronic spectrum at $\Delta + \omega_0$ when assuming a sharply peaked bosonic mode at ω_0 in the pairing glue.

The authors of Refs. [114, 115] were able to explain tunneling data in BSCCO qualitatively by such a sharp mode with an energy⁸ close to the spin resonance frequency seen in neutron scattering. Note that for BSCCO inelastic tunneling seems to be mostly absent as there is no clear background conductance visible in the majority of the experiments, see also Figure 1.9. Nevertheless, depending on the the surface sheets and tunneling direction also spectra showing a clear background conductance and/or pseudogaps have been observed above T_c [167, 168], and even a phonon mode has been detected using IETS [86, 198, 199]. The reason for the absence of a background conductance for many BSCCO spectra could originate from the different shape of the Fermi surface or from enhanced tunneling through an insulating oxide in YBCO. The explanation of the dip due to a sharp resonance mode in YBCO is however unlikely, because the position of the dip relative to the superconducting coherence peak is significantly below the value of the resonance mode as seen in neutron scattering experiments [60, 181]. Furthermore, the strong broadening seen for the coherence peak should also reduce the magnitude of possible strong coupling effects significantly. Therefore, the clear background conductance and the nice agreement of the dip position below $\Delta + \omega_{\text{res}}$ is a strong argument for the inelastic tunneling theory in YBCO. Also the pseudogap in the cuprates can be ruled out as the origin of the background conductance, because the magnitude of the pseudogap is of the order of the superconducting gap as has been seen by ARPES and tunneling experiments, see also Section 5.1.

5.3.3. Asymmetric matrix element for inelastic tunneling

One feature that is seen in various experiments, e.g. in LiFeAs or FeSe/STO, is that the inelastic features seem to be weaker on the negative bias side. In Ref. [200] such an asymmetry has been explained by a voltage dependence of the tunneling matrix elements. Let us quickly sketch the main idea to show that this mechanism is probably not sufficient to explain the observed magnitude of the suppression of the inelastic tunneling. Following Wolf [29] we approximate the elastic amplitude for the tunneling of an electron through a barrier by the WKB expression

$$t^e(E, eV) \sim \exp\left[-\int_0^d dx \sqrt{\frac{m[U(x, V) - E]}{2\hbar^2}}\right], \quad (5.5)$$

where $U(x, V)$ is the barrier potential. In the case of vacuum tunneling like STM the barrier potential is essentially the work function of the materials⁹, see also Figure 5.9 where the corresponding energy band structure is shown. In the following we denote with ϕ_t and ϕ_m the work functions of the tip and the metal, which are extrapolated linearly in between because the vacuum is an insulator. Consequently, a linear barrier potential between the tip and the metal develops. In the following, we always measure the particle energy E with respect to the Fermi energy of the metal. When applying a finite voltage V , the barrier potential reads

$$U(x) = eV + \phi_t + \frac{\phi_m - (\phi_t + eV)}{d} \cdot x. \quad (5.6)$$

⁸Other attempts to explain the tunneling data in BSCCO involves Van-Hove singularities and the not self-consistent coupling to a bosonic mode in the superconductors [116, 195, 196]. Similar to Ref. [197] we think that their analysis lacks of a self-consistent evaluation of the corresponding self-energies and is therefore not capable of explaining the dip feature in these systems.

⁹The work function for tunnel barrier should in general be larger than 1eV for good tunneling junctions, otherwise one already expects a U-shaped background conductance from the tunnel matrix element [27]. For STM experiments one therefore should use a metal with a high work functions, e.g. tungsten as in the Pb experiments of Refs. [19, 24].

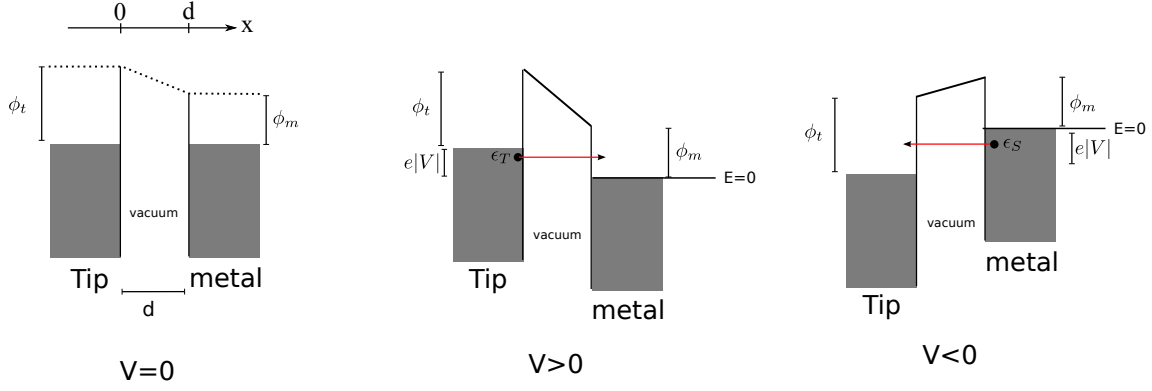


Figure 5.9.: Barrier potential $U(x, V)$ in a vacuum tunneling junction for different applied voltages V .

Here, $x = 0$ corresponds to the tip position and $x = d$ is the surface of the probe. The average potential of the barrier is then

$$\bar{U} = \frac{1}{d} \int_0^d dx U(x) = \frac{\phi_t + \phi_m}{2} + \frac{eV}{2} = \bar{\phi} + \frac{eV}{2}, \quad (5.7)$$

where we defined $\bar{\phi} = \frac{\phi_t + \phi_m}{2}$ as the mean work function of the two electrodes. Using this average barrier height, we can approximate

$$\begin{aligned} t^e(E, eV) &\sim \exp\left[-\int_0^d dx \sqrt{\frac{m[U(x, V) - E]}{2\hbar^2}}\right] \approx \exp\left[-\sqrt{\frac{m[\bar{U} - E]}{2\hbar^2}} \cdot d\right] \\ &= \exp\left[-\sqrt{\frac{m[\bar{\phi} + \frac{eV}{2} - E]}{2\hbar^2}} \cdot d\right]. \end{aligned}$$

For the inelastic tunneling channel this bias dependency of the tunneling amplitude gives rise to different inelastic tunneling probability for the tip-to-metal and metal-to-tip transitions. Let us first consider the tip-to-metal tunneling process for a bosonic mode with energy Ω_{bos} , where we need the threshold voltage $eV \approx \Omega_{\text{bos}}$ for inelastic processes. The tunneling occurs first elastically with energy $E \approx \Omega_{\text{bos}}$, followed by an inelastic boson-scattering to a state near the Fermi surface of the metal. Thus, the typical inelastic tunneling amplitude of Eq. (3.24) for the tip-to-metal transition reads

$$t_{m \rightarrow t}^i \approx \frac{t^e(\Omega_{\text{bos}}, \Omega_{\text{bos}}) \cdot \alpha}{E_{\text{off}}}. \quad (5.8)$$

In contrast, for the reverse process an electron near the Fermi surface of the metal first scatters inelastically and thereby loses energy. With the energy $E \approx -\Omega_{\text{bos}}$ it occupies the off-shell state and can then tunnel elastically for voltages $eV \approx -\Omega_{\text{bos}}$, see Figure 5.10. Hence, for the metal-to-tip tunneling the inelastic amplitude reads

$$t_{t \rightarrow m}^i \approx \frac{t^e(-\Omega_{\text{bos}}, -\Omega_{\text{bos}}) \cdot \alpha}{E_{\text{off}}}. \quad (5.9)$$

For typical values $d \approx 6\text{\AA}$, $\bar{\phi} = 4\text{eV}$ (e.g. the tungsten tip) and $\Omega_{\text{bos}} = 10\text{meV}$ (spin mode in iron pnictides), we get that

$$\frac{|t_{m \rightarrow t}^i|^2}{|t_{t \rightarrow m}^i|^2} \approx 1.02. \quad (5.10)$$

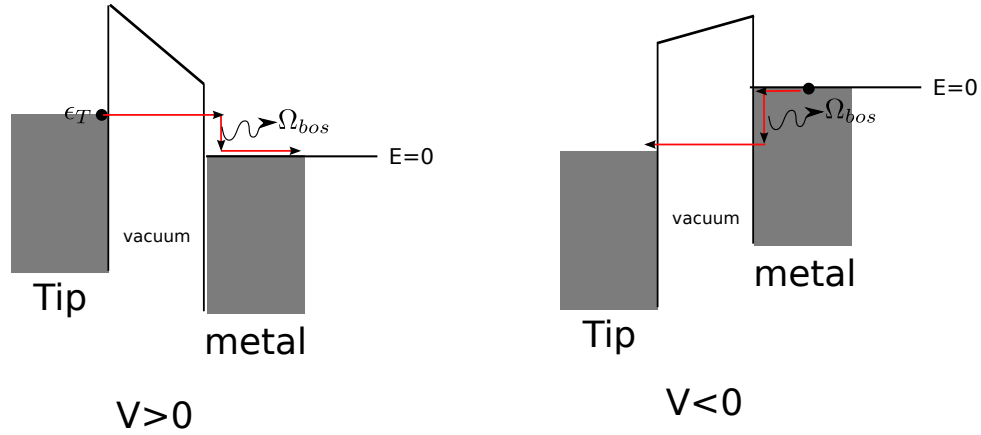


Figure 5.10.: Sketch of inelastic tunneling processes in different directions.

We therefore can conclude that the energy and bias dependency of the matrix element is probably not the origin of the observed asymmetry of the inelastic contributions in the tunneling spectra. However we emphasize, that the WKB expression for the tunneling matrix element is just a rough estimate of the electron tunnel probability, such that final conclusions cannot be drawn from this simple picture.

5.4. Conclusion of Chapter 5

In this chapter we have successfully applied our extended tunneling formalism that combines EETS and IETS to understand various tunneling spectra of unconventional superconductors showing a background conductance. In the normal state we can explain the V-shaped background conductance by inelastic scattering off overdamped spin-fluctuations during the tunneling process [125]. In the superconducting state the phenomenological spin-fermion model already gives the key ingredients to capture the important features seen in the experimental tunneling conductances: A gap in both the electronic **and** the bosonic spin spectrum below T_c . The peak-dip-hump feature could be traced back to the shift of inelastic tunneling contributions to higher energies when entering the superconducting state, which overshadows the strong-coupling Eliashberg features that occur at exactly the same position in energy. Indeed, when looking at iron-pnictide tunneling experiments without background conductance, where we expect the fine-structure to originate from the coupling to virtual bosons, the features in the electronic spectrum are often very weak (see e.g. Figure 1.10(a),(b)). Future works with the extended tunneling theory should also involve a more detailed modeling of the pure electronic spectrum, including possible effects from multiband physics [201].

The agreement of our theoretical conductances and tunneling spectra seen in LiFeAs and YBCO is excellent and we could even improve the fitting by assuming a non-constant normal state DOS and a d-wave superconducting spectrum, respectively. This demonstrates the capability of IETS as an experimental tool for accessing the bosonic spectrum of correlated materials in the superconducting state. Of course, IETS is only present in unconventional superconductors when a clear background conductance can be seen in the normal and superconducting state and one has to be sure that the minimum of the conductance at zero bias does not originate from additional gaps, e.g. from charge- or spin-density waves. Additionally, the different inelastic tunneling amplitudes seen in various experiments, which

could originate from momentum-selective matrix-elements or oxide-layer/impurity-assisted tunneling, have to be further investigated. Also the reduction of inelastic tunneling on the negative bias side seen in some materials is an issue that has to be further investigated, possible origins might be band-structure or matrix-element physics.

6. Superconducting Light Emitting Diode

In this chapter we investigate theoretically the properties of the emitted light of a semiconducting $p-n$ junction with proximity-effect-induced superconducting order. The following analysis is based on Ref. [202] and we call this setup a superconducting light emitting diode (SLED). We show that the presence of a superconducting gap Δ in the particle and hole bands can lead to an increase of the electro-luminescence in a sharp frequency window and that an additional luminescence peak from Cooper pair tunneling occurs on resonance. We also demonstrate that the emitted light can be squeezed and that the squeezing amplitude can be controlled by changing the relative phase of the superconducting order parameter between the junction, revealing how the macroscopic coherence of a superconductor can be used to produce non-classical light.

6.1. Modeling the SLED

The main motivation for investigating the SLED is the question: “Is it possible to transfer the macroscopic quantum coherence of Cooper pairs to light?” A simple solid state device that efficiently produces entangled and/or squeezed photon pairs [203] is desired in many research fields, e.g. for the quantum information processing and communication [204–206]. Such an on-demand production of entangled photon pairs due to the recombination of Cooper pairs has been investigated theoretically [202, 207–213] for various different setups. The fabrication of superconductor-semiconductor hybrid nanostructures has turned out to be challenging and some promising candidates are quantum dots [214], semiconducting quantum wells [215–218] and self-organizing semiconductor-superconductor-heterostructures of unconventional superconductors [219]. In the $p-n$ junctions [215, 218, 220] as well as for InAs quantum dots [217], where the semiconducting heterostructure is combined with a superconducting Niobium lead on the n side of the junction, a strong increase of the electro-luminescence has been observed below the superconducting transition temperature T_c . Thus, the n -side of the junction has been superconducting, whereas the p -side is the normal state.

6.1.1. SLED Hamiltonian

Here, we consider a semiconducting $p-n$ junction sandwiched between two superconducting leads¹ as first proposed in Ref. [211], which is also sketched in Figure 6.1. The system

¹ So far, the realization of such a system has not been achieved, because the superconducting materials that can be grown on the p -side have a lattice mismatch and have to be hole superconductors. However, this is just an engineering issue and not a fundamental problem of the proposed setup.

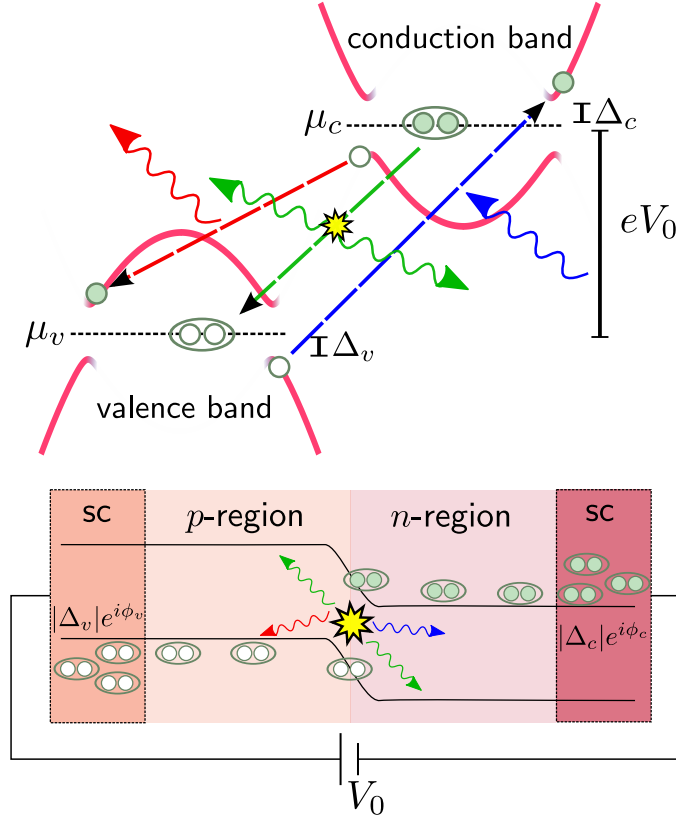


Figure 6.1.: Schematic setup of superconducting light emitting diode with p - n junction coupled to superconducting (sc) leads operated under forward bias voltage V_0 . Basic recombination processes at low temperature $T < |\Delta_c|, |\Delta_v|$: (i) recombination of conduction particle and valence hole upon radiation of a photon (red) with energy $\omega_q \leq eV_0 - |\Delta_c| - |\Delta_v|$, (ii) absorption of a photon (blue) with energy $\omega_q \geq eV_0 + |\Delta_c| + |\Delta_v|$ upon transfer of an electron from valence to conduction band, and (iii) Cooper pair tunneling upon emission or absorption of two photons (green) with energy $\omega_q = eV_0$. The superconducting gaps are denoted Δ_v (Δ_c) for valence (conduction) band. Taken from Ref. [202].

will be biased by a voltage $eV = \mu_c - \mu_v$, where $\mu_{c/v}$ are the chemical potential of the conduction/valence bands on the n/p -side of the junction. Due to the proximity effect [221] Cooper pairs can tunnel into the active region of the light emitting diode (LED), where the recombination of the particle and holes occur. The Hamiltonian of the entire system reads

$$H = H_c + H_v + H_{\text{ph}} + H_{\text{el-ph}} + H_{\text{ph}}^{\text{bath}}. \quad (6.1)$$

Let us describe the different parts of the Hamiltonian in detail: $H_{c/v}$ depict the isolated physics of the conduction and valence bands and takes the form

$$H_\alpha - \mu_\alpha N_\alpha = \sum_{\mathbf{k}, \sigma=\uparrow, \downarrow} (\epsilon_\alpha(\mathbf{k}) - \mu_\alpha) \hat{a}_{\mathbf{k}\sigma}^\dagger \hat{a}_{\mathbf{k}\sigma} + \sum_{\mathbf{k}} (\Delta_\alpha \hat{a}_{\mathbf{k}\uparrow}^\dagger \hat{a}_{-\mathbf{k}\downarrow}^\dagger + \text{h.c.}), \quad (6.2)$$

where $\hat{a}_{\mathbf{k}\sigma}^\dagger$ is the creation operator for an electron in the conduction/valence band ($\alpha = (c, v)$) with momentum \mathbf{k} and spin σ . The band dispersion is assumed as a simple quadratic dispersion $\epsilon_\alpha(\mathbf{k}) = \mathbf{k}^2/2m_\alpha$ with the effective masses $m_c > 0$ and $m_v < 0$ describing electron- and hole-like quasiparticles centered around the Γ -point, supporting direct radiative

electron-hole-recombinations. The proximity-induced superconducting gaps are denoted by Δ_α . So far, we have not applied the bias V to the system, which will be done later when switching to an action-based description of the model. The next part of the Hamiltonian describes the bare photonic system via

$$H_{\text{ph}} = \sum_{\mathbf{q}} \omega_{\mathbf{q}} \hat{b}_{\mathbf{q}}^\dagger \hat{b}_{\mathbf{q}} \quad (6.3)$$

with linear photon-dispersion $\omega_{\mathbf{q}} = c \cdot |\mathbf{q}|$ and photon creation operator $\hat{b}_{\mathbf{q}}^\dagger$. We only consider one photon polarization here and restrict ourselves to spin-conserving recombinations, however the extension of our model to circularly polarized photons is straightforward and does not alter the conclusions drawn in the remainder of the chapter. The radiative recombination of electrons and holes is described by

$$H_{\text{el-ph}} = - \sum_{\mathbf{k}, \mathbf{k}', \sigma} (g_0 \hat{b}_{\mathbf{k}-\mathbf{k}'} \hat{c}_{\mathbf{k}, \sigma}^\dagger \hat{v}_{\mathbf{k}', \sigma} + \text{h.c.}), \quad (6.4)$$

where g_0 is the electron-photon coupling constant between the valence and conduction electrons, which is assumed to be momentum independent for the electrons and holes at the Fermi edges. When operating the junction under forward bias, photons will be constantly produced by the LED and the need for an external absorption mechanism becomes apparent. Hence, we add a bath Hamiltonian [222, 223]

$$H_{\text{ph}}^{\text{bath}} = \sum_{\mathbf{q}} \nu_{\mathbf{q}} \hat{a}_{\mathbf{q}}^\dagger \hat{a}_{\mathbf{q}} - \sum_{\mathbf{q}, \mathbf{q}'} (\lambda_{\mathbf{q}, \mathbf{q}'} \hat{b}_{\mathbf{q}}^\dagger \hat{a}_{\mathbf{q}'} + \text{h.c.}). \quad (6.5)$$

The photon operator $\hat{a}_{\mathbf{q}}^\dagger$ creates a bath photon with frequency \mathbf{q} and the coupling between the external bath and the photon system in the LED is denoted by $\lambda_{\mathbf{q}, \mathbf{q}'}$. The bath can effectively absorb generated photons and thus effectively models the emission of light of the LED.

Let us note the close relationship between the Hamiltonian (6.1) and the inelastic tunneling Hamiltonian for superconducting tunneling. Besides the external bath, the main difference lies in the energy scale of the applied bias V and therefore of the bosons that are involved in the inelastic tunneling process. For superconductor tunneling experiments on metals the applied bias is usually of order 10 – 100mV (e.g. phonons, magnons, spin fluctuations), whereas in semiconductors the forward bias usually operates at $\sim 1\text{V}$ (optical photons).

6.1.2. Energy scales of the system

Before proceeding with the calculations, let us quickly summarize the important energy scales of the system. For the following estimates we use realistic values of GaAs semiconductors. There are five important energy scales in the system:

- (1) The applied voltage V that is of the order of the semiconducting band gap $D \approx 1\text{eV}$, which is by far the largest energy scale of the system. The energy $\omega_{\mathbf{q}} \approx eV$ as well as the photon momentum $|\mathbf{q}| = eV/c$ of the emitted photons is set by the applied voltage or the band gap respectively.

- (2) The semiconducting Fermi-energy E_F , measured relative to the band-edges of the conduction and valence bands, which is typically of the order $E_F \sim 10^{-2} \text{ eV} - 10^{-1} \text{ eV}$. With the typical effective masses $m_{c/v} \sim 0.05 m_e - 0.1 m_e$ the Fermi velocity can be estimated to be $v_F = \sqrt{2E_F/m} \sim 10^{-3}c$.
- (3) The proximity induced gap $\Delta_{c/v}$, which will be assumed to be $|\Delta_{c/v}| = 1\text{meV}$ typical for conventional superconductors.
- (4) The electron-photon coupling energy $|g_0|^2 \nu_F \sim 10^{-5} \text{ eV} - 10^{-6} \text{ eV}$ [211], where ν_F is the DOS of the fermionic quasiparticles.
- (5) The coupling to the external bath, which will give rise to a bath decay rate η , see Section 6.2.3. The steady-state condition implies that the bath decay rate η has to be larger than the photon production rate.

6.2. Effective photon action

6.2.1. Derivation of effective photon action

Since we are interested in the feedback of the superconducting electrons and holes on the emitted photons, we will employ a Keldysh path-integral formalism to integrate out the electronic quasiparticles that leads to an effective action for the photons. This effective action contain detailed information about the electro-luminescence and squeezing properties of the emitted light. The small parameter that controls our perturbative approach is the electron-photon coupling energy $|g_0|^2 \nu_F \ll |\Delta|, E_F$ for the superconducting and normal state. We also require the system to be in a steady state and will discuss the lasing conditions later in Section 6.4.

The Keldysh action² of the Hamiltonian (6.1) reads

$$S = \int_C dt \left[\sum_{\mathbf{k}, \sigma} \left(\bar{c}_{\mathbf{k}, \sigma} i \partial_t c_{\mathbf{k}, \sigma} + \bar{v}_{\mathbf{k}, \sigma} i \partial_t v_{\mathbf{k}, \sigma} \right) + \sum_{\mathbf{q}} \left(\bar{b}_{\mathbf{q}} i \partial_t b_{\mathbf{q}} + \bar{a}_{\mathbf{q}} i \partial_t a_{\mathbf{q}} \right) - H \right]. \quad (6.6)$$

Here, the $c_{\mathbf{k}, \sigma}, v_{\mathbf{k}, \sigma}$ are Grassmann fields and $a_{\mathbf{q}}, b_{\mathbf{q}}$ are complex fields that arise when using the path-integral formalism. It is convenient to apply the bias $eV = \mu_c - \mu_v$ at this stage, which can be done by performing the gauge transformation $\alpha_{\mathbf{k}, \sigma} \rightarrow e^{i\mu_\alpha t} \alpha_{\mathbf{k}, \sigma}$, see also Appendix B. After this transformation the dispersions $\epsilon_\alpha(\mathbf{k}) \rightarrow \xi_\alpha(\mathbf{k}) = \epsilon_\alpha(\mathbf{k}) - \mu_\alpha$ are measured relative to the respective chemical potential and the electron-photon coupling acquires a time-dependent phase $g_0 \rightarrow g(t) = g_0 e^{ieVt}$. However, we can reabsorb this phase by introducing the new photon fields $B_{\mathbf{q}} = b_{\mathbf{q}} e^{ieVt}$ with dispersion $\bar{\omega}_{\mathbf{q}} = \omega_{\mathbf{q}} - eV$ and $A_{\mathbf{q}} = a_{\mathbf{q}} e^{ieVt}$ with dispersion $\bar{\nu}_{\mathbf{q}} = \nu_{\mathbf{q}} - eV$. Let us now introduce the following electronic and photonic spinors

$$\Delta_{\mathbf{k}}^\zeta = \begin{pmatrix} v_{\mathbf{k}, \uparrow}^\zeta \\ c_{\mathbf{k}, \uparrow}^\zeta \\ \bar{v}_{-\mathbf{k}, \downarrow}^\zeta \\ \bar{c}_{-\mathbf{k}, \downarrow}^\zeta \end{pmatrix} \quad \dot{\Phi}_{\mathbf{q}}^\zeta = \begin{pmatrix} B_{\mathbf{q}}^\zeta \\ \bar{B}_{-\mathbf{q}}^\zeta \end{pmatrix}, \quad (6.7)$$

²See also the introduction to Keldysh theory in Appendix C.

with $\zeta = \text{cl}, \text{q}$ for the fermionic and $\zeta = 1, 2$ for the bosonic case. We also defined the corresponding Keldysh vectors

$$\hat{\Psi}_{\mathbf{k}} = \begin{pmatrix} \Delta \hat{\Psi}_{\mathbf{k}}^{\text{cl}} \\ \Delta \hat{\Psi}_{\mathbf{k}}^{\text{q}} \end{pmatrix} \quad \hat{\Phi}_{\mathbf{q}} = \begin{pmatrix} \mathring{\Phi}_{\mathbf{q}}^{\text{cl}} \\ \mathring{\Phi}_{\mathbf{q}}^{\text{q}} \end{pmatrix}, \quad (6.8)$$

where the \wedge -superscript denotes the Keldysh-space, the Δ -superscript the extended conductance-valence Nambu-spinor and the \circ -superscript the particle-hole photon space. In terms of the defined spinors, the Keldysh action can be written in a compact form

$$S = \int_{-\infty}^{\infty} dt dt' \left\{ \sum_{\mathbf{k}} \hat{\Psi}_{\mathbf{k}}^{\dagger}(t) \hat{G}_{0,\mathbf{k}}^{-1}(t, t') \hat{\Psi}_{\mathbf{k}}(t') + \frac{1}{2} \sum_{\mathbf{q}} \hat{\Phi}_{\mathbf{q}}^T(t) \hat{D}_{0,\mathbf{q}}^{-1}(t, t') \hat{\Phi}_{-\mathbf{q}}(t') \right. \\ \left. + \sum_{\mathbf{k}, \mathbf{k}'} \hat{\Psi}_{\mathbf{k}}(t) V_{\mathbf{k}-\mathbf{k}'}(t) \hat{\Psi}_{\mathbf{k}'}(t') \delta(t-t') \right\} + S_{\text{ph}}^{\text{bath}}. \quad (6.9)$$

The factor $1/2$ in front of the bosonic propagators comes from the “real” choice of the photon spinor $\mathring{\Phi}$. The bare electronic propagator is given by

$$\hat{G}_{0,\mathbf{k}}(t, t') = -i \langle \hat{\Psi}_{\mathbf{k}}(t) \hat{\Psi}_{\mathbf{k}}^{\dagger}(t') \rangle_0 = \begin{pmatrix} \hat{G}_{0,\mathbf{k}}^R(t, t') & \hat{G}_{0,\mathbf{k}}^K(t, t') \\ 0 & \hat{G}_{0,\mathbf{k}}^A(t, t') \end{pmatrix} \quad (6.10)$$

$$\hat{G}_{0,\mathbf{k}}^{R/A}(t-t') = -i \langle \hat{\Psi}_{\mathbf{k}}^{1/2}(t) [\hat{\Psi}_{\mathbf{k}}^{2/1}(t')]^{\dagger} \rangle_0 = \begin{pmatrix} G_{0,\mathbf{k},v}^{(p),R/A} & 0 & F_{0,\mathbf{k},v}^{R/A} & 0 \\ 0 & G_{0,\mathbf{k},c}^{(p),R/A} & 0 & F_{0,\mathbf{k},c}^{R/A} \\ \bar{F}_{0,\mathbf{k},v}^{R/A} & 0 & G_{0,\mathbf{k},v}^{(h),R/A} & 0 \\ 0 & \bar{F}_{0,\mathbf{k},c}^{R/A} & 0 & G_{0,\mathbf{k},c}^{(h),R/A} \end{pmatrix}_{t,t'}$$

where $\langle \rangle_0$ is the average with respect to the free, uncoupled action $S(g_0 = 0)$. The particle and hole propagators of the conduction/valence band are denoted by $G_{c/v}^{(p)}, G_{c/v}^{(h)}$ and the anomalous propagators that arise in the superconducting state by F and \bar{F} . The energy-momentum representation, as derived via a Fourier-transformation, takes the usual form for the retarded and advanced propagators

$$\begin{pmatrix} G_{0,\alpha}^{(p)} & F_{0,\alpha} \\ \bar{F}_{0,\alpha} & G_{0,\alpha}^{(h)} \end{pmatrix}_{\omega, \mathbf{k}}^{R/A} = \frac{(\omega + i0) \cdot \mathbf{1} + \xi_{\alpha}(\mathbf{k}) \cdot \sigma_z - \Delta_{\alpha} \cdot \sigma_+ - \Delta_{\alpha}^* \cdot \sigma_-}{(\omega \pm i0)^2 - \xi_{\alpha}(\mathbf{k})^2 - |\Delta_{\alpha}|^2}, \quad (6.11)$$

where $\sigma_{\pm} = \frac{1}{2}(\sigma_x \pm i\sigma_y)$. We assume the electrons to be in thermal equilibrium, therefore their equilibration time is much shorter than the typical recombination rate of the LED and we can express the Keldysh component of the Green's function as

$$\hat{G}_{0,\mathbf{k}}^K(\omega) = F(\omega) [\hat{G}_{0,\mathbf{k}}^R(\omega) - \hat{G}_{0,\mathbf{k}}^A(\omega)] \quad (6.12)$$

with the fermionic distribution function $F(\omega) = 1 - 2n_F(\omega) = \tanh(\omega/2T_F)$ and the fermionic temperature T_F . For the photonic system, the propagator is given by

$$\hat{D}_{0,\mathbf{q}}(t, t') = -i \langle \hat{\Phi}_{\mathbf{q}}(t) \hat{\Phi}_{-\mathbf{q}}^T(t') \rangle_0 = \begin{pmatrix} \mathring{D}_{0,\mathbf{q}}^K(t, t') & \mathring{D}_{0,\mathbf{q}}^R(t, t') \\ \mathring{D}_{0,\mathbf{q}}^A(t, t') & 0 \end{pmatrix}. \quad (6.13)$$

with the retarded and advanced blocks

$$\begin{aligned}\dot{D}_{0,\mathbf{q}}^{R/A}(t-t') &= -i\langle \hat{\Phi}_{\mathbf{q}}^{\text{cl}/\text{q}}(t) [\hat{\Phi}_{-\mathbf{q}}^{\text{q}/\text{cl}}(t')]^T \rangle_0 \\ &= \begin{pmatrix} 0 & d_{0,\mathbf{q}}^{R/A}(t-t') \\ d_{0,\mathbf{q}}^{A/R}(t'-t) & 0 \end{pmatrix}.\end{aligned}\quad (6.14)$$

Here, the bare photon propagator reads $[d_{0,\mathbf{q}}^{R/A}(\omega)]^{-1} = \omega - \bar{\omega}_{\mathbf{q}} \pm i0$. Similar to the fermionic system, the photon system is for the uncoupled case in thermal equilibrium and thus the Keldysh component reads

$$\dot{D}_{0,\mathbf{q}}^K(\omega) = B_0(\omega) [\dot{D}_{0,\mathbf{q}}^R(\omega) - \dot{D}_{0,\mathbf{q}}^A(\omega)] \quad (6.15)$$

with the bosonic distribution function $B_0(\omega) = 1 + 2n_B(\omega)$ with the initial photon temperature T_B . However, as we will see soon this initial bosonic distribution function will not be of importance for the following analysis in the steady-state. The actual photon distribution function will rather be determined by the interplay between the photon distribution of the bath and the radiative processes of the LED.

The electron-photon part of the action can be written down as

$$V_{\mathbf{k}-\mathbf{k}'}(t) = \sum_{\alpha=\text{cl},\text{q}} \sum_{i=1,2} \hat{\gamma}^\alpha \hat{g}_i [\hat{\Phi}_{\mathbf{k}-\mathbf{k}'}^\alpha(t)]_i \quad (6.16)$$

with the vertex matrices $\hat{\gamma}^{\text{cl}} = \hat{1}$ and $\hat{\gamma}^{\text{q}} = \hat{\sigma}_x$ in Keldysh space and the coupling matrices

$$\begin{aligned}\hat{g}_1 &= \frac{g_0}{\sqrt{2}} \begin{pmatrix} 0 & 0 & 0 & 0 \\ 1 & 0 & 0 & 0 \\ 0 & 0 & 0 & -1 \\ 0 & 0 & 0 & 0 \end{pmatrix}, \\ \hat{g}_2 &= \frac{\bar{g}_0}{\sqrt{2}} \begin{pmatrix} 0 & 1 & 0 & 0 \\ 0 & 0 & 0 & 0 \\ 0 & 0 & 0 & 0 \\ 0 & 0 & -1 & 0 \end{pmatrix}.\end{aligned}\quad (6.17)$$

Finally, let us also give the part of the action that describes the photon bath and its coupling to the LED

$$S_{\text{ph}}^{\text{bath}} = \int_{\mathcal{C}} dt \left[\sum_{\mathbf{q}} A_{\mathbf{q}}^\dagger (i\partial_t - \bar{\nu}_{\mathbf{q}}) A_{\mathbf{q}} + \sum_{\mathbf{q},\mathbf{q}'} (\lambda_{\mathbf{q}\mathbf{q}'} B_{\mathbf{q}}^\dagger A_{\mathbf{q}'} + c.c.) \right]. \quad (6.18)$$

Let us now derive the effective action for the SLED photons by integrating over the fermionic degrees of freedom and the external bath photons. As explained in Appendix D such an integration gives rise to two contributions for the photon propagators in terms of the self-energies $\hat{\Pi}_{\mathbf{q}}^{\text{el}}(t, t')$ from the electron-hole recombinations and $\hat{\Pi}_{\mathbf{q}}^{\text{bath}}(t, t')$ from the absorption of photons into the bath, yielding an action of the form

$$S_{\text{ph}}^{\text{eff}} = \frac{1}{2} \sum_{\mathbf{q}} \int_{-\infty}^{\infty} dt dt' \hat{\Phi}_{\mathbf{q}}^T(t) \left[\hat{D}_{0,\mathbf{q}}^{-1}(t, t') - \hat{\Pi}_{\mathbf{q}}^{\text{el}}(t, t') - \hat{\Pi}_{\mathbf{q}}^{\text{bath}}(t, t') \right] \hat{\Phi}_{-\mathbf{q}}(t'). \quad (6.19)$$

The bath self-energy can be treated exactly, whereas the electron-induced self-energy has to be handled within some approximations. We will continue by first calculating the $\mathring{\Pi}_{\mathbf{q}}^{\text{el}}(t, t')$ self-energy within the random-phase approximation (RPA) and show how the presence of superconductivity gives rise to correlated photon pairs. Hereafter, we discuss the role of the photon bath for the evolution of a steady-state of the SLED.

6.2.2. Electronic feedback

The effect of radiative electron-hole recombination can be described in our theory by the self-energy $\mathring{\Pi}_{\mathbf{q}}^{\text{el}}(t, t')$, which contains the information about photon absorption and emission processes that involve transitions of electrons between the conduction and valence band. Our gauge for the photon fields is chosen such that the structure of the self-energy

$$\mathring{\Pi}_{\mathbf{q}}^{\text{el}}(t, t') = \begin{pmatrix} e^{i\phi_0} \tilde{\Pi}_{11, \mathbf{q}}^{\text{el}}(t - t') & \Pi_{12, \mathbf{q}}^{\text{el}}(t - t') \\ \Pi_{21, \mathbf{q}}^{\text{el}}(t - t') & e^{-i\phi_0} \tilde{\Pi}_{22, \mathbf{q}}^{\text{el}}(t - t') \end{pmatrix}, \quad (6.20)$$

is time-translational invariant, which is in contrast to the definition in Ref. [202]. This choice has the advantage, that the inversion of the Dyson equation is trivial, because the convolutions that occur can be easily Fourier-transformed and there is no need for a Wigner transformation. The phase $\phi_0 = \phi_v - \phi_c + 2\phi_g$ is dependent on the phase $\phi_{c/v} = \arg(\Delta_{c/v})$ of the superconducting order parameters and of the coupling constant $\phi_g = \arg(g_0)$. We treat this self-energies in the RPA-approximation, which means that we take into account only the leading order one-loop diagrams shown in Figure 6.1, and can write them down explicitly as

$$\Pi_{ij, \mathbf{q}}^{\text{el}, \alpha\beta}(t, t') = -i \sum_{\mathbf{k}} \text{tr}[\hat{\gamma}^\alpha \hat{g}_i \hat{G}_{0, \mathbf{k}}(t, t') \hat{\gamma}^\beta \hat{g}_j \hat{G}_{0, \mathbf{k}+\mathbf{q}}(t', t)]. \quad (6.21)$$

In the following, we will summarize the resulting self-energies in the normal- and superconducting state and interpret the physical processes behind the observed features. The actual calculations of the self-energies are performed in the $T = 0$ limit and are given in detail in Appendix D.

6.2.2.1. Normal conducting leads

Let us start by assuming that the external superconducting leads are forced to the normal state, e.g. by an external magnetic field or by increasing the temperature above T_c . In this case the superconducting order parameters $\Delta_v = \Delta_c = 0$ vanish and also the diagonal elements of the self-energy matrix in Eq. (6.20) are zero. For an analytic evaluation of the occurring momentum sums we make additional assumptions about the band-structure: We demand symmetric but mirrored dispersions with $m_c = -m_v$ (and equal gap amplitudes $|\Delta_c| = |\Delta_v| = \Delta$ later in the superconducting state) for the conduction and valence bands. As a result, the electronic dispersions fulfill $\xi_c(\mathbf{k}) = -\xi_v(\mathbf{k})$. The electronic DOS is furthermore only weakly energy-depend in an energy range $|\omega| \ll E_F$ with $\nu_c(\omega) = \nu_v(-\omega) \equiv \nu(\omega)$, with $\nu(0) = \nu_F$. In Figure 6.3 the situation is sketched and we emphasize that assuming more general dispersion do not alter the main conclusions drawn in the following analysis and can in principle be included via numerical integrations. The retarded

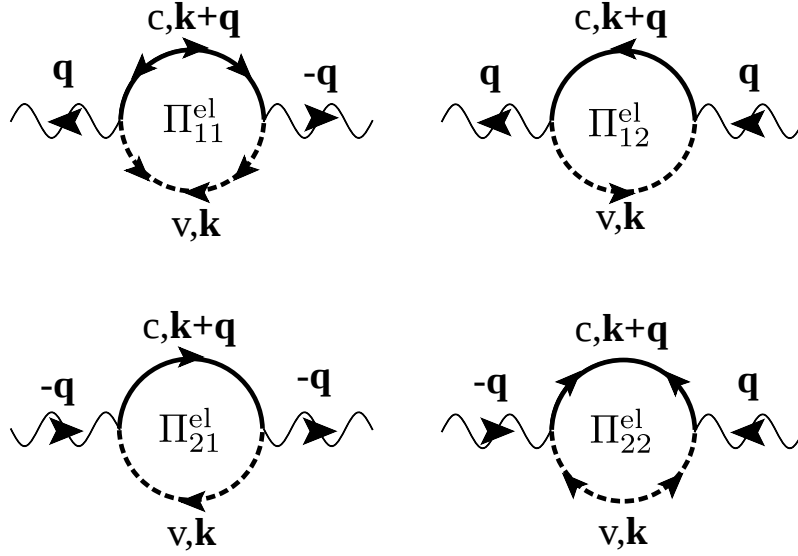


Figure 6.2.: Feynman graphs of the one-loop bosonic self-energy $\Pi_{ij,q}^{\text{el}}$ due to the coupling to conduction (c) and valence (v) electrons, see Eq. (6.21). External photon propagators (wiggly lines) are not part of the self-energy. Each vertex is associated with a coupling constant $|g_0|$. Wiggly lines denote photons, solid (dashed) lines denote conduction (valence) electron propagators. The anomalous contributions $\tilde{\Pi}_{11}^{\text{el}}, \tilde{\Pi}_{22}^{\text{el}}$ appear only for superconducting leads $\Delta_c, \Delta_v \neq 0$. Adapted from Ref. [202].

self-energies in the normal state can be easily calculated for $T_F = 0$ and are given by

$$\begin{aligned} \Pi_{21,q}^{\text{el},R}(\omega) &= -i\pi |g_0|^2 \nu \left(\frac{\omega}{2}\right) \begin{cases} \frac{\omega}{v_F|\mathbf{q}|} & \text{for } |\omega| < v_F|\mathbf{q}| \\ \text{sign}(\omega) & \text{for } |\omega| > v_F|\mathbf{q}| \end{cases} \\ \Pi_{12,q}^{\text{el},R}(\omega) &= \Pi_{12,q}^{\text{el},A}(-\omega), \end{aligned} \quad (6.22)$$

and are shown in Figure 6.4(a). We neglected the real part, because it only depends weakly on frequency and because we are in the weak-coupling limit the renormalization of the photon dispersion can be neglected in the normal state. Since the fermions are assumed to be in thermal equilibrium, the Keldysh components of the self-energies just reads

$$\Pi_{ij,q}^{\text{el},K}(\omega) = \coth\left(\frac{\omega}{2T_F}\right) \left[\Pi_{ij,q}^{\text{el},R}(\omega) - \Pi_{ij,q}^{\text{el},A}(\omega) \right]. \quad (6.23)$$

The imaginary part of the self-energy describes the production and decay rate of the photons from the recombination and creation of particle-hole excitations. In Figure 6.3 we see that for $T_F = 0$ there are only two possible transitions: (i) the emission of photons with energy $\omega_q < eV$ via the recombination of an electron from the valence band and a hole in the conduction band, (ii) the absorption of photons, which creates a particle-hole excitation for photon energies $\omega_q > eV$. Note that due to our chosen gauge of the photon fields $B_{\mathbf{q}} = b_{\mathbf{q}} e^{ieVt}$, the Π_{12} self-energy defined here is measured with respect to the applied bias voltage eV . Thus, the absorption/emission of photons is associated with a negative/positive imaginary part in the retarded photonic self-energy $\Pi_{21,q}^{\text{el},R}(\omega)$ as can be seen from the blue curve in Figure 6.4(a). The linear region for $|\omega| < v_F\mathbf{q}$ originates from a restricted phase space and the saturation to a constant value comes from the linearization around the Fermi energies.

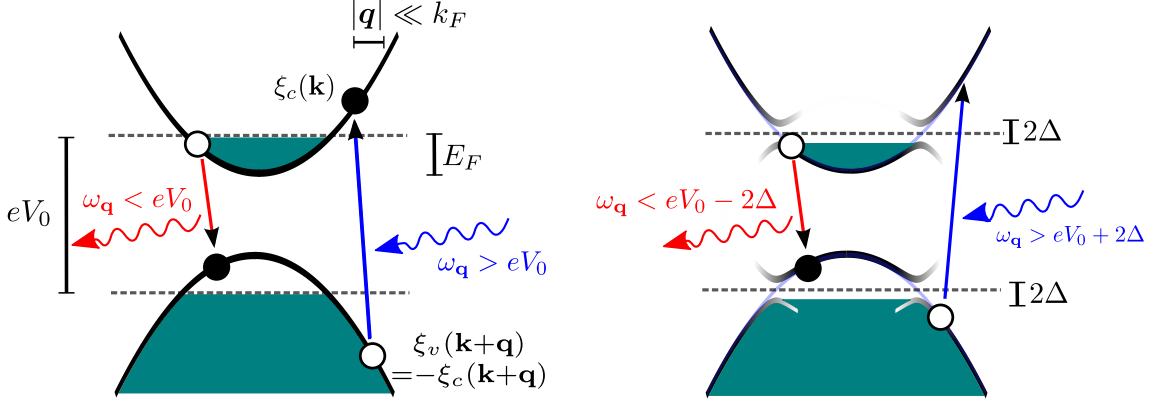


Figure 6.3.: Schematic of the symmetric electronic band dispersion model for normal conducting leads. Conduction and valence band dispersion obey $\xi_c(\mathbf{k}) = -\xi_v(\mathbf{k})$, v_F denotes the Fermi velocity, k_F the Fermi momentum, E_F is the Fermi energy and thus the filling factor of the bands and eV is the applied bias voltage. Electronic transitions involving photon emission (absorption) are possible at photon energies $\omega_{\mathbf{q}} < eV$ ($\omega_{\mathbf{q}} > eV$). Photon momentum $\mathbf{q} \ll \mathbf{k}_F$ is properly taken into account and results in electronic transitions that are not vertical. In the presence of superconductivity the electrons at the Fermi edges are gapped out by the superconducting gap Δ , resulting in allowed transitions only for $|\omega_{\mathbf{q}} - eV| > 2\Delta$. Taken from Ref. [202].

Note, that the production of photons is described by a positive imaginary part in the $\Pi_{21,\mathbf{q}}^{\text{el},R}(\omega)$ self-energy that occurs at frequencies $\omega < 0$. If there were no additional contributions to the photon self-energy, this positive imaginary part would lead to a violation of the analytic structure of the theory, because the retarded self-energy has to have a negative imaginary part for all energies $\omega > -eV$ for bosonic particles³. Physically, this indicates an instability of the system and tells us that a steady state cannot evolve if there is no absorption mechanism for the produced photons of the LED. Hence, the photon number would grow without bound, resulting in a LASER state (Light Amplification by Stimulated Emission of Radiation). For this reason, we had to include the coupling to the external bath that leads in total to a negative imaginary part for all energies. Later, we will also discuss the LASER conditions for our model.

6.2.2.2. Superconducting leads

When the system is in the superconducting state, there exist non-zero anomalous fermionic Green's functions F, \bar{F} . These lead to the anomalous terms in the diagonal of the bosonic self-energy $\tilde{\Pi}_{\mathbf{q}}^{\text{el}}(t, t')$, which induce anomalous photon expectation values such as $\langle b_{\mathbf{q}}^{\dagger}(t)b_{-\mathbf{q}}^{\dagger}(t) \rangle$. As we will see later, this can lead to non-classical, squeezed states of the emitted light. As shown in Appendix D the one-loop self-energies in the energy representation can be written down as

$$\tilde{\Pi}_{11,\mathbf{q}}^{\text{el},R}(\omega) = 2|g_0^2| \sum_{\mathbf{k}} \left[\frac{u_{\mathbf{k},v}v_{\mathbf{k},v}u_{\mathbf{k}+\mathbf{q},c}v_{\mathbf{k}+\mathbf{q},c}}{\omega - E_v(\mathbf{k}) - E_c(\mathbf{k}+\mathbf{q}) + i0} - \frac{u_{\mathbf{k},v}v_{\mathbf{k},v}u_{\mathbf{k}+\mathbf{q},c}v_{\mathbf{k}+\mathbf{q},c}}{\omega + E_v(\mathbf{k}) + E_c(\mathbf{k}+\mathbf{q}) + i0} \right],$$

$$\Pi_{21,\mathbf{q}}^{\text{el},R}(\omega) = 2|g_0^2| \sum_{\mathbf{k}} \left[\frac{v_{\mathbf{k},v}^2 u_{\mathbf{k}+\mathbf{q},c}^2}{\omega - E_v(\mathbf{k}) - E_c(\mathbf{k}+\mathbf{q}) + i0} - \frac{u_{\mathbf{k},v}^2 v_{\mathbf{k}+\mathbf{q},c}^2}{\omega + E_v(\mathbf{k}) + E_c(\mathbf{k}+\mathbf{q}) + i0} \right].$$

³Remember that we measure our bosonic energy relative to $eV > 0$. Usually, the imaginary part of the bosonic self-energy has a sign-change from positive to negative at $\omega = 0$, hence for our self-energy this should occur at $\omega = -eV$.

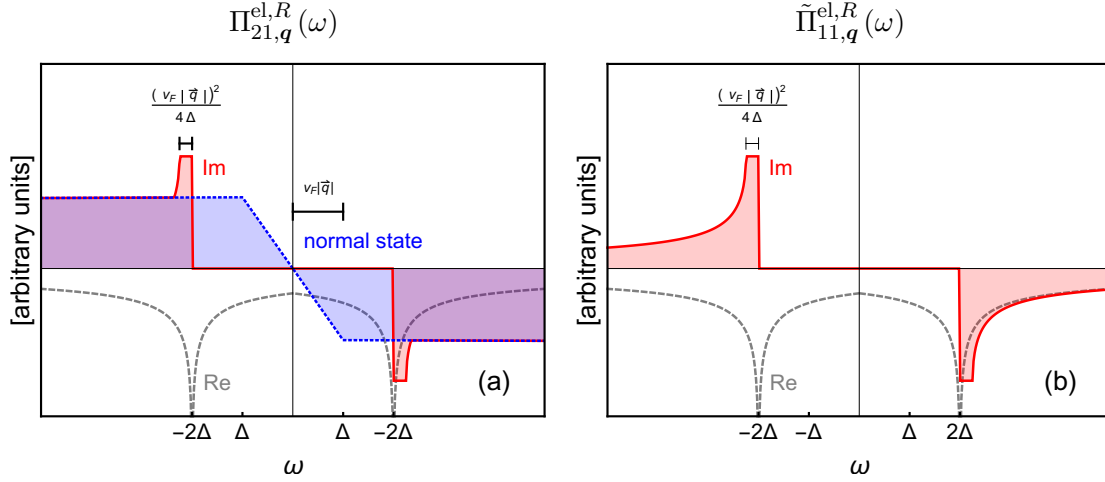


Figure 6.4.: Self-energies in the normal (blue= $\text{Im } \Pi^{\text{el},R}$) and superconducting (red= $\text{Im } \Pi^{\text{el},R}$, gray= $\text{Re } \Pi^{\text{el},R}$) state: (a) Particle self-energy $\Pi_{21,q}^{\text{el},R}(\omega)$ at fixed momentum \mathbf{q} as function of frequency ω . Positive/negative sign of the imaginary parts corresponds to photon emission and absorption, (b) Anomalous self-energy $\tilde{\Pi}_{11,q}^{\text{el},R}(\omega)$ in the superconducting state showing similar structures as the particle self-energy. Adapted from Ref. [202].

$$\begin{aligned}\Pi_{12,q}^{\text{el},R}(\omega) &= \Pi_{21,q}^{\text{el},A}(-\omega), \\ \tilde{\Pi}_{22,q}^{\text{el},R}(\omega) &= \tilde{\Pi}_{11,q}^{\text{el},R}(\omega).\end{aligned}\tag{6.24}$$

Here, $u_{\mathbf{k},\alpha} = \sqrt{\frac{1}{2}\left(1 + \frac{\xi_{\mathbf{k},\alpha}}{E_{\alpha}(\mathbf{k})}\right)}$ and $v_{\mathbf{k},\alpha} = \sqrt{\frac{1}{2}\left(1 - \frac{\xi_{\mathbf{k},\alpha}}{E_{\alpha}(\mathbf{k})}\right)}$ are the superconducting coherence factors and $E_{\alpha}(\mathbf{k}) = \sqrt{\xi_{\alpha}(\mathbf{k})^2 + |\Delta_{\alpha}|^2}$ the superconducting quasiparticle dispersion of the conduction and valence band. The corresponding Keldysh propagators are related by Eq. (6.23). The explicit form of the retarded normal and anomalous self-energies in the superconducting state in Eq. (6.24) are given in Appendix D for the realistic parameter choice $v_F |\mathbf{q}| \ll 2\Delta$ and symmetric bands. In Figure 6.4 they are shown for the important region $\omega \approx 0$, which corresponds to $\omega_{\mathbf{q}} \approx eV$, and obviously both the normal and anomalous self-energy show a very similar behavior. Their imaginary part vanishes for $|\omega| < 2\Delta$. At the border of these regions the functions exhibit a jump in the imaginary part of size

$$\lim_{\delta \rightarrow 0^+} |\text{Im } \Pi_{21,q}^{\text{el},R}(eV_0 + 2\Delta + \delta)| = \frac{\pi^2}{2} |g_0|^2 \nu_F \frac{\Delta}{v_F |\mathbf{q}|},\tag{6.25}$$

then they remain constant over a frequency window of the order of $v_F^2 |\mathbf{q}|^2 / \Delta$. This plateau comes from the finite momentum $\mathbf{q} \neq 0$ that cuts off the squareroot divergence⁴ that would occur for zero momentum [211]. The imaginary part finally decays towards the result for normal conducting leads, see Eq. (6.22), further away from the gapped region. The Kramers-Kronig-relations [224] directly tell us that a jump in the imaginary part is related to a logarithmic divergence in the real part. Since the electron-photon coupling $\nu_F |g_0|^2 \ll \Delta$ is the smallest energy scale of the system, see also Section 6.1.2, this logarithmic divergence is only of importance very close to $|\omega| = 2\Delta$.

⁴Note, that it is absolutely essential to take into account a finite momentum, since otherwise we could never realize a steady-state in our model as we will see later.

As in the normal state, the imaginary part is proportional to the absorption/emission rate of the LED. Thus, the vanishing of the imaginary part for $|\omega| < 2\Delta$ can be understood since there can be no photons absorbed or emitted for photons with energy $\omega_{\mathbf{q}} \in [eV - 2\Delta, eV + 2\Delta]$ for zero temperature, which is easily seen in Figure 6.3. However, the coherence peaks in the fermionic DOS at $\pm\Delta$ lead to an enhanced emission and absorption of photons for photon energies that couple the quasiparticles at the superconducting band edges, which explains the enhancement of the imaginary part in comparison to the normal state at energies $|\omega| > 2\Delta$. For these energies the divergence of the real part indicates the strong renormalization of the photon dispersion due to the coupling to the Bogoliubov quasiparticles at the coherence peaks.

6.2.3. Role of the photon bath

In Section 6.2.2.1 the issue of a LASER instability has been mentioned and here we will show how the external bath can serve as an absorption reservoir for achieving a steady state for our model. The coupling to the bath system gives rise to the self-energy $\hat{\Pi}^{\text{bath}}$ with the retarded component

$$\hat{\Pi}_{\mathbf{q}}^{\text{bath},R}(\omega) = \begin{pmatrix} 0 & -\Pi_{\mathbf{q}}^{\text{bath},R}(-\omega + eV) \\ \Pi_{\mathbf{q}}^{\text{bath},R}(\omega + eV) & 0 \end{pmatrix} \quad (6.26)$$

and

$$\Pi_{\mathbf{q}}^{\text{bath},R}(\omega) = -i\pi |\lambda(\omega)|^2 \rho_{\text{bath}}(\omega). \quad (6.27)$$

For the derivation we used the usual assumptions [222, 223] that the coupling $\lambda_{\mathbf{p},\mathbf{p}'} = \lambda(\omega_{\mathbf{p}})$ is only depending on the photon energy and defined $\rho_{\text{bath}}(\omega)$ as the bath photon DOS. Since the microscopic details of the external bath are in general unknown, we assume an Ohmic bath

$$\pi |\lambda(\omega)|^2 \rho_{\text{bath}}(\omega) = \eta \theta(\omega) \frac{\omega^2}{\omega^2 + \Lambda^2} \quad (6.28)$$

with low-energy cutoff $\Lambda \ll eV$ that quickly saturates at the constant absorption rate⁵ η for $\omega > \Lambda$. We neglect any real part, which is assumed to be basically featureless and unimportant for our following analysis. The vanishing of the imaginary part of the retarded self-energy in Eq. (6.27) for $\omega \rightarrow 0$ is of crucial importance for the proper structure of the Keldysh self-energy⁶

$$\hat{\Pi}_{\mathbf{q}}^{\text{bath},K}(\omega, T) = \begin{pmatrix} 0 & \Pi_{\mathbf{q}}^{\text{bath},K}(-\omega + eV) \\ \Pi_{\mathbf{q}}^{\text{bath},K}(\omega + eV) & 0 \end{pmatrix} \quad (6.29)$$

with component

$$\Pi_{\mathbf{q}}^{\text{bath},K}(\omega) = \coth\left(\frac{\omega}{2T_B}\right) [\Pi_{\mathbf{q}}^{\text{bath},R}(\omega) - \Pi_{\mathbf{q}}^{\text{bath},A}(\omega)], \quad (6.30)$$

that would otherwise diverge for particle propagator for $\omega \rightarrow -eV$.

⁵The bath self-energy corresponds to a absorption channel for the photons, because the imaginary part is negative.

⁶We assume the external bath to be at thermal equilibrium with temperature T_B , however general distribution functions can be easily incorporated.

6.2.4. Photon propagators

The photon propagators can be easily calculated by solving

$$[\hat{D}_{0,q}^{-1} - \hat{\Pi}_q] \hat{D}_q = \hat{\mathbb{1}}, \quad (6.31)$$

where we Fourier-transformed our effective action (6.19) and use the usual convention $q = (\omega, \mathbf{q})$. Note that in contrast to Ref. [202] we do not have to perform a more complicated Wigner-transformation to obtain the photon propagator due to the gauge transformation of our photon fields. We can separate the Keldysh and retarded/advanced component of Eq. (6.31) as

$$([\mathring{D}_{0,q}^{R/A}]^{-1} - \mathring{\Pi}_q^{R/A}) \mathring{D}_q^{R/A} = \mathring{\mathbb{1}}, \quad (6.32)$$

$$([\mathring{D}_{0,q}^R]^{-1} - \mathring{\Pi}_q^R) \mathring{D}_q^K = \mathring{\Pi}_q^K \mathring{D}_q^A. \quad (6.33)$$

Solving these equations for the dressed retarded and Keldysh photon propagators yields

$$\begin{aligned} \mathring{D}_q^R(\omega) &= \frac{\tilde{\Pi}_{11,\mathbf{q}}^R(\omega) \cdot [\cos(\phi_0) \cdot \hat{\mathbb{1}} - i \sin(\phi_0) \cdot \hat{\sigma}_z] + [\omega + \bar{\omega}_{\mathbf{q}} + \Pi_{12,\mathbf{q}}^R(\omega)] \cdot \hat{\sigma}_+ - [\omega - \bar{\omega}_{\mathbf{q}} - \Pi_{21,\mathbf{q}}^R(\omega)] \cdot \hat{\sigma}_-}{[\omega - \bar{\omega}_{\mathbf{q}} - \Pi_{21,\mathbf{q}}^R(\omega)] [\omega + \bar{\omega}_{\mathbf{q}} + \Pi_{12,\mathbf{q}}^R(\omega)] + [\tilde{\Pi}_{11,\mathbf{q}}^R(\omega)]^2}, \\ \mathring{D}_q^K(\omega) &= \mathring{D}_q^R(\omega) \mathring{\Pi}_q^K(\omega) \mathring{D}_q^A(\omega). \end{aligned} \quad (6.34)$$

By inverting the Dyson equation we have summed up the complete RPA series of bubble diagrams from the electronic particle-hole processes and the absorption contributions of the bath. The imaginary part of the retarded propagator determines the excitation spectrum of the photon. When looking at energies $|\omega| \gtrsim 2\Delta$, which corresponds to photons with frequency $\approx eV \pm 2\Delta$, one can observe an enhanced spectral weight for these energies. This corresponds to photon-exciton bound states or polaritons, where a photon creates a particle-hole pair that decays into a photon that creates a particle-hole pair and so on. Since the DOS of the two superconducting bands diverge at $\pm|\Delta|$ (measured from the the Fermi energy), only scattering processes with a photon matching the energy difference $\approx eV_0 \pm 2\Delta$ give rise to a large effective coupling between photons and electrons and to the formation of polaritons.

6.3. Luminescence and Squeezing of the SLED

In this section, we discuss the properties of the light that is emitted by the SLED, both in the normal and superconducting state. Therefore, we use the photon propagators that contain all the information about the luminescence and squeezing properties.

6.3.1. Luminescence

We define the luminescence as the expectation value of the number of photons in a state with momentum \mathbf{q}

$$\mathcal{L}(\omega_{\mathbf{q}}) = \langle b_{\mathbf{q}}^\dagger(t) b_{\mathbf{q}}(t) \rangle = \langle B_{\mathbf{q}}^\dagger(t) B_{\mathbf{q}}(t) \rangle = i \int_{-\infty}^{\infty} \frac{d\omega}{2\pi} D_{12,\mathbf{q}}^<(\omega) \quad (6.35)$$

with the lesser propagator $D_{12,\mathbf{q}}^<(t,t') = -i\langle b_{\mathbf{q}}^{\dagger}(t)\bar{b}_{\mathbf{q}}^{-}(t')\rangle$, that can be expressed via a linear combination $D_{12,\mathbf{q}}^< = \frac{1}{2}(D_{12,\mathbf{q}}^K - D_{12,\mathbf{q}}^R + D_{12,\mathbf{q}}^A)$ of retarded, advanced and Keldysh Green's functions. For the numerical evaluation of the luminescence we used parameters that are consistent with our discussion in Section 6.1.2. The superconducting gap, which is of the order $\Delta \sim 1\text{meV}$, is used to express all other parameters in the following. We explicitly set $|g_0|^2 \nu_F = \Delta/50$, $v_F/c = 10^{-3}$ and $eV = 1000\Delta$. Further, we assume an electronic normal state DOS $\nu(\epsilon) = \nu_F \sqrt{1 + \epsilon/E_F}$ of a three dimensional electron gas with Fermi energy $E_F = V/10 = 100\Delta$. The bath decay rate η has to be chosen in such a way that the analytic structure of our theory remains intact, therefore it has to be larger than the maximum of $\text{Im} \Pi_{21,\mathbf{q}}^{\text{el},R}(\omega)$, see Section 6.4. This corresponds to a minimum

$$\eta_{\min} = \frac{\pi^2 |g_0|^2 \nu_F \Delta}{2(v_F/c)\omega_{\mathbf{q}}}. \quad (6.36)$$

We choose $\eta = 1.5\eta_{\min}$ here since even larger decay rates will result in a larger linewidth for the photons, which will smear out the features of the SLED with the energy scale $\sim \Delta$. For smaller $\eta < \eta_{\min}$ our steady state is unstable and the system exhibits lasing.

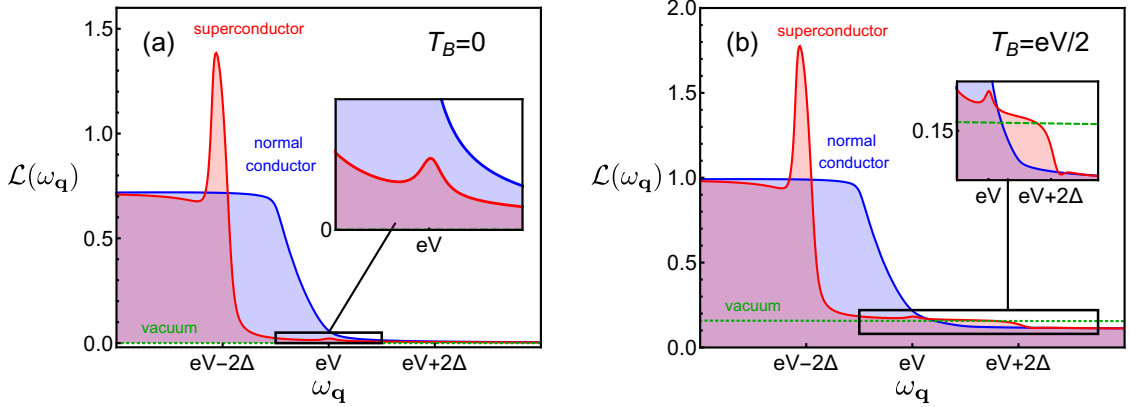


Figure 6.5.: Luminescence $\mathcal{L}(\omega_{\mathbf{q}}) = \langle b_{\mathbf{q}}^{\dagger} b_{\mathbf{q}} \rangle$ in the superconducting (red) and normal conducting state (blue) as a function of photon frequency $\omega_{\mathbf{q}} = c|\mathbf{q}|$: (a) Bath temperature $T_B = 0$. In the superconducting state an enhanced luminescence around $\omega_{\mathbf{q}} = eV_0 - 2|\Delta|$ is found due to quasi-particle transitions from the band-edges of the superconducting dispersion. In the inset also shows an additional peak at resonance $\omega_{\mathbf{q}} = eV_0$ from Cooper pair tunneling. (b) High bath temperature $T_B = V/2$ which induces thermal photons in the LED. These thermal photons can now also be absorbed via the creation of particle-hole pairs for $\omega_{\mathbf{q}} > eV$ (normal state) or $\omega_{\mathbf{q}} > eV + 2\Delta$ (superconductor), which can be clearly seen in the inset. Adapted from Ref. [202].

In Figure 6.5 we present the luminescence for different external bath temperatures, which models different initial distribution functions when the LED is turned off ($V = 0$). Let us first consider the case $T_B = 0$ in Figure 6.5(a), where no background photons are present. When biasing the LED in the normal state (blue curve) we see that it only produces photons with energy $\omega_{\mathbf{q}} < eV$, which becomes clear because electronic transitions from the conduction to the valence band are only allowed for this energy at $T_F = 0$, see Figure 6.3. Similar to the normal state self-energy (6.22) the frequency scale of the increase of the luminescence seen is given by $v_F |\mathbf{q}|$ here, where $|\mathbf{q}| = eV/c$ is a small momentum. When the external leads are superconducting a clear peak in the luminescence at $\omega_{\mathbf{q}} = eV - 2\Delta$ is observed, which comes from the large number of electrons and holes that are pushed out of the gap region to the superconducting band edges and recombine via the emission of a

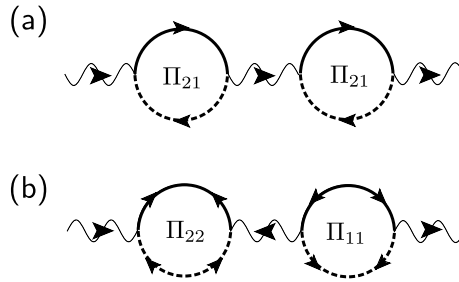


Figure 6.6.: Contribution to the luminescence in the superconducting state in next-to-leading order g_0^4 : (a) Normal contribution from the Bogoliubov quasi-particle contributing to the peak at $\omega_{\mathbf{q}} = eV - 2\Delta$, (b) Anomalous contribution giving rise to the Cooper pair peak in the luminescence. Taken from Ref. [202].

photon, see red transitions in Figure 6.1. An enhancement of the photon excitations for this energy has been seen in the experiments of Ref. [214], however they looked at a system where only the n -doped side was coupled to a superconducting lead⁷. A second interesting feature in the superconducting state is the occurrence of a Cooper pair peak at resonance $\omega_{\mathbf{q}}$, which stems from the recombination of electronic Cooper pairs with hole Cooper pairs as shown as the green transitions in Figure 6.1. This peaks comes from second order processes shown in Figure 6.6(b) involving the anomalous self-energies Π_{11}, Π_{22} . These contributions of higher order are taken into account automatically in our calculation via the self-consistent RPA summation and is a feature the leading order analysis of Ref. [211] misses. The peaks in the luminescence are characterized by a linewidth $\delta\omega = \max[\eta, (\frac{v_F|\mathbf{q}|}{2\Delta})^2|\Delta|]$.

We also considered the possibility of thermal photons in the LED, which can be incorporated easily by the assumption of a finite bath temperature $T_B = eV/2$. In the normal state, photons can not only be created by the LED for photon frequencies $\omega_{\mathbf{q}} < eV$, but also the possible absorption of the thermal photons for $\omega_{\mathbf{q}} > eV$ can be seen clearly in Figure 6.5(b) when comparing the normal state photon distribution with the vacuum. In the superconducting state, this absorption is forbidden up to frequencies $\omega_{\mathbf{q}} > eV + 2\Delta$ because of the superconducting order parameters in the conduction and valence bands. In addition, one can clearly observe an additional absorption dip at $\omega_{\mathbf{q}} = eV + 2\Delta$ in the presence of superconductivity.

6.3.2. Photon squeezing

One of the main motivations for the SLED setup discussed in this chapter has been the question if it is possible to transfer the coherence and entanglement of Cooper pairs to the emitted light. In this section, we will investigate the statistical properties of the photons and show that the SLED can in principle produces two-mode squeezed light. This can be traced back to the occurrence of anomalous photon expectation values $\langle b_{\mathbf{q}}^\dagger b_{-\mathbf{q}}^\dagger \rangle$ induced by the superconducting state of the electrons, which can push the uncertainty of one two-mode quadrature operator⁸ below the value of coherent light. In contrast to Ref. [211], where the light-squeezing at resonance $\omega_{\mathbf{q}} = eV$ was only determined in leading order (where the photon number vanishes), we here also incorporate self-consistently a finite photon number

⁷We also performed some calculations based on our formalism with only one superconducting lead. Here, we could only observe such an enhancement at $\omega_{\mathbf{q}} = eV - \Delta$ when one of the two bands is significantly heavier than the other band.

⁸For a detailed introduction into quantum optics see e.g. the book by Scully [225].

$\langle b_q^\dagger b_q \rangle$ for the squeezed photon modes. This allows for a quantitative description of the squeezing properties for our theoretical model.

Since the recombination of Cooper pairs with net momentum zero can only lead to the emission of two entangled photons with momenta \mathbf{q} and $-\mathbf{q}$, the interesting two-mode quadrature operator is

$$\begin{aligned}\hat{A}_q^+ &= \frac{1}{2^{3/2}} [\tilde{b}_q^\dagger + \tilde{b}_{-q}^\dagger + \text{h.c.}], \\ \hat{A}_q^- &= \frac{1}{2^{3/2}i} [\tilde{b}_q^\dagger + \tilde{b}_{-q}^\dagger - \text{h.c.}],\end{aligned}\quad (6.37)$$

where we defined the photon operators in the rotating frame $\tilde{b}_q = \hat{b}_q e^{i\omega_q t}$. The fluctuations of the operators can be easily calculated for our model as

$$(\Delta \hat{A}_q^\pm)^2 = \langle (\Delta \hat{A}_q^\pm)^2 \rangle = \langle (\hat{A}_q^\pm - \langle \hat{A}_q^\pm \rangle)^2 \rangle = \frac{1 + 2\langle \tilde{b}_q^\dagger \tilde{b}_q \rangle \pm 2 \mathbf{Re} \langle \tilde{b}_q \tilde{b}_{-q} \rangle}{4}. \quad (6.38)$$

The Heisenberg uncertainty principle tells us that $(\Delta \hat{A}_q^+)(\Delta \hat{A}_q^-) \geq \frac{1}{2} |\langle [\hat{A}_q^+, \hat{A}_q^-] \rangle| = \frac{1}{4}$. The state is then called squeezed if for one of the quadrature operators the fluctuations fall below $\frac{1}{4}$. From Eq. (6.40) we can see that squeezing can only occur if the luminescence $\mathcal{L}(\omega_q) = \langle \tilde{b}_q^\dagger \tilde{b}_q \rangle$ is smaller than the magnitude of the anomalous luminescence, which we define as

$$\begin{aligned}\mathcal{L}_A(\omega_q) &= e^{i2(eV - \omega_q)t} e^{i\phi_0} \langle \tilde{b}_q(t) \tilde{b}_{-q}(t) \rangle = e^{i\phi_0} \langle B_q(t) B_{-q}(t) \rangle \\ &= e^{i\phi_0} \int_{-\infty}^{\infty} \frac{d\omega}{2\pi} D_{12,q}^<(\omega)\end{aligned}\quad (6.39)$$

Therefore, we restrict ourselves to small bath temperatures to reduce the number of thermal photons in the SLED. For the photons on resonance $\omega_q = eV$ the electro-luminescence is of order g_0^4 , whereas the anomalous luminescence is already of order g_0^2 . When separating the amplitude and the phase of the anomalous luminescence we can express the quadrature amplitude as

$$(\Delta \hat{A}_q^\pm)^2 = \frac{1 + 2\mathcal{L}(\omega_q) \pm 2 |\mathcal{L}_A(\omega_q)| \cos[2(\omega_q - eV)t - \phi_0 + \arg[\mathcal{L}_A(\omega_q)]]}{4}. \quad (6.40)$$

From this expression it becomes clear that squeezing can only occur if $|\mathcal{L}_A(\omega_q)| > \mathcal{L}(\omega_q)$, which is the case for the photons on resonance that show a peak at $\omega_q = eV$ in the anomalous luminescence, see Figure 6.7(a). The origin of the strong squeezing and therefore entanglement of the photon pairs on resonance comes from the coherent recombination of Cooper electron pairs of the conduction band with Cooper hole pairs of the valence band, as is depicted in Figure 6.1. We emphasize, that it is not necessary that the two photons emerge from a single cooper pair since different pairs are phase coherent. Thus, even photons that emerge from two different cooper pairs will be entangled (for momenta \mathbf{q} and $-\mathbf{q}$), because the emission is from a condensate of Cooper pairs and not due to isolated Cooper pairs as it would be in a small quantum dot. There is also a second strong peak in the anomalous luminescence at $\omega_q = eV - 2\Delta$ coming from the Bogoliubov

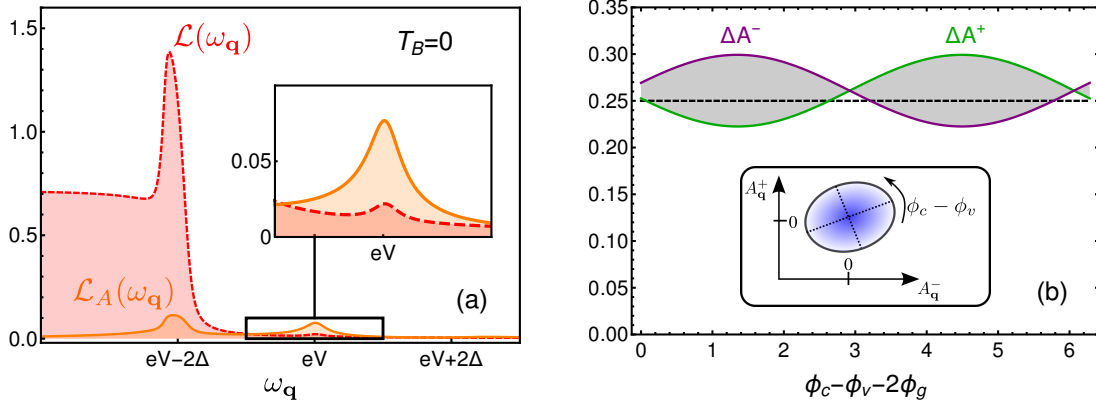


Figure 6.7.: Squeezing properties of the SLED for superconducting leads: (a) Normal and anomalous luminescence for the parameters defined in Section 6.3.1, (b) Quadrature amplitude ΔA_q^\pm for photons on resonance $\omega_q = eV$ showing a squeezed light state that can fall below the symmetric Heisenberg uncertainty limit $1/4$. The inset shows how the (initial) squeezing angle can be tuned by changing the relative phase $\phi_c - \phi_v$ between the two superconducting leads. Adapted from Ref. [202].

quasiparticle recombination⁹, however for these photons there is no squeezing because the normal luminescence dominates for these energies.

In Figure 6.7(b) the fluctuation of the quadrature amplitudes ΔA_q^\pm are plotted over the difference of the phases of the superconducting order parameters in the conduction and valence band. For our realistic choice of parameters one of the two fluctuations fall below the Heisenberg uncertainty limit for a broad range of relative phases. In an experiment we can control the relative phase $\phi_c - \phi_v$ by inducing a magnetic flux into a parallel configuration of SLED, which is effectively a Superconducting Quantum Interference Device (SQUID). Therefore, the squeezing properties of the SLED can be conveniently controlled by an external magnetic field.

6.4. Steady state and LASER condition

In Section 6.2.2 and 6.3.1 we already discussed shortly the possibility of our setup to generate a lasing state if the external absorption mechanism of the bath is too small to absorb the number of photons emitted by the SLED. Here, we will discuss this issue in more detail for our model and show two distinct ways to understand the steady state conditions for our parameters.

6.4.1. Lasing condition from effective action

Let us follow Ref. [226] and derive the lasing condition from the properties of our non-equilibrium Green's functions. We discuss first the normal state and can generalize the result to the case of superconducting leads. As stated before the luminescence can be expressed in terms of the retarded, advanced and Keldysh propagators. Their inverse can

⁹The third peak at $\omega_q = eV + 2\Delta$ is really small and is only due to the finite photon lifetime, because for $T_F = T_B = 0$ there are never any photons or fermions present at this energy.

be conveniently parametrized via

$$\begin{aligned} [D_{12,\mathbf{q}}^{R/A}(\omega)]^{-1} &= A_{\mathbf{q}}(\omega) \pm iB_{\mathbf{q}}(\omega) \\ [D_{12,\mathbf{q}}^K(\omega)]^{-1} &= iC_{\mathbf{q}}(\omega), \end{aligned} \quad (6.41)$$

where $A_{\mathbf{q}}(\omega)$, $B_{\mathbf{q}}(\omega)$ and $C_{\mathbf{q}}(\omega)$ are defined as real functions. $A_{\mathbf{q}}(\omega)$ is the real part of the inverse retarded propagator and describes the excitation spectrum of the photons, whereas the imaginary part $B_{\mathbf{q}}(\omega)$ contains the information about the decay/emission of the LED photons and the Keldysh component knows the details about the occupation of the mode. It is necessary that if the real part has a resonance at $\omega_{\mathbf{q}}^*$, thus $A_{\mathbf{q}}(\omega_{\mathbf{q}}^*) = 0$, the corresponding imaginary part $B_{\mathbf{q}}(\omega_{\mathbf{q}}^*) > 0$ has to be positive to ensure the proper analytical structure of the retarded propagator with the poles lying in the lower complex plane.

Inverting the Keldysh matrix in Eq. (6.13) we obtain the usual results for the Green's functions

$$\begin{aligned} D_{12,\mathbf{q}}^{R/A}(\omega) &= [A_{\mathbf{q}}(\omega) \pm iB_{\mathbf{q}}(\omega)]^{-1} \\ D_{12,\mathbf{q}}^K(\omega) &= -\frac{[D_{12,\mathbf{q}}^K(\omega)]^{-1}}{[D_{12,\mathbf{q}}^R(\omega)]^{-1}[D_{12,\mathbf{q}}^A(\omega)]^{-1}}. \end{aligned} \quad (6.42)$$

In the normal state, we can explicitly write down

$$\begin{aligned} A_{\mathbf{q}}(\omega) &= \omega - \bar{\omega}_{\mathbf{q}} = \omega - \omega_{\mathbf{q}} + eV \\ B_{\mathbf{q}}(\omega) &= -\mathbf{Im} \Pi_{21,\mathbf{q}}^{\text{el},R}(\omega) - \mathbf{Im} \Pi_{21,\mathbf{q}}^{\text{bath},R}(\omega), \end{aligned} \quad (6.43)$$

where we neglected the real parts of the self-energies because they only give an unimportant shift for the photon dispersion. We can also express the lesser propagator

$$D_{12,\mathbf{q}}^<(\omega) = -\frac{i}{2} \frac{C_{\mathbf{q}}(\omega) - 2B_{\mathbf{q}}(\omega)}{[A_{\mathbf{q}}(\omega)]^2 + [B_{\mathbf{q}}(\omega)]^2}. \quad (6.44)$$

and thereby the luminescence via the above defined functions. We can explicitly calculate the luminescence for a given \mathbf{q} and $\bar{\omega}_{\mathbf{q}}$ under the assumption that the change in the imaginary part is sub-dominant compared to the real part

$$\begin{aligned} \mathcal{L}(\omega_{\mathbf{q}}) &= \frac{1}{2} \int_{-\infty}^{\infty} \frac{d\omega}{2\pi} \frac{C_{\mathbf{q}}(\omega) - 2B_{\mathbf{q}}(\omega)}{[A_{\mathbf{q}}(\omega)]^2 + [B_{\mathbf{q}}(\omega)]^2} \approx \frac{1}{2} \int_{-\infty}^{\infty} \frac{d\omega}{2\pi} \frac{C_{\mathbf{q}}(\bar{\omega}_{\mathbf{q}}) - 2B_{\mathbf{q}}(\bar{\omega}_{\mathbf{q}})}{[\omega - \bar{\omega}_{\mathbf{q}}]^2 + [B_{\mathbf{q}}(\bar{\omega}_{\mathbf{q}})]^2} \\ &= \frac{C_{\mathbf{q}}(\bar{\omega}_{\mathbf{q}}) - 2B_{\mathbf{q}}(\bar{\omega}_{\mathbf{q}})}{4|B_{\mathbf{q}}(\bar{\omega}_{\mathbf{q}})|} = \frac{C_{\mathbf{q}}(\bar{\omega}_{\mathbf{q}})}{4|B_{\mathbf{q}}(\bar{\omega}_{\mathbf{q}})|} - \frac{\text{sign}[B_{\mathbf{q}}(\bar{\omega}_{\mathbf{q}})]}{2} \end{aligned} \quad (6.45)$$

We can directly see that a zero in the imaginary part $B_{\mathbf{q}}(\bar{\omega}_{\mathbf{q}})$ leads to a diverging photon number for a certain mode if the Keldysh component $C_{\mathbf{q}}(\bar{\omega}_{\mathbf{q}})$ is not able to compensate for this. For us, the imaginary part $B_{\mathbf{q}}(\omega)$ consists of two contributions as can be seen in Eq. (6.43): The electronic feedback $\mathbf{Im} \Pi_{21,\mathbf{q}}^{\text{el},R}(\omega)$ and the photon bath self-energy $\mathbf{Im} \Pi_{21,\mathbf{q}}^{\text{bath},R}(\omega)$. In the interesting region $\omega_{\mathbf{q}} \approx eV$ and thus $\bar{\omega}_{\mathbf{q}} \approx 0$ the bath decay rate is

constant $\mathbf{Im} \Pi_{21,\mathbf{q}}^{\text{bath},R}(0) = -\eta < 0$, see Section 6.2.3. The electron-induced self-energy has a sign-change for $\omega = 0$, such that the imaginary part reads for $\omega \approx 0$

$$B_{\mathbf{q}}(\omega) = \pi |g_0|^2 \nu_F \text{sign}(\omega) \min\left[\frac{|\omega|}{v_F |\mathbf{q}|}, 1\right] + \eta \quad (6.46)$$

and the Keldysh component is for $T_B \ll eV$ given by

$$C_{\mathbf{q}}(\omega) = \pi |g_0|^2 \nu_F \min\left[\frac{|\omega|}{v_F |\mathbf{q}|}, 1\right] + \eta. \quad (6.47)$$

Obviously, the Keldysh component will not be zero. Therefore, if

$$\pi |g_0|^2 \nu_F = \eta_{\min} > \eta \quad (6.48)$$

we expect a diverging photon number for photons with energy

$$\pi |g_0|^2 \nu_F \frac{\bar{\omega}_{\mathbf{q}}}{v_F |\mathbf{q}|} + \eta < 0 \quad \rightarrow \quad \omega_{\mathbf{q}} < eV - \frac{\eta v_F |\mathbf{q}|}{\pi |g_0|^2 \nu_F} \quad (6.49)$$

Thus, whenever we have simultaneous zero of $A_{\mathbf{q}}(\omega^*)$ and $B_{\mathbf{q}}(\omega^*)$ the mode with the momentum \mathbf{q} will be macroscopically occupied, which characterizes the lasing regime for the system. A similar approach also works in the superconducting state, where the lasing threshold reads

$$\eta_{\min} = \frac{\pi^2}{2} |g_0|^2 \nu_F \frac{\Delta}{v_F |\mathbf{q}|}. \quad (6.50)$$

for the photons at $\omega_{\mathbf{q}} \approx eV - 2\Delta$. This implies, that in the superconducting state the SLED it is easier to get a LASER due to the increased photon emission for these energies. Let us also note that the sign-change in the imaginary part can also be understood as a shift of the ‘‘chemical potential’’ for the photons to higher energies. The divergence of the luminescence then appears at this position of the new chemical potential.

6.4.2. Rate equation approach

An alternative way to obtain the lasing conditions is to derive the rate equations for the photon occupation number. Thus, we look at the change of the photon number $\hat{n}_{\text{ph}} = \sum_{\mathbf{q}} b_{\mathbf{q}}^\dagger b_{\mathbf{q}}$, that is given using the Heisenberg equation of motion

$$\Gamma_{\text{ph}} = \frac{d}{dt} \langle \hat{n}_{\text{ph}}(t) \rangle = -i \langle [\hat{n}_{\text{ph}}(t), \hat{H}(t)] \rangle, \quad (6.51)$$

The calculation of the expectation value can be done in analogy to the derivation of the elastic and inelastic tunneling currents in Chapter 3 using the Keldysh technique. The corresponding diagrams that occur in leading order of the electron-photon coupling g_0 are shown in Figure 6.8(a) and (d). The (a) diagram describes the emission/absorption of

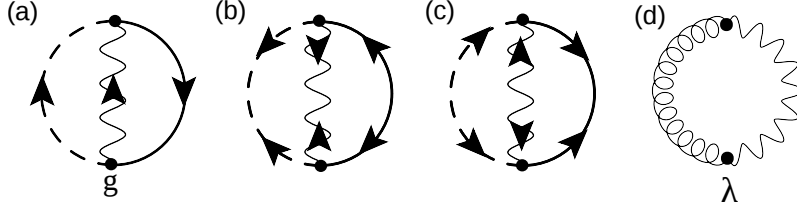


Figure 6.8.: Feynman graphs of the rate equation: Solid (dashed) lines denote conduction (valence) electron propagators, solid wiggly lines denote the free photon propagators and the curly lines denote bath photon propagators. The first three diagrams represent the contribution to the rate from emission and absorption of photons involving electronic transitions in the superconducting LED. The fourth graph describes the photon exchange with the external bath. Adapted from Ref. [202].

photons due to the recombination of electron-hole excitations of the Bogoliubov quasiparticles. Diagram (d) describes the exchange of photons of the SLED with the external bath. Further, the additional contributions (b) and (c) can occur in the superconducting state. Since they involve anomalous electronic and photonic propagators, thus they describe the decay and absorptions of Cooper pairs along the junction. The diagrams can be compactly written down using the propagators and self-energies evaluated in the previous parts of this chapter as $\Gamma = \Gamma_{\text{bath}} + \Gamma_{\text{SLED}}$ with

$$\Gamma_{\text{bath}} = -2 \sum_{\mathbf{q}} \int \frac{d\omega}{\pi} \mathbf{Im} \Pi_{21,\mathbf{q}}^{\text{bath},R}(\omega - eV) \mathbf{Im} D_{12,\mathbf{q}}^A(\omega - eV) [n^{\text{bath}}(\omega) - n_{\mathbf{q}}(\omega)] \quad (6.52)$$

$$\begin{aligned} \Gamma_{\text{SLED}} = & 2 \sum_{\mathbf{q}} \int \frac{d\omega}{\pi} \mathbf{Im} \Pi_{21,\mathbf{q}}^{\text{el},R}(\omega - eV) \mathbf{Im} D_{12,\mathbf{q}}^A(\omega - eV) \times \\ & \left([1 + n_{\mathbf{q}}(\omega)] \theta(eV - \omega) + n_{\mathbf{q}}(\omega) \theta(\omega - eV) \right) \\ & - \frac{1}{\pi} \sum_{\mathbf{q}} \int \frac{d\omega}{\pi} \mathbf{Re} [\tilde{\Pi}_{11,\mathbf{q}}^{\text{el},R}(\omega) D_{11,\mathbf{q}}^A(\omega)], \end{aligned} \quad (6.53)$$

where $n_{\mathbf{q}}(\omega)$ and $n^{\text{bath}}(\omega)$ are the occupation function for the SLED photons and the bath photons respectively. The bath contribution to the rate equation Γ_{bath} drives the SLED occupation number towards the bath photon distribution $n_{\mathbf{q}}(\omega) \rightarrow n^{\text{bath}}(\omega)$. The electronic contributions Γ_{SLED} produces photons via spontaneous and stimulated emission for energies $\omega < eV$ and absorbs photons for $\omega > eV$, which is apparent from Figure 6.3. The last contribution mainly contributes to the tunneling of the Cooper pairs on resonance, which is a process of order g_0^4 .

Let us continue by analyzing the leading order contribution in g_0 . Here, it is sufficient to use the bare photon propagators $\mathbf{Im} D_{12,\mathbf{q}}^R(\omega) \approx -\pi \delta(\omega + eV - \omega)$ and $\mathbf{Im} D_{1,\mathbf{q}}^R(\omega) \approx 0$, because the occurring self-energies are already of order g_0^2 . As a result, we obtain the leading order rate equation

$$\begin{aligned} \Gamma = & -2 \sum_{\mathbf{q}} \left[\mathbf{Im} \Pi_{21,\mathbf{q}}^{\text{bath},R}(\omega_{\mathbf{q}} - eV) [n^{\text{bath}}(\omega_{\mathbf{q}}) - n(\omega_{\mathbf{q}})] \right. \\ & \left. + \mathbf{Im} \Pi_{21,\mathbf{q}}^{\text{el},R}(\omega_{\mathbf{q}} - eV) \left([1 + n(\omega_{\mathbf{q}})] \theta(eV - \omega_{\mathbf{q}}) + n(\omega_{\mathbf{q}}) \theta(\omega_{\mathbf{q}} - eV) \right) \right] \\ = & \sum_{\mathbf{q}} \Gamma_{\mathbf{q}}, \end{aligned} \quad (6.54)$$

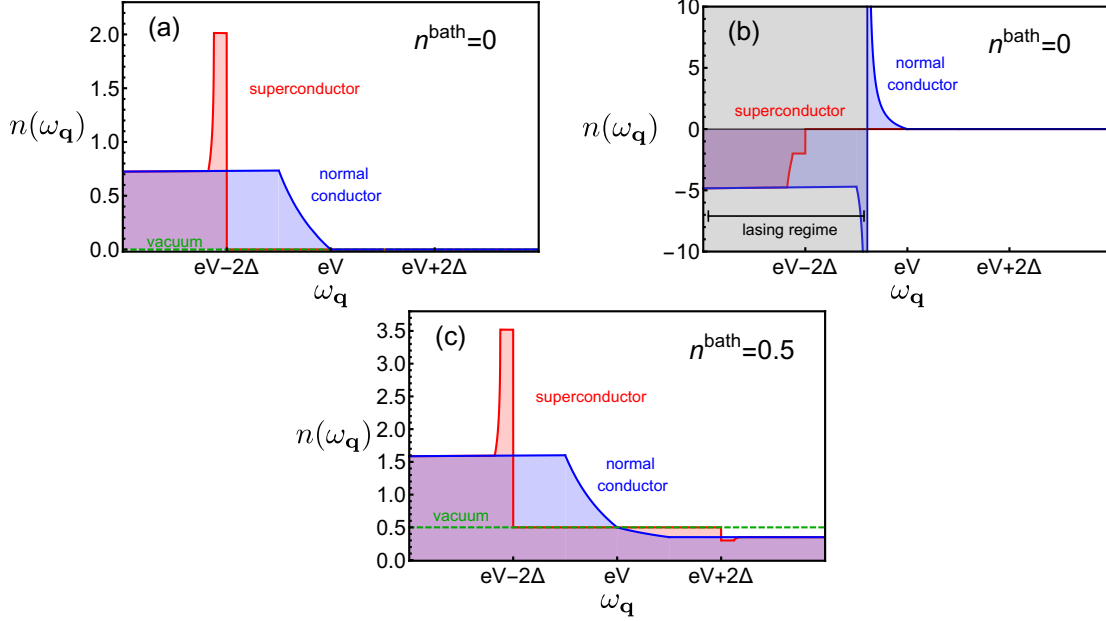


Figure 6.9.: Photon occupation for the SLED in leading order g_0 in the normal (blue), superconducting (red) and vacuum state (green): (a) Photon number for $\eta > \eta_{\min}$ in the steady state without thermal photons in the system, (b) SLED with $\eta < \eta_{\min}$, where a lasing instability occurs for the frequencies in the grey shaded area, (c) Photon number for $\eta > \eta_{\min}$, but with thermal photons, which can be absorbed for $\omega_q > eV$ in the normal and $\omega_q > eV + 2\Delta$ in the superconducting state.

where the SLED photon number now only depends on the photon energy ω_q . In the regime of interest $\omega_q \approx eV$ the bath self-energy $\mathbf{Im} \Pi_{21,q}^{\text{bath},R}(\omega_q - eV) \simeq -\eta < 0$ is constant and positive and the electron-induced self-energy has a sign change like $\text{sign}[\mathbf{Im} \Pi_{21,q}^{\text{el},R}(\omega)] = -\text{sign}(\omega)$. In the steady state, the photon emission and absorptions rates Γ_q for each mode \mathbf{q} have to be balanced. Therefore we can demand $\Gamma_q = 0$ in the steady state, resulting in the SLED occupation factor

$$n(\omega_q) = \frac{|\mathbf{Im} \Pi_{21,q}^{\text{el},R}(\omega_q - eV)| \theta(eV_0 - \omega_q) + |\mathbf{Im} \Pi_q^{\text{bath},R}(\omega_q - eV)| n^{\text{bath}}(\omega_q)}{-\mathbf{Im} \Pi_q^{\text{bath},R}(\omega_q - eV) - \mathbf{Im} \Pi_{21,q}^{\text{el},R}(\omega_q - eV)}. \quad (6.55)$$

For $\omega_q > eV$ the distribution function is always positive and finite, whereas for $\omega_q < eV$ the denominator with the imaginary part of the total photon self-energy $\Pi_{21,q}^R(\omega) = \Pi_q^{\text{bath},R}(\omega) - \Pi_{21,q}^{\text{el},R}(\omega)$ may become zero. At this point the photon number diverges, which indicates the lasing instability of the system and is similar to the conditions $\eta < \eta_{\min}$ derived in the previous section 6.4.1. The advantage of the rate approach is its physical transparency as we can see that the lasing frequency is the one where the photon production of the LED and the photon absorption of the bath are equal.

In Figure 6.9 we plotted the photon occupation number, which is proportional to the luminescence in leading order in g_0 . In Figure 6.9(a) and (c) we can clearly see again the enhanced luminescence in the superconducting state for photon with $\omega_q \approx eV$ as well as the possible absorption of thermal photons for energies $\omega_q > eV$ for the steady state. In Figure 6.9(b) the bath absorption rate is chosen as $\eta < \eta_{\min}$, such that a lasing instability occurs at energies $\omega_q < \omega_q^* < eV$. At this point the photon number diverges

as $n(\omega_q) \sim (\omega_q - \omega_q^*)^{-1}$, indicating the lasing instability. For the grey shaded area the photon number is negative, however the above rate equations do only hold for the steady state and therefore the curves are unphysical for this frequencies. Instead, one would have to use a coherent LASER state to investigate the physics of these modes [226], which is an interesting open question for the future.

6.5. Conclusion of Chapter 6

We have shown that the proposed SLED setup, with a semiconducting p - n -junction coupled to superconducting leads, is capable of transferring the superconducting coherence to the emitted photons. The recombination of Cooper pairs from the conduction to the valence bands lead to entangled photon pairs on resonance $\omega_q = eV$ with net momentum zero, whose squeezing properties can be controlled by changing the relative phase between the superconducting order parameters. For realistic parameters the emitted light can be truly squeezed, thus the fluctuations of one of the two-mode quadrature operators falls below the Heisenberg uncertainty limit. Further, the photons emitted via the particle-hole recombination of Bogoliubov quasiparticles leads to an enhanced luminescence in a frequency window of the order of the superconducting order parameter Δ for photons with energy $\omega_q = eV - 2\Delta$. Such an effect has also been observed in superconductor-semiconductor experiments with only one superconducting lead, however our setup does not describe exactly this setup. This demonstrates that the SLED would be an ideal device for the on-demand of non-classical light and entangled photon pairs motivating the ongoing search for its experimental realization.

For the future two main questions remain open: (i) Can we invert the ideas, thus is it possible to induce or enhance superconductivity via squeezed light? Similar ideas for squeezed phonons [227] could then be generalized to squeezed microwaves. (ii) Is the model realistic enough to describe the strongly enhanced luminescence seen in p -semiconductor- n -superconductor junctions [215, 218, 220] and quantum dots [217] or do we have to incorporate more details like indirect transitions via phonons here?

Conclusion

In this thesis we have investigated the role of inelastic tunneling transitions in superconducting junctions. The main focus of the work concentrated on SIN junctions for both planar and STM setups in conventional superconductors and unconventional superconductors. An additional project covered the entanglement and luminescence properties of a Superconducting Light Emitting Diode (SLED). Here, we wish to summarize the main results and conclusions of the dissertation.

In **Chapter 3** it has been demonstrated that inelastic tunneling naturally occurs when describing superconductivity in a low-energy model like the BCS or Eliashberg theory. Besides the **elastic** tunneling processes, where an electron travels from one electrode to the other without energy loss, also **inelastic** tunneling events can happen. Here, the electron excites or absorbs a collective boson (e.g. phonon, magnon, spin fluctuation) during the transition. The actual process behind these inelastic transitions has been demonstrated to be as follows: An electron first tunnels elastically from the left electrode to an high-energy state of the right electrode. From this virtual off-shell state, the electron then scatters inelastically via the excitation/absorption of a boson and finally ends up in a final low-energy state near the Fermi surface of the right electrode. Explicit forms for the elastic and inelastic tunneling current have been derived from an effective low-energy transfer Hamiltonian and the occurring terms have been traced back to different physical tunneling processes. The main results of this analysis are the following: In the normal state, the IETS spectrum $d^2I(V)/dV^2 \sim \alpha^2 F_{\text{tun}}(eV)$ is proportional to the (coupling-element weighted) boson DOS, which naturally explains the phonon spectra seen in normal state planar junctions [17, 18, 50] and STM experiments [19, 20]. For an SIN experiment this picture changes and the bias dependence of the conductance has to be determined using the developed extended tunneling theory that combines both elastic and inelastic contributions. The elastic conductance is given by a thermally smeared electron DOS, whereas the inelastic conductance can be calculated by a convolution of both the electronic and bosonic spectrum.

The explicit application of the developed extended tunneling theory to conventional superconductors, where the dominant interaction¹⁰ is the one between electrons and phonons, has been demonstrated in **Chapter 4**. The approximate equivalence of the phonon tunneling spectrum and the Eliashberg function has been explicitly proven for a realistic phonon spectrum of a cubic system. Furthermore, it has been shown that for a phonon mode with energy ω_{ph} in the superconducting state, inelastic processes lead to pronounced peaks in $d^2I(V)/dV^2$ just below $eV = \Delta + \omega_{\text{ph}}$. In contrast, the elastic contributions create a dip at this position. For STM experiments on Pb [24], this leads to antisymmetric peak-dip

¹⁰besides the Coulomb interaction

features around the zero-axis in the $d^2I(V)/dV^2$ spectra at energies¹¹ $eV = \Delta + \omega_{t/1}$. The agreement between the theoretical prediction and the experimental tunneling data demonstrates the potential of the extended tunneling theory for describing both elastic and inelastic tunneling on equal footing.

The implications of the presented tunneling theory for the interpretation of unconventional superconductors, where the superconducting pairing glue is presumably of electronic nature, is an even more interesting question. It is covered in **Chapter 5** based on the spin-fermion model. The importance of inelastic processes in tunneling experiments becomes apparent from the pronounced background conductance seen in various different high- T_c compounds. The extended tunneling theory can naturally explain the linear increase of the conductance by inelastic scattering off overdamped spin fluctuations for the tunneling electrons [125]. When entering the superconducting state, the inelastic tunneling spectrum changes significantly since both the electronic and the bosonic spin spectra are now gapped by Δ and ω_{res} , respectively. This results in a threshold for the inelastic conductance of $eV = \Delta + \omega_{\text{res}}$, followed by a strong increase for higher biases. The total tunneling spectrum, consisting of the elastic and inelastic conductance, shows a peak-dip-hump feature for biases $eV \sim \Delta$ as well as a linear background conductance for higher-biases in the superconducting state. We emphasize that the dip does not originate from strong-coupling physics, but from the additional inelastic contributions to the tunneling current. The similarities between our theory and the experimental data of many cuprate and iron pnictide superconductors indicate that the spin-fermion model and the extended tunneling theory already contain the essential physics necessary for the interpretation of the tunneling spectra in unconventional superconductors [25].

In addition, a more quantitative analysis of tunneling data has been explicitly performed for the high-temperature superconductors YBCO and LiFeAs. It could be shown that using more realistic inputs for the electronic and bosonic spectrum, we can understand additional aspects of tunneling spectra like particle-hole asymmetry, d -wave gap structures, and additional isolated peaks¹² far above the superconducting coherence peaks. The analysis of **Chapter 5** explicitly demonstrates the need of the extended tunneling theory when dealing with tunneling spectra that show a clear valley-like background conductance.

In the final **Chapter 6**, the light properties of the SLED have been investigated on the basis of an optical transfer Hamiltonian [202]. The SLED consists of a semiconducting $p-n$ junction, where the gap Δ in the conduction and valence band is proximity-induced by externally coupled superconducting leads. Under forward bias $V > 0$, an enhanced luminescence for photons with energy $\omega_q = eV - 2\Delta$ is predicted below T_c . These photons are emitted from particle-hole recombinations of Bogoliubov quasiparticles at the superconducting band-edges. An additional suppressed luminescence peak appears on resonance $\omega_q = eV$ due to the recombination of Cooper pairs of the conduction and valence band. The photon pairs emitted via the latter transitions show a strong entanglement, which can result in a squeezed light state. When arranging two SLEDs in a SQUID setup, the squeezing angle of the quadrature ellipse can be conveniently controlled by an external magnetic field. This proves that one may transfer the macroscopic coherence of an electronic superconducting condensate to photon pairs in the proposed SLED setup.

¹¹With the energies of the van-Hove singularities $\omega_{t/1}$ of the transversal and longitudinal phonon branch and the superconducting gap Δ .

¹²without a following dip

In conclusion, we showed that the inclusion of elastic **and** inelastic processes is essential for the correct interpretation of tunneling experiments in both conventional and unconventional superconductors. The feasibility and applicability of the developed extended tunneling theory has been explicitly demonstrated for various systems. The analysis of tunneling data could be further improved by including more realistic theoretical models for the electronic and bosonic excitations of the system, e.g. by using ab-initio or multiband calculations, which is however beyond the scope of this thesis. Another interesting proposal for future work is the development of inelastic QPI, where the elastic QPI theory is extended using the inelastic tunneling Hamiltonian of Chapter 3. Inelastic QPI is a promising candidate for the energy- and momentum-resolved determination of bosonic excitations in condensed matter systems. The ultimate goal is to use the insights gained from tunneling data and complementary experiments to better understand the underlying physics of the unconventional superconductors. This might finally unravel the origin of the high transition temperatures and the other interesting properties of the cuprate and iron pnictide superconductors.

Acknowledgements

Of course, this thesis would never have been possible without the staggering support of many people. Especially I have to thank my supervisor Prof. Jörg Schmalian for giving me the opportunity to do research on the multifaceted world of condensed matter physics. I have been very lucky to work for such an exceptional scientist, who shaped and sharpened my physical world view tremendously. I also have to express my gratitude for Prof. Wulf Wulfhökel, who did not only agree to be the co-referee of this thesis but also worked hard for our joint publication.

A special thanks also goes to my other collaborators Peter Orth and Jasmin Jandke, with whom I worked together here at the KIT. Further, I am extremely grateful to Prof. Srinivas Raghu, who gave me the opportunity to spend some time in Stanford, and to my collaborators from there: Maxwell Shapiro, Akash Maharaj, Alexander Hristov and Prof. Ian Fisher. Without all their help my time during my doctorate would certainly have been much less fruitful.

Further, I have to mention the amazing atmosphere at the TKM Institute and the many fruitful discussions. In particular, I like to thank my roommates Michael Schütt, Elio König, Nikolaos Kainaris, Mathias Scheurer, Mareike Hoyer, Pia Gagel and Stefan Beyl who have never refused to discuss physics-related questions and have always been open for some fun. I also have to mention Julia Link, Bhilahari Jeevanesan, Philip Wollfarth, Pablo Schad and Ulf Briskot as well as the administrative skills and patience of Andreas Pönecké, who always helped me when my computer went on strike.

Also, I also have to say a huge thank you to Pablo Schad, Mathias Scheurer, Mareike Hoyer, Nikolaos “Greeko” Kainaris, Jasmin Jandke, Peter Orth, Philip Wollfarth and Julia Link for proof reading this thesis.

Finally, I have to thank my family, who gave me an enormous amount of support during my PhD. Especially the personal time with my wife Yvonne and son Sam always helped me to stay motivated during the time of my doctorate.

Notation

In this thesis, we are working with the following definitions and notations:

- We use $\hbar = k_{\text{B}} = 1$ unless stated otherwise.
- If not stated otherwise we are using the Einstein summation notation.
- We define $\beta = 1/T$ as the inverse of the physical temperature T in the investigated system.
- We will fluently switch between the 4-vector notation and the energy-momentum notation $k = (i\omega_n, \mathbf{k})$.
- Capital $\Omega_m = 2\pi mT$ indicate bosonic and small $\omega_n = (2n+1)\pi T$ fermionic Matsubara frequencies.
- We abbreviate $\frac{T}{V} \sum_{\mathbf{k}, \Omega_m} = \int_{\mathbf{k}}$.
- $\hat{\sigma}_i$ and $\hat{\tau}_i$ both describe the usual Pauli matrices:

$$\hat{\sigma}_x = \begin{pmatrix} 0 & 1 \\ 1 & 0 \end{pmatrix} \quad \hat{\sigma}_y = \begin{pmatrix} 0 & -i \\ i & 0 \end{pmatrix} \quad \hat{\sigma}_z = \begin{pmatrix} 1 & 0 \\ 0 & -1 \end{pmatrix} \quad (6.56)$$

Also, we define $\hat{\sigma}_0 = \mathbb{1}_2$ and $\sigma_{\pm} = \sigma_x \pm i\sigma_y$.

- $n_{B/F}(x) = [\exp(-\beta x) \mp 1]^{-1}$ denotes the Bose-Einstein and Fermi-Dirac distribution.
- $\Theta(x) = \begin{cases} 1 & , x \geq 0 \\ 0 & , x < 0 \end{cases}$ denotes the Heaviside function.
- The Fourier-transform connecting the time-space representation and the energy-momentum representation is defined via

$$\begin{aligned} f(t, \mathbf{x}) &= \int_{\mathbf{k}} f(\omega, \mathbf{k}) e^{i(\mathbf{k} \cdot \mathbf{x} - \omega \cdot t)} \\ f(\omega, \mathbf{k}) &= \int d\mathbf{x} dt f(t, \mathbf{x}) e^{-i(\mathbf{k} \cdot \mathbf{x} - \omega \cdot t)} \end{aligned} \quad (6.57)$$

- $\hat{A} \otimes \hat{B}$ denotes the Kronecker product of two matrices or operators.

- List of physical constants:
 - Boltzmann constant k_B
 - Free electron mass m_e
 - Reduced Planck constant \hbar
 - Electron charge e
 - Vacuum speed of light c

Acronyms

AC Alternating Current

AFV Antiferromagnetic Ordering Vector

ARPES Angle-Resolved Photoemission Spectroscopy

BCS Bardeen-Cooper-Schrieffer

BSCCO $\text{Bi}_2\text{Sr}_2\text{CaCu}_2\text{O}_{8+\delta}$

DFT Density Functional Theory

DOS Density of States

EETS Elastic Electron Tunneling Spectroscopy

fcc face centered cubic

FWHM full-width at half-maximum

HBCCO Hg-Ba-Ca-Cu-O

HWHM half-width at half-maximum

IETS Inelastic Electron Tunneling Spectroscopy

KIT Karlsruhe Institute of Technology

LASER Light Amplification by Stimulated Emission of Radiation

LED Light Emitting Diode

LSCO $\text{La}_{2-x}\text{Sr}_x\text{CuO}_4$

NBCO $\text{NdBa}_2\text{Cu}_3\text{O}_{7-\delta}$

OD oxygen-deuterium

PLCCO $\text{Pr}_{1-x}\text{LaCe}_x\text{CuO}_4$

QPI Quasiparticle Interference

RG Renormalization Group

RPA Random-Phase Approximation

SIN Superconductor-Isolator-Normalconductor

SIS Superconductor-Isolator-Superconductor

SLED Superconducting Light Emitting Diode

spEELS spin-polarized Electron Energy Loss Spectroscopy

SQUID Superconducting Quantum Interference Device

STM Scanning Tunneling Microscopy

STO SrTiO_3

UHV Ultra High Vacuum

WKB Wentzel-Kramers-Brillouin

YBCO $\text{YBa}_2\text{Cu}_3\text{O}_{7-\delta}$

Appendix

A. Hot-spot theory

A.1. Derivation of Eliashberg equations for spin-mediated superconductivity

Here, we derive the Eliashberg equations for the spin-fermion model starting with the introduction of the extended Nambu spinor

$$\Psi_k = \begin{pmatrix} \psi_{k,\uparrow} \\ \psi_{k,\downarrow} \\ \bar{\psi}_{-k,\uparrow} \\ \bar{\psi}_{-k,\downarrow} \end{pmatrix}, \quad \bar{\Psi}_k = \begin{pmatrix} \bar{\psi}_{k,\uparrow} & \bar{\psi}_{k,\downarrow} & \psi_{-k,\uparrow} & \psi_{-k,\downarrow} \end{pmatrix}. \quad (\text{A.1})$$

We are now able to rewrite the spin-fermion action (2.36) in this new basis

$$S = -\frac{1}{2} \int_k \bar{\Psi}_k \hat{G}_k^{-1} \Psi_k + \frac{1}{2} \int_q \chi_{q,0}^{-1} \mathbf{S}_q \mathbf{S}_{-q} + \frac{g}{2} \int_{k,q} (\bar{\Psi}_{k+q} \boldsymbol{\alpha} \Psi_k) \mathbf{S}_q, \quad (\text{A.2})$$

where we defined the free fermion propagator matrix $\hat{G}_{k,0}$ and the α matrices as

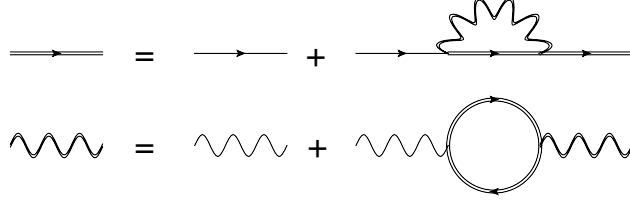
$$\hat{G}_{k,0} = \begin{pmatrix} G_{k,0}^{(p)} & 0 & 0 & 0 \\ 0 & G_{k,0}^{(p)} & 0 & 0 \\ 0 & 0 & G_{k,0}^{(h)} & 0 \\ 0 & 0 & 0 & G_{k,0}^{(h)} \end{pmatrix}, \quad \begin{aligned} \hat{\alpha}_x &= \begin{pmatrix} \sigma_x & 0 \\ 0 & -\sigma_x \end{pmatrix} \\ \hat{\alpha}_y &= \begin{pmatrix} \sigma_y & 0 \\ 0 & \sigma_y \end{pmatrix} \\ \hat{\alpha}_z &= \begin{pmatrix} \sigma_z & 0 \\ 0 & -\sigma_z \end{pmatrix} \end{aligned}. \quad (\text{A.3})$$

Here, the electron and hole propagators is defined in the usual way as $G_{k,0}^{(p)/(h)} = i\omega_n \mp \epsilon_k$. The spin-fermion coupling gives rise to an effective attractive spin-spin interaction between the quasiparticles, thereby the fermions can form Cooper pairs and we expect a superconducting phase transition below a critical temperature T_c . Thus, we introduce the dressed propagator matrix for the extended spinor via

$$\langle \Psi_k \bar{\Psi}_k \rangle = -\hat{G}_k = - \begin{pmatrix} G_k^{(p)} & 0 & 0 & F_k \\ 0 & G_k^{(p)} & -F_k & 0 \\ 0 & -F_k^* & G_k^{(h)} & 0 \\ F_k^* & 0 & 0 & G_k^{(h)} \end{pmatrix}, \quad (\text{A.4})$$

with the anomalous Green's functions F_k, F_k^* that appear only in the superconducting phase. Performing a perturbation theory (neglecting vertex corrections [110]) we find the coupled integral equations

$$\begin{aligned}\hat{G}_p &= \hat{G}_{p,0} + g^2 \int_q \sum_i \hat{G}_{p,0} \hat{\alpha}^i (\chi_q \hat{G}_{p-q}) \hat{\alpha}^i \hat{G}_p, \\ \chi_q &= \chi_{q,0} + \frac{g^2}{2} \int_p \sum_i \chi_{q,0} \text{tr}(\hat{G}_{p,0} \hat{\alpha}^z \hat{G}_{p,0} \hat{\alpha}^z) \chi_q,\end{aligned}\tag{A.5}$$



Note that in contrast to the conventional Eliashberg theory, we here also have to consider the renormalization of the bosonic spectrum as the dynamics of the spin spectrum is generated by the coupling to the fermionic quasiparticles. Using a real choice $F = F^*$ of the gap and reducing the above matrix equations we end up with a set of scalar self-consistent equations

$$\begin{aligned}G_p^{(p)} &= G_{p,0}^{(p)} (1 + \Phi_p F_p^* + \Sigma_p G_p^{(p)}), \\ F_p &= G_{-p,0}^{(p)} (\Sigma_{-p} F_p - \Phi_p G_p^{(p)}), \\ \chi_q &= \chi_{q,0} + \chi_{q,0} \Pi_q \chi_q,\end{aligned}\tag{A.6}$$

We introduced the self-energies:

$$\begin{aligned}\Sigma_p &= 3g^2 \int_q \chi_q G_{p-q}^{(p)}, \\ \Phi_p &= 3g^2 \int_q \chi_q F_{p-q}, \\ \Pi_q &= 2g^2 \int_k [G_k^{(p)} G_{k+q}^{(p)} + F_k F_{k+q}].\end{aligned}\tag{A.7}$$

Note the different definition of Φ_p compared to the phonon-mediated pairing in (2.22), which has a relative $+$ sign compared to the normal self-energy. This will give rise to unconventional pairing, because the order parameter must have a sign change between different states on the Fermi surface connected by the interaction potential χ_q . If we again assume particle-hole symmetry we find the same expressions as in (2.24).

$$\begin{aligned}G_p^{(p)} &= \frac{Z_p i\omega_n + \epsilon_p}{[Z_p i\omega_n]^2 - \epsilon_p^2 - \Phi_p^2}, \\ F_p &= \frac{\Phi_p}{[Z_p i\omega_n]^2 - \epsilon_p^2 - \Phi_p^2}, \\ \chi_q &= \frac{1}{\chi_{q,0}^{-1} - \Pi_q}.\end{aligned}\tag{A.8}$$

with the usual definition of the renormalization factor $Z_k = 1 - \frac{\Sigma_k}{i\omega_n}$.

A.2. Linearization at the hot-spots

In order to calculate the momentum sum over particles which are connected by the AVF \mathbf{Q} we consider in general a term of the form

$$\frac{1}{L^2} \sum_{\mathbf{k}} f(\epsilon_{\mathbf{k}}, \epsilon_{\mathbf{k}+\mathbf{Q}}, \Delta_{\mathbf{k}}, \Delta_{\mathbf{k}+\mathbf{Q}}) = \int \frac{d^2k}{(2\pi)^2} f(\epsilon_{\mathbf{k}}, \epsilon_{\mathbf{k}+\mathbf{Q}}, \Delta_{\mathbf{k}}, \Delta_{\mathbf{k}+\mathbf{Q}}). \quad (\text{A.9})$$

Since \mathbf{Q} only connects the hot spots and no other points on the Fermi surface, the important contributions will come from \mathbf{k}_h . The dispersion on the Fermi surface is assumed to be described as a free fermion with effective mass m . We let \mathbf{Q} show in the y -direction and thus can parameterize:

$$\mathbf{k}_h = k_F \begin{pmatrix} \cos \theta \\ \sin \theta \end{pmatrix}, \quad \mathbf{k}_h + \mathbf{Q} = k_F \begin{pmatrix} \cos \theta \\ -\sin \theta \end{pmatrix},$$

where k_F is the Fermi momentum. Now we expand $\mathbf{k} = \mathbf{k}_h + \mathbf{q}$ with $|\mathbf{q}| \ll k_F$ and obtain for the dispersions

$$\begin{aligned} \epsilon_{\mathbf{k}} &= \epsilon_{\mathbf{k}_h + \mathbf{q}} \approx \frac{\mathbf{k}_h^2}{2m} - \mu + \frac{\mathbf{k}_h \cdot \mathbf{q}}{m} = \frac{k_F}{m} \cos \theta q_{\perp} + \frac{k_F}{m} \sin \theta q_{\parallel} = v_{\perp} q_{\perp} + v_{\parallel} q_{\parallel}, \\ \epsilon_{\mathbf{k}+\mathbf{Q}} &= v_{\perp} q_{\perp} - v_{\parallel} q_{\parallel}, \end{aligned} \quad (\text{A.10})$$

where q_{\parallel} is the projection of \mathbf{q} on the direction of \mathbf{Q} and q_{\perp} the perpendicular component. A rotation in the momentum space

$$\begin{pmatrix} \epsilon \\ \epsilon' \end{pmatrix} = \underbrace{\begin{pmatrix} v_{\perp} & v_{\parallel} \\ v_{\perp} & -v_{\parallel} \end{pmatrix}}_J \begin{pmatrix} q_{\perp} \\ q_{\parallel} \end{pmatrix} \quad (\text{A.11})$$

yields the Jacobian determinant $|J| = 2v_{\perp}v_{\parallel}$. We further assume that the parallel and perpendicular Fermi velocities relative to \mathbf{Q} are equal $v_{\perp} = v_{\parallel} = v_F/\sqrt{2}$ (as seen e.g. in BSCCO) in order to simplify the occurring terms. We note that we do not need to use this assumptions about v_{\perp} and v_{\parallel} and that this scheme works as long as the Fermi velocities at connected hot-spots are not parallel to each other. We are now able to write the integral (A.9) as

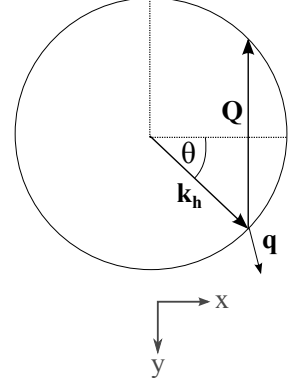
$$\frac{1}{L^2} \sum_{\mathbf{k}} f(\epsilon_{\mathbf{k}}, \epsilon_{\mathbf{k}+\mathbf{Q}}, \Delta_{\mathbf{k}}, \Delta_{\mathbf{k}+\mathbf{Q}}) = \frac{N}{4\pi^2 v_F^2} \int d\epsilon d\epsilon' f(\epsilon, \epsilon', \Delta, \pm\Delta). \quad (\text{A.12})$$

Here, we used a sign-changing gap symmetry for the hot spots $\Delta_{\mathbf{k}_h + \mathbf{Q}} = \pm\Delta_{\mathbf{k}_h} = \pm\Delta$ connected by the AVF. Finally the factor N appears, because we have the contributions of the N hot spots on the Fermi surface, which are the same due to the tetragonal symmetry of the system.

For a sum of the form

$$\frac{1}{L^2} \sum_{\mathbf{q}} \chi_{\mathbf{q}} f(\epsilon_{\mathbf{k}_h - \mathbf{q}}) = \frac{1}{L^2} \sum_{\delta\mathbf{q}} \chi_{\mathbf{Q} + \delta\mathbf{q}} f(\epsilon_{\mathbf{k}_h - \mathbf{Q} - \delta\mathbf{q}}) \quad (\text{A.13})$$

it is clear that the contributions will come from momenta $\mathbf{q} \approx \mathbf{Q}$, such that we expand $\mathbf{q} \approx \mathbf{Q} + \delta\mathbf{q}$. Next, the integration is split in a component $\delta\mathbf{q}_{\parallel}$ parallel and $\delta\mathbf{q}_{\perp}$



perpendicular to the Fermi surface at the hot spot $\mathbf{k}'_h = \mathbf{k}_h - \mathbf{Q}$. With the assumption of slow bosonic modes we can then separate the two integrations similar to the approach in Section 2.2 and get

$$\frac{1}{L^2} \sum_{\mathbf{q}} \chi_{\mathbf{q}} f(\epsilon_{\mathbf{k}_h - \mathbf{q}}) \approx \frac{1}{(2\pi)^2} \int dq_{\parallel} \chi_{\mathbf{Q} + \delta \mathbf{q}_{\parallel}} \int dq_{\perp} f(\epsilon_{\mathbf{k}_h - \mathbf{Q} - \delta \mathbf{q}_{\parallel}}). \quad (\text{A.14})$$

B. Derivation of elastic and inelastic tunneling currents

In this chapter, we present the detailed derivation of the elastic and inelastic tunneling currents from Section 3.2. We will start from the effective low-energy tunneling Hamiltonian (3.21) that was derived in Section 3.1. For an STM setup the tunneling current¹³ is given by the elementary charge times the change of the number of electrons $\hat{n}_s = \sum_{\mathbf{k},\sigma} \hat{s}_{\mathbf{k},\sigma}^\dagger \hat{s}_{\mathbf{k},\sigma}$ in the superconductor

$$I(t) = e \frac{d}{dt} \langle \hat{n}_s(t) \rangle = e \frac{d}{dt} \frac{\text{tr}(\hat{\rho}(t) \hat{n}_s)}{\text{tr}(\hat{\rho}(t))} = e \frac{d}{dt} \frac{\text{tr}(\hat{\rho} \hat{n}_s(t))}{\text{tr}(\hat{\rho}_0)} = e \frac{d}{dt} \text{tr}(\hat{\rho} \hat{n}_s(t)). \quad (\text{B.1})$$

Here, $\hat{\rho}(t) = \hat{U}(t, -\infty) \hat{\rho}_0 \hat{U}^\dagger(t, -\infty)$ is the time-dependent density matrix in the Heisenberg picture with the time-evolution operator \hat{U} and $\hat{\rho}_0 = e^{-\beta \mathcal{H}} / \text{tr}(e^{-\beta \mathcal{H}})$ the (normalized) density matrix of the system in thermal equilibrium¹⁴. Using the invariance under cyclic permutation of the trace and the Heisenberg equation of motion $d\hat{A}(t)/dt = -i[\hat{A}(t), \mathcal{H}(t)]$, we can express the tunneling current as

$$I(t) = e \frac{d}{dt} \text{tr}(\hat{\rho}_0 \hat{n}_s(t)) = -ie \text{tr}(\hat{\rho}_0 [\hat{n}_s(t), \mathcal{H}(t)]) = -ie \langle [\hat{n}_s(t), \mathcal{H}(t)] \rangle. \quad (\text{B.2})$$

We denote $\langle \dots \rangle = \text{tr}(\hat{\rho}_0 \dots)$ as the expectation value in thermal equilibrium. Using the transfer Hamiltonian (3.23) as well as the usual fermionic anticommutator relations $\{\hat{s}_{\mathbf{k},\sigma}, \hat{s}_{\mathbf{k}',\sigma'}^\dagger\} = \{\hat{t}_{\mathbf{k},\sigma}, \hat{t}_{\mathbf{k}',\sigma'}^\dagger\} = \delta_{\mathbf{k},\mathbf{k}'} \delta_{\sigma,\sigma'}$ (all other anticommutators of fermionic field operators vanish), the commutator in (B.2) can easily be calculated as

$$\begin{aligned} [\hat{n}_s(t), \mathcal{H}(t)] &= [\hat{n}_s(t), \mathcal{H}_{\text{tun}}(t)] \\ &= \sum_{\substack{\mathbf{k}, \mathbf{k}' \\ \sigma, \sigma'}} \left[T_{(\mathbf{k},\sigma),(\mathbf{k}',\sigma')}(t) \hat{s}_{\mathbf{k},\sigma}^\dagger(t) \hat{t}_{\mathbf{k}',\sigma'}(t) - [T_{(\mathbf{k},\sigma),(\mathbf{k}',\sigma')}(t)]^* \hat{t}_{\mathbf{k}',\sigma'}^\dagger(t) \hat{s}_{\mathbf{k},\sigma}(t) \right]. \end{aligned} \quad (\text{B.3})$$

Here, we defined $T_{(\mathbf{k},\sigma),(\mathbf{k}',\sigma')}(t) = t_{\mathbf{k},\mathbf{k}'}^e \delta_{\sigma,\sigma'} + \sum_{\mathbf{q},n} t_{(\mathbf{k},\sigma),(\mathbf{k}',\sigma'),\mathbf{q},n}^i \hat{\Phi}_{\mathbf{q}}^n(t)$. When using the Keldysh technique we can calculate the expectation value (B.2) for the current as

$$\begin{aligned} I(t) &= -ie \langle \sum_{\substack{\mathbf{k}, \mathbf{k}' \\ \sigma, \sigma'}} \left[T_{(\mathbf{k},\sigma),(\mathbf{k}',\sigma')}(t) \hat{s}_{\mathbf{k},\sigma}^\dagger(t) \hat{t}_{\mathbf{k}',\sigma'}(t) - [T_{(\mathbf{k},\sigma),(\mathbf{k}',\sigma')}(t)]^* \hat{t}_{\mathbf{k}',\sigma'}^\dagger(t) \hat{s}_{\mathbf{k},\sigma}(t) \right] \rangle \\ &= -ie \langle \sum_{\substack{\mathbf{k}, \mathbf{k}' \\ \sigma, \sigma'}} \left[T_{(\mathbf{k},\sigma),(\mathbf{k}',\sigma')}^-(t) \bar{s}_{\mathbf{k},\sigma}^-(t) t_{\mathbf{k}',\sigma'}^+(t) - [T_{(\mathbf{k},\sigma),(\mathbf{k}',\sigma')}^+(t)]^* \bar{t}_{\mathbf{k}',\sigma'}^-(t) s_{\mathbf{k},\sigma}^+(t) \right] \rangle \\ &= -ie \langle \sum_{\substack{\mathbf{k}, \mathbf{k}' \\ \sigma, \sigma'}} \left(\bar{s}_{\mathbf{k},\sigma}^-(t) \right)^\dagger \underbrace{\begin{pmatrix} 0 & T_{(\mathbf{k},\sigma),(\mathbf{k}',\sigma')}^-(t) \\ -[T_{(\mathbf{k}',\sigma'),(\mathbf{k},\sigma)}^+(t)]^* & 0 \end{pmatrix}}_{\hat{A}_{(\mathbf{k},\sigma),(\mathbf{k}',\sigma')}(t)} \underbrace{\begin{pmatrix} s_{\mathbf{k}',\sigma'}^+(t) \\ t_{\mathbf{k}',\sigma'}^+(t) \end{pmatrix}}_{\hat{\Psi}_{\mathbf{k}',\sigma'}^+(t)} \rangle \quad (\text{B.4}) \end{aligned}$$

with the redefinition $T_{(\mathbf{k},\sigma),(\mathbf{k}',\sigma')}^\pm(t) = t_{\mathbf{k},\mathbf{k}'}^e \delta_{\sigma,\sigma'} + \sum_{\mathbf{q},n} t_{(\mathbf{k},\sigma),(\mathbf{k}',\sigma'),\mathbf{q},n}^i \Phi_{\mathbf{q}}^{\pm,n}(t)$. Note that we switched our notation from the operator basis to the Keldysh-path integral formalism (for a short introduction to the Keldysh formalism see Appendix C), which is indicated by the fact that the electronic operators $\hat{s}, \hat{t} \rightarrow s^\pm, t^\pm$ have to be replaced by Grassmann fields

¹³as measured from the tip to the superconductor

¹⁴We assume that the tunneling current is so small that the steady state of the connected system does not affect the thermal equilibrium of the tip and sample subsystems.

that lie on the upper or lower Keldysh contour and similarly for the complex bosonic field $\hat{\Phi} \rightarrow \Phi^\pm$. In order to conserve the correct ordering we had to pin the annihilation operators on the upper and the creation operators on the lower Keldysh contour. This formal way to deal with the ordering of operators can also be understood in a more physical picture: Of course an electron first has to be “destroyed” on the one electrode before it can be “created” on the other electrode during this transition. Moreover, the bosonic field Φ has to lie at the same contour as the s fields, because the scattering will only take place in the sample and not in the tip. When using the Keldysh technique we can calculate an expectation value like in Eq. (B.2) via

$$\langle \dots \rangle = \int D[\Psi, \bar{\Psi}] \dots e^{iS}, \quad (\text{B.5})$$

where S is the corresponding action of the fields $\Psi = (s, t, \Phi)$ that occur in the theory. For us, the Keldysh action reads $S = S_0 + S_{\text{tun}}$ with the uncoupled action $S_0 = S_t + S_s$ that describes the electrons in the tip and the electronic and bosonic degrees of freedom in the investigated sample. The tunneling action is then given by

$$\begin{aligned} S_{\text{tun}} &= - \int_{\mathcal{C}} dt \sum_{\substack{\mathbf{k}, \mathbf{k}' \\ \sigma, \sigma'}} [T_{(\mathbf{k}, \sigma), (\mathbf{k}', \sigma')}(t) \bar{s}_{\mathbf{k}, \sigma}(t) t_{\mathbf{k}', \sigma'}(t) + [T_{(\mathbf{k}, \sigma), (\mathbf{k}', \sigma')}(t)]^* \bar{t}_{\mathbf{k}', \sigma'}(t) s_{\mathbf{k}, \sigma}(t)] \\ &= - \int_{-\infty}^{\infty} dt \sum_{\alpha=\pm} \alpha \cdot \sum_{\substack{\mathbf{k}, \mathbf{k}' \\ \sigma, \sigma'}} [T_{(\mathbf{k}, \sigma), (\mathbf{k}', \sigma')}^\alpha(t) \bar{s}_{\mathbf{k}, \sigma}^\alpha(t) t_{\mathbf{k}', \sigma'}^\alpha(t) + [T_{(\mathbf{k}, \sigma), (\mathbf{k}', \sigma')}^\alpha(t)]^* \bar{t}_{\mathbf{k}', \sigma'}^\alpha(t) s_{\mathbf{k}, \sigma}^\alpha(t)] \\ &= - \int_{-\infty}^{\infty} dt \sum_{\alpha=\pm} \alpha \cdot \sum_{\substack{\mathbf{k}, \mathbf{k}' \\ \sigma, \sigma'}} \begin{pmatrix} \bar{s}_{\mathbf{k}, \sigma}^\alpha(t) \\ \bar{t}_{\mathbf{k}, \sigma}^\alpha(t) \end{pmatrix}^\dagger \underbrace{\begin{pmatrix} 0 & T_{(\mathbf{k}, \sigma), (\mathbf{k}', \sigma')}^\alpha(t) \\ [T_{(\mathbf{k}', \sigma'), (\mathbf{k}, \sigma)}^\alpha(t)]^* & 0 \end{pmatrix}}_{\hat{B}_{(\mathbf{k}, \sigma), (\mathbf{k}', \sigma')}^\alpha(t)} \begin{pmatrix} s_{\mathbf{k}', \sigma'}^\alpha(t) \\ t_{\mathbf{k}', \sigma'}^\alpha(t) \end{pmatrix}. \end{aligned} \quad (\text{B.6})$$

The introduction of a finite voltage between the tip and the sample is done by performing two different gauge transformations $s_{\mathbf{k}', \sigma'}(t) \rightarrow s_{\mathbf{k}', \sigma'}(t) e^{-i\mu_s t}$, $t_{\mathbf{k}', \sigma'}(t) \rightarrow t_{\mathbf{k}', \sigma'}(t) e^{-i\mu_t t}$ with the condition $eV = \mu_T - \mu_S$ for the tunneling term in the Hamiltonian¹⁵. This transforms the tunnel matrix element to

$$T_{(\mathbf{k}, \sigma), (\mathbf{k}', \sigma')}^\pm(t) = \left[t_{\mathbf{k}, \mathbf{k}'}^e \delta_{\sigma, \sigma'} + \sum_{\mathbf{q}, n} t_{(\mathbf{k}, \sigma), (\mathbf{k}', \sigma'), \mathbf{q}, n}^i \Phi_{\mathbf{q}}^{\pm, n}(t) \right] e^{-ieVt}. \quad (\text{B.7})$$

A closer look at Eq. (B.4) shows that the tunneling current in leading order of the tunneling matrix element t^e vanishes, because for the uncoupled system with expectation value $\langle \dots \rangle_0 = \int D[\Psi, \bar{\Psi}] \dots e^{iS_0}$ it holds $\langle s\bar{t} \rangle_0 = \langle t\bar{s} \rangle_0$. Therefore, we perform a perturbative expansion in leading order t^e of the tunneling action via

$$\begin{aligned} I(t) &= -ie \langle \sum_{\substack{\mathbf{k}, \mathbf{k}' \\ \sigma, \sigma'}} [\hat{\Psi}_{\mathbf{k}, \sigma}^-(t)]^\dagger \hat{A}_{(\mathbf{k}, \sigma), (\mathbf{k}', \sigma')}(t) \hat{\Psi}_{\mathbf{k}', \sigma'}^+(t) \rangle \\ &= -ie \langle \sum_{\substack{\mathbf{k}, \mathbf{k}' \\ \sigma, \sigma'}} [\hat{\Psi}_{\mathbf{k}, \sigma}^-(t)]^\dagger \hat{A}_{(\mathbf{k}, \sigma), (\mathbf{k}', \sigma')}(t) \hat{\Psi}_{\mathbf{k}', \sigma'}^+(t) e^{iS_{\text{tun}}} \rangle_0 \\ &= e \langle \sum_{\substack{\mathbf{k}, \mathbf{k}' \\ \sigma, \sigma'}} [\hat{\Psi}_{\mathbf{k}, \sigma}^-(t)]^\dagger \hat{A}_{(\mathbf{k}, \sigma), (\mathbf{k}', \sigma')}(t) \hat{\Psi}_{\mathbf{k}', \sigma'}^+(t) S_{\text{tun}} \rangle_0 + \mathcal{O}([t^e]^4) \end{aligned}$$

¹⁵We should not do this for the S_0 part of the action since this would change our chemical potentials in the bands (so the dispersion for the tip and sample), which will not be the case as both are assumed to be metals and the total voltage will drop in the insulating vacuum region between the tip and the sample.

$$\begin{aligned} &\approx -e \int_{-\infty}^{\infty} dt' \sum_{\substack{\mathbf{k}, \mathbf{k}', \mathbf{p}, \mathbf{p}' \\ \sigma, \sigma', \lambda, \lambda'}} \sum_{\alpha=\pm} \alpha \times \\ &\langle [\hat{\Psi}_{\mathbf{k}, \sigma}^{-}(t)]^{\dagger} \hat{A}_{(\mathbf{k}, \sigma), (\mathbf{k}', \sigma')}(t) \hat{\Psi}_{\mathbf{k}', \sigma'}^{+}(t) [\hat{\Psi}_{\mathbf{p}, \lambda}^{\alpha}(t')]^{\dagger} \hat{B}_{(\mathbf{p}, \lambda), (\mathbf{p}', \lambda')}(t') \hat{\Psi}_{\mathbf{p}', \lambda'}^{\alpha}(t') \rangle_0. \end{aligned} \quad (\text{B.8})$$

Since the expectation value is evaluated under the uncoupled system and only the sample s can be superconducting (the tip t is always in the trivial normal conducting state), there is only one way to contract the occurring electronic and bosonic fields via

$$\begin{aligned} \langle \hat{\Psi}_{\mathbf{k}, \sigma}^{\alpha}(t) [\hat{\Psi}_{\mathbf{k}', \sigma'}^{\alpha}(t')]^{\dagger} \rangle_0 &= i \underbrace{\begin{pmatrix} G_{s, \mathbf{k}, \sigma}^{\alpha, \beta}(t-t') & 0 \\ 0 & G_{t, \mathbf{k}, \sigma}^{\alpha, \beta}(t-t') \end{pmatrix}}_{\hat{G}_{\mathbf{k}, \sigma}(t-t')} \delta_{\mathbf{k}, \mathbf{k}'} \delta_{\sigma, \sigma'}, \\ \langle \Phi_{\mathbf{q}}^{\alpha, n}(t) \Phi_{-\mathbf{q}}^{\beta, m}(t') \rangle_0 &= \langle \Phi_{\mathbf{q}}^{\alpha, n}(t) [\Phi_{\mathbf{q}'}^{\beta, m}(t')]^* \rangle_0 = i D_{\mathbf{q}, n}^{\alpha, \beta}(t-t') \delta_{\mathbf{q}, \mathbf{q}'} \delta_{m, n} \end{aligned} \quad (\text{B.9})$$

where $G_{s/t, \mathbf{k}, \sigma}(t-t')$ are the equilibrium particle Green's functions ($t^e = 0$) of the sample and tip electrons and $D_{\mathbf{q}, n}(t-t')$ the bosonic propagator of the real field $[\Phi_{\mathbf{q}}^{\alpha, n}]^* = \Phi_{-\mathbf{q}, n}^{\alpha, n}$. Performing the above contraction yields¹⁶

$$\begin{aligned} I &= -e \int_{-\infty}^{\infty} dt' \sum_{\substack{\mathbf{k}, \mathbf{k}' \\ \sigma, \sigma'}} \sum_{\alpha=\pm} \alpha \cdot \langle \text{tr} \left(\hat{G}_{\mathbf{k}, \sigma}^{\alpha, -}(t-t') \hat{A}_{(\mathbf{k}, \sigma), (\mathbf{k}', \sigma')}(t) \hat{G}_{\mathbf{k}', \sigma'}^{+, \alpha}(t-t') \hat{B}_{(\mathbf{k}', \sigma'), (\mathbf{k}, \sigma)}(t') \right) \rangle_0 \\ &= -e \int_{-\infty}^{\infty} dt' \sum_{\substack{\mathbf{k}, \mathbf{k}' \\ \sigma, \sigma'}} \sum_{\alpha=\pm} \alpha \cdot \left[\langle T_{(\mathbf{k}, \sigma), (\mathbf{k}', \sigma')}^{-}(t) [T_{(\mathbf{k}, \sigma), (\mathbf{k}', \sigma')}^{\alpha}(t')]^* G_{s, \mathbf{k}, \sigma}^{\alpha, -}(t-t') G_{t, \mathbf{k}', \sigma'}^{+, \alpha}(t-t') \rangle_0 \right. \\ &\quad \left. - \langle [T_{(\mathbf{k}', \sigma'), (\mathbf{k}, \sigma)}^{+}(t)]^* T_{(\mathbf{k}', \sigma'), (\mathbf{k}, \sigma)}^{\alpha}(t') G_{t, \mathbf{k}, \sigma}^{\alpha, -}(t-t') G_{s, \mathbf{k}', \sigma'}^{+, \alpha}(t-t') \rangle_0 \right] \\ &= -e \int_{-\infty}^{\infty} dt' \sum_{\substack{\mathbf{k}, \mathbf{k}' \\ \sigma, \sigma'}} \sum_{\alpha=\pm} \alpha \times \\ &\quad \left[e^{-ieV(t-t')} G_{s, \mathbf{k}, \sigma}^{\alpha, -}(t-t') G_{t, \mathbf{k}', \sigma'}^{+, \alpha}(t-t') \left(|t_{\mathbf{k}, \mathbf{k}'}^e|^2 \delta_{\sigma, \sigma'} \right. \right. \\ &\quad \left. \left. + \sum_{\substack{\mathbf{q}, \mathbf{q}' \\ n, m}} t_{(\mathbf{k}, \sigma), (\mathbf{k}', \sigma'), \mathbf{q}, n}^i [t_{(\mathbf{k}, \sigma), (\mathbf{k}', \sigma'), \mathbf{q}', m}^i]^* \langle \Phi_{\mathbf{q}}^{-, n}(t) [\Phi_{\mathbf{q}'}^{\alpha, m}(t')]^* \rangle_0 \right) \right. \\ &\quad \left. - e^{ieV(t-t')} G_{t, \mathbf{k}, \sigma}^{\alpha, -}(t-t') G_{s, \mathbf{k}', \sigma'}^{+, \alpha}(t-t') \left(|t_{\mathbf{k}', \mathbf{k}}^e|^2 \delta_{\sigma, \sigma'} \right. \right. \\ &\quad \left. \left. + \sum_{\substack{\mathbf{q}, \mathbf{q}' \\ n, m}} [t_{(\mathbf{k}', \sigma'), (\mathbf{k}, \sigma), \mathbf{q}, n}^i]^* t_{(\mathbf{k}', \sigma'), (\mathbf{k}, \sigma), \mathbf{q}', m}^i \langle [\Phi_{\mathbf{q}}^{+, n}(t)]^* \Phi_{\mathbf{q}'}^{\alpha, m}(t') \rangle_0 \right) \right] \\ &= -e \int_{-\infty}^{\infty} dt' \sum_{\substack{\mathbf{k}, \mathbf{k}' \\ \sigma, \sigma'}} \sum_{\alpha=\pm} \alpha \times \\ &\quad \left[e^{-ieV(t-t')} G_{s, \mathbf{k}, \sigma}^{\alpha, -}(t-t') G_{t, \mathbf{k}', \sigma'}^{+, \alpha}(t-t') \left(|t_{\mathbf{k}, \mathbf{k}'}^e|^2 \delta_{\sigma, \sigma'} + \sum_{\mathbf{q}, n} |t_{(\mathbf{k}, \sigma), (\mathbf{k}', \sigma'), \mathbf{q}, n}^i|^2 i D_{\mathbf{q}, n}^{-, \alpha}(t-t') \right) \right. \\ &\quad \left. - e^{ieV(t-t')} G_{t, \mathbf{k}, \sigma}^{\alpha, -}(t-t') G_{s, \mathbf{k}', \sigma'}^{+, \alpha}(t-t') \left(|t_{\mathbf{k}', \mathbf{k}}^e|^2 \delta_{\sigma, \sigma'} + \sum_{\mathbf{q}, n} |t_{(\mathbf{k}', \sigma'), (\mathbf{k}, \sigma), \mathbf{q}, n}^i|^2 i D_{\mathbf{q}, n}^{\alpha, +}(t-t') \right) \right] \end{aligned}$$

¹⁶The current $I(t) = I$ is of course not time-dependent as we assume our system to be in a steady state.

$$\begin{aligned}
&= -e \int_{-\infty}^{\infty} d\tau e^{-ieV\tau} \sum_{\substack{\mathbf{k}, \mathbf{k}' \\ \sigma, \sigma'}} \sum_{\alpha=\pm} \alpha \times \left[|t_{\mathbf{k}, \mathbf{k}'}^e|^2 \delta_{\sigma, \sigma'} \left(G_{s, \mathbf{k}, \sigma}^{\alpha, -}(-\tau) G_{t, \mathbf{k}', \sigma'}^{+, \alpha}(\tau) - G_{s, \mathbf{k}, \sigma}^{+, \alpha}(-\tau) G_{t, \mathbf{k}', \sigma'}^{\alpha, -}(\tau) \right) \right. \\
&\quad \left. + \sum_{\mathbf{q}, n} |t_{(\mathbf{k}, \sigma), (\mathbf{k}', \sigma'), \mathbf{q}, n}^i|^2 i \left(D_{\mathbf{q}, n}^{-, \alpha}(\tau) G_{s, \mathbf{k}, \sigma}^{\alpha, -}(-\tau) G_{t, \mathbf{k}', \sigma'}^{+, \alpha}(\tau) - D_{\mathbf{q}, n}^{\alpha, +}(\tau) G_{s, \mathbf{k}, \sigma}^{+, \alpha}(-\tau) G_{t, \mathbf{k}', \sigma'}^{\alpha, -}(\tau) \right) \right].
\end{aligned} \tag{B.10}$$

We can now explicitly perform the sum over α for the elastic

$$\begin{aligned}
&\sum_{\alpha} \alpha \left[G_s^{\alpha, -}(-\tau) G_t^{+, \alpha}(\tau) - G_s^{+, \alpha}(-\tau) G_t^{\alpha, -}(\tau) \right] \\
&= G_s^< G_t^T - G_s^T G_t^< - (G_s^{\tilde{T}} G_t^< - G_s^< G_t^{\tilde{T}}) \\
&= G_s^< (G_t^< + G_t^R) - (G_s^< + G_s^R) G_t^< - (G_s^< - G_s^A) G_t^< + G_s^< (G_t^< - G_t^A) \\
&= G_s^< (G_t^R - G_t^A) - (G_s^R - G_s^A) G_t^< \\
&= -2 \left(\mathbf{Im} G_s^< \mathbf{Im} G_t^R - \mathbf{Im} G_s^R \mathbf{Im} G_t^< \right)
\end{aligned} \tag{B.11}$$

and inelastic contributions

$$\begin{aligned}
&\sum_{\alpha} \alpha \left[D^{-, \alpha}(\tau) G_s^{\alpha, -}(-\tau) G_t^{+, \alpha}(\tau) - D^{\alpha, +}(\tau) G_s^{+, \alpha}(-\tau) G_t^{\alpha, -}(\tau) \right] \\
&= D^> G_s^< G_t^T - D^T G_s^T G_t^< - [D^{\tilde{T}} G_s^{\tilde{T}} G_t^< - D^> G_s^< G_t^{\tilde{T}}] \\
&= D^> G_s^< (G_t^< + G_t^R) - D^T (G_s^< + G_s^R) G_t^< - D^{\tilde{T}} (G_s^< - G_s^A) G_t^< + D^> G_s^< (G_t^< - G_t^A) \\
&= (2D^> - \underbrace{D^T}_{D^>+D^A} - \underbrace{D^{\tilde{T}}}_{D^>-D^R}) G_s^< G_t^< + D^> G_s^< (G_t^R - G_t^A) - \underbrace{D^T}_{D^<+D^R} G_s^R G_t^< + \underbrace{D^{\tilde{T}}}_{D^<-D^A} G_s^A G_t^< \\
&= (D^R - D^A) G_s^< G_t^< + D^> G_s^< (G_t^R - G_t^A) - D^< (G_s^R - G_s^A) G_t^< \\
&= -2i \left[\mathbf{Im} D^R \mathbf{Im} G_s^< \mathbf{Im} G_t^< - \mathbf{Im} D^< \mathbf{Im} G_s^R \mathbf{Im} G_t^< + \mathbf{Im} D^> \mathbf{Im} G_s^< \mathbf{Im} G_t^R \right].
\end{aligned} \tag{B.12}$$

Here, we only used the information about the causal structure of the occurring Green's functions $G^{R/A}(\tau), D^{R/A}(\tau) \sim \Theta(\pm\tau)$. Let us now use the following identities to switch to energy representation

$$\begin{aligned}
\int_{-\infty}^{\infty} d\tau e^{-ieV\tau} G_s(-\tau) G_t(\tau) &= \int_{-\infty}^{\infty} \frac{d\epsilon}{2\pi} G_s(\epsilon) G_t(\epsilon - eV), \\
\int_{-\infty}^{\infty} d\tau e^{-ieV\tau} D(\tau) G_s(-\tau) G_t(\tau) &= \int_{-\infty}^{\infty} \frac{d\omega d\epsilon}{(2\pi)^2} D(\omega) G_s(\epsilon) G_t(\epsilon - \omega - eV).
\end{aligned} \tag{B.13}$$

For the fermionic propagators we have the following relations in energy representation (see e.g. Eq. (C.20))

$$\begin{aligned}
\mathbf{Im} G_{s/t, \mathbf{k}, \sigma}^R(\omega) &= -\pi A_{s/t, \mathbf{k}, \sigma}(\omega), \\
\mathbf{Im} G_{s/t, \mathbf{k}, \sigma}^<(\omega) &= 2\pi n_F(\omega) A_{s/t, \mathbf{k}, \sigma}(\omega),
\end{aligned} \tag{B.14}$$

and for the bosonic propagators

$$\begin{aligned}
\mathbf{Im} D_{\mathbf{q}, n}^R(\omega) &= -\pi [A_{\mathbf{q}, n}(\omega) - A_{-\mathbf{q}, n}(-\omega)], \\
\mathbf{Im} D_{\mathbf{q}, n}^<(\omega) &= -2\pi n_B(\omega) [A_{\mathbf{q}, n}(\omega) - A_{-\mathbf{q}, n}(-\omega)], \\
\mathbf{Im} D_{\mathbf{q}, n}^<(\omega) &= -2\pi [1 + n_B(\omega)] [A_{\mathbf{q}, n}(\omega) - A_{-\mathbf{q}, n}(-\omega)].
\end{aligned} \tag{B.15}$$

The spectral weight functions are defined in the usual way as

$$\begin{aligned} A_{s/t,\mathbf{k},\sigma}(\omega) &= -\frac{1}{\pi} \mathbf{Im} G_{s/t,\mathbf{k},\sigma}^R(\omega), \\ A_{\mathbf{q},n}(\omega) &= -\frac{1}{\pi} \mathbf{Im} D_{\mathbf{q},n}^R(\omega) \cdot \Theta(\omega), \end{aligned} \quad (\text{B.16})$$

where we confined the bosonic spectral function to positive energies¹⁷. When we insert the expressions (B.13)-(B.4) in our expression (B.12) for the current we find the following expression for the elastic current

$$I^e(V) = 2\pi e \int_{-\infty}^{\infty} d\epsilon \sum_{\mathbf{k},\mathbf{k}',\sigma} |t_{\mathbf{k},\mathbf{k}'}^e|^2 A_{s,\mathbf{k},\sigma}(\epsilon) A_{t,\mathbf{k}',\sigma'}(\epsilon - eV) [n_F(\epsilon - eV) - n_F(\epsilon)]. \quad (\text{B.17})$$

For the inelastic current the expression is given by

$$\begin{aligned} I^i(V) &= 2\pi e \int_{-\infty}^{\infty} d\epsilon d\omega \sum_{\substack{\mathbf{k},\mathbf{k}',\mathbf{q} \\ \sigma,\sigma',n}} |t_{(\mathbf{k},\sigma),(\mathbf{k}',\sigma'),\mathbf{q},n}^i|^2 \times \\ &\quad \left[A_{\mathbf{q},n}(\omega) A_{s,\mathbf{k},\sigma}(\epsilon) A_{t,\mathbf{k}',\sigma'}(\epsilon - \omega - eV) \cdot \right. \\ &\quad \left(n_F(\epsilon - \omega - eV) n_B(\omega) [1 - n_F(\epsilon)] - n_F(\epsilon) [1 + n_B(\omega)] [1 - n_F(\epsilon - \omega - eV)] \right) \\ &\quad + A_{\mathbf{q},n}(\omega) A_{s,\mathbf{k},\sigma}(\epsilon) A_{t,\mathbf{k}',\sigma'}(\epsilon + \omega - eV) \\ &\quad \left. \left(n_F(\epsilon + \omega - eV) [1 + n_B(\omega)] [1 - n_F(\epsilon)] - n_F(\epsilon) n_B(\omega) [1 - n_F(\epsilon + \omega - eV)] \right) \right]. \end{aligned} \quad (\text{B.18})$$

¹⁷Negative energies correspond to the absorption of a boson that is captured by the antisymmetric definition of the retarded, lesser and greater boson propagator in Eq. (B.15).

C. Keldysh perturbation theory

In the following paragraph, we wish to give a short introduction to the Keldysh perturbation theory. For further insights in the Keldysh theory we refer to the literature [102, 103], which deals e.g. with other non-equilibrium aspects of the perturbation theory (dynamical external fields, evolution of squeezed systems, Boltzmann transport theory/kinetic equation). Also, in Chapter 6 the effect of the interactions of fermions with photons in a superconducting light emitting diode setup is presented for a steady state, which gives insight into the general structure of calculations using the Keldysh formalism.

C.1. Closed time contour

We consider a quantum system with time-dependent Hamiltonian $\mathcal{H}(t)$. For $t = -\infty$ the system is assumed to be described by a density matrix $\hat{\rho}(-\infty)$, which is associated with the Hamiltonian $\mathcal{H}(-\infty)$. We shall also assume a non-interacting system for $t = -\infty$, and the interactions are then switched on adiabatically to reach their actual physical strength prior the observation time t . The “true” time dependence of the Hamiltonian (e.g. external fields or boundary conditions) can drive the density matrix away from equilibrium. Let us write the normalized density matrix for $t = -\infty$ as

$$\hat{\rho}(-\infty) = \sum_n \rho_n |n\rangle\langle n|, \quad (\text{C.1})$$

where $|n\rangle$ are the many-body eigenstates of $\mathcal{H}(-\infty)$ and ρ_n the probability to find the system in the corresponding state, e.g. in thermal equilibrium $\rho_n = e^{-\beta\langle n|\mathcal{H}(-\infty)|n\rangle}/Z$ with the partition function $Z = \text{tr}(e^{-\beta\mathcal{H}(-\infty)})$. The time evolution of the density matrix is described by the Von-Neumann equation

$$\partial_t \hat{\rho}(t) = -i[\mathcal{H}(t), \hat{\rho}(t)], \quad (\text{C.2})$$

which can be verified using the time evolution of the states in (C.1) described by the time dependent Schrödinger equation. Using the time evolution operator that fulfills

$$i\partial_t \hat{U}_{t,t'} = \mathcal{H}(t)\hat{U}_{t,t'} \quad (\text{C.3})$$

we can formally write

$$\hat{\rho}(t) = \hat{U}_{t,-\infty} \hat{\rho}(-\infty) \hat{U}_{-\infty,t}^\dagger. \quad (\text{C.4})$$

Since the Hamiltonian is time-dependent, it holds in general that $[\mathcal{H}(t), \mathcal{H}(t')] \neq 0$ and the time evolution operator is given by

$$U_{t,t'} = \mathcal{T}_t \exp\left[-i \int_{t'}^t \mathcal{H}(\tau) d\tau\right] \quad (\text{C.5})$$

with the time-ordering operator \mathcal{T}_t . We are now interested in the time-evolution of the observable \hat{O} for time t and therefore

$$\begin{aligned} \langle \hat{O}(t) \rangle &= \frac{\text{tr}[\hat{O}\hat{\rho}(t)]}{\text{tr}[\hat{\rho}(t)]} = \frac{\text{tr}[\hat{O}\hat{U}_{t,-\infty}\hat{\rho}(-\infty)\hat{U}_{-\infty,t}^\dagger]}{\text{tr}[\hat{U}_{t,-\infty}\hat{\rho}(-\infty)\hat{U}_{-\infty,t}^\dagger]} = \frac{\text{tr}[\hat{U}_{-\infty,t}\hat{O}\hat{U}_{t,-\infty}\hat{\rho}(-\infty)]}{\text{tr}[\hat{\rho}(-\infty)]} \\ &= \text{tr}[\hat{U}_{-\infty,t}\hat{O}\hat{U}_{t,-\infty}\hat{\rho}(-\infty)]. \end{aligned} \quad (\text{C.6})$$

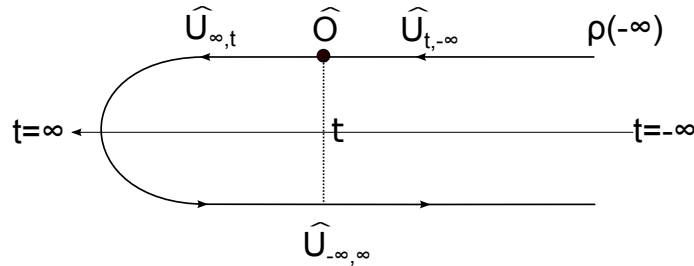


Figure C.1.: Keldysh-contour with observable on the forward branch.

The expression in the trace described (read from right to left) an evolution from the initial density matrix from $-\infty$ to t , then the observable is calculated, and then back to $-\infty$. Therefore, in order to calculate the time evolution of \hat{O} we have to evolve the initial state “backward and forward”.

In equilibrium physics for $T = 0$ one uses a trick to get rid of the backward evolution. Here, we search for the expectation value $\langle GS | \hat{O} | GS \rangle$, where $|GS\rangle$ is the many-body ground state of the interacting Hamiltonian $\mathcal{H} = \mathcal{H}_0 + \hat{V}$. Since we have adiabatically switched on and off the interaction in the distant past and future, we get

$$\langle GS | \hat{O} | GS \rangle = \langle 0 | \hat{U}_{t,-\infty}^\dagger \hat{O} \hat{U}_{t,-\infty} | 0 \rangle, \quad (\text{C.7})$$

with $|0\rangle$ is the simple many-body ground state of the non-interacting Hamiltonian (in case of fermions for $T = 0$ the filled Fermi sea). Now comes the trick: One argues that $\hat{U}_{\infty,-\infty} | 0 \rangle = e^{i\phi} | 0 \rangle$ with $\phi \in \mathbb{R}$. Therefore, the time evolution from $-\infty$ to ∞ of $|0\rangle$ only gives us a phase, because for $t = \pm\infty$ the system has to be in the non-interacting ground state again, which are connected due to the adiabatic change of the Hamiltonian. Because of the normalization we can only get a phase and we are able to write

$$\begin{aligned} \langle GS | \hat{O} | GS \rangle &= \langle 0 | \hat{U}_{-\infty,t} \hat{O} \hat{U}_{t,-\infty} | 0 \rangle = \langle 0 | \hat{U}_{-\infty,\infty} \hat{U}_{\infty,t} \hat{O} \hat{U}_{t,-\infty} | 0 \rangle \\ &= e^{-i\phi} \langle 0 | \hat{U}_{\infty,t} \hat{O} \hat{U}_{t,-\infty} | 0 \rangle = \frac{\langle 0 | \hat{U}_{\infty,t} \hat{O} \hat{U}_{t,-\infty} | 0 \rangle}{\langle 0 | \hat{U}_{\infty,-\infty} | 0 \rangle}. \end{aligned} \quad (\text{C.8})$$

We have now the evolution from $-\infty$ to t , where the observable \hat{O} is evaluated, and finally the evolution from t to ∞ . Therefore, we have only “forward evolution”. A similar strategy works also for finite temperatures T in equilibrium, where the Boltzmann factor $e^{-\beta H}$ works as an evolution operator in imaginary time $\tau \in [0, \beta)$. Nevertheless, the elimination of the backward evolution comes with a price: The normalization denominator in Eq. (C.8). In a diagrammatic language it will cancel the disconnected vacuum diagrams.

In non-equilibrium physics the above trick does not work. The non-adiabatic change of $\mathcal{H}(t)$ due to external fields or boundary conditions can drive the system away from equilibrium and instead of remaining in the ground state during the evolution we might end up with a superposition of excited states. Even if in the distant future all fields are switched off, the system can’t relax in the ground state and the “backward evolution” can’t be eliminated, because in time-dependent problems the energy of processes is not necessarily conserved. Nevertheless, it is still convenient to extend the evolution of Eq. (C.6) toward $t = \infty$ and then back to t using $\hat{U}_{t,\infty} \hat{U}_{\infty,t} = \mathbf{1}$. We can write¹⁸

$$\langle \hat{O}(t) \rangle = \text{tr}[\hat{U}_{-\infty,t} \hat{O} \hat{U}_{t,-\infty} \hat{\rho}(-\infty)] = \text{tr}[\hat{U}_{-\infty,\infty} \hat{U}_{\infty,t} \hat{O} \hat{U}_{t,-\infty} \hat{\rho}(-\infty)]$$

¹⁸Note that one could equally well put the observable \hat{O} on the backward branch of the contour. The most convenient choice is to take a half sum of these two equivalent representations.

$$= \text{tr}[\mathcal{T}\hat{U}_C\hat{O}|_t\hat{\rho}(-\infty)], \quad (\text{C.9})$$

where we defined the closed contour evolution operator $\hat{U}_C \stackrel{\text{def}}{=} \hat{U}_{-\infty,\infty}\hat{U}_{\infty,-\infty}$. This evolution from $-\infty$ to ∞ and backwards is known as the so-called Keldysh contour and is shown in Figure C.1.

C.2. Keldysh path integral formalism

Let us start by considering the expectation value for a bosonic system that has at $t = -\infty$ the equilibrium density matrix

$$\hat{\rho}_0 = \rho(-\infty) = e^{-\beta\mathcal{H}}/Z \quad \text{with } Z = \text{tr}(e^{-\beta\mathcal{H}}). \quad (\text{C.10})$$

The bosons are assumed to be described by the Hamiltonian

$$\mathcal{H} = \underbrace{\sum_{\mathbf{q}} \omega_{\mathbf{q}} \hat{\phi}_{\mathbf{q}}^{\dagger} \hat{\phi}_{\mathbf{q}}}_{\mathcal{H}_0} + \mathcal{H}_I, \quad (\text{C.11})$$

where the interaction as well as external influences such as external fields are described by \mathcal{H}_I . Employing the usual discretization via infinitesimal time steps and inserting coherent bosonic states $\hat{\phi} | \phi \rangle = \phi | \phi \rangle$, see e.g. Refs. [102, 103], the expectation value of two bosonic fields can be expressed in terms of the path integral

$$\langle \hat{\phi}_{\mathbf{q}}(t) \hat{\phi}_{\mathbf{q}'}(t') \rangle = \int D[\bar{\phi}, \phi] \phi_{\mathbf{q}}^{-}(t) \phi_{\mathbf{q}'}^{+}(t'), e^{iS}. \quad (\text{C.12})$$

Here, the ϕ^{\pm} fields are located on the upper/lower Keldysh contour ensuring the correct order of the bosonic field operators. The non-interacting Keldysh action is given by¹⁹

$$\begin{aligned} S_0 &= \underbrace{\int_{\mathcal{C}} dt \sum_{\mathbf{q}} \bar{\phi}_{\mathbf{q}}(t) (i\partial_t - \omega_{\mathbf{q}}) \phi_{\mathbf{q}}(t)}_{S_0} \\ &= \int_{-\infty}^{\infty} dt \sum_{\mathbf{q}} [\bar{\phi}_{\mathbf{q}}^{+}(t) (i\partial_t - \omega_{\mathbf{q}}) \phi_{\mathbf{q}}^{+}(t) - \bar{\phi}_{\mathbf{q}}^{-}(t) (i\partial_t - \omega_{\mathbf{q}}) \phi_{\mathbf{q}}^{-}(t)]. \end{aligned} \quad (\text{C.13})$$

In the continuum representation it looks as if the two Keldysh branches were uncoupled, however at $t = \infty$ there is a finite matrix element that connects the + and the - contour. This coupling leads to the following four Green's functions for the non-interacting case [103]

$$\begin{aligned} G_{\mathbf{q}}^{<}(t, t') &= -i \langle \phi_{\mathbf{q}}^{+}(t) \bar{\phi}_{\mathbf{q}}^{-}(t') \rangle_0 = -in_B(\omega_{\mathbf{q}}) e^{-i\omega_{\mathbf{q}}(t-t')}, \\ G_{\mathbf{q}}^{>}(t, t') &= -i \langle \phi_{\mathbf{q}}^{-}(t) \bar{\phi}_{\mathbf{q}}^{+}(t') \rangle_0 = -i[n_B(\omega_{\mathbf{q}}) + 1] e^{-i\omega_{\mathbf{q}}(t-t')}, \\ G_{\mathbf{q}}^{\text{T}}(t, t') &= -i \langle \phi_{\mathbf{q}}^{+}(t) \bar{\phi}_{\mathbf{q}}^{+}(t') \rangle_0 = G^{>}(t, t') \Theta_0(t-t') + G^{<}(t, t') \Theta(t'-t), \\ G_{\mathbf{q}}^{\bar{\text{T}}}(t, t') &= -i \langle \phi_{\mathbf{q}}^{-}(t) \bar{\phi}_{\mathbf{q}}^{-}(t') \rangle_0 = G^{>}(t, t') \Theta_0(t'-t) + G^{<}(t, t') \Theta(t-t'), \end{aligned} \quad (\text{C.14})$$

where the bare expectation value is defined as $\langle \dots \rangle_0 = \int D[\bar{\phi}, \phi] \dots e^{iS_0}$. This non-trivial coupling of the upper and lower Keldysh contour is hard to formulate for the continuous

¹⁹Interactions are translated straightforward from the Hamiltonian to the action by converting the operators $\hat{\phi}$ by fields ϕ and an additional minus sign.

time-notation in the basis of the ϕ^+ and ϕ^- fields. The task is facilitated by the observation that not all four Green's functions defined in (C.14) are independent

$$G_q^{\mathbb{T}}(t, t') + G_q^{\tilde{\mathbb{T}}}(t, t') - G_q^>(t, t') - G_q^<(t, t') = 0. \quad (\text{C.15})$$

Thus, we can perform a rotation to simplify the relations between the fields by introducing the new fields (classical and quantum)

$$\begin{pmatrix} \phi_q^{\text{cl}} \\ \phi_q^{\text{q}} \end{pmatrix} = \hat{U} \begin{pmatrix} \phi_q^+ \\ \phi_q^- \end{pmatrix}, \quad \text{with } \hat{U} = \frac{1}{\sqrt{2}} \begin{pmatrix} 1 & 1 \\ 1 & -1 \end{pmatrix}. \quad (\text{C.16})$$

The correlators of these new fields are

$$\left\langle \begin{pmatrix} \phi_q^{\text{cl}}(t) \\ \phi_q^{\text{q}}(t) \end{pmatrix} \begin{pmatrix} \phi_q^{\text{cl}}(t') \\ \phi_q^{\text{q}}(t') \end{pmatrix}^\dagger \right\rangle = \hat{U} \left\langle \begin{pmatrix} \phi_q^+(t) \\ \phi_q^-(t) \end{pmatrix} \begin{pmatrix} \phi_q^+(t') \\ \phi_q^-(t') \end{pmatrix}^\dagger \right\rangle \hat{U}^\dagger = \hat{U} \left\langle \begin{pmatrix} iG_q^{\mathbb{T}}(t, t') & iG_q^<(t, t') \\ iG_q^>(t, t') & iG_q^{\tilde{\mathbb{T}}}(t, t') \end{pmatrix} \right\rangle \hat{U}^\dagger, \quad (\text{C.17})$$

which can be rewritten as

$$\langle \phi_q^\alpha(t) \bar{\phi}_q^\beta(t') \rangle = iG_q^{\alpha, \beta}(t, t') = \begin{pmatrix} iG_q^K(t, t') & iG_q^R(t, t') \\ iG_q^A(t, t') & 0 \end{pmatrix}, \quad (\text{C.18})$$

with the corresponding retarded, advanced and Keldysh propagators²⁰

$$\begin{aligned} G_q^K(t, t') &= G_q^{\text{cl,cl}}(t, t') = \frac{1}{2} [G_q^{\mathbb{T}} + G_q^{\tilde{\mathbb{T}}} + G_q^> + G_q^<] = G_q^> + G_q^<, \\ G_q^R(t, t') &= G_q^{\text{cl,q}}(t, t') = \frac{1}{2} [G_q^{\mathbb{T}} - G_q^{\tilde{\mathbb{T}}} + G_q^> - G_q^<] = (G_q^> - G_q^<) \Theta(t - t'), \\ G_q^A(t, t') &= G_q^{\text{q,cl}}(t, t') = \frac{1}{2} [G_q^{\mathbb{T}} - G_q^{\tilde{\mathbb{T}}} - G_q^> + G_q^<] = (G_q^< - G_q^>) \Theta(t' - t). \end{aligned} \quad (\text{C.19})$$

The new basis is often also referred to as the RAK-basis in contrast to the \pm -basis. The inverse relations read:

$$\begin{aligned} G_q^<(t, t') &= G_q^{+, \cdot}(t, t') = \frac{1}{2} [G_q^K - G_q^R + G_q^A], \\ G_q^>(t, t') &= G_q^{\cdot, +}(t, t') = \frac{1}{2} [G_q^K + G_q^R - G_q^A], \\ G_q^{\mathbb{T}}(t, t') &= G_q^{+, +}(t, t') = \frac{1}{2} [G_q^K + G_q^R + G_q^A] = G_q^< + G_q^R = G_q^> + G_q^A, \\ G_q^{\tilde{\mathbb{T}}}(t, t') &= G_q^{\cdot, \cdot}(t, t') = \frac{1}{2} [G_q^K - G_q^R - G_q^A] = G_q^< - G_q^A = G_q^> - G_q^R. \end{aligned} \quad (\text{C.20})$$

For our free bosons the propagators in the RAK-basis are given by

$$\begin{aligned} G_q^K(t, t') &= -i[2n_B(\omega_0) + 1]e^{-i\omega_0(t-t')}, \\ G_q^R(t, t') &= -i\Theta(t - t')e^{-i\omega_0(t-t')}, \\ G_q^A(t, t') &= i\Theta(t' - t)e^{-i\omega_0(t-t')}, \end{aligned} \quad (\text{C.21})$$

and performing the Fourier-transform of these quantities we find the usual form of the RAK-propagators in energy-representation

$$G_q^R(\epsilon) \stackrel{(\text{C.19})}{=} -i \int d(t - t') e^{-i\omega_q(t-t')} \Theta(t - t') e^{i(\epsilon+i0)(t-t')} = \frac{1}{\epsilon - \omega_q + i0},$$

²⁰These Green's functions indeed correspond with to the usual definition of the retarded, advanced and Keldysh propagators in the operator language.

$$G_q^A(\epsilon) \stackrel{\text{(C.19)}}{=} i \int d(t-t') e^{-i\omega_q(t-t')} \Theta(t'-t) e^{i(\epsilon-i0)(t-t')} = \frac{1}{\epsilon - \omega_q - i0}, \quad (\text{C.22})$$

$$G_q^K(\epsilon) \stackrel{\text{(C.19)}}{=} -i \int d(t-t') e^{-i\omega_q(t-t')} [2n_B(\omega_q) + 1] e^{i\epsilon(t-t')} = -i [2n_B(\omega_q) + 1] 2\pi\delta(\epsilon - \omega_q).$$

In the fermionic case, there are only a few minor changes:

1. Instead of complex fields ϕ one has to use Grassmann fields to account for the anticommuting nature of the fermions.
2. The Bose-Funktion n_B has to be replaced by the Fermi function n_F .
3. Instead of quantum and classic fields $\phi^{\text{cl,q}}$ one introduced the $\psi^{1/2}$ fermionic fields via

$$\begin{aligned} \begin{pmatrix} \psi^1 \\ \psi^2 \end{pmatrix} &= \frac{1}{\sqrt{2}} \begin{pmatrix} 1 & 1 \\ 1 & -1 \end{pmatrix} \begin{pmatrix} \psi^+ \\ \psi^- \end{pmatrix} = \hat{U} \begin{pmatrix} \psi^+ \\ \psi^- \end{pmatrix}, \\ \begin{pmatrix} \bar{\psi}^1 \\ \bar{\psi}^2 \end{pmatrix} &= \frac{1}{\sqrt{2}} \begin{pmatrix} 1 & -1 \\ 1 & 1 \end{pmatrix} \begin{pmatrix} \bar{\psi}^+ \\ \bar{\psi}^- \end{pmatrix} = \bar{U} \begin{pmatrix} \psi^+ \\ \psi^- \end{pmatrix}. \end{aligned} \quad (\text{C.23})$$

This leads to a different structure of the RAK-basis $G^R = G^{11}$, $G^A = G^{22}$ and $G^K = G^{12}$. However, the relations between the RAK and the \pm -basis is still the same as for the bosonic case, see Eqs. (C.19,C.20).

D. SLED calculations

The calculations in this appendix are based on Ref. [202].

D.1. Integrating out the electrons and bath

Let us start by integrating out the electronic degrees of freedom of the action (6.9), which can be achieved using the usual rules of Gaussian integration

$$\begin{aligned} \int D[\Psi, \bar{\Psi}] e^{i[S_c + S_v + S_{\text{int}}]} &= \int D[\Psi, \bar{\Psi}] e^{i \sum_{\mathbf{k}, \mathbf{k}'} \int_{-\infty}^{\infty} dt dt' \hat{\Psi}_{\mathbf{k}}^\dagger(t) \left(\hat{G}_{0, \mathbf{k}}^{-1}(t, t') \delta_{\mathbf{k}, \mathbf{k}'} + \hat{V}_{\mathbf{k}, \mathbf{k}'}(t) \delta(t-t') \right) \hat{\Psi}_{\mathbf{k}}(t')} \\ &= e^{\text{tr} \ln [1 + \hat{G}_0 \hat{V}]}. \end{aligned} \quad (\text{D.1})$$

We can then expand the trace-log term in our perturbative parameter g and perform the trace in the time and momentum space

$$\begin{aligned} \text{tr} \ln [1 + \hat{G}_0 \hat{V}] &= \sum_{n=1}^{\infty} \frac{(-1)^{n+1}}{n} \text{tr} [(\hat{G}_0 \hat{V})^n] = -\frac{1}{2} \text{tr} [(\hat{G}_0 \hat{V})^2] + \dots \\ &\approx -\frac{1}{2} \int dt dt' \sum_{\mathbf{k}, \mathbf{k}'} \text{tr} [\hat{G}_{0, \mathbf{k}}(t', t) \hat{V}_{\mathbf{k}, \mathbf{k}'}(t) \hat{G}_{\mathbf{k}', \mathbf{k}}(t, t') \hat{V}_{\mathbf{k}', \mathbf{k}}(t')] \\ &= -\frac{1}{2} \int dt dt' \sum_{\mathbf{k}, \mathbf{q}} \text{tr} \left[\hat{G}_{0, \mathbf{k}}(t', t) \left[\sum_{\substack{\alpha=\text{q,cl} \\ i=1,2}} \hat{g}_i^\alpha \Phi_{\mathbf{q}, i}^\alpha(t) \right] \hat{G}_{0, \mathbf{k}-\mathbf{q}}(t, t') \left[\sum_{\substack{\beta=\text{q,cl} \\ j=1,2}} \hat{g}_j^\beta \Phi_{-\mathbf{q}, j}^\beta(t') \right] \right] \\ &= -\frac{1}{2} \int dt dt' \sum_{\mathbf{q}} \sum_{\substack{i, j=1,2 \\ \alpha, \beta=\text{q,cl}}} \Phi_{\mathbf{q}, i}^\alpha(t) \underbrace{\left(\sum_{\mathbf{k}} \text{tr} [\hat{G}_{0, \mathbf{k}}(t', t) \hat{g}_i^\alpha \hat{G}_{0, \mathbf{k}-\mathbf{q}}(t, t') \hat{g}_j^\beta \hat{G}_{\mathbf{q}}] \right)}_{:=i[\Pi^{\text{el}}]_{ij, \mathbf{q}}^{\alpha\beta}(t, t')} \Phi_{-\mathbf{q}, j}^\beta(t') \\ &= -\frac{i}{2} \int dt dt' \sum_{\mathbf{q}} \hat{\Phi}_{\mathbf{q}}^T(t) \hat{\Pi}_{\mathbf{q}}^{\text{el}}(t, t') \hat{\Phi}_{-\mathbf{q}, j}(t'). \end{aligned} \quad (\text{D.2})$$

With the definition

$$[\Pi^{\text{el}}]_{ij, \mathbf{q}}^{\alpha\beta}(t, t') = -i \sum_{\mathbf{k}} \text{tr} [\hat{g}_i^\alpha \hat{G}_{0, \mathbf{k}}(t, t') \hat{g}_j^\beta \hat{G}_{0, \mathbf{k}+\mathbf{q}}(t', t)] \quad (\text{D.3})$$

the occurring photon self-energies that arise from the interaction with the electronic quasiparticles can be conveniently summarized as

$$\begin{aligned} \hat{\Pi}_{\mathbf{q}}^{\text{el}}(t, t') &= \begin{pmatrix} 0 & \hat{\Pi}_{\mathbf{q}}^{\text{el}, A}(t, t') \\ \hat{\Pi}_{\mathbf{q}}^{\text{el}, R}(t, t') & \hat{\Pi}_{\mathbf{q}}^{\text{el}, K}(t, t') \end{pmatrix}, \\ \hat{\Pi}_{\mathbf{q}}^{\text{el}, R}(t, t') &= \begin{pmatrix} [\Pi^{\text{el}}]_{11, \mathbf{q}}^{\text{q,cl}}(t, t') & [\Pi^{\text{el}}]_{12, \mathbf{q}}^{\text{q,cl}}(t, t') \\ [\Pi^{\text{el}}]_{21, \mathbf{q}}^{\text{q,cl}}(t, t') & [\Pi^{\text{el}}]_{22, \mathbf{q}}^{\text{q,cl}}(t, t') \end{pmatrix}, \\ \hat{\Pi}_{\mathbf{q}}^{\text{el}, A}(t, t') &= \begin{pmatrix} [\Pi^{\text{el}}]_{11, \mathbf{q}}^{\text{cl, q}}(t, t') & [\Pi^{\text{el}}]_{12, \mathbf{q}}^{\text{cl, q}}(t, t') \\ [\Pi^{\text{el}}]_{21, \mathbf{q}}^{\text{cl, q}}(t, t') & [\Pi^{\text{el}}]_{22, \mathbf{q}}^{\text{cl, q}}(t, t') \end{pmatrix}, \\ \hat{\Pi}_{\mathbf{q}}^{\text{el}, K}(t, t') &= \begin{pmatrix} [\Pi^{\text{el}}]_{11, \mathbf{q}}^{\text{cl, cl}}(t, t') & [\Pi^{\text{el}}]_{12, \mathbf{q}}^{\text{cl, cl}}(t, t') \\ [\Pi^{\text{el}}]_{21, \mathbf{q}}^{\text{cl, cl}}(t, t') & [\Pi^{\text{el}}]_{22, \mathbf{q}}^{\text{cl, cl}}(t, t') \end{pmatrix}. \end{aligned}$$

In a similar way, the bath photons A_q can be integrated out. First, we define the spinors

$$\begin{aligned}\hat{\Upsilon}_q^\zeta(t) &= \begin{pmatrix} A_q^\zeta \\ \bar{A}_{-q}^\zeta \end{pmatrix}, \\ \hat{\Upsilon}_q &= \begin{pmatrix} \hat{\Upsilon}_q^{\text{cl}} \\ \hat{\Upsilon}_q^{\text{q}} \end{pmatrix}.\end{aligned}\tag{D.4}$$

The interaction between the path and the LED photons can then be written as

$$S_{\text{ph}}^{\text{bath}} = \int_{-\infty}^{\infty} dt dt' \left[\frac{1}{2} \sum_q \hat{\Upsilon}_q^T(t) \hat{D}_{0,A,q}^{-1}(t, t') \hat{\Upsilon}_{-q}(t') + \sum_{q, q'} \delta(t - t') \hat{\Phi}_q^T(t) \hat{\lambda}_{q, q'} \hat{\Upsilon}_{q'}(t) \right].\tag{D.5}$$

with

$$\hat{\lambda}_{q, q'} = (\hat{\sigma}_x \otimes \hat{\sigma}_x) \cdot \lambda_{q q'}.\tag{D.6}$$

Using the usual identities for Gaussian integration the following bath self-energies occur

$$\begin{aligned}\hat{\Pi}_q^{\text{bath}}(t, t') &= \begin{pmatrix} 0 & \hat{\Pi}_q^{\text{bath}, A}(t, t') \\ \hat{\Pi}_q^{\text{bath}, R}(t, t') & \hat{\Pi}_q^{\text{bath}, K}(t, t') \end{pmatrix}, \\ \hat{\Pi}_q^{\text{bath}, R/A/K}(t, t') &= \sum_p |\lambda_{q, p}|^2 \begin{pmatrix} 0 & d_{\text{bath}, p}^{A/R/K}(t', t) \\ d_{\text{bath}, p}^{R/A/K}(t, t') & 0 \end{pmatrix},\end{aligned}$$

with

$$\begin{aligned}d_{\text{bath}, q}^{R/A}(\omega) &= \frac{1}{\omega + eV - \nu_q \pm i0}, \\ d_{\text{bath}, q}^K(\omega) &= B_0(\omega + eV) [d_{\text{bath}, q}^R(\omega) - d_{\text{bath}, q}^A(\omega)],\end{aligned}$$

The assumption of a momentum-independent coupling $\lambda_{p, p'} = \lambda(\omega_{p'})$ and an Ohmic bath leads to the simple expressions for the bath self-energies in Eqs. (6.26)-(6.30).

D.2. Calculation of the $\hat{\Pi}^{\text{el}}$ self-energies

Let us now perform the traces over the Keldysh space for the electron-induced self-energy in Eq. (D.3)

$$\begin{aligned}[\Pi^{\text{el}}]_{ij, q}^R(t, t') &= [\Pi^{\text{el}}]_{ij, q}^{\text{q}, \text{cl}}(t, t') = -i \sum_{\mathbf{k}} \text{tr} [\hat{\gamma}^{\text{q}} \hat{g}_i \hat{G}_{0, \mathbf{k}}^\Delta(t, t') \hat{\gamma}^{\text{cl}} \hat{g}_j \hat{G}_{\mathbf{k}+q}^\Delta(t', t)] \\ &= -i \sum_{\mathbf{k}} \text{tr}_\Delta \text{tr}_\wedge \left[\begin{pmatrix} 0 & 1 \\ 1 & 0 \end{pmatrix} \hat{g}_i \begin{pmatrix} \hat{G}_{0, \mathbf{k}}^R(t, t') & \hat{G}_{0, \mathbf{k}}^K(t, t') \\ 0 & \hat{G}_{0, \mathbf{k}}^A(t, t') \end{pmatrix} \times \right. \\ &\quad \left. \begin{pmatrix} 1 & 0 \\ 0 & 1 \end{pmatrix} \hat{g}_j \begin{pmatrix} \hat{G}_{0, \mathbf{k}+q}^R(t', t) & \hat{G}_{0, \mathbf{k}+q}^K(t', t) \\ 0 & \hat{G}_{0, \mathbf{k}+q}^A(t', t) \end{pmatrix} \right] \\ &= -i \sum_{\mathbf{k}} \text{tr}_\Delta [\hat{g}_i \hat{G}_{0, \mathbf{k}}^R(t, t') \hat{g}_j \hat{G}_{0, \mathbf{k}+q}^K(t', t) + \hat{g}_i \hat{G}_{0, \mathbf{k}}^K(t, t') \hat{g}_j \hat{G}_{0, \mathbf{k}+q}^A(t', t)], \\ [\Pi^{\text{el}}]_{ij, q}^A(t, t') &= -i \sum_{\mathbf{k}} \text{tr}_\Delta [\hat{g}_i \hat{G}_{0, \mathbf{k}}^A(t, t') \hat{g}_j \hat{G}_{0, \mathbf{k}+q}^K(t', t) + \hat{g}_i \hat{G}_{0, \mathbf{k}}^K(t, t') \hat{g}_j \hat{G}_{0, \mathbf{k}+q}^R(t', t)],\end{aligned}$$

$$\begin{aligned}
[\Pi_{ij,\mathbf{q}}^{\text{el}}]^K(t, t') = & -i \sum_{\mathbf{k}} \text{tr}_{\Delta} \left[\overset{\Delta}{g}_i \overset{\Delta}{G}_{0,\mathbf{k}}^K(t, t') \overset{\Delta}{g}_j \overset{\Delta}{G}_{0,\mathbf{k}+\mathbf{q}}^K(t', t) \right. \\
& \left. - \overset{\Delta}{g}_i [\overset{\Delta}{G}_{0,\mathbf{k}}^R(t, t') - \overset{\Delta}{G}_{0,\mathbf{k}}^A(t, t')] \overset{\Delta}{g}_j [\overset{\Delta}{G}_{0,\mathbf{k}+\mathbf{q}}^R(t', t) - \overset{\Delta}{G}_{0,\mathbf{k}+\mathbf{q}}^A(t', t)] \right].
\end{aligned} \tag{D.7}$$

As next step, we extract the phase of the superconducting order parameters $\Delta_{v/c} = |\Delta_{v/c}| e^{i\phi_{v/c}}$ from the anomalous propagators $F_{c/v}$ and $\bar{F}_{c/v}$ by defining the new propagators

$$P_{0,\mathbf{k},v/c}^R(\omega) = e^{-i\phi_{v/c}} F_{0,\mathbf{k},v/c}^R(\omega) = -\frac{|\Delta_{c/v}|}{(\omega \pm i0)^2 - \xi_{v/c}(\mathbf{k})^2 - |\Delta_{c/v}|^2}, \tag{D.8}$$

and similarly for the advanced and Keldysh component. After Fourier-transforming and performing the remaining trace over the extended Nambu-space, we end up with the expressions

$$\begin{aligned}
\tilde{\Pi}_{11,\mathbf{q}}^{\text{el},R/A}(\omega) &= i |g_0^2| \sum_{\mathbf{k}} \int_{-\infty}^{\infty} \frac{d\omega_1}{2\pi} \left[|P_{0,\mathbf{k},v}^{R/A}(\omega_1)| |P_{0,\mathbf{k}+\mathbf{q},c}^K(\omega_1 - \omega)| + |P_{0,\mathbf{k},v}^K(\omega_1)| |P_{0,\mathbf{k}+\mathbf{q},c}^{A/R}(\omega_1 - \omega)| \right] \\
\Pi_{12,\mathbf{q}}^{\text{el},R/A}(\omega) &= -i |g_0^2| \sum_{\mathbf{k}} \int_{-\infty}^{\infty} \frac{d\omega_1}{2\pi} \left[G_{0,\mathbf{k},v}^{(p),R/A}(\omega_1) G_{0,\mathbf{k}+\mathbf{q},c}^{(p),K}(\omega_1 - \omega) + G_{0,\mathbf{k},v}^{(p),K}(\omega_1) G_{0,\mathbf{k}+\mathbf{q},c}^{(p),A/R}(\omega_1 - \omega) \right] \\
\Pi_{21,\mathbf{q}}^{\text{el},R/A}(\omega) &= -i |g_0^2| \sum_{\mathbf{k}} \int_{-\infty}^{\infty} \frac{d\omega_1}{2\pi} \left[G_{0,\mathbf{k},v}^{(h),R/A}(\omega_1) G_{0,\mathbf{k}+\mathbf{q},c}^{(h),K}(\omega_1 - \omega) + G_{0,\mathbf{k},v}^{(h),K}(\omega_1) G_{0,\mathbf{k}+\mathbf{q},c}^{(h),A/R}(\omega_1 - \omega) \right] \\
\tilde{\Pi}_{22,\mathbf{q}}^{\text{el},R/A}(\omega) &= i |g_0^2| \sum_{\mathbf{k}} \int_{-\infty}^{\infty} \frac{d\omega_1}{2\pi} \left[|P_{0,\mathbf{k},v}^{R/A}(\omega_1)| |P_{0,\mathbf{k}+\mathbf{q},c}^K(\omega_1 - \omega)| + |P_{0,\mathbf{k},v}^K(\omega_1)| |P_{0,\mathbf{k}+\mathbf{q},c}^{A/R}(\omega_1 - \omega)| \right]
\end{aligned} \tag{D.9}$$

for the retarded self-energies. Note that we extracted the superconducting phases in the anomalous self-energies by the definition of the $\tilde{\Pi}_{11}$ and $\tilde{\Pi}_{22}$ self-energies as in Eq. (6.20). The inherent symmetries of the propagators can then be used to relate the self-energies as shown in Eq. (6.24).

D.2.1. Normal conductor

In the normal state the superconducting gaps vanish as well as the P, \bar{P} propagators and the anomalous self-energies $\Pi_{11}^{\text{el}} = \Pi_{22}^{\text{el}} = 0$. The remaining particle self-energy is just given by

$$\Pi_{21,\mathbf{q}}^{\text{el},R/A}(\omega) = 2 |g_0^2| \sum_{\mathbf{k}} \frac{n_F[\xi_v(\mathbf{k})] - n_F[\xi_c(\mathbf{k} + \mathbf{q})]}{\omega + \xi_v(\mathbf{k}) - \xi_c(\mathbf{k} + \mathbf{q}) \pm i0}. \tag{D.10}$$

We now choose our particle and hole bands $\xi_c(\mathbf{k}) = -\xi_v(\mathbf{k})$ as well as the superconducting gaps $|\Delta_v| = |\Delta_c| = \Delta$ to be symmetric. We can then linearize our dispersions around the Fermi surface

$$\begin{aligned}
\xi_c(\mathbf{k}) &= v_F(|\mathbf{k}| - k_F), \\
\xi_c(\mathbf{k} + \mathbf{q}) &= v_F(|\mathbf{k}| - k_F) + \mathbf{v}_F \cdot \mathbf{q} = \xi_c(\mathbf{k}) + v_F q \cos(\theta),
\end{aligned} \tag{D.11}$$

where $q = |\mathbf{q}|$ and θ is the angle between the momentum $\mathbf{k} \parallel \mathbf{v}_F$ and the small photon momentum \mathbf{q} . This allows us to execute the momentum summation via the integrals

$$\sum_{\mathbf{k}} f[\xi_v(\mathbf{k}), \xi_c(\mathbf{k} + \mathbf{q})] = \int_{-1}^1 \frac{d \cos \theta}{2} \int_{-E_F}^{\infty} d\xi \nu(\xi) f[-\xi, \xi + v_F q \cos(\theta)]$$

$$= \int_{-v_F q}^{v_F q} \frac{d\alpha}{2v_F q} \int_{-E_F}^{\infty} d\xi \nu(\xi) f[-\xi, \xi + \alpha]. \quad (\text{D.12})$$

Here, E_F is the Fermi energy as measured from the band-edge of the conductance band. One can omit the real part of the self-energy in the weak-coupling limit, because it is featureless and only gives a negligible correction to the photonic dispersion. The imaginary part can under the assumption of a only weakly energy-dependent DOS in the zero temperature limit be calculated as

$$\begin{aligned} \text{Im } \Pi_{21,q}^{\text{el},R/A}(\omega) &= \mp 2\pi |g_0^2| \int_{-v_F q}^{v_F q} \frac{d\alpha}{2v_F q} \int_{-E_F}^{\infty} d\xi \nu(\xi) \left(n_F[-\xi] - n_F[\xi + \alpha] \right) \delta[\omega - 2\xi - \alpha] \\ &= \mp \frac{\pi |g_0^2|}{2v_F q} \int_{-v_F q}^{v_F q} d\alpha \underbrace{\nu\left(\frac{\omega - \alpha}{2}\right)}_{\approx \nu(\omega/2)} \left(n_F\left[\frac{-\omega + \alpha}{2}\right] - n_F\left[\frac{\omega + \alpha}{2}\right] \right) \\ &\approx \mp \frac{\pi |g_0^2|}{2v_F q} \nu(\omega/2) \int_{-v_F q}^{v_F q} d\alpha \left[\theta(\omega - \alpha) - \theta(-\omega - \alpha) \right] \\ &= \mp \pi |g_0^2| \nu(\omega/2) \text{sign}(\omega) \min\left[1, \frac{|\omega|}{v_F q}\right]. \end{aligned} \quad (\text{D.13})$$

D.2.2. Superconductor

In the superconducting state, it is convenient to use the following parametrization of the normal and anomalous electronic Green's functions ($T = 0$)

$$\begin{aligned} A_{0,\mathbf{k},v/c}^{R/A}(\omega) &= \frac{\alpha_{A,\mathbf{k},v/c}}{\omega - E_{v/c}(\mathbf{k}) \pm i0} + \frac{\beta_{A,\mathbf{k},v/c}}{\omega - E_{v/c}(\mathbf{k}) \pm i0}, \quad (\text{D.14}) \\ A_{0,\mathbf{k},v/c}^K(\omega) &= [1 - 2n_F(\omega)] \left(A_{0,\mathbf{k},v/c}^R(\omega) - A_{0,\mathbf{k},v/c}^A(\omega) \right) \\ &= -2\pi i \left(\alpha_{A,\mathbf{k},v/c} \delta[\omega - E_{v/c}(\mathbf{k})] + \beta_{A,\mathbf{k},v/c} \delta[\omega + E_{v/c}(\mathbf{k})] \right). \end{aligned}$$

Here, $E_{v/c}(\mathbf{k}) = \sqrt{\xi_{v/c}(\mathbf{k})^2 + |\Delta_{v/c}|^2}$ is the superconducting dispersion and we defined the coherence factors in the usual way

A	$G^{(p)}$	$G^{(h)}$	$ P $
$\alpha_{A,\mathbf{k},v/c}$	$u_{\mathbf{k},c/v}^2$	$v_{\mathbf{k},c/v}^2$	$-u_{\mathbf{k},c/v} v_{\mathbf{k},c/v}$
$\beta_{A,\mathbf{k},v/c}$	$v_{\mathbf{k},c/v}^2$	$u_{\mathbf{k},c/v}^2$	$u_{\mathbf{k},c/v} v_{\mathbf{k},c/v}$

$$\begin{aligned} u_{\mathbf{k},c/v} &= \sqrt{\frac{1}{2} \left(1 + \frac{\xi_{c/v}(\mathbf{k})}{E_{c/v}(\mathbf{k})} \right)} \\ v_{\mathbf{k},c/v} &= \sqrt{\frac{1}{2} \left(1 - \frac{\xi_{c/v}(\mathbf{k})}{E_{c/v}(\mathbf{k})} \right)} \end{aligned} \quad (\text{D.15})$$

Putting this parametrization into Eqs. (D.9) we arrive at the following expressions

$$\begin{aligned} \tilde{\Pi}_{11,q}^{\text{el},R/A}(\omega) &= 2 |g_0^2| \sum_{\mathbf{k}} \left[\frac{u_{\mathbf{k},v} v_{\mathbf{k},v} u_{\mathbf{k}+\mathbf{q},c} v_{\mathbf{k}+\mathbf{q},c}}{\omega - E_v(\mathbf{k}) - E_c(\mathbf{k} + \mathbf{q}) \pm i0} - \frac{u_{\mathbf{k},v} v_{\mathbf{k},v} u_{\mathbf{k}+\mathbf{q},c} v_{\mathbf{k}+\mathbf{q},c}}{\omega + E_v(\mathbf{k}) + E_c(\mathbf{k} + \mathbf{q}) \pm i0} \right], \\ \Pi_{21,q}^{\text{el},R/A}(\omega) &= 2 |g_0^2| \sum_{\mathbf{k}} \left[\frac{v_{\mathbf{k},v}^2 u_{\mathbf{k}+\mathbf{q},c}^2}{\omega - E_v(\mathbf{k}) - E_c(\mathbf{k} + \mathbf{q}) \pm i0} - \frac{u_{\mathbf{k},v}^2 v_{\mathbf{k}+\mathbf{q},c}^2}{\omega + E_v(\mathbf{k}) + E_c(\mathbf{k} + \mathbf{q}) \pm i0} \right]. \end{aligned} \quad (\text{D.16})$$

Let us start by calculating the anomalous self-energy. Using the linearization technique of Eq. (D.12) and defining the dimensionless frequency $\tilde{\omega} = \omega/\Delta$ we can express it as

$$\tilde{\Pi}_{11,q}^{\text{el},R}(\omega) = \frac{|g_0^2| \nu_F \Delta}{4v_F q} \int_{-v_F q/\Delta}^{v_F q/\Delta} d\alpha \int_{-E_F/\Delta}^{\infty} dx \frac{1}{\sqrt{x^2 + 1} \sqrt{(x + \alpha)^2 + 1}} \times \quad (\text{D.17})$$

$$\left[\frac{1}{\tilde{\omega} - \sqrt{x^2 + 1} - \sqrt{(x + \alpha)^2 + 1} + i0} - \frac{1}{\tilde{\omega} + \sqrt{x^2 + 1} + \sqrt{(x + \alpha)^2 + 1} + i0} \right],$$

where we approximated the DOS as ν_F because the self-energy rapidly decays to zero for $\omega \gg \Delta$. The real part of the self-energy is symmetric and the imaginary part is antisymmetric in frequency. We can thus restrict ourselves to positive $\omega > 0$. Let us first calculate the real part given by

$$\begin{aligned} \mathbf{Re} \tilde{\Pi}_{11,q}^{\text{el},R}(\omega) &= \frac{|g_0^2| \nu_F \Delta}{4v_F q} \mathcal{P} \int_{-v_F q/\Delta}^{v_F q/\Delta} d\alpha \int_{-E_F/\Delta}^{\infty} dx \frac{1}{\sqrt{x^2 + 1} \sqrt{(x + \alpha)^2 + 1}} \times \\ &\quad \left[\frac{1}{\tilde{\omega} - \sqrt{x^2 + 1} - \sqrt{(x + \alpha)^2 + 1}} - \frac{1}{\tilde{\omega} + \sqrt{x^2 + 1} + \sqrt{(x + \alpha)^2 + 1}} \right]. \end{aligned} \quad (\text{D.18})$$

We see that the integrand will have a singularity if

$$\tilde{\omega} = \sqrt{x^2 + 1} + \sqrt{(x + \alpha)^2 + 1} \geq 2\sqrt{1 + (\alpha/2)^2} = \tilde{\omega}_\alpha, \quad \text{for } x_{\min} = -\alpha/2. \quad (\text{D.19})$$

Thus, the interesting physics seems to occur at $\tilde{\omega} = 2$ (note that $\alpha \in [-v_F q, v_F q]$). Let us therefore focus on the region $\omega \approx 2\Delta$, where it is convenient to separate the singular region $x_{\min} \approx -\alpha/2$ of the integrand

$$\begin{aligned} \mathbf{Re} \tilde{\Pi}_{11,q}^{\text{el},R}(\omega \approx 2\Delta) &= g_q(\omega) + \frac{|g_0^2| \nu_F \Delta}{4v_F q} \mathcal{P} \int_{-v_F q/\Delta}^{v_F q/\Delta} d\alpha \int_{-\alpha/2-\delta x}^{-\alpha/2+\delta x} dx \times \\ &\quad \frac{1}{\sqrt{x^2 + 1} \sqrt{(x + \alpha)^2 + 1}} \frac{1}{\tilde{\omega} - \sqrt{x^2 + 1} - \sqrt{(x + \alpha)^2 + 1}} \\ &\stackrel{x \approx -\alpha/2}{\approx} g_q(\omega) + \frac{|g_0^2| \nu_F \Delta}{4v_F q} \mathcal{P} \int_{-v_F q/\Delta}^{v_F q/\Delta} d\alpha \int_{-\alpha/2-\delta x \rightarrow -\infty}^{-\alpha/2+\delta x \rightarrow \infty} dx \frac{4}{\omega_\alpha^2} \frac{1}{\tilde{\omega} - \tilde{\omega}_\alpha - \frac{8(x+\alpha/2)^2}{\tilde{\omega}_\alpha^3}} \\ &= g_q(\omega) - \frac{\pi |g_0^2| \nu_F \Delta}{\sqrt{2} v_F q} \int_0^{v_F q/\Delta} d\alpha \frac{\theta(\tilde{\omega}_\alpha - \tilde{\omega})}{\sqrt{\tilde{\omega}_\alpha} \sqrt{\tilde{\omega}_\alpha - \tilde{\omega}}} \\ &\approx g_q(\omega) - \frac{\pi |g_0^2| \nu_F \Delta}{v_F q} \ln \left[\sqrt{1 + \frac{(\frac{v_F q}{2\Delta})^2}{|2 - \tilde{\omega}|}} + \frac{\frac{v_F q}{2\Delta}}{\sqrt{|2 - \tilde{\omega}|}} \right]. \end{aligned} \quad (\text{D.20})$$

Here, $g_q(\omega)$ stands for some non-singular parts of the integral, which will be neglected because $|g_0|^2 \nu_F \ll \Delta$, E_F, eV is the smallest parameter of the theory and therefore $g_q(\omega)$ only gives negligible contributions to the photonic dispersion. Hence, we will neglect this part in the following. Also the imaginary parts can be calculated using the same methods for $\omega \approx 2\Delta$.

$$\begin{aligned} \mathbf{Im} \tilde{\Pi}_{11,q}^{\text{el},R}(\omega) &= -\frac{|g_0^2| \pi \nu_F \Delta}{4v_F q} \int_{-v_F q/\Delta}^{v_F q/\Delta} d\alpha \int dx \frac{\delta[\tilde{\omega} - \sqrt{x^2 + 1} - \sqrt{(x + \alpha)^2 + 1}]}{\sqrt{x^2 + 1} \sqrt{(x + \alpha)^2 + 1}} \\ &\stackrel{\omega \approx 2\Delta}{\approx} -\frac{|g_0^2| \pi \nu_F \Delta}{4v_F q} \int_{-v_F q/\Delta}^{v_F q/\Delta} d\alpha \int dx \frac{4}{\tilde{\omega}_\alpha^2} \delta\left[\tilde{\omega} - \tilde{\omega}_\alpha - \frac{8(x + \alpha/2)^2}{\tilde{\omega}_\alpha^3}\right] \theta(\tilde{\omega} - 2) \\ &= -\frac{|g_0^2| \pi \nu_F \Delta}{2\sqrt{2} v_F q} \int_{-v_F q/\Delta}^{v_F q/\Delta} d\alpha \int dy \frac{1}{\sqrt{\tilde{\omega}_\alpha}} \delta[\tilde{\omega} - \tilde{\omega}_\alpha - y^2] \theta(\tilde{\omega} - 2) \end{aligned}$$

$$\begin{aligned}
&= -\frac{|g_0^2| \pi \nu_F \Delta}{2\sqrt{2}v_F q} \int_{-v_F q/\Delta}^{v_F q/\Delta} d\alpha \frac{\theta(\tilde{\omega} - \tilde{\omega}_\alpha)}{\sqrt{\tilde{\omega}_\alpha} \sqrt{\tilde{\omega} - \tilde{\omega}_\alpha}} \theta(\tilde{\omega} - 2) \\
&\approx -\frac{|g_0^2| \pi \nu_F}{2(\frac{v_F q}{2\Delta})} \arcsin \left[\frac{\min[\frac{v_F q}{2\Delta}, \sqrt{\tilde{\omega} - 2}]}{\sqrt{\tilde{\omega} - 2}} \right] \theta(\tilde{\omega} - 2)
\end{aligned} \tag{D.21}$$

As can be seen from this expression, the imaginary part $\mathbf{Im} \tilde{\Pi}_{11,q}^{\text{el},R}(\omega) \xrightarrow{\omega \gg \Delta} \frac{1}{\omega^2}$ decays rapidly for higher energies. It is therefore not of importance for energies $|\omega| \gg \Delta$ and we can approximate the $\mathbf{Im} \tilde{\Pi}_{11,q}^{\text{el},R}(\omega)$ by the expression derived for $\omega \approx 2\Delta$ for the whole energy range.

Using the approximations performed in the just presented calculations, it is easy to show that near $\omega \approx 2\Delta$ the normal self-energies look exactly like the anomalous ones. However, for energies $\omega \gg \Delta$ much larger than the superconducting gap their behavior is like the normal conducting self-energies. In between, we may interpolate between these two limits and can thus write down the two self-energies as

$$\begin{aligned}
\tilde{\Pi}_{11,q}^{\text{el},R}(\omega) &\approx -\frac{\pi |g_0^2| \nu_F}{2(\frac{v_F q}{2\Delta})} \ln \left[\sqrt{1 + \frac{(\frac{v_F q}{2\Delta})^2}{|2 - |\tilde{\omega}||} + \frac{\frac{v_F q}{2\Delta}}{\sqrt{|2 - |\tilde{\omega}||}}} \right] \\
&\quad - i \frac{|g_0^2| \pi \nu_F}{2(\frac{v_F q}{2\Delta})} \arcsin \left(\frac{\min[\frac{v_F q}{2\Delta}, \sqrt{|\tilde{\omega}| - 2}]}{\sqrt{|\tilde{\omega}| - 2}} \right) \text{sign}(\omega) \theta(|\tilde{\omega}| - 2),
\end{aligned} \tag{D.22}$$

$$\begin{aligned}
\Pi_{21,q}^{\text{el},R}(\omega) &\approx -\frac{\pi |g_0^2| \nu_F}{2(\frac{v_F q}{2\Delta})} \ln \left[\sqrt{1 + \frac{(\frac{v_F q}{2\Delta})^2}{|2 - |\tilde{\omega}||} + \frac{\frac{v_F q}{2\Delta}}{\sqrt{|2 - |\tilde{\omega}||}}} \right] \\
&\quad - i \max \left[\frac{|g_0^2| \pi \nu_F}{2(\frac{v_F q}{2\Delta})} \arcsin \left(\frac{\min[\frac{v_F q}{2\Delta}, \sqrt{|\tilde{\omega}| - 2}]}{\sqrt{|\tilde{\omega}| - 2}} \right), \pi |g_0|^2 \nu(\omega/2) \right] \text{sign}(\omega) \theta(|\tilde{\omega}| - 2).
\end{aligned} \tag{D.23}$$

Bibliography

- [1] Onnes, H. On the sudden Rate at Which the Resistance of Mercury Disappears. *Leiden Comm.* **122b**. (1911). (see pp. [v](#), [15](#)).
- [2] Onnes, H. On the sudden change in the rate at which the resistance of mercury disappears. *Leiden Comm.* **124c**. (1911). (see pp. [v](#), [15](#)).
- [3] Meissner, W. & Ochsenfeld, R. Ein neuer Effekt bei Eintritt der Supraleitfähigkeit. *Naturwissenschaften* **21**, 787–788 (1933). URL <http://dx.doi.org/10.1007/BF01504252>. (see pp. [v](#), [15](#)).
- [4] Elschner, S. *et al.* New Experimental Method for Investigating AC Losses in Concentric HTS Power Cables. *IEEE Transactions on Applied Superconductivity* **25**, 1–5 (2015). (see p. [v](#)).
- [5] London, F. & London, H. The Electromagnetic Equations of the Supraconductor. *Proceedings of the Royal Society of London A: Mathematical, Physical and Engineering Sciences* **149**, 71–88 (1935). (see pp. [v](#), [15](#)).
- [6] Ginzburg, V. & Landau, L. To the Theory of Superconductivity. *Zh. Eksp. Teor. Fiz.* **20** (1950). (see pp. [v](#), [15](#)).
- [7] Bardeen, J., Cooper, L. N. & Schrieffer, J. R. Microscopic Theory of Superconductivity. *Phys. Rev.* **106**, 162–164 (1957). URL <http://link.aps.org/doi/10.1103/PhysRev.106.162>. (see pp. [v](#), [15](#)).
- [8] Bardeen, J., Cooper, L. N. & Schrieffer, J. R. Theory of Superconductivity. *Phys. Rev.* **108**, 1175–1204 (1957). URL <http://link.aps.org/doi/10.1103/PhysRev.108.1175>. (see pp. [v](#), [15](#)).
- [9] Eliashberg, G. Interactions Between electrons and lattice vVibration in a Superconductor. *JETP* **11**, 696 (1960). URL <http://www.jetp.ac.ru/cgi-bin/e/index/e/11/3/p696?a=list>. (see pp. [v](#), [5](#), [18](#), [21](#), [79](#)).
- [10] Eliashberg, G. Temperature Green’s Function for Electrons in a Superconductor. *JETP* **12**, 1000 (1961). URL <http://www.jetp.ac.ru/cgi-bin/e/index/e/12/5/p1000?a=list>. (see pp. [v](#), [5](#), [18](#), [21](#), [79](#)).
- [11] Parks, R. D. Superconductivity : I (1969). (see pp. [v](#), [4](#), [5](#), [25](#), [49](#), [54](#), [58](#), [59](#), [61](#), [62](#),

- 63, 66, 67).
- [12] Carbotte, J. P. Properties of boson-exchange superconductors. *Rev. Mod. Phys.* **62**, 1027–1157 (1990). URL <http://link.aps.org/doi/10.1103/RevModPhys.62.1027>. (see pp. v, 24).
- [13] Bardeen, J. Tunnelling from a Many-Particle Point of View. *Phys. Rev. Lett.* **6**, 57–59 (1961). URL <http://link.aps.org/doi/10.1103/PhysRevLett.6.57>. (see pp. vi, 1, 2).
- [14] Cohen, M. H., Falicov, L. M. & Phillips, J. C. Superconductive Tunneling. *Phys. Rev. Lett.* **8**, 316–318 (1962). URL <http://link.aps.org/doi/10.1103/PhysRevLett.8.316>. (see pp. vi, 1, 2).
- [15] McMillan, W. L. & Rowell, J. M. Lead Phonon Spectrum Calculated from Superconducting Density of States. *Phys. Rev. Lett.* **14**, 108–112 (1965). URL <http://link.aps.org/doi/10.1103/PhysRevLett.14.108>. (see pp. vi, 4, 5, 24, 60, 61, 67, 79).
- [16] McMillan, W. L. Transition Temperature of Strong-Coupled Superconductors. *Phys. Rev.* **167**, 331–344 (1968). URL <http://link.aps.org/doi/10.1103/PhysRev.167.331>. (see pp. vi, 5, 20, 24, 60).
- [17] Jaklevic, R. C. & Lambe, J. Molecular Vibration Spectra by Electron Tunneling. *Phys. Rev. Lett.* **17**, 1139–1140 (1966). URL <http://link.aps.org/doi/10.1103/PhysRevLett.17.1139>. (see pp. vi, 7, 46, 49, 57, 107).
- [18] Lambe, J. & Jaklevic, R. C. Molecular Vibration Spectra by Inelastic Electron Tunneling. *Phys. Rev.* **165**, 821–832 (1968). URL <http://link.aps.org/doi/10.1103/PhysRev.165.821>. (see pp. vi, 7, 46, 49, 57, 107).
- [19] Schackert, M. *et al.* Local Measurement of the Eliashberg Function of Pb Islands: Enhancement of Electron-Phonon Coupling by Quantum Well States. *Phys. Rev. Lett.* **114**, 047002 (2015). URL <http://link.aps.org/doi/10.1103/PhysRevLett.114.047002>. (see pp. vi, 8, 46, 50, 51, 55, 57, 59, 61, 62, 64, 81, 107).
- [20] Boschker Hans, Richter Christoph, Fillis-Tsirakis Evangelos, Schneider Christof W. & Mannhart Jochen. Electron-phonon Coupling and the Superconducting Phase Diagram of the LaAlO₃-SrTiO₃ Interface. *Scientific Reports* **5**, 12309 (2015). (see pp. vi, 46, 107).
- [21] McCann, E. & Fal'ko, V. I. A tunnel junction between a ferromagnet and a normal metal: magnon-assisted contribution to thermopower and conductance. *Journal of magnetism and magnetic materials* **268**, 123–131 (2004). (see pp. vi, 8).
- [22] Gao, C. L. *et al.* Spin Wave Dispersion on the Nanometer Scale. *Phys. Rev. Lett.* **101**, 167201 (2008). URL <http://link.aps.org/doi/10.1103/PhysRevLett.101.167201>. (see pp. vi, 8).
- [23] Balashov, T. *et al.* Inelastic electron-magnon interaction and spin transfer torque.

- Phys. Rev. B* **78**, 174404 (2008). URL <http://link.aps.org/doi/10.1103/PhysRevB.78.174404>. (see pp. vi, 8).
- [24] Jandke, J., Hlobil, P., Schackert, M., Wulfhchel, W. & Schmalian, J. Coupling to real and virtual phonons in tunneling spectroscopy of superconductors. *Phys. Rev. B* **93**, 060505(R) (2016). URL <http://link.aps.org/doi/10.1103/PhysRevB.93.060505>. (see pp. vi, viii, 8, 42, 46, 49, 50, 51, 55, 57, 59, 60, 62, 64, 65, 81, 107).
- [25] Hlobil, P., Jandke, J., Wulfhchel, W. & Schmalian, J. Tracing the electronic pairing glue in unconventional superconductors via inelastic Scanning Tunneling Spectroscopy. *arXiv preprint arXiv:1603.05288* (2016). (see pp. viii, 35, 38, 40, 69, 70, 72, 108).
- [26] Giaever, I. Energy Gap in Superconductors Measured by Electron Tunneling. *Phys. Rev. Lett.* **5**, 147–148 (1960). URL <http://link.aps.org/doi/10.1103/PhysRevLett.5.147>. (see p. 1).
- [27] Duke, C. B. *Tunneling in solids*. Solid state physics : Supplement 10 (Acad. Pr., New York, 1969). (see pp. 2, 3, 81).
- [28] Prange, R. E. Tunneling from a Many-Particle Point of View. *Phys. Rev.* **131**, 1083–1086 (1963). URL <http://link.aps.org/doi/10.1103/PhysRev.131.1083>. (see p. 2).
- [29] Wolf, E. L. *Principles of electron tunneling spectroscopy* (OUP Oxford, 2011). (see pp. 3, 81).
- [30] Giaever, I., Hart, H. R. & Megerle, K. Tunneling into Superconductors at Temperatures below 1K. *Phys. Rev.* **126**, 941–948 (1962). URL <http://link.aps.org/doi/10.1103/PhysRev.126.941>. (see p. 4).
- [31] Rowell, J. M., Anderson, P. W. & Thomas, D. E. Image of the Phonon Spectrum in the Tunneling Characteristic Between Superconductors. *Phys. Rev. Lett.* **10**, 334–336 (1963). URL <http://link.aps.org/doi/10.1103/PhysRevLett.10.334>. (see p. 4).
- [32] Brockhouse, B. N., Arase, T., Caglioti, G., Rao, K. R. & Woods, A. D. B. Crystal Dynamics of Lead. I. Dispersion Curves at 100° K. *Phys. Rev.* **128**, 1099–1111 (1962). URL <http://link.aps.org/doi/10.1103/PhysRev.128.1099>. (see pp. 5, 60, 61).
- [33] Stedman, R., Almqvist, L. & Nilsson, G. Phonon-Frequency Distributions and Heat Capacities of Aluminum and Lead. *Phys. Rev.* **162**, 549–557 (1967). URL <http://link.aps.org/doi/10.1103/PhysRev.162.549>. (see pp. 5, 7, 60, 61).
- [34] Roy, A. & Brockhouse, B. Lattice frequency spectra of Pb and Pb40Tl60 by neutron spectrometry. *Canadian Journal of Physics* **48**, 1781–1788 (1970). (see pp. 5, 60, 61).
- [35] Binnig, G., Rohrer, H., Gerber, C. & Weibel, E. Tunneling through a controllable vacuum gap. *Applied Physics Letters* **40**, 178–180 (1982). URL <http://scitation>.

- aip.org/content/aip/journal/apl/40/2/10.1063/1.92999. (see p. 5).
- [36] Tersoff, J. & Hamann, D. R. Theory of the scanning tunneling microscope. *Phys. Rev. B* **31**, 805–813 (1985). URL <http://link.aps.org/doi/10.1103/PhysRevB.31.805>. (see pp. 5, 51).
- [37] Hoffman, J. *et al.* Imaging quasiparticle interference in $\text{Bi}_2\text{Sr}_2\text{CaCu}_2\text{O}_{8+\delta}$. *Science* **297**, 1148–1151 (2002). URL <http://science.sciencemag.org/content/early/2002/07/25/science.1072640>. (see p. 6).
- [38] Roushan, P. *et al.* Topological surface states protected from backscattering by chiral spin texture. *Nature* **460**, 1106–1109 (2009). URL <http://www.nature.com/nature/journal/v460/n7259/full/nature08308.html>. (see p. 6).
- [39] Kreisel, A. *et al.* Interpretation of Scanning Tunneling Quasiparticle Interference and Impurity States in Cuprates. *Phys. Rev. Lett.* **114**, 217002 (2015). URL <http://link.aps.org/doi/10.1103/PhysRevLett.114.217002>. (see p. 6).
- [40] Walmsley, D. & Tomlin, J. Compilation of inelastic electron tunnelling spectra of molecules chemisorbed on metal oxides. *Progress in Surface Science* **18**, 247–447 (1985). URL <http://www.sciencedirect.com/science/article/pii/0079681685900103>. (see p. 7).
- [41] Stipe, B. C., Rezaei, M. A. & Ho, W. Single-Molecule Vibrational Spectroscopy and Microscopy. *Science* **280**, 1732–1735 (1998). URL <http://science.sciencemag.org/content/280/5370/1732>. <http://science.sciencemag.org/content/280/5370/1732.full.pdf>. (see p. 7).
- [42] Kim, Y., Komeda, T. & Kawai, M. Single-Molecule Reaction and Characterization by Vibrational Excitation. *Phys. Rev. Lett.* **89**, 126104 (2002). URL <http://link.aps.org/doi/10.1103/PhysRevLett.89.126104>. (see p. 7).
- [43] Pascual, J. I. *et al.* Adsorbate-Substrate Vibrational Modes of Benzene on Ag(110) Resolved with Scanning Tunneling Spectroscopy. *Phys. Rev. Lett.* **86**, 1050–1053 (2001). URL <http://link.aps.org/doi/10.1103/PhysRevLett.86.1050>. (see p. 7).
- [44] Pascual J. I., Lorente N., Song Z., Conrad H. & Rust H.-P. Selectivity in vibrationally mediated single-molecule chemistry. *Nature* **423**, 525–528 (2003). (see p. 7).
- [45] Chynoweth, A. G., Logan, R. A. & Thomas, D. E. Phonon-Assisted Tunneling in Silicon and Germanium Esaki Junctions. *Phys. Rev.* **125**, 877–881 (1962). URL <http://link.aps.org/doi/10.1103/PhysRev.125.877>. (see p. 7).
- [46] Steinrisser, F., Davis, L. C. & Duke, C. B. Electron and Phonon Tunneling Spectroscopy in Metal-Germanium Contacts. *Phys. Rev.* **176**, 912–914 (1968). URL <http://link.aps.org/doi/10.1103/PhysRev.176.912>. (see p. 7).
- [47] Davis, L. C. & Steinrisser, F. One-Electron and Phonon-Assisted Tunneling in n -Ge Schottky Barriers. *Phys. Rev. B* **1**, 614–623 (1970). URL <http://link.aps.org/>

- [doi/10.1103/PhysRevB.1.614](https://doi.org/10.1103/PhysRevB.1.614). (see p. 7).
- [48] Salace, G. & Patat, J. Tunneling spectroscopy possibilities in metal-oxide-semiconductor devices with a very thin oxide barrier. *Thin Solid Films* **207**, 213–219 (1992). URL <http://www.sciencedirect.com/science/article/pii/004060909290126V>. (see p. 7).
- [49] Leger, A. & Klein, J. Experimental evidence for superconductivity enhancement mechanism. *Physics Letters A* **28**, 751–752 (1969). URL <http://www.sciencedirect.com/science/article/pii/037596016990601X>. (see pp. 7, 46, 49).
- [50] Rowell, J. M., McMillan, W. L. & Feldmann, W. L. Phonon Emission and Self-Energy Effects in Normal-Metal Tunneling. *Phys. Rev.* **180**, 658–668 (1969). URL <http://link.aps.org/doi/10.1103/PhysRev.180.658>. (see pp. 7, 8, 46, 49, 50, 59, 107).
- [51] Burstein, E. & Lundqvist, S. *Tunneling phenomena in solids* (Springer, 1969). (see p. 8).
- [52] Duif, A., Jansen, A. & Wyder, P. Point-contact spectroscopy. *Journal of Physics: Condensed Matter* **1**, 3157 (1989). (see p. 8).
- [53] Naidyuk, Y. G. & Yanson, I. K. *Point-contact spectroscopy*, vol. 145 (Springer Science & Business Media, 2005). (see p. 8).
- [54] Bednorz, J. G. & Müller, K. A. Possible highT_c superconductivity in the Ba-La-Cu-O system. *Zeitschrift für Physik B Condensed Matter* **64**, 189–193 (1986). URL <http://dx.doi.org/10.1007/BF01303701>. (see p. 8).
- [55] Schilling A., Cantoni M., Guo J. D. & Ott H. R. Superconductivity above 130 K in the Hg-Ba-Ca-Cu-O system. *Nature* **363**, 56–58 (1993). 10.1038/363056a0. (see p. 8).
- [56] Abrikosov, A. & Gor'kov, L. Contribution to the theory of superconducting alloys with paramagnetic impurities. *JETP* **12**, 1243 (1961). (see p. 8).
- [57] Yoichi Kamihara, Takumi Watanabe, Masahiro Hirano & Hideo Hosono†. Iron-Based Layered Superconductor LaO_{1-x}F_xFeAs (x=0.05-0.12) with T_c = 26K. *Journal of the American Chemical Society* **130**, 3296–3297 (2008). URL <http://dx.doi.org/10.1021/ja800073m>. PMID: 18293989, <http://dx.doi.org/10.1021/ja800073m>. (see p. 9).
- [58] Zhi-An, R. *et al.* Superconductivity at 55 K in iron-based F-doped layered quaternary compound Sm[O_{1-x}F_x]FeAs. *Chinese Physics Letters* **25**, 2215 (2008). (see p. 9).
- [59] Inosov D. S. *et al.* Normal-state spin dynamics and temperature-dependent spin-resonance energy in optimally doped BaFe_{1.85}Co_{0.15}As₂. *Nat Phys* **6**, 178–181 (2010). URL http://www.nature.com/nphys/journal/v6/n3/supinfo/nphys1483_S1.html. 10.1038/nphys1483. (see pp. 9, 73).

- [60] Rossat-Mignod & Regnault, L. Neutron Scattering Study of the $\text{YBa}_2\text{Cu}_3\text{O}_{6+x}$ system. *Physica C: Superconductivity and Its Applications (Amsterdam, Netherlands)* **185-189**, 86–92 (1991). URL http://ac.els-cdn.com/0921453491919554/1-s2.0-0921453491919554-main.pdf?_tid=f80e0c3e-42c9-11e2-92a1-00000aab0f27&acdnt=1355144779_bc8898e9ac34dc132caa78227b1fe4a8. (see pp. 9, 73, 81).
- [61] Bourges, P. *et al.* High-energy spin excitations in $\text{YBa}_2\text{Cu}_3\text{O}_{6.5}$. *Phys. Rev. B* **56**, R11439–R11442 (1997). URL <http://link.aps.org/doi/10.1103/PhysRevB.56.R11439>. (see p. 9).
- [62] Yu G., Li Y., Motoyama E. M. & Greven M. A universal relationship between magnetic resonance and superconducting gap in unconventional superconductors. *Nat Phys* **5**, 873–875 (2009). URL http://www.nature.com/nphys/journal/v5/n12/suppinfo/nphys1426_S1.html. 10.1038/nphys1426. (see pp. 9, 73, 78).
- [63] Christianson A. D. *et al.* Unconventional superconductivity in $\text{Ba}_{0.6}\text{K}_{0.4}\text{Fe}_2\text{As}_2$ from inelastic neutron scattering. *Nature* **456**, 930–932 (2008). URL http://www.nature.com/nature/journal/v456/n7224/suppinfo/nature07625_S1.html. 10.1038/nature07625. (see p. 9).
- [64] Lumsden, M. D. *et al.* Two-dimensional resonant magnetic excitation in $\text{BaFe}_{1.84}\text{Co}_{0.16}\text{As}_2$. *Phys. Rev. Lett.* **102**, 107005 (2009). URL <http://link.aps.org/doi/10.1103/PhysRevLett.102.107005>. (see p. 9).
- [65] Wakimoto, S. *et al.* Degradation of Superconductivity and Spin Fluctuations by Electron Overdoping in $\text{LaFeAsO}_{1-x}\text{Fx}$. *Journal of the Physical Society of Japan* **79**, 074715 (2010). URL <http://dx.doi.org/10.1143/JPSJ.79.074715>. (see p. 9).
- [66] Sato N. K. *et al.* Strong coupling between local moments and superconducting /‘heavy/’ electrons in UPd_2Al_3 . *Nature* **410**, 340–343 (2001). 10.1038/35066519. (see p. 9).
- [67] Stock, C., Broholm, C., Hudis, J., Kang, H. J. & Petrovic, C. Spin Resonance in the *d*-Wave Superconductor CeCoIn_5 . *Phys. Rev. Lett.* **100**, 087001 (2008). URL <http://link.aps.org/doi/10.1103/PhysRevLett.100.087001>. (see p. 9).
- [68] Bulut, N., Scalapino, D. J. & Scalettar, R. T. Nodeless *d*-wave pairing in a two-layer Hubbard model. *Phys. Rev. B* **45**, 5577–5584 (1992). URL <http://link.aps.org/doi/10.1103/PhysRevB.45.5577>. (see p. 9).
- [69] Ding H. *et al.* Spectroscopic evidence for a pseudogap in the normal state of underdoped high-Tc superconductors. *Nature* **382**, 51–54 (1996). 10.1038/382051a0. (see pp. 9, 69).
- [70] Hashimoto Makoto, Vishik Inna M., He Rui-Hua, Devereaux Thomas P. & Shen Zhi-Xun. Energy gaps in high-transition-temperature cuprate superconductors. *Nat Phys* **10**, 483–495 (2014). (see p. 9).

- [71] Wollman, D. A., Van Harlingen, D. J., Giapintzakis, J. & Ginsberg, D. M. Evidence for $d_{x^2-y^2}$ Pairing from the Magnetic Field Modulation of YBa₂Cu₃O₇-Pb Josephson Junctions. *Phys. Rev. Lett.* **74**, 797–800 (1995). URL <http://link.aps.org/doi/10.1103/PhysRevLett.74.797>. (see p. 9).
- [72] Tsuei, C. C. *et al.* Pairing Symmetry and Flux Quantization in a Tricrystal Superconducting Ring of YBa₂Cu₃O_{7- δ} . *Phys. Rev. Lett.* **73**, 593–596 (1994). URL <http://link.aps.org/doi/10.1103/PhysRevLett.73.593>. (see p. 9).
- [73] Dynes, R. Electron tunneling into high T_c superconductors. *Journal of Physics and Chemistry of Solids* **52**, 1477–1479 (1991). (see pp. 10, 11, 70, 74, 75, 80).
- [74] Valles, J. M. *et al.* Electron tunneling into single crystals of YBa₂Cu₃O_{7- δ} . *Phys. Rev. B* **44**, 11986–11996 (1991). URL <http://link.aps.org/doi/10.1103/PhysRevB.44.11986>. (see pp. 10, 11, 76, 80).
- [75] Cucolo, A. M., Di Leo, R., Nigro, A., Romano, P. & Bobba, F. Linear normal conductance in copper oxide tunnel junctions. *Phys. Rev. B* **54**, R9686–R9688 (1996). URL <http://link.aps.org/doi/10.1103/PhysRevB.54.R9686>. (see p. 10).
- [76] Nishiyama, M. *et al.* Low Temperature Scanning Tunneling Spectroscopy Studies of High J_c NdBa₂Cu₃O_{7- δ} Single Crystals. *Journal of superconductivity* **15**, 351–354 (2002). (see pp. 10, 11).
- [77] F. C. Niestemski, S. K. S. Z. S. L. H. D. Z. W. P. D. . V. M. A distinct bosonic mode in an electron-doped high-transition-temperature superconductor. *Nature* **450**, 1058–1061 (2007). URL <http://www.nature.com/nature/journal/v450/n7172/abs/nature06430.html>. (see pp. 10, 11, 76, 77).
- [78] Kato, T., Morimoto, H., Katagiri, A., Okitsu, S. & Sakata, H. Scanning tunneling microscopy and spectroscopy on La_{2- x} Sr _{x} CuO₄. *Physica C: Superconductivity* **392-396**, Part 1, 221–223 (2003). URL <http://www.sciencedirect.com/science/article/pii/S0921453403010761>. Proceedings of the 15th International Symposium on Superconductivity (ISS 2002): Advances in Superconductivity XV. Part I. (see pp. 10, 11).
- [79] Hanaguri T. *et al.* Quasiparticle interference and superconducting gap in Ca_{2-x}NaxCuO₂Cl₂. *Nat Phys* **3**, 865–871 (2007). 10.1038/nphys753. (see pp. 10, 11).
- [80] Yeh, N.-C. *et al.* Investigating the pairing state of cuprate superconductors via quasiparticle tunneling and spin injection. *Physica C: Superconductivity* **367**, 174–180 (2002). URL <http://www.sciencedirect.com/science/article/pii/S0921453401010085>. (see pp. 10, 11).
- [81] Yan, Y. J. *et al.* Electron-Doped Sr₂IO₄: An Analogue of Hole-Doped Cuprate Superconductors Demonstrated by Scanning Tunneling Microscopy. *Phys. Rev. X* **5**, 041018 (2015). URL <http://link.aps.org/doi/10.1103/PhysRevX.5.041018>. (see pp. 10, 11).

- [82] Renner, C. & Fischer, O. Vacuum tunneling spectroscopy and asymmetric density of states of $\text{Bi}_2\text{Sr}_2\text{CaCu}_2\text{O}_{8+\delta}$. *Phys. Rev. B* **51**, 9208–9218 (1995). URL <http://link.aps.org/doi/10.1103/PhysRevB.51.9208>. (see pp. 10, 12).
- [83] Sakata, H., Katagiri, A., Yokoi, M., Kato, T. & Morimoto, H. Tunneling Conductance Dependence of the Tunneling Spectra in $\text{Bi}_2\text{Sr}_2\text{CaCu}_2\text{O}_8$. *Journal of Low Temperature Physics* **131**, 275–279 (2003). URL <http://dx.doi.org/10.1023/A:1022933304618>. (see pp. 10, 12, 52).
- [84] Misra, S. *et al.* Atomic Scale Imaging and Spectroscopy of a CuO_2 Plane at the Surface of $\text{Bi}_2\text{Sr}_2\text{CaCu}_2\text{O}_{8+\delta}$. *Phys. Rev. Lett.* **89**, 087002 (2002). URL <http://link.aps.org/doi/10.1103/PhysRevLett.89.087002>. (see pp. 10, 12).
- [85] Maggio-Aprile, I., Renner, C., Erb, A., Walker, E. & Fischer, Ø. Direct Vortex Lattice Imaging and Tunneling Spectroscopy of Flux Lines on $\text{YBa}_2\text{Cu}_3\text{O}_{7-\delta}$. *Phys. Rev. Lett.* **75**, 2754–2757 (1995). URL <http://link.aps.org/doi/10.1103/PhysRevLett.75.2754>. (see pp. 11, 50).
- [86] Lee Jinho *et al.* Interplay of electron–lattice interactions and superconductivity in $\text{Bi}_2\text{Sr}_2\text{CaCu}_2\text{O}_{8+\delta}$. *Nature* **442**, 546–550 (2006). URL http://www.nature.com/nature/journal/v442/n7102/supinfo/nature04973_S1.html. 10.1038/nature04973. (see pp. 12, 77, 81).
- [87] Hanaguri, T., Niitaka, S., Kuroki, K. & Takagi, H. Unconventional s-Wave Superconductivity in $\text{Fe}(\text{Se},\text{Te})$. *Science* **328**, 474–476 (2010). URL <http://science.sciencemag.org/content/328/5977/474>. <http://science.sciencemag.org/content/328/5977/474.full.pdf>. (see p. 13).
- [88] Shan, L. *et al.* Evidence of a Spin Resonance Mode in the Iron-Based Superconductor $\text{Ba}_{0.6}\text{K}_{0.4}\text{Fe}_2\text{As}_2$ from Scanning Tunneling Spectroscopy. *Phys. Rev. Lett.* **108**, 227002 (2012). URL <http://link.aps.org/doi/10.1103/PhysRevLett.108.227002>. (see p. 13).
- [89] Yin, Y. *et al.* Scanning Tunneling Spectroscopy and Vortex Imaging in the Iron Pnictide Superconductor $\text{BaFe}_{1.8}\text{Co}_{0.2}\text{As}_2$. *Phys. Rev. Lett.* **102**, 097002 (2009). URL <http://link.aps.org/doi/10.1103/PhysRevLett.102.097002>. (see pp. 13, 50).
- [90] Wang Zhenyu *et al.* Close relationship between superconductivity and the bosonic mode in $\text{Ba}_{0.6}\text{K}_{0.4}\text{Fe}_2\text{As}_2$ and $\text{Na}(\text{Fe}_{0.975}\text{Co}_{0.025})\text{As}$. *Nat Phys* **9**, 42–48 (2013). URL <http://www.nature.com/nphys/journal/v9/n1/abs/nphys2478.html#supplementary-information>. 10.1038/nphys2478. (see pp. 13, 78).
- [91] Chi, S. *et al.* Scanning Tunneling Spectroscopy of Superconducting LiFeAs Single Crystals: Evidence for Two Nodeless Energy Gaps and Coupling to a Bosonic Mode. *Phys. Rev. Lett.* **109**, 087002 (2012). URL <http://link.aps.org/doi/10.1103/PhysRevLett.109.087002>. (see pp. 13, 74, 75, 76, 77, 78).
- [92] Yang Huan *et al.* In-gap quasiparticle excitations induced by non-magnetic Cu impurities in $\text{Na}(\text{Fe}_{0.96}\text{Co}_{0.03}\text{Cu}_{0.01})\text{As}$ revealed by scanning tunnelling spectroscopy.

- Nat Commun* **4** (2013). Supplementary information available for this article at http://www.nature.com/ncomms/2013/131119/ncomms3749/supinfo/ncomms3749_S1.html. (see p. 13).
- [93] Fasano, Y. *et al.* Local Quasiparticle Density of States of Superconducting $\text{SmFeAsO}_{1-x}\text{F}_x$ Single Crystals: Evidence for Spin-Mediated Pairing. *Phys. Rev. Lett.* **105**, 167005 (2010). URL <http://link.aps.org/doi/10.1103/PhysRevLett.105.167005>. (see p. 13).
- [94] Maxwell, E. Isotope Effect in the Superconductivity of Mercury. *Phys. Rev.* **78**, 477–477 (1950). URL <http://link.aps.org/doi/10.1103/PhysRev.78.477>. (see p. 15).
- [95] Reynolds, C. A., Serin, B., Wright, W. H. & Nesbitt, L. B. Superconductivity of Isotopes of Mercury. *Phys. Rev.* **78**, 487–487 (1950). URL <http://link.aps.org/doi/10.1103/PhysRev.78.487>. (see p. 15).
- [96] Fröhlich, H. Theory of the Superconducting State. I. The Ground State at the Absolute Zero of Temperature. *Phys. Rev.* **79**, 845–856 (1950). URL <http://link.aps.org/doi/10.1103/PhysRev.79.845>. (see p. 15).
- [97] Bardeen, J. & Pines, D. Electron-Phonon Interaction in Metals. *Phys. Rev.* **99**, 1140–1150 (1955). URL <http://link.aps.org/doi/10.1103/PhysRev.99.1140>. (see p. 16).
- [98] Cooper, L. N. Bound Electron Pairs in a Degenerate Fermi Gas. *Phys. Rev.* **104**, 1189–1190 (1956). URL <http://link.aps.org/doi/10.1103/PhysRev.104.1189>. (see p. 16).
- [99] Migdal, A. Interaction between Electrons and Lattice Vibrations in a Normal Metal. *JETP* **7**, 996 (1958). URL <http://www.jetp.ac.ru/cgi-bin/e/index/e/7/6/p996?a=list>. (see pp. 18, 19).
- [100] Mahan, G. *Many-Particle Physics*. Physics of Solids and Liquids (Springer, 2000). URL <https://books.google.de/books?id=xzSgZ4-yyMEC>. (see pp. 19, 21).
- [101] Abanov, A., Chubukov, A. V., Eschrig, M., Norman, M. R. & Schmalian, J. Neutron Resonance in the Cuprates and its Effect on Fermionic Excitations. *Phys. Rev. Lett.* **89**, 177002 (2002). URL <http://link.aps.org/doi/10.1103/PhysRevLett.89.177002>. (see pp. 20, 73).
- [102] Altland, A. & Simons, B. *Condensed Matter Field Theory* (Cambridge University Press, 2010). URL <https://books.google.de/books?id=gk4hAwAAQBAJ>. (see pp. 20, 37, 126, 128).
- [103] Kamenev, A. *Field theory of non-equilibrium systems* (Cambridge Univ. Press, Cambridge, 2011), 1. publ. edn. (see pp. 20, 126, 128).
- [104] Morel, P. & Anderson, P. W. Calculation of the Superconducting State Parameters with Retarded Electron-Phonon Interaction. *Phys. Rev.* **125**, 1263–1271 (1962).

- URL <http://link.aps.org/doi/10.1103/PhysRev.125.1263>. (see p. 20).
- [105] Schrieffer, J. R., Scalapino, D. J. & Wilkins, J. W. Effective Tunneling Density of States in Superconductors. *Phys. Rev. Lett.* **10**, 336–339 (1963). URL <http://link.aps.org/doi/10.1103/PhysRevLett.10.336>. (see p. 21).
- [106] Gor'kov, L. On the Energy Spectrum of Superconductors. *JETP* **7**, 505 (1958). URL <http://www.jetp.ac.ru/cgi-bin/e/index/e/7/3/p505?a=list>. (see p. 21).
- [107] Freericks, J. K., Nicol, E. J., Liu, A. Y. & Quong, A. A. Vertex-corrected tunneling inversion in electron-phonon mediated superconductors: Pb. *Phys. Rev. B* **55**, 11651–11658 (1997). URL <http://link.aps.org/doi/10.1103/PhysRevB.55.11651>. (see p. 21).
- [108] Schmalian, J., Langer, M., Grabowski, S. & Bennemann, K. Self-consistent summation of many-particle diagrams on the real frequency axis and its application to the FLEX approximation. *Computer Physics Communications* **93**, 141–151 (1996). URL <http://www.sciencedirect.com/science/article/pii/S0010465595001344>. (see pp. 25, 28, 30, 32).
- [109] Abanov, A., Chubukov, A. V. & Schmalian, J. Quantum-critical theory of the spin-fermion model and its application to cuprates: Normal state analysis. *Advances in Physics* **52**, 119–218 (2003). URL <http://dx.doi.org/10.1080/0001873021000057123>. <http://dx.doi.org/10.1080/0001873021000057123>. (see pp. 27, 70).
- [110] Chubukov, A. V. & Schmalian, J. Superconductivity due to massless boson exchange in the strong-coupling limit. *Phys. Rev. B* **72**, 174520 (2005). URL <http://link.aps.org/doi/10.1103/PhysRevB.72.174520>. (see pp. 28, 118).
- [111] Hlobil, P., Narozhny, B. & Schmalian, J. Strong coupling behavior of the neutron resonance mode in unconventional superconductors. *Phys. Rev. B* **88**, 205104 (2013). URL <http://link.aps.org/doi/10.1103/PhysRevB.88.205104>. (see pp. 29, 70).
- [112] Abanov, A., Chubukov, A. V. & Schmalian, J. Fingerprints of spin mediated pairing in cuprates. *Journal of Electron Spectroscopy and Related Phenomena* **117–118**, 129–151 (2001). URL <http://www.sciencedirect.com/science/article/pii/S0368204801002511>. Strongly correlated systems. (see p. 30).
- [113] Musaelian, K. A., Betouras, J., Chubukov, A. V. & Joynt, R. Mixed-symmetry superconductivity in two-dimensional Fermi liquids. *Phys. Rev. B* **53**, 3598–3603 (1996). URL <http://link.aps.org/doi/10.1103/PhysRevB.53.3598>. (see pp. 32, 80).
- [114] Ahmadi, O., Coffey, L., Zasadzinski, J. F., Miyakawa, N. & Ozyuzer, L. Eliashberg Analysis of Tunneling Experiments: Support for the Pairing Glue Hypothesis in Cuprate Superconductors. *Phys. Rev. Lett.* **106**, 167005 (2011). URL <http://link.aps.org/doi/10.1103/PhysRevLett.106.167005>. (see pp. 32, 76, 81).
- [115] Zasadzinski, J. F., Coffey, L., Romano, P. & Yusof, Z. Tunneling spectroscopy of

- $\text{Bi}_2\text{Sr}_2\text{CaCu}_2\text{O}_{8+\delta}$ Eliashberg analysis of the spectral dip feature. *Phys. Rev. B* **68**, 180504 (2003). URL <http://link.aps.org/doi/10.1103/PhysRevB.68.180504>. (see pp. 32, 76, 81).
- [116] Eschrig, M. & Norman, M. R. Neutron Resonance: Modeling Photoemission and Tunneling Data in the Superconducting State of $\text{Bi}_2\text{Sr}_2\text{CaCu}_2\text{O}_{8+\delta}$. *Phys. Rev. Lett.* **85**, 3261–3264 (2000). URL <http://link.aps.org/doi/10.1103/PhysRevLett.85.3261>. (see pp. 32, 81).
- [117] Weiß, P. S., Narozhny, B. N., Schmalian, J. & Wölfle, P. Interference of quantum critical excitations and soft diffusive modes in a disordered antiferromagnetic metal. *Phys. Rev. B* **93**, 045128 (2016). URL <http://link.aps.org/doi/10.1103/PhysRevB.93.045128>. (see p. 38).
- [118] Zhang Yuanbo *et al.* Giant phonon-induced conductance in scanning tunnelling spectroscopy of gate-tunable graphene. *Nat Phys* **4**, 627–630 (2008). URL http://www.nature.com/nphys/journal/v4/n8/supinfo/nphys1022_S1.html. 10.1038/nphys1022. (see pp. 39, 49).
- [119] Bennett, A. J., Duke, C. B. & Silverstein, S. D. Theory of the Tunneling Spectroscopy of Collective Excitations. *Phys. Rev.* **176**, 969–992 (1968). URL <http://link.aps.org/doi/10.1103/PhysRev.176.969>. (see pp. 40, 44).
- [120] Sheng, L., Xing, D. Y. & Sheng, D. N. Theory of the zero-bias anomaly in magnetic tunnel junctions: Inelastic tunneling via impurities. *Phys. Rev. B* **70**, 094416 (2004). URL <http://link.aps.org/doi/10.1103/PhysRevB.70.094416>. (see p. 41).
- [121] Zawadowski, A. General Theory of Tunneling in Oxide Diodes. *Phys. Rev.* **163**, 341–351 (1967). URL <http://link.aps.org/doi/10.1103/PhysRev.163.341>. (see p. 43).
- [122] Caroli, C., Combescot, R., Nozieres, P. & Saint-James, D. Direct calculation of the tunneling current. *Journal of Physics C: Solid State Physics* **4**, 916 (1971). URL <http://stacks.iop.org/0022-3719/4/i=8/a=018>. (see p. 43).
- [123] Klein, J., Léger, A., Belin, M., Défourneau, D. & Sangster, M. J. L. Inelastic-Electron-Tunneling Spectroscopy of Metal-Insulator-Metal Junctions. *Phys. Rev. B* **7**, 2336–2348 (1973). URL <http://link.aps.org/doi/10.1103/PhysRevB.7.2336>. (see pp. 44, 47, 55, 57, 58, 60).
- [124] Taylor, M. Inelastic processes in tunnelling electrodes. *Ultramicroscopy* **42**, 215–222 (1992). (see p. 44).
- [125] Kirtley, J. R. & Scalapino, D. J. Inelastic-tunneling model for the linear conductance background in the high- T_c superconductors. *Phys. Rev. Lett.* **65**, 798–800 (1990). URL <http://link.aps.org/doi/10.1103/PhysRevLett.65.798>. (see pp. 44, 69, 70, 71, 72, 83, 108).
- [126] Nie, Y.-m. & Coffey, L. Elastic and spin-fluctuation-mediated inelastic Josephson tunneling between anisotropic superconductors. *Phys. Rev. B* **57**, 3116–3122 (1998).

- URL <http://link.aps.org/doi/10.1103/PhysRevB.57.3116>. (see p. 44).
- [127] Nishio, T. *et al.* Superconducting Pb Island Nanostructures Studied by Scanning Tunneling Microscopy and Spectroscopy. *Phys. Rev. Lett.* **101**, 167001 (2008). URL <http://link.aps.org/doi/10.1103/PhysRevLett.101.167001>. (see pp. 50, 64, 65).
- [128] Renner, C., Revaz, B., Kadowaki, K., Maggio-Aprile, I. & Fischer, Ø. Observation of the Low Temperature Pseudogap in the Vortex Cores of $\text{Bi}_2\text{Sr}_2\text{CaCu}_2\text{O}_{8+\delta}$. *Phys. Rev. Lett.* **80**, 3606–3609 (1998). URL <http://link.aps.org/doi/10.1103/PhysRevLett.80.3606>. (see pp. 50, 69).
- [129] Huang, Q., Zasadzinski, J. F. & Gray, K. E. Phonon spectroscopy of superconducting Nb using point-contact tunneling. *Phys. Rev. B* **42**, 7953–7959 (1990). URL <http://link.aps.org/doi/10.1103/PhysRevB.42.7953>. (see pp. 51, 65).
- [130] Berthod, C. & Giamarchi, T. Tunneling conductance and local density of states in tight-binding junctions. *Phys. Rev. B* **84**, 155414 (2011). URL <http://link.aps.org/doi/10.1103/PhysRevB.84.155414>. (see p. 51).
- [131] Gold, A. V. The density of states in lead. *Philosophical Magazine* **5**, 70–77 (1960). URL <http://dx.doi.org/10.1080/14786436008241201>. <http://dx.doi.org/10.1080/14786436008241201>. (see pp. 60, 63).
- [132] Zhang, L., Miyamachi, T., Tomanić, T., Dehm, R. & Wulfhchel, W. A compact sub-Kelvin ultrahigh vacuum scanning tunneling microscope with high energy resolution and high stability. *Review of Scientific Instruments* **82** (2011). URL <http://scitation.aip.org/content/aip/journal/rsi/82/10/10.1063/1.3646468>. (see p. 60).
- [133] Decker, D. L., Mapother, D. E. & Shaw, R. W. Critical Field Measurements on Superconducting Lead Isotopes. *Phys. Rev.* **112**, 1888–1898 (1958). URL <http://link.aps.org/doi/10.1103/PhysRev.112.1888>. (see p. 60).
- [134] Brun, C. *et al.* Reduction of the Superconducting Gap of Ultrathin Pb Islands Grown on Si(111). *Phys. Rev. Lett.* **102**, 207002 (2009). URL <http://link.aps.org/doi/10.1103/PhysRevLett.102.207002>. (see pp. 60, 64, 65).
- [135] Eom, D., Qin, S., Chou, M.-Y. & Shih, C. K. Persistent Superconductivity in Ultrathin Pb Films: A Scanning Tunneling Spectroscopy Study. *Phys. Rev. Lett.* **96**, 027005 (2006). URL <http://link.aps.org/doi/10.1103/PhysRevLett.96.027005>. (see pp. 60, 64, 65).
- [136] Altfeder, I. B., Matveev, K. A. & Chen, D. M. Electron Fringes on a Quantum Wedge. *Phys. Rev. Lett.* **78**, 2815–2818 (1997). URL <http://link.aps.org/doi/10.1103/PhysRevLett.78.2815>. (see p. 60).
- [137] Weitering, H. H., Heslinga, D. R. & Hibma, T. Structure and growth of epitaxial Pb on Si(111). *Phys. Rev. B* **45**, 5991–6002 (1992). URL <http://link.aps.org/doi/10.1103/PhysRevB.45.5991>. (see p. 60).

- [138] Jal/ochowski, M., Knoppe, H., Lilienkamp, G. & Bauer, E. Photoemission from ultrathin metallic films: Quantum size effect, electron scattering, and film structure. *Phys. Rev. B* **46**, 4693–4701 (1992). URL <http://link.aps.org/doi/10.1103/PhysRevB.46.4693>. (see p. 60).
- [139] Sklyadneva, I. Y., Heid, R., Bohnen, K.-P., Echenique, P. M. & Chulkov, E. V. Mass enhancement parameter in free-standing ultrathin Pb(111) films: The effect of spin-orbit coupling. *Phys. Rev. B* **87**, 085440 (2013). URL <http://link.aps.org/doi/10.1103/PhysRevB.87.085440>. (see p. 60).
- [140] Heid, R., Bohnen, K.-P., Sklyadneva, I. Y. & Chulkov, E. V. Effect of spin-orbit coupling on the electron-phonon interaction of the superconductors Pb and Tl. *Phys. Rev. B* **81**, 174527 (2010). URL <http://link.aps.org/doi/10.1103/PhysRevB.81.174527>. (see p. 60).
- [141] Beck, P. A. & Claus, H. Density of States Information from Low Temperature Specific Heat Measurements. *JOURNAL OF RESEARCH of the National Bureau of Standards - A. Physics and Chemistry* 449–454 (1970). (see p. 63).
- [142] Bose Sangita *et al.* Observation of shell effects in superconducting nanoparticles of Sn. *Nat Mater* **9**, 550–554 (2010). URL http://www.nature.com/nmat/journal/v9/n7/supinfo/nmat2768_S1.html. 10.1038/nmat2768. (see p. 64).
- [143] Kittel, C. *Introduction to solid state physics* (Wiley, 2005). (see p. 64).
- [144] Nishio, T., Ono, M., Eguchi, T., Sakata, H. & Hasegawa, Y. Superconductivity of nanometer-size Pb islands studied by low-temperature scanning tunneling microscopy. *Applied Physics Letters* **88** (2006). URL <http://scitation.aip.org/content/aip/journal/apl/88/11/10.1063/1.2184758>. (see pp. 64, 65).
- [145] Qin, S., Kim, J., Niu, Q. & Shih, C.-K. Superconductivity at the Two-Dimensional Limit. *Science* **324**, 1314–1317 (2009). URL <http://science.sciencemag.org/content/324/5932/1314>. <http://science.sciencemag.org/content/324/5932/1314.full.pdf>. (see p. 64).
- [146] Dynes, R. C., Narayanamurti, V. & Garno, J. P. Direct Measurement of Quasiparticle-Lifetime Broadening in a Strong-Coupled Superconductor. *Phys. Rev. Lett.* **41**, 1509–1512 (1978). URL <http://link.aps.org/doi/10.1103/PhysRevLett.41.1509>. (see p. 64).
- [147] Mitrović, B. & Rozema, L. A. On the correct formula for the lifetime broadened superconducting density of states. *Journal of Physics: Condensed Matter* **20**, 015215 (2008). URL <http://stacks.iop.org/0953-8984/20/i=1/a=015215>. (see p. 65).
- [148] García-García, A. M. & Ribeiro, P. Quantifying Fluctuations from the Tunnelling Differential Conductance. *Journal of Superconductivity and Novel Magnetism* **25**, 1365–1367 (2012). URL <http://dx.doi.org/10.1007/s10948-012-1662-6>. (see p. 65).
- [149] Ruby, M., Heinrich, B. W., Pascual, J. I. & Franke, K. J. Experimen-

- tal Demonstration of a Two-Band Superconducting State for Lead Using Scanning Tunneling Spectroscopy. *Phys. Rev. Lett.* **114**, 157001 (2015). URL <http://link.aps.org/doi/10.1103/PhysRevLett.114.157001>. (see p. 65).
- [150] Zeljkovic Ilija *et al.* Nanoscale determination of the mass enhancement factor in the lightly doped bulk insulator lead selenide. *Nat Commun* **6** (2015). Supplementary information available for this article at http://www.nature.com/ncomms/2015/150327/ncomms7559/supinfo/ncomms7559_S1.html. (see p. 67).
- [151] Duke, C. B., Silverstein, S. D. & Bennett, A. J. Zero-Bias Tunnel-Conductance Minima Due to the Excitation of Collective Modes in the Barrier. *Phys. Rev. Lett.* **19**, 315–318 (1967). URL <http://link.aps.org/doi/10.1103/PhysRevLett.19.315>. (see p. 69).
- [152] Rochlin, G. I. & Hansma, P. K. Electron Tunneling Cr-Cr₂O₃-Metal Junctions. *Phys. Rev. B* **2**, 1460–1463 (1970). URL <http://link.aps.org/doi/10.1103/PhysRevB.2.1460>. (see p. 69).
- [153] Singh, D. J. & Du, M.-H. Density Functional Study of LaFeAsO_{1-x}F_x: A Low Carrier Density Superconductor Near Itinerant Magnetism. *Phys. Rev. Lett.* **100**, 237003 (2008). URL <http://link.aps.org/doi/10.1103/PhysRevLett.100.237003>. (see p. 69).
- [154] Rhee, H. B. & Pickett, W. E. Contrast of LiFeAs with Isostructural, Isoelectronic, and Non-superconducting MgFeGe. *Journal of the Physical Society of Japan* **82**, 034714 (2013). URL <http://dx.doi.org/10.7566/JPSJ.82.034714>. <http://dx.doi.org/10.7566/JPSJ.82.034714>. (see pp. 69, 78).
- [155] Li, B., Xing, Z. W., Huang, G. Q. & Xing, D. Y. Electron-phonon coupling enhanced by the FeSe/SrTiO₃ interface. *Journal of Applied Physics* **115** (2014). URL <http://scitation.aip.org/content/aip/journal/jap/115/19/10.1063/1.4876750>. (see p. 69).
- [156] Tranquada J. M., Sternlieb B. J., Axe J. D., Nakamura Y. & Uchida S. Evidence for stripe correlations of spins and holes in copper oxide superconductors. *Nature* **375**, 561–563 (1995). 10.1038/375561a0. (see p. 69).
- [157] Hoffman, J. E. *et al.* A Four Unit Cell Periodic Pattern of Quasi-Particle States Surrounding Vortex Cores in Bi₂Sr₂CaCu₂O_{8+δ}. *Science* **295**, 466–469 (2002). URL <http://science.sciencemag.org/content/295/5554/466>. <http://science.sciencemag.org/content/295/5554/466.full.pdf>. (see p. 69).
- [158] Shen, K. M. *et al.* Nodal Quasiparticles and Antinodal Charge Ordering in Ca_{2-x}Na_xCuO₂Cl₂. *Science* **307**, 901–904 (2005). URL <http://science.sciencemag.org/content/307/5711/901>. <http://science.sciencemag.org/content/307/5711/901.full.pdf>. (see p. 69).
- [159] Wise W. D. *et al.* Charge-density-wave origin of cuprate checkerboard visualized by scanning tunnelling microscopy. *Nat Phys* **4**, 696–699 (2008). 10.1038/nphys1021.

(see p. 69).

- [160] Ghiringhelli, G. *et al.* Long-Range Incommensurate Charge Fluctuations in (Y,Nd)Ba₂Cu₃O_{6+x}. *Science* **337**, 821–825 (2012). URL <http://science.sciencemag.org/content/337/6096/821>. <http://science.sciencemag.org/content/337/6096/821.full.pdf>. (see p. 69).
- [161] Chang J. *et al.* Direct observation of competition between superconductivity and charge density wave order in YBa₂Cu₃O_{6.67}. *Nat Phys* **8**, 871–876 (2012). URL <http://www.nature.com/nphys/journal/v8/n12/abs/nphys2456.html#supplementary-information>. 10.1038/nphys2456. (see p. 69).
- [162] Comin, R. *et al.* Charge Order Driven by Fermi-Arc Instability in Bi₂Sr_{2-x}La_xCuO_{6+δ}. *Science* **343**, 390–392 (2014). URL <http://science.sciencemag.org/content/343/6169/390>. <http://science.sciencemag.org/content/343/6169/390.full.pdf>. (see p. 69).
- [163] Renner, C., Revaz, B., Genoud, J.-Y., Kadowaki, K. & Fischer, Ø. Pseudogap Precursor of the Superconducting Gap in Under- and Overdoped Bi₂Sr₂CaCu₂O_{8+δ}. *Phys. Rev. Lett.* **80**, 149–152 (1998). URL <http://link.aps.org/doi/10.1103/PhysRevLett.80.149>. (see p. 69).
- [164] Loeser, A. G. *et al.* Excitation Gap in the Normal State of Underdoped Bi₂Sr₂CaCu₂O_{8+δ}. *Science* **273**, 325–329 (1996). URL <http://science.sciencemag.org/content/273/5273/325>. <http://science.sciencemag.org/content/273/5273/325.full.pdf>. (see p. 69).
- [165] Norman M. R. *et al.* Destruction of the Fermi surface in underdoped high-Tc superconductors. *Nature* **392**, 157–160 (1998). 10.1038/32366. (see p. 69).
- [166] He, R.-H. *et al.* From a Single-Band Metal to a High-Temperature Superconductor via Two Thermal Phase Transitions. *Science* **331**, 1579–1583 (2011). URL <http://science.sciencemag.org/content/331/6024/1579>. <http://science.sciencemag.org/content/331/6024/1579.full.pdf>. (see p. 69).
- [167] Kugler, M., Fischer, Ø., Renner, C., Ono, S. & Ando, Y. Scanning Tunneling Spectroscopy of Bi₂Sr₂CuO_{6+δ}: New Evidence for the Common Origin of the Pseudogap and Superconductivity. *Phys. Rev. Lett.* **86**, 4911–4914 (2001). URL <http://link.aps.org/doi/10.1103/PhysRevLett.86.4911>. (see pp. 70, 81).
- [168] Lv, Y.-F. *et al.* Out-of-Plane Effects on the Superconductivity of Bi₂Sr₂CuO_{6+δ} and Bi₂Sr₂CaCu₂O_{8+δ}. *arXiv preprint arXiv:1512.09230* (2015). (see pp. 70, 81).
- [169] Rotter, L. D. *et al.* Dependence of the infrared properties of single-domain YBa₂Cu₃O_{7-y} on oxygen content. *Phys. Rev. Lett.* **67**, 2741–2744 (1991). URL <http://link.aps.org/doi/10.1103/PhysRevLett.67.2741>. (see p. 70).
- [170] Orenstein, J. *et al.* Frequency- and temperature-dependent conductivity in YBa₂Cu₃O_{6+x}. *Phys. Rev. B* **42**, 6342–6362 (1990). URL <http://link.aps.org/doi/10.1103/PhysRevB.42.6342>. (see p. 70).

- [171] Hwang J., Timusk T. & Gu G. D. High-transition-temperature superconductivity in the absence of the magnetic-resonance mode. *Nature* **427**, 714–717 (2004). 10.1038/nature02347. (see p. 70).
- [172] Littlewood, P. B. & Varma, C. M. Anisotropic tunneling and resistivity in high-temperature superconductors. *Phys. Rev. B* **45**, 12636–12639 (1992). URL <http://link.aps.org/doi/10.1103/PhysRevB.45.12636>. (see p. 70).
- [173] Millis, A. J., Monien, H. & Pines, D. Phenomenological model of nuclear relaxation in the normal state of $\text{YBa}_2\text{Cu}_3\text{O}_7$. *Phys. Rev. B* **42**, 167–178 (1990). URL <http://link.aps.org/doi/10.1103/PhysRevB.42.167>. (see p. 71).
- [174] Pines, D. dx²-y² pairing and spin fluctuations in the cuprate superconductors: Experiment meets theory. *Physica C: Superconductivity* **235**, 113–121 (1994). URL <http://www.sciencedirect.com/science/article/pii/0921453494913277>. (see p. 71).
- [175] Aeppli, G., Mason, T. E., Hayden, S. M., Mook, H. A. & Kulda, J. Nearly Singular Magnetic Fluctuations in the Normal State of a High-Tc Cuprate Superconductor. *Science* **278**, 1432–1435 (1997). URL <http://science.sciencemag.org/content/278/5342/1432>. <http://science.sciencemag.org/content/278/5342/1432.full.pdf>. (see p. 71).
- [176] Mook H. A. *et al.* Spin fluctuations in $\text{YBa}_2\text{Cu}_3\text{O}_{6.6}$. *Nature* **395**, 580–582 (1998). 10.1038/26931. (see p. 71).
- [177] Chen, H. *et al.* Coexistence of the spin-density wave and superconductivity in $\text{Ba}_{1-x}\text{K}_x\text{Fe}_2\text{As}_2$. *EPL (Europhysics Letters)* **85**, 17006 (2009). URL <http://stacks.iop.org/0295-5075/85/i=1/a=17006>. (see p. 71).
- [178] Ikeda, H., Arita, R. & Kuneš, J. Doping dependence of spin fluctuations and electron correlations in iron pnictides. *Phys. Rev. B* **82**, 024508 (2010). URL <http://link.aps.org/doi/10.1103/PhysRevB.82.024508>. (see p. 71).
- [179] Sharifi, F., Pargellis, A. & Dynes, R. C. Tunneling density of states in the lead-bismuth-oxide superconductors. *Phys. Rev. Lett.* **67**, 509–511 (1991). URL <http://link.aps.org/doi/10.1103/PhysRevLett.67.509>. (see p. 71).
- [180] Shapiro, S. M., Shirane, G. & Axe, J. D. Measurements of the electron-phonon interaction in Nb by inelastic neutron scattering. *Phys. Rev. B* **12**, 4899–4908 (1975). URL <http://link.aps.org/doi/10.1103/PhysRevB.12.4899>. (see p. 72).
- [181] Bourges, P. *et al.* Spin dynamics in the metallic state of the high-Tc superconducting system $\text{YBa}_2\text{Cu}_3\text{O}_{6+x}$. *Physica B: Condensed Matter* **215**, 30–40 (1995). URL <http://www.sciencedirect.com/science/article/pii/0921452695000244>. Magnetism and Superconductivity. (see pp. 73, 81).
- [182] Bourges, P. *et al.* Spin dynamics in high-TC superconductors. *AIP Conference Proceedings* **483**, 207–212 (1999). URL <http://scitation.aip.org/content/aip/proceeding/aipcp/10.1063/1.59619>. (see pp. 73, 79, 80).

- [183] Christensen, N. B. *et al.* Dispersive Excitations in the High-Temperature Superconductor $\text{La}_{2-x}\text{Sr}_x\text{CuO}_4$. *Phys. Rev. Lett.* **93**, 147002 (2004). URL <http://link.aps.org/doi/10.1103/PhysRevLett.93.147002>. (see p. 73).
- [184] Qureshi, N. *et al.* Inelastic Neutron-Scattering Measurements of Incommensurate Magnetic Excitations on Superconducting LiFeAs Single Crystals. *Phys. Rev. Lett.* **108**, 117001 (2012). URL <http://link.aps.org/doi/10.1103/PhysRevLett.108.117001>. (see pp. 73, 77).
- [185] Kee, H.-Y., Kivelson, S. A. & Aeppli, G. Spin-1 Neutron Resonance Peak Cannot Account for Electronic Anomalies in the Cuprate Superconductors. *Phys. Rev. Lett.* **88**, 257002 (2002). URL <http://link.aps.org/doi/10.1103/PhysRevLett.88.257002>. (see p. 73).
- [186] Tinkham, M. Dover Books on Physics. *Introduction to Superconductivity* **1** (2004). (see p. 76).
- [187] Borisenko, S. V. *et al.* Superconductivity without Nesting in LiFeAs. *Phys. Rev. Lett.* **105**, 067002 (2010). URL <http://link.aps.org/doi/10.1103/PhysRevLett.105.067002>. (see pp. 76, 78).
- [188] Umezawa, K. *et al.* Unconventional Anisotropic *s*-Wave Superconducting Gaps of the LiFeAs Iron-Pnictide Superconductor. *Phys. Rev. Lett.* **108**, 037002 (2012). URL <http://link.aps.org/doi/10.1103/PhysRevLett.108.037002>. (see pp. 76, 78).
- [189] Borisenko S. V. *et al.* Direct observation of spin-orbit coupling in iron-based superconductors. *Nat Phys* **12**, 311–317 (2016). URL <http://www.nature.com/nphys/journal/v12/n4/abs/nphys3594.html#supplementary-information>. (see pp. 76, 78).
- [190] Jandke, J. *et al.* Scanning tunneling spectroscopy on $\text{SrFe}_2(\text{As}_{1-x}\text{P}_x)_2$. *Phys. Rev. B* **93**, 104528 (2016). URL <http://link.aps.org/doi/10.1103/PhysRevB.93.104528>. (see pp. 76, 77).
- [191] Taylor, A. E. *et al.* Antiferromagnetic spin fluctuations in LiFeAs observed by neutron scattering. *Phys. Rev. B* **83**, 220514 (2011). URL <http://link.aps.org/doi/10.1103/PhysRevB.83.220514>. (see p. 77).
- [192] Chu, C. *et al.* The synthesis and characterization of LiFeAs and NaFeAs. *Physica C: Superconductivity* **469**, 326–331 (2009). URL <http://www.sciencedirect.com/science/article/pii/S0921453409000653>. Superconductivity in Iron-Pnictides. (see p. 77).
- [193] Allan M. P. *et al.* Identifying the 'fingerprint' of antiferromagnetic spin fluctuations in iron pnictide superconductors. *Nat Phys* **11**, 177–182 (2015). URL <http://www.nature.com/nphys/journal/v11/n2/abs/nphys3187.html#supplementary-information>. (see p. 77).
- [194] Shein, I. R. & Ivanovskii, A. L. Band structure of a new (16–18 K) superconductor LiFeAs compared to $\text{Li}_{0.5}\text{FeAs}$ and LiCoAs . *JETP Letters* **88**, 329–333 (2009). URL

- <http://dx.doi.org/10.1134/S0021364008170098>. (see p. 78).
- [195] Hoogenboom, B. W., Berthod, C., Peter, M., Fischer, Ø. & Kordyuk, A. A. Modeling scanning tunneling spectra of $\text{Bi}_2\text{Sr}_2\text{CaCu}_2\text{O}_{8+\delta}$. *Phys. Rev. B* **67**, 224502 (2003). URL <http://link.aps.org/doi/10.1103/PhysRevB.67.224502>. (see p. 81).
- [196] Levy de Castro, G., Berthod, C., Piriou, A., Giannini, E. & Fischer, Ø. Preeminent Role of the Van Hove Singularity in the Strong-Coupling Analysis of Scanning Tunneling Spectroscopy for Two-Dimensional Cuprate Superconductors. *Phys. Rev. Lett.* **101**, 267004 (2008). URL <http://link.aps.org/doi/10.1103/PhysRevLett.101.267004>. (see p. 81).
- [197] Onufrieva, F. & Pfeuty, P. Comment on “Preeminent Role of the Van Hove Singularity in the Strong-Coupling Analysis of Scanning Tunneling Spectroscopy for Two-Dimensional Cuprate Superconductors”. *Phys. Rev. Lett.* **105**, 099701 (2010). URL <http://link.aps.org/doi/10.1103/PhysRevLett.105.099701>. (see p. 81).
- [198] Pilgram, S., Rice, T. M. & Sigrist, M. Role of Inelastic Tunneling through the Insulating Barrier in Scanning-Tunneling-Microscope Experiments on Cuprate Superconductors. *Phys. Rev. Lett.* **97**, 117003 (2006). URL <http://link.aps.org/doi/10.1103/PhysRevLett.97.117003>. (see p. 81).
- [199] Scalapino, D. J. Superconductivity: Pairing glue or inelastic tunnelling? *Nature Physics* **2**, 593–594 (2006). URL <http://www.nature.com/nphys/journal/v2/n9/abs/nphys398.html>. (see p. 81).
- [200] Grajcar, M., Plecenik, A., Seidel, P., Vojtanik, V. & Barholz, K.-U. Asymmetry and quasilinear background of differential conductance characteristics of high- T_c -superconductor/metal tunnel junctions. *Phys. Rev. B* **55**, 11738–11744 (1997). URL <http://link.aps.org/doi/10.1103/PhysRevB.55.11738>. (see p. 81).
- [201] Zasadzinski, J. & Iavarone, M. Comparison of Tunneling in Fe-based Superconductors with Multi-band MgB_2 . *Bulletin of the American Physical Society* (2016). (see p. 83).
- [202] Hlobil, P. & Orth, P. P. Luminescence and squeezing of a superconducting light-emitting diode. *Phys. Rev. B* **91**, 205303 (2015). URL <http://link.aps.org/doi/10.1103/PhysRevB.91.205303>. (see pp. 85, 86, 91, 92, 93, 94, 96, 97, 98, 100, 103, 108, 131).
- [203] Yuen, H. P. Two-photon coherent states of the radiation field. *Phys. Rev. A* **13**, 2226–2243 (1976). URL <http://link.aps.org/doi/10.1103/PhysRevA.13.2226>. (see p. 85).
- [204] Nielsen, M. A. & Chuang, I. L. *Quantum computation and quantum information* (Cambridge university press, 2010). (see p. 85).
- [205] O’Brien Jeremy L., Furusawa Akira & Vuckovic Jelena. Photonic quantum technologies. *Nat Photon* **3**, 687–695 (2009). 10.1038/nphoton.2009.229. (see p. 85).

- [206] Gisin Nicolas & Thew Rob. Quantum communication. *Nat Photon* **1**, 165–171 (2007). URL [10.1038/nphoton.2007.22](https://doi.org/10.1038/nphoton.2007.22). (see p. 85).
- [207] Hanamura, E. Superradiance from p–n Junction of Hole- and Electron-Superconductors. *physica status solidi (b)* **234**, 166–171 (2002). URL [http://dx.doi.org/10.1002/1521-3951\(200211\)234:1<166::AID-PSSB166>3.0.CO](http://dx.doi.org/10.1002/1521-3951(200211)234:1<166::AID-PSSB166>3.0.CO). (see p. 85).
- [208] Asano, Y., Suemune, I., Takayanagi, H. & Hanamura, E. Luminescence of a Cooper Pair. *Phys. Rev. Lett.* **103**, 187001 (2009). URL <http://link.aps.org/doi/10.1103/PhysRevLett.103.187001>. (see p. 85).
- [209] Recher, P., Nazarov, Y. V. & Kouwenhoven, L. P. Josephson Light-Emitting Diode. *Phys. Rev. Lett.* **104**, 156802 (2010). URL <http://link.aps.org/doi/10.1103/PhysRevLett.104.156802>. (see p. 85).
- [210] Godschalk, F., Hassler, F. & Nazarov, Y. V. Proposal for an Optical Laser Producing Light at Half the Josephson Frequency. *Phys. Rev. Lett.* **107**, 073901 (2011). URL <http://link.aps.org/doi/10.1103/PhysRevLett.107.073901>. (see p. 85).
- [211] Baireuther, P., Orth, P. P., Vekhter, I. & Schmalian, J. Manipulation of a Two-Photon Pump in Superconductor-Semiconductor Heterostructures. *Phys. Rev. Lett.* **112**, 077003 (2014). URL <http://link.aps.org/doi/10.1103/PhysRevLett.112.077003>. (see pp. 85, 88, 94, 98).
- [212] Hayat, A., Kee, H.-Y., Burch, K. S. & Steinberg, A. M. Cooper-pair-based photon entanglement without isolated emitters. *Phys. Rev. B* **89**, 094508 (2014). URL <http://link.aps.org/doi/10.1103/PhysRevB.89.094508>. (see p. 85).
- [213] Schroer, A. & Recher, P. Detection of nonlocal spin entanglement by light emission from a superconducting $p - n$ junction. *Phys. Rev. B* **92**, 054514 (2015). URL <http://link.aps.org/doi/10.1103/PhysRevB.92.054514>. (see p. 85).
- [214] Mou, S. S. *et al.* Optical observation of superconducting density of states in luminescence spectra of InAs quantum dots. *Phys. Rev. B* **92**, 035308 (2015). URL <http://link.aps.org/doi/10.1103/PhysRevB.92.035308>. (see pp. 85, 98).
- [215] Hayashi, Y. *et al.* Superconductor-based Light Emitting Diode: Demonstration of Role of Cooper Pairs in Radiative Recombination Processes. *Applied Physics Express* **1**, 011701 (2008). URL <http://stacks.iop.org/1882-0786/1/i=1/a=011701>. (see pp. 85, 105).
- [216] Takayanagi, H., Inoue, R., Akazaki, T., Tanaka, K. & Suemune, I. Superconducting transport in an {LED} with Nb electrodes. *Physica C: Superconductivity* **470**, 814–817 (2010). URL <http://www.sciencedirect.com/science/article/pii/S0921453410001814>. Vortex Matter in Nanostructured Superconductors. (see p. 85).
- [217] Inoue, R., Takayanagi, H., Akazaki, T., Tanaka, K. & Suemune, I. Transport characteristics of a superconductor-based LED. *Superconductor Science and Technology*

- 23**, 034025 (2010). URL <http://stacks.iop.org/0953-2048/23/i=3/a=034025>. (see pp. 85, 105).
- [218] Suemune, I. *et al.* A Cooper-Pair Light-Emitting Diode: Temperature Dependence of Both Quantum Efficiency and Radiative Recombination Lifetime. *Applied Physics Express* **3**, 054001 (2010). URL <http://stacks.iop.org/1882-0786/3/i=5/a=054001>. (see pp. 85, 105).
- [219] Ignatov, A., Yuan, R. & Wang, N. Photo luminescence of Cooper pairs in a naturally occurring heretostucture $K_{0.75}Fe_{1.75}Se_2$. *arXiv preprint arXiv:1307.3471* (2013). (see p. 85).
- [220] Sasakura, H. *et al.* Enhanced Photon Generation in a Nb/n – InGaAs/p – InP Superconductor/Semiconductor-Diode Light Emitting Device. *Phys. Rev. Lett.* **107**, 157403 (2011). URL <http://link.aps.org/doi/10.1103/PhysRevLett.107.157403>. (see pp. 85, 105).
- [221] McMillan, W. L. Tunneling Model of the Superconducting Proximity Effect. *Phys. Rev.* **175**, 537–542 (1968). URL <http://link.aps.org/doi/10.1103/PhysRev.175.537>. (see p. 86).
- [222] Szymańska, M. H., Keeling, J. & Littlewood, P. B. Nonequilibrium Quantum Condensation in an Incoherently Pumped Dissipative System. *Phys. Rev. Lett.* **96**, 230602 (2006). URL <http://link.aps.org/doi/10.1103/PhysRevLett.96.230602>. (see pp. 87, 95).
- [223] Szymańska, M. H., Keeling, J. & Littlewood, P. B. Mean-field theory and fluctuation spectrum of a pumped decaying Bose-Fermi system across the quantum condensation transition. *Phys. Rev. B* **75**, 195331 (2007). URL <http://link.aps.org/doi/10.1103/PhysRevB.75.195331>. (see pp. 87, 95).
- [224] Kronig, R. d. L. On the Theory of Dispersion of X-Rays. *J. Opt. Soc. Am.* **12**, 547–557 (1926). URL <http://www.osapublishing.org/abstract.cfm?URI=josa-12-6-547>. (see p. 94).
- [225] Scully, M. O. & Zubairy, M. S. *Quantum optics* (Cambridge university press, 1997). (see p. 98).
- [226] Keeling, J., Szymańska, M. H. & Littlewood, P. B. *Optical Generation and Control of Quantum Coherence in Semiconductor Nanostructures*, chap. Keldysh Green’s function approach to coherence in a non-equilibrium steady state: connecting Bose-Einstein condensation and lasing, 293–329 (Springer Berlin Heidelberg, Berlin, Heidelberg, 2010). URL http://dx.doi.org/10.1007/978-3-642-12491-4_12. (see pp. 100, 105).
- [227] Hakioglu, T., Ivanov, V. A., Shumovsky, A. S. & Tanatar, B. Phonon squeezing via correlations in the superconducting electron-phonon interaction. *Phys. Rev. B* **51**, 15363–15368 (1995). URL <http://link.aps.org/doi/10.1103/PhysRevB.51.15363>. (see p. 105).